CHARACTERIZATION OF PREFORM PERMEABILITY AND FLOW BEHAVIOR FOR LIQUID COMPOSITE MOLDING

By

Stephen Joseph Sommerlot

A THESIS

Submitted to
Michigan State University
in partial fulfillment of the requirements
for the degree of

Mechanical Engineering – Master of Science

2015

ABSTRACT

CHARACTERIZATION OF PREFORM PERMEABILITY AND FLOW BEHAVIOR FOR LIQUID COMPOSITE MOLDING

By

Stephen Joseph Sommerlot

Preform characterization is an important step in the processing of high-performance parts with liquid composite molding. A better understanding of preform compressibility and permeability creates more accurate process models, ultimately leading to high-quality finished composites. Without characterization, mold design and processing parameters are subject to guess-work and ad hoc optimization methods, which can result in poor infusions and inconsistent part quality. In this study, a complex architecture fiber reinforcement was characterized in compaction and permeability for liquid composite molding. Preforms of a four-harness satin carbon fabric were assembled with and without a novel inter-layer tackifier for experimentation. Compaction and permeability were measured to investigate the effects of the tackifier system, debulking, preform layup, and other processing parameters. Permeability and flow behavior was measured through saturated and unsaturated techniques, including investigations of fluid effects and high-flow rate infusions. The tackifier was seen to decrease permeability in both saturated and unsaturated cases, while notably influencing the orientation of first principal permeability. Tackified preforms also displayed a sensitivity to fluid type that non-tackified samples did not. Experimentally derived permeability was also used to generate numerical mold fill simulations of radially injected infusions, which produced favorable results.

This thesis is dedicated to Renee.

ACKNOWLEDGEMENTS

Firstly, I would like to acknowledge my advisor, Dr. Alfred Loos, for giving me the opportunity to conduct research during my undergraduate at the Composite Vehicle Research Center and, of course, for allowing me to attend graduate school at Michigan State University to study Mechanical Engineering. His guidance, advice, and support were invaluable during my years in college.

I would also like to acknowledge Tim Luchini, my collaborative lab-mate on our project, whose experience, thoughtful input, and intellect were instrumental in my research and studies.

I would finally like to thank General Electric Aviation and the fine people there for the valuable collaboration of the GE-MSU Advanced Composite Research Program. Acknowledgements are due to Gregory Gemeinhardt, Casey Berschback, Bryant Walker, Folusho Oyerokun, and Swapnil Dhumal. Without the opportunity and funding from GE, this research would not be possible.

TABLE OF CONTENTS

LIST OF TABLES

LIST OF FIGURES

KEY TO SYMBOLS

English symbols:

A	area
A_w	fabric areal weight
A_{1fiber}	surface area of one fiber
a	experimental constant or fiber volume fraction for initial compaction pressure
a_{dry}	empirical constant for dry compaction
a_{wet}	empirical constant for wetted compaction
b	experimental constant or compaction stiffening index
b_{dry}	empirical constant for dry compaction
b_{wet}	empirical constant for wetted compaction
C	mean circumference of the Du Noüy ring
Ca	capillary number
C_k	Kozeny constant
$C_{\parallel}$	parallel fiber packing arrangement constant
$C_{\perp}$	perpendicular fiber packing arrangement constant
c	experimental constant or pressure decay after 1s in compaction
c_f	Du Noüy ring correction factor
c_T	experimental constant in the Hoffman-Voinov-Tanner law
c_{wet}	empirical constant for wetted compaction
d	experimental constant, characteristic length, relaxation index in compaction

d_f	fiber diameter
d_p	particle diameter
E	Young's modulus
E_c	critical error
E_{nD}	non-Darcy error
e	exponential function
F	form factor or external source vector
F_w	measured wetting force
Fo	Forchheimer number
Fo_c	critical Forchheimer number
g	gravitational constant
h	race-tracking gap thickness
K	spring constant
K_0	initial spring constant
k	analytical fiber network compaction parameter
L	preform length in direction of flow
L_{tow}	length between tows
ln	natural logarithm
l_{tow}	length between fiber within a tow
M	representative reinforcement rigidity
M_w	molecular weight
m	slope parameter in saturated and unsaturated permeability formulation
m_1	first empirical constant in second order fit for fluid flow through porous media

m_2	second empirical constant in second order fit for fluid flow through porous media
n	number of fabric layers
P	compaction or fluid pressure
P_{app}	applied pressure
P_{atm}	applied atmospheric pressure
P_c	capillary pressure
P_f	pressure supported by the fiber preform
P_{inj}	injection pressure
P_r	resin pressure
P_0	initially supplied compaction pressure
p	wetted perimeter
p_1	pressure at inlet for gaseous flows
p_2	pressure at outlet for gaseous flows
Q	volumetric flow rate
Q_p	pump flow rate
q	Darcy flux
q_x	Darcy flux in x-direction
q_y	Darcy flux in y-direction
q_z	Darcy flux in z-direction
R	universal gas constant or radius of the Du Noüy ring
Re	Reynolds number
Re^{max}	maximum Reynolds number
RV_f	representative fiber volume fraction

r	radius of the Du Noüy ring wire
r_f	fiber radius or flow front radius for radial permeability
r_h	hydraulic radius
r_0	inlet radius for radial permeability
S	permeability
S^{Darcy}	Darcy fit derived permeability
S_f	surface area of interface per unit volume of the fluid
$S^{For.}$	Forchheimer fit derived permeability
S_{gap}	permeability of race-tracking gap
S_{geo}	geometrical permeability
S^{rel}	relative permeability
S^{sat}	saturated permeability
S^{unsat}	unsaturated permeability
S_{xx}	permeability in fabric warp direction
S_{yy}	permeability in fabric weft direction
S_{zz}	through thickness or transverse permeability
$S_{xx}{}'$	permeability in the off-axis direction
S_{11}	first principal permeability
S_{22}	second principal permeability
S_{33}	third principal permeability
T	temperature or transformation matrix
t	time or thickness
$V_a{}'$	empirically defined maximum available fiber volume fraction

V_f fiber volume fraction

V_{fmax} maximum fiber volume fraction

V_{f0} fiber volume fraction of unsheared fabric

$V_{f\infty}$ fiber volume fraction at maximum compression

V_{1fiber} volume of one fiber

W_A work of adhesion

W_A^a advancing work of adhesion

W_A^r receding work of adhesion

x fabric warp direction of flow front location

x_0 inlet radius for radial permeability

x_f flow front position for radial permeability

y fabric weft direction

y_0 inlet radius for radial permeability

y_f flow front position for radial permeability

z transverse direction or gas compressibility factor

Greek symbols:

α viscous resistance

α_s sink term

β orientation of first principal permeability in reference to the fabric warp direction

γ non-Darcy coefficient

η reinforcement compaction parameter

θ fluid/fiber/air contact angle

θ_{dyn}	dynamic contact angle
θ_0	contact angle at thermodynamic equilibrium
μ	fluid viscosity
v	superficial fluid velocity
v^*	interstitial velocity or average particle velocity
ρ	density
ρ_{air}	air density
ρ_f	fiber density
ρ_{fluid}	fluid density
ρ_p	fluid density in the pump for gaseous flows
σ	fluid surface tension or applied stress in reinforcement compaction
σ'	raw fluid surface tension reading
τ_{ij}	stress tensor
φ	porosity

1. Introduction

1.1 Background

1.1.1 Presence and Benefits of Composite Materials

In recent years, integration of advanced composite materials in structural vehicle components has become more prevalent. Due to increased regulations for efficiency and demand for high performance, composites are a preferred choice for aircraft components. This is driven by their exceptional properties and light-weighting potential for the aerospace industry. An excellent example of this is the Boeing 787 Dreamliner. This new generation of aircraft has an airframe that is composed of 50% advanced composite material which offers weight savings on average of 20% compared to conventional aluminum designs. Composite implementation also requires less scheduled and non-routine maintenance for structures compared to those of traditional metals [1]. Composite materials have good fatigue performance, while also possessing a great resistance to environmental effects.

Further technological advances, regarding the use of advanced composites, can be seen powering the 787; the General Electric next generation (GEnx) jet engine. The GEnx is produced with both a fan case and fan blades fabricated from composite materials. Carbon fiber composite fan blades are lighter than their traditional metal counterparts, which means less energy is generated in the rare case of a blade-out event. This allows a composite fan case to successfully contain the projectile, offering further major weight savings. GE has claimed to have saved around 350 pounds per engine with this composite implementation [2]. These features offer weight reduction, which in turn reduces fuel consumption, while component durability is increased.

Soutis [3] states, “Carbon fiber composites are here to stay in terms of future aircraft construction since significant weight savings can be achieved”.

Direct implementation of advanced composite materials into aerospace design involves many technical challenges, including the processing of the material itself. Material and processing costs have been cited as one of the main challenges restricting the use of carbon fiber reinforced plastics (CFRP) in industry [3]. Time and money must be invested in the processing to produce a desired part that meets standards of quality and performance. Care must be taken during processing, as wasted material can be costly, thus optimization of the fabrication process is highly desired. Many resulting properties of an advanced composite are dependent on the processing and fabrication steps. Due to this, processing continues to be a highly researched subset in the advanced composite arena.

1.1.2 Liquid Composite Molding

In general, composites can be split into two categories: those that use a thermoset matrix and those that use a thermoplastic matrix. The main difference between these two types of composites are that thermosets undergo an irreversible chemical crosslinking when they are cured, while thermoplastics can be cured then later reheated, melted, and reprocessed [4]. Processing these different categories of composites involves many different methods and techniques. For thermosetting based composites, liquid composite molding (LCM) techniques generally are used to infuse a fibrous reinforcement with a thermosetting resin and cure a finished part. LCM is an umbrella term including specific methods like resin transfer molding (RTM) and its variations including compression resin transfer molding (CRTM), and vacuum

assisted resin transfer molding (VARTM). Other LCM methods include structural injection molding (SRIM), resin film infusion (RFI), and resin infusion under flexible tooling (RFIT) technologies, including company-patented processes like Seemann Composites Resin Infusion Molding Process (SCRIMP). RTM and RFI have been cited as the predominant curing processes being developed today, while VARTM is considered to be the manufacturing process of choice for the future in the aircraft industry [3]. RTM processes are attractive due to the potential high rate of production and high quality of finished parts. This also allows for efficient fabrication of large complex components [5].

The RTM process involves loading a fibrous preform into a mold cavity of set thickness and then a low-viscosity thermoset polymer resin is injected, often at elevated temperatures. Then, the mold is heated to cure the resin and produce a finished composite part [5]. This process in itself contains many processing parameters and variables: part geometry, reinforcement material, resin type and viscosity, injection flow rate/pressure, air vent locations, tool temperature, resin injection temperature, etc. These process parameters can affect the mold fill and ultimately the finished part quality. Thus, it is important to accurately represent and understand these parameters in RTM mold design. There are three basic stages of the RTM process: preforming, mold filling, and curing. Variation can start in the preforming stage; the reinforcement can become deformed when being placed in a mold, especially those of complex shapes. This deformation will alter the fiber orientation of the reinforcement, which in turn will alter the resin flow during injection [6]. In the mold filling stage, the injected resin's flow path and fabric saturation is subject to the fabric parameters such as architecture and geometry. Darcy's law has been used to describe the resin flow through fabric reinforcements in LCM where resin viscosity

and preform permeability are the two important parameters that control fiber wet-out and impregnation rate of the preform [5]. These factors drive experimental characterization so that accurate process models can be developed to optimize the manufacturing process. Resin properties must be investigated through rheology and due to the large variety of fabric types and architectures, preform permeability characterization is necessary.

The focus of this research will be on the topic of preform and flow characterization for RTM modeling. Methods and experimental approaches for permeability measurement and fluid properties will be discussed in detail in later chapters. Process modeling's main function is to make fabrication more cost effective and efficient, producing the highest quality parts possible. Originally, trial-and-error approaches were the only options available to develop process cycles [7]. Success can be found with these types of methods, but they can come at considerable costs due to material and energy waste. A process modeling approach is a natural direction to take in LCM research. Simulation of a resin injection prior to an actual infusion allows engineers to optimize mold vent locations, injection pressures, and injection locations, while mold fill time and possible areas of trouble (dry-spotting, race-tracking, etc.) can be investigated before money is spent on physical mold creation and materials.

Resin flow is a critical issue in the process; it affects the fiber volume fraction distribution, formation of resin rich regions and final part dimensions [7]. Modelling this can be very complex as the resin flow, heat transfer, and curing reaction are all coupled. However, in most cases, the mold is filled before curing takes place, and before the resin viscosity is significantly affected. This allows the flow problem to be uncoupled from the heat transfer and cure kinetics, i.e. create

an isothermal flow analysis [6]. This isothermal flow assumption permits investigation of fluid flow through a fibrous reinforcement to be isolated for experimental characterization and implemented in process models to produce accurate results. Cure kinetics and heat transfer analyses can then be implemented after the mold filling stage to fully simulate the process.

1.1.3 Preforming and the Use of Tackifiers/Binders

In RTM, the fibrous reinforcement is initially dry and generally is assembled outside the mold. This fibrous assembly is what is referred to as the preform, which often is constructed in the final part shape before being set in the mold [8]. Preforms are constructed of many different types of fabrics manufactured by methods such as weaving, braiding, knitting, and stitching. Fabrics are often composed of glass, carbon, or aramid fibers. This study will focus on a harness satin weave carbon fabric reinforcement, which is used for composite structural aerospace components.

The preforming stage of RTM consists of cutting the reinforcement of interest to the part shape and laying it up in a desired stacking sequence if necessary. This process is often done by hand and can be very time consuming, while maintaining the fiber orientations and conforming the reinforcement into part shape can be difficult [8]. Due to these challenges, reinforcements are often treated with tackifiers or binders which enable fiber position to be maintained and aid in preform construction. These tackifiers are generally thermoplastic polymers or thermoset resins that are solid until enough heat is applied to melt them, which then allows fibers of the reinforcement to bond together upon cooling. These tackifiers are commonly applied to reinforcements in powder, liquid spray, or veil forms [9]. Tackifiers and binders give additional benefits of preform consolidation, decreasing preform springback, reducing slip between

reinforcement layers by adding sufficient tack, and overall aiding in net-shape production. In performance aerospace composites, a partially reacted matrix resin is often used, called a reactive tackifier. This is usually a tackifier of chemistry that is compatible to the RTM resin, which helps ensure that degradation of mechanical properties does not occur [8].

Adding a tackifier in the preforming stage of a can have multiple effects on the RTM filling stage [9]–[12] and final part properties [10], [12]. The presence of tackifier in a preform alters the total preform geometry and permeability/resin flow can be affected greatly. The assumption that a fiber preform with and without a tackifier will produce the same permeability and resin flow characteristics is not accurate without validation. Neglecting an investigation of the permeability change could lead to processing issues and failed parts. With many aerospace components employing a tackifier for RTM preforming, this is a research area that needs more investigation. Tackifier type, pre-processing (e.g. debulking before infusion), and fabric geometry all produce a variety of physical effects than can alter preform compaction, permeability, resin flow and ultimately the RTM mold fill and final part quality.

1.2 Research Objectives

In this study, research was conducted largely on an experimental front with a complex architecture carbon fiber fabric with and without a low areal weight tackifier. Experimental measurements of compaction, permeability, and flow front propagation were conducted on preforms to determine the effects of tackifier, and allow for mathematical representation for use in component process modeling of resin transfer molding. Research in tackified preforms for

permeability and fiber wet out is limited compared to general investigations of neat fabric infusions. Specifically, the objectives of this research will address:

- Compaction
    - Effect of tackifier
- Saturated permeability measurements
    - In-plane permeability
        - Determination of principal permeabilities
        - Effect of tackifier
    - Transverse permeability
        - Effect of tackifier
- Unsaturated permeability measurements
    - Effect of tackifier on mold fill time and principal permeability orientation
- Fluid effects on preforms with and without tackifier
    - Capillary effects
        - Surface tension and contact angle of differing fluid types
- Non-Darcy Flow
    - High flow rate infusion investigation and possible situations of error with Darcy's law assumption for permeability

Ultimately, industry interest lies in the ability to create accurate component mold-fill simulations in LCM and understand how altering preform parameters will affect resulting infusions and component quality. A latter chapter in this thesis will introduce simple mold fill simulations produced from experimental preform characterization. Knowledge of resin flow behavior aids in the mold design process, where optimal location of vents and gates can be investigated for better

infusions. Improper mold design and poor understanding of preform permeability can lead to defects in processed components including race-tracking, void formations, and ultimately poorer quality finished parts. This presented research will address these issues through an LCM-related characterization study of a complex architecture carbon fabric with a previously unstudied tackifier additive.

1.3 Materials

The reinforcement of interest in this study is a four harness satin, carbon fabric. This fabric is woven of IM7 carbon fibers in 6K bundles. For ease of representation, this fabric will be expressed as "IM7-4HS" in the following chapters. Also, a tackified version of this fabric was used in experimentation. This tackified IM7-4HS uses the Cytec CYCOM PR 520-1 low areal weight film, which is pre-impregnated on the fabric's surface by the manufacturer and acts as a tackifier for preforming purposes. The exact wt% distributed on the fabric is proprietary. Seen in Table 1.1, are the basic weave architecture and composition properties of the IM7-4HS fabric. The areal weight displayed here was determined experimentally, while other data is provided by the manufacturer.

Table 1.1: IM7-4HS Basic Properties

Weave	Areal Weight (g/m^2)	Fiber Type	Tow Size	Fiber Density (g/cm^3)	Fiber Diameter (microns)
4-Harness Satin	204	IM7	6K	1.78	5.2

For permeability and flow testing, SAE 40 single weight motor oil was used as the baseline test fluid. This oil has a constant viscosity at room temperature of 0.24 Pa-s. This test fluid allows for constant viscosity at temperature similar in value to those seen in common RTM and VARTM resin systems. The SAE 40 oil also offers ease of use as the standard test fluid. It is benign in

relation to test equipment, whereas resins require extra cleanup time and preparation work so that equipment is not destroyed. While investigating the effect of fluid type on permeability, a second test fluid will be introduced: Applied Poleramic's SC-15 epoxy resin. This resin will be described in more detail in later chapters and is used in limited test settings.

2. Literature Review

For decades, researchers have studied liquid composite molding (LCM) processes and have investigated the key process parameters and their resulting effects. Accurate and robust LCM process modeling has been a continually sought goal in the field of advanced composite manufacturing. Application of well-tuned process models allows for manufacturing optimization and leads to better designed tooling and high quality finished composite parts. This present research will overview LCM processes with a focus on Resin Transfer Molding (RTM) and go further to survey the relevant work conducted on preform characterization including compressibility and permeability for process modeling. These material parameters are of the most important factors in creating an accurate LCM infusion model. Experimental techniques will be discussed for both preform compressibility and permeability characterization. Modeling approaches of empirical, analytical and numerical nature will also be surveyed for these parameters.

2.1 Liquid Composite Molding

Liquid composite molding is a class of composite manufacturing that is generally applied to the infusion of fibrous reinforcement with a thermosetting resin. In general, LCM processes consist of injecting a resin into a dry bed of fiber reinforcement housed in a mold, which is then cured to create a finished composite part. The LCM family of processes consists of multiple techniques. Some of the most popular techniques include resin transfer molding (RTM), compression resin transfer molding (CRTM), RTM light, vacuum-assisted resin transfer molding, (VARTM), resin infusion (RI), structural injection molding (SRIM), resin film infusion (RFI), and Seemann Composite Resin Infusion Molding Process (SCRIMP). These various techniques offer different advantages depending on the application. RTM, a rigid closed mold technique, has found application in the automotive and aerospace industries due to its potential for high production rates and quality of finished parts [5]. RTM light possesses a similar setup to RTM but offers the ability to visually observe the progress of the resin impregnation through translucent flexible tooling. VARTM consists of vacuum-bagging the fiber reinforcement to a tool, which is essentially an open mold process where a vacuum pump drives the resin infusion. The VARTM process has been used produce medium to large, high performance composite parts, often in the marine and aerospace industry, where the equipment cost is much lower than that of RTM [13]. In the SCRIMP method, channels are used in the tooling to reduce flow resistance during infusions, which distribute the resin quickly across the part then wets out the preform [14]. The SCRIMP technique is used to produce large composites such as boats or decks while offering a safer alternative compared to the traditional hand lay-up or spray-up techniques used for those products, which produce high volatile organic compound emissions [15]. This research will focus on the RTM method, and further literature will be reviewed on this subset. Other LCM

techniques will not be discussed in detail here, but further background can be found in [14], [16], [17].

Traditionally, optimization of composite manufacturing was an experience based and trial-and-error approach, but in the last few decades, engineers have begun implementing process modeling to mitigate manufacturing expenses [17]. The modeling of an LCM processes can include reinforcement draping, impregnation, and curing. Of these aspects, understanding the flow process is of utmost importance for all the liquid molding processes [14]. Poor reinforcement saturation or fiber wet-out can produce low quality or unusable finished parts. Using process modeling, simulations can be used to predict resin flow through the fiber reinforcement and bring to light potential problem areas in the tooling or infusion. Based on these simulation results, tooling, material, and process parameters can be optimized before any high-cost decisions are made. LCM process parameters have been studied for decades and still can present difficulties in manufacturing environments. Specifically, the RTM process and parameters will be reviewed next.

2.1.1 Resin Transfer Molding

The basic RTM method involves injected a thermosetting resin into a dry fiber reinforcement inside a closed mold. The mold is then heated to cure the matrix and opened to reveal a finished composite part. RTM was first developed mainly for use in the aerospace sector, and has grown to be a widely used method for composite manufacturing in not only aerospace, but also in the automotive, civil, and sporting goods industries [14]. Now, RTM is considered the state-of-the-art method for producing textile reinforced composite parts [18]. Although RTM processing has

been studied for many years, it is still considered to be underutilized, while reproducibility and better understanding of the resin flow are considered to be the main obstacles holding this technology back [14]. In a general sense, the RTM process can be split into three steps: fiber preforming, resin infusion, and part curing.

2.1.1.1 Fiber Preforming

In RTM, the fiber reinforcement is often assembled outside of the mold into a preform, which is in the shape of the finished part [8]. For complex shape composite parts, the fiber reinforcements need to deform to the shape of the mold surface [19], thus a need for the dry reinforcement to hold these contours is born. Here, preforming allows for easier handling of the reinforcement and the ability to prepare for near net-shape production. The most common preforming techniques involve the use of fabrics where a polymer binder/tackifier or stitching and embroidery techniques are often employed to hold fiber orientation and multiple layers together [20]. For this study, particular focus will be applied to the use of binders or tackifiers.

Tackifiers are most commonly thermoplastic or thermosetting resins that retain a solid structure at room temperature but melt with applied heat. The advantage of these resins are that upon cooling, resolidification allows the bonding of plies or tows into a consolidated preform [8]. Preforms then can be handled without the loss of fibers in a final-part form which can then be infused in an LCM process. Methods of tackifier application utilize powder, liquid, veil or string forms that are applied to the reinforcement at some point during the manufacturing process [8], [21]. Tackifiers have been studied for their effect on preform springback [9], [22], effected finished-part mechanical properties [21], [23], [24], and permeability and fiber wet-out [9]–[12].

While several studies exist, compared to other parameters involving permeability and resin flow, the effect of tackifiers in RTM and other LCM processes has been investigated on a much smaller scale. Due to the variety of different tackifier forms and concentrations, and the added variation of pre-processing abilities with tackifiers, the resulting influence on resin flow is inherently complex. A main focus of this study will aim to clarify and quantify the effect of a specific tackifier on preform compaction and permeability.

2.1.1.2 Resin Infusion

The majority of this thesis will investigate preform parameters and their effects during the infusion stage of the RTM process. In this step, resin is injected at pressure or flow rate into the closed mold and infiltrates the preform. Major quality problems have stated to come from unbalanced resin flow during the infusion step [25], and thus has become a significant area of research. The mold filling stage of the RTM and LCM processes are critical in the development of a quality finished composite part. Poor infusion or misunderstanding of preform permeability may lead to defects including dry spotting or void formations and can be avoided with appropriate prediction methods [26]. These are important considerations as the standard of US aeronautics rejects parts that contain more than 2% of void defects [27].

To understand the resin infusion, one must first consider the general multiphase flow and thermodynamics inherent to the process. On a general level, the infusion can be considered as non-isothermal fluid flow through a porous media, which can be modeled on the basis of fluid velocity, pressure and temperature into the media [14]. This can become a very complex problem when considering heat transfer from the mold to the preform and resin. The heat transfer, fluid

flow, and resin cure reaction are all coupled and must be solved simultaneously. The governing equations for this general approach will not be discussed in detail here; more background can be found in [14]. For simplification purposes, most researchers apply an isothermal flow assumption. This allows investigators to approach the fluid flow uncoupled from heat transfer and resin cure kinetics and the permeating fluid can be considered constant in viscosity [6].

Regarding isothermal flow and with the assumption of low Reynolds number, resin flow through fibrous preforms has generally been considered to be modeled as flow through porous media governed by Darcy's law seen in Equation 1.

$$Q = \frac{SA}{\mu}\frac{\Delta P}{L} \tag{1}$$

In this relationship, Q is the volumetric fluid flow rate, A is the medium's area normal to the flow direction, μ is the fluid viscosity, L is the medium length in direction of flow, ΔP is the measured pressure drop across that length, and S is the porous medium's permeability. Permeability is proportionality constant in this relation and describes the ease of flow through a porous media with units of length squared. Preform permeability is the key parameter that drives the flow in RTM [25]. Depending on the preform geometry, fiber content and flow direction, permeability can vary on the order of magnitudes. Significant research has been made in experimental and theoretical fronts to define permeability for fiber reinforcements. This study will extend research further to investigate flow properties and permeability with reinforcement treated with a novel tackifier. Further background and research trends will be surveyed regarding preform permeability and flow in Section 2.3.

2.1.1.3 Curing

Ideally after the preform is completely saturated with resin, the RTM mold is heated in a specific cycle to cure the composite part. Resin curing is usually sought to be inhibited during the infusion stage in order to maintain a low resin viscosity for quick fiber wet out and allow for full saturation before the resin gels [28]. For a general, coupled solution, a cure kinetic model can be introduced as an auxiliary equation directly into the heat and mass balance equations, as well as relating to the flow model by virtue of resin viscosity [29]. Again, this is complex and specific integration of this method is described in more detail in [29]. By using the isothermal flow assumption as discussed earlier, a simpler thermal model can be used to describe cure. This assumption can be justified if the mold fill time is much shorter than the time required for the cure to affect viscosity of the resin [6]. This is often the case and will be a basis assumption for the work in this thesis. Although resin cure and kinetics are an important aspects of the RTM process, this is outside the scope of this study.

2.2 Reinforcement Compaction/Compressibility

Inherent to LCM processes are the manufacturing steps of loading the reinforcement in a tool or mold, closing the mold, infusing, and unloading the finished part. These loading and unloading portions of the manufacturing process can apply compression to the preform or reinforcement. For example, in the RTM the reinforcement is compressed by the closing of the mold, and with VARTM, a vacuum bag and vacuum pressure applies a compressive force to the preform. Also, debulking techniques may be applied in the preform process before infusion resulting in desired deformations or reinforcement compaction. The amount of compression experienced by reinforcement can be directly related to the fiber volume fraction and therefore is an essential

area of interest for LCM, as the fiber content will influence permeability and the resin infusion. Also for RTM, to acquire a desired fiber volume fraction, the tooling must be able to supply and withstand sufficient compressive force, while in VARTM, the vacuum pressure and compressibility of the preform will govern the finished part thickness [30]. The relaxation or spring-back of a reinforcement may also be relevant in certain the manufacturing situations, which is a studied phenomenon and should not be overlooked. These considerations are paramount to design of a good LCM process. Understanding of the compression behavior in a preform leads to a better understanding towards local preform variations, mold design, and ultimately leads to the production of better finished parts.

2.2.1 Defining Compressibility

Typically, the compression/compaction of a reinforcement can be quantified by relating the applied pressure on the material to the resulting reinforcement thickness or fiber volume fraction. As compaction pressure increases on a reinforcement, the thickness is generally seen to drop, while also the fiber volume fraction increases. Chen et al. [31] reviewed previous experimental compaction data [32] for woven fabrics and redefined four regimes existing on a typical compressibility curve of thickness versus pressure based on the works of [32], [33]. The authors first described a Regime 0 as an initial point where no pressure is applied to the reinforcement. Regime 1 was described as a linear portion of the thickness/pressure curve where compaction is initiated and slight pressure is produced. Regime 2 then was described as a nonlinear stage where the reinforcement is compacted further and large voids in the fabric's structure are filled and the reinforcement deforms. The researchers explained that the total deformation in this regime was due to both compression of the fibers and compression of the voids in the

architecture. Finally, Chen et al. [31] described Regime 3, a linear region of the curve where high pressure is applied. This region exhibits deformation of the fibers only as the porosity has reached a constant minimum. Reinforcements are also measured during unloading of supplied compaction pressure. Often, the unloading of a sample will exhibit a hysteresis phenomenon evident during compaction cycles as a fully unloaded reinforcement often will possess a higher volume fraction than what it initially had before the loading cycle. This difference can be attributed to fiber rearrangement, breakage and sliding during a cycle [34].

Another important consideration of reinforcement compressibility is the relaxation of the fiber network. Dependent on the loading cycle, the reinforcement may experience a viscoelastic recovery, permanent deformation, and/or elastic spring-back. Studying these phenomena has also been the aim of many researchers in LCM. The presence of resin or a test fluid in a preform during compaction also has been seen to influence compressibility and is of interest for certain LCM applications.

Quantifying the compressibility of reinforcements has been of interest in LCM research for many years. Experimental methods including empirical modeling have been used successfully by many researchers. Investigators have also created theoretical models based on beam theory, micromechanical structures, and consideration of the reinforcement during nonlinear elastic and viscoelastic behavior [30].

2.2.2 Measurement Techniques

While some theoretical models for the compressibility of fibrous reinforcements have been created, they are idealized for specific materials and non-robust so experimental characterization of preform compaction under loading and unloading is commonly employed. A common compaction experiment will include the loading and unloading of fibrous reinforcement in a matched metal mold to empirically derive a relationship between loading/supplied pressure and the resulting preform fiber volume fraction/porosity. Li et al. [35] described a fixture used for both transverse compaction and permeability measurements of fibrous reinforcements. The fixture allowed a fiber bed to be compressed in a cavity under constant compaction pressure while micrometers with dial indicators measured the change in the reinforcement's thickness. They used the relationship in Equation 2 to define the reinforcement's fiber volume fraction in terms of the measured thickness.

$$V_f = \frac{nA_w}{t\rho_f} \tag{2}$$

Here, V_f is the fiber volume fraction, A_w is the reinforcement areal weight, n is the number of layers of the reinforcement, t is the sample thickness, and ρ_f is the density of the fibers constituting the reinforcement. The fixture also featured porous compaction plates so that a test fluid could be introduced during compaction experiments. Grimsley et al. [36], [37] performed preform compaction experiments for VARTM characterization with a fixture that employed a vacuum bag for compression and allowed for resin infusion. A linear variable displacement transducer (LVDT) and a laser gage were used to measure the instantaneous preform thickness. The fiber volume fractions for these measurements were also derived from Equation 2. Somashekar et al. [38] used fixture that was loaded in an electromechanical testing frame. The fixture consisted of a top compression platen attached to the testing frame's crosshead and load

cell, while the material to be compacted was placed on a bottom platen. Laser gages were used to measure the sample thickness during loading and unloading while a specified strain rate of compaction was applied. The compaction study performed in this thesis reflects this method of Somashekar et al. [38]. The details of which will be described in Chapter 3.

Additionally, the relaxation of a reinforcement may be studied using a similar setup to compaction experiments. A typical relaxation experiment involves applying some type of loading/unloading cycle or strain rate to a reinforcement sample, then stopping the load and measuring the stress as a function of time as sample thickness is kept constant [39]. Somashekar et al. [38] used their compaction fixture to investigate the viscoelastic recovery of reinforcements through single compaction hold and quick release experiments and cyclical loading and unloading experiments.

2.2.3 Empirical Models and Experimental Trends

To quantify the compaction of wool samples, Van Wyk [40] applied a power law model, seen in Equation 3 based on beam theory, to empirically relate the applied stress, σ, the fiber volume fraction, V_f, and experimental constants a and b.

$$\sigma = a\left(V_f\right)^b \tag{3}$$

Although this model is simplistic in nature and lacks certain physical and geometrical consideration, it has been found to be successful spawning similar variations from following researchers [30]. Batch et al. [41] used a heuristic method to describe the applied compaction pressure in terms of the reinforcement's spring constant, K, which is defined as a function of fiber volume fraction, and V_0 is the initial fiber volume fraction. This is seen in Equation 4.

$$P = K(V_f)\left(V_f - V_0\right) \tag{4}$$

The spring constant was defined to be independent of fiber volume fraction or $K = K_0$ when V_f is less than V_{cont}, defined in Equation 5 where V_a is the high limit fiber volume fraction and η is a parameter of the reinforcement architecture.

$$V_{cont} = \left(\frac{1}{V_0} - \eta\left(\frac{1}{V_0} - \frac{1}{V_a}\right)\right)^{-1} \tag{5}$$

Batch et al. [41] further defined the spring constant for $V_f \geq V_{cont}$ as

$$K = K_0\left(\frac{1/V_{cont} - 1/V_a}{1/V_f - 1/V_a}\right) \tag{6}$$

They denoted that the parameters K_0, V_{cont}, V_0, and V_a are all to be fitted to experimental compaction curves. Others [42] have employed a least squares polynomial fit for their experimental compaction curves. Several researchers [43]–[46] have found good empirical fits of reinforcement loading curves to follow the simple power law of form in Equation 7 where P is the supplied compaction pressure.

$$V_f = a(P)^b \tag{7}$$

Robitaille and Gauvin [46] reviewed multiple published compressibility experiments of random mats and woven fabrics and fitted the compaction results to Equation 7. The researchers also fitted relaxation experiments to the empirical model seen in Equation 8 where P_0 is the initial supplied compaction pressure, t is the elapsed time, and c and d are experimentally derived constants.

$$\frac{P}{P_0} = 1 - ct^{(1/d)} \tag{8}$$

Robitaille and Gauvin [46] further went to give meaning to the empirical constants a through d used in Equation 7 and Equation 8. They defined a as the fiber volume fraction for compaction

pressure equal to 1 Pa (or essentially the initial fiber volume fraction), and b was defined as the compaction stiffening index, which is a value less than 1. For the relaxation model, c was defined as the pressure decay after 1 second, and d was called the relaxation index. The authors further defined a representative rigidity of the reinforcement, M, which was based on the linear slope of a line passing through a low pressure point and the maximum compaction pressure reached. The fiber volume fraction reached during each experiment was defined as the representative fiber volume fraction or RV_f. Using these parameters, the investigators made several generalizations over the experimental results surveyed. As the number of plies in the reinforcements increased, M and a were found to increase while b decreased and RV_f decreased for the oven materials. The compaction curves were seen to move progressively lower as the fiber volume fraction reached RV_f. Successive compaction cycles for the same sample were seen to increase a and RV_f while b descreased. An increase in M was also seen for woven fabrics in this case. For relaxation experiments, less relaxation was seen as the applied pressure increased. More relaxation was seen as the number of reinforcement plies or layers increased.

Regarding the observed hysteresis of loading/unloading cycles, in general, this phenomenon has been found to be low for 2D fiber arrangements [34]. Although, significant hysteresis has been found with compaction of glass fiber reinforcements [39] and in alumina preforms [47]. These preforms of high compaction cycle hysteresis are stated by Michaud and Mortensen [34] to possess fibers or binder material oriented along orthogonal to the testing axis. The researchers also stated that there is no current model for reinforcement relaxation when hysteresis is significant, and therefore phenomenological fitting is used.

Another important consideration during compaction experiments is the presence of a fluid. In some debulking and LCM processes, the compaction of a resin saturated or partially saturated preform may be relevant. This is especially pertinent to the VARTM process where first the reinforcement experiences dry compaction, and then upon resin infiltration, a wetting compaction and spring-back occur [36], [37]. To study this, researchers have performed wetted compaction experiments. Under wetted conditions, the arrangement of the fibrous network is altered due a lubricating effect from the wetting fluid and results in an increase of compaction [36]. Robitaille and Gauvin [46] also noted this trend in their review of compaction experiments as they noted the addition of a lubricant raises the representative fiber volume fraction (RV_f).

For the VARTM process or with the presence of resin in the reinforcement, the transverse equilibrium inside the mold has been defined as the pressure balance seen in Equation 9 [36], [37]. Here, P_{atm} is the applied atmospheric pressure, P_r is the resin pressure, and P_f is the pressure supported by the fiber preform.

$$P_{atm} = P_r + P_f \tag{9}$$

Grimsley et al. [36], [37] used the relation in Equation 10 to define fiber volume fraction during their VARTM compaction experiments in terms of the compressive strain rate, ε, and the initial reinforcement porosity, φ_0.

$$V_f = \frac{1 - \varphi_0}{1 - \varepsilon} \tag{10}$$

Initially in VARTM, the preform is compacted in a dry state by the vacuum pressure. Then resin is injected and the local net pressure applied to the preform drops as described in Equation 9 [37]. With these physics of the VARTM process in mind, Grimsley et al. [36], [37] described the compressive strain experienced by the preform with a dry loading compaction test fitted to the

empirical formula in Equation 11. Additionally, they used a wet unloading compaction test fitted with Equation 12 to describe the wetted strain experienced in the preform.

$$\varepsilon_{dry} = a_{dry}\left(1 - e^{(b_{dry}P_f)}\right) \tag{11}$$

$$\varepsilon_{wet} = a_{wet} + b_{wet}\left(\frac{P_f}{c_{wet} + P_f}\right) \tag{12}$$

The wet and dry strains are defined in terms of the fiber pressure, P_f, while a, b and c are constants from either the wet or dry compaction curves.

Regarding to the reproducibility in experimental results, compaction pressure will vary among samples. Generally, greater variation in compaction results are seen in preforms that allow significant nesting between layers [48]. Variation not caused by significant nesting has also been noted in literature. Bickerton et al. [49] have noted significant variations in compaction stresses, which were attributed to the variability in the structure of the reinforcement itself and also the variability introduced from the stacking of preform layers. Experimental variables should be controlled as best as possible by the investigator to avoid significant compaction variation between samples. This although, as reported by Bickerton et al. [49], will not guarantee good sample repeatability. The relative stochastic nature of fibrous reinforcements may always play a role in compaction experiments.

2.2.4 Analytical, Semi-analytical, and Numerical Models

Cai and Gutowski [50] described the deformation of a fiber bundle by considering the fibers as beams that are bent between fiber contact points under compressive forces. The authors defined the following relationship in Equation 13.

$$P_f = \frac{3\pi E}{\beta^4} \frac{\left(1 - \sqrt{\frac{V_f}{V_0}}\right)}{\left(\sqrt{\frac{V_a}{V_f}} - 1\right)^4} \tag{13}$$

In this model, E is the Young's modulus of the fiber, β is the span length-to-height ratio for the fibers treated as beams, V_0 is the initial fiber volume fraction, and V_a is the maximum available fiber volume fraction. This model has generally been applied semi-analytically to fit experimental curves as the parameters β and V_a are difficult measure directly [35]. Toll et al. [51], [52] employed micromechanical theory to develop a relationship of compaction pressure and fiber volume fraction for fiber networks including a general 3D wad, a planar mat of dispersed fibers, a bundle of parallel fibers and woven mats. Using statistical determination of fiber contact points, power law relationships were developed for each configuration. Michaud and Mortensen [34] summarized these relationships into the form seen in Equation 14.

$$P_f = kE\left(V_f - V_0\right)^n \tag{14}$$

In this equation, k and n are analytical parameters dependent on the arrangement of the fiber network. Chen et al. [33], [53], [54] applied a unit cell approach to model compaction behavior of woven fabrics. The researchers created analytical expressions for the idealized geometries used. They concluded that their compaction models delivered good quantification of the preform geometry allowing for better representation of the resin flow channels than their previous models. Verpoest and Lomov [55] applied a robust approach where micromechanical models for compaction were integrated with WiseTex, a software package that allows generation of the unit cell internal geometries of woven, braided, knitted, and multi-axial multi-ply stitched non-crimp fabrics (NCF). Lin et al. [56] used a similar unit cell geometrical software tool in TexGen, an

open source code developed at Nottingham University, to model fabric compression. The researchers applied a finite element modeling technique with TexGen created geometry of a plain weave fabric. They found that the model captured the fabric compression response including material nonlinearities, yarn interactions, as well as hysteresis. Nguyen et al. [57] also applied a meso-scale unit cell modeling approach using the finite element method for a woven fabric. They created their unit cell geometry and meshes with software developed by Hivet and Boisse [58]. With this computational setup, the investigators were able to carry out simulated compaction tests with multiple layers of the woven fabric.

In recent years, numerical models for compaction have offered a much promise, incorporating the detailed geometric consideration that analytic models lack. Numerical models are now becoming more robust and moving towards a more ideal approach, where draping models including preform compaction are now being coupled directly with resin infiltration models [20].

2.3 Reinforcement/Preform Permeability

2.3.1 Defining Permeability

2.3.1.1 Darcy's Law

The most critical parameter of the RTM mold filling stage is the preform permeability [43]. Permeability describes the ease of fluid flow through a porous media. Henry Darcy [59] first described the flow through a porous media by observing water flow through sand beds. He concluded the following empirical relationship seen in Equation 15.

$$Q = \frac{SA}{\mu}\frac{\Delta P}{L} \tag{15}$$

Darcy's law equates the volumetric flow rate of fluid, Q, to a quantity of the permeability, S, fluid viscosity, μ, cross-sectional area normal to the flow, A, and pressure difference, ΔP, over a length in the direction of flow, L. By dividing each side of the equation by the area, Darcy's law can also be expressed in the fashion seen in Equation 16.

$$q = -\frac{1}{\mu}[\mathrm{S}]\nabla P \tag{16}$$

Here, q is the fluid superficial velocity, and ∇P is the pressure gradient, which is the pressure difference over the length in the direction of flow. As discussed at the beginning of this review, Darcy's law has been widely accepted in the composite processing community to describe flow through a fibrous reinforcement in LCM processes. Here, permeability is the key parameter of units of meters squared. Permeability is function of the reinforcement geometry and fiber volume fraction. The fiber volume fraction of the reinforcement or V_f is directly related to the porosity or φ of the medium by the relationship seen in Equation 17.

$$\varphi = 1 - V_f \tag{17}$$

In general, permeability decreases as fiber volume fraction of a fibrous reinforcement increases. This relationship is well understood and has been reported in a review of experimental permeability measurements [60]. Higher fiber volume fraction directly relates to less porous zones for fluids to permeate, creating a greater pressure differential needed to overcome the permeability. As for geometry, tightly woven fabrics are seen to have a lower permeability in LCM processes than loosely woven/braided fabrics as resin has less porous zones and gaps to more easily permeate. Defining this permeability parameter has been researched widely through experimental and theoretical work for varying reinforcements and preforms.

Permeability is a tensor and a directional property depending on preform type. Preforms composed of random fiber mats have been found to be isotropic in nature, where permeability is found to be the same in all directions of the reinforcement [60]. For anisotropic preforms, a three dimensional form of Darcy's law must applied to describe the flow. This is seen in open form in Equation 18.

$$\begin{Bmatrix} q_x \\ q_y \\ q_z \end{Bmatrix} = -\frac{1}{\mu}\begin{bmatrix} S_{xx} & S_{xy} & S_{xz} \\ S_{yx} & S_{yy} & S_{yz} \\ S_{zx} & S_{zy} & S_{zz} \end{bmatrix}\begin{bmatrix} \partial P/\partial x \\ \partial P/\partial y \\ \partial P/\partial z \end{bmatrix} \tag{18}$$

The x-, y- and z-directions are represented here where the x- and y-components represent the in-plane directions and the z-direction is through the thickness. Often for directional fabric reinforcements, the x-direction is defined to be parallel to the warp, and the y-direction is along the weft/fill or 90° from the warp. The z-direction is then normal to the x-y plane. The permeability tensor can be diagonalized by a coordinate transformation seen in Equation 19 to produce a set of three principal permeabilities S_{11}, S_{22}, and S_{33} where T is the transformation matrix.

$$\begin{bmatrix} S_{xx} & S_{xy} & S_{xz} \\ S_{yx} & S_{yy} & S_{yz} \\ S_{zx} & S_{zy} & S_{zz} \end{bmatrix} = [T]\begin{bmatrix} S_{11} & 0 & 0 \\ 0 & S_{22} & 0 \\ 0 & 0 & S_{33} \end{bmatrix}[T]^T \tag{19}$$

The principal permeabilities and their directions are often of interest for RTM modeling. Generally, preforms can often be considered orthotropic in nature. For these orthotropic preforms, three-dimensional Darcy's law seen in Equation 18 will reduce to a one-dimensional form for the x-, y- and z-directions [44]. These relations can be seen in Equation 20.

$$q_x = -\frac{S_{xx}}{\mu}\frac{dP}{dx} \tag{20a}$$

$$q_y = -\frac{S_{yy}}{\mu}\frac{dP}{dy} \tag{20b}$$

$$q_z = -\frac{S_{zz}}{\mu}\frac{dP}{dz} \tag{20c}$$

With this formulation, a series of one-dimensional experiments are able to be carried out to determine the permeability tensor of an orthotropic preform or reinforcement of interest. Using the formulation in Equation 20, measurements can be made in the in-plane domain (x-y plane), including an x-direction, y-direction and an off-axis measurement of 45° from the x-axis. This allows a two-dimensional diagonalization of the permeability tensor to be performed resulting in in-plane principal permeabilities S_{11} and S_{22} and their orientations, while a final measurement in the z-direction will effectively produce the third principal permeability [45]. Considering two-dimensional permeability or the in-plane directions only, the permeability tensor takes the form seen in Equation 21.

$$[S] = \begin{bmatrix} S_{xx} & S_{xy} \\ S_{xy} & S_{yy} \end{bmatrix} \tag{21}$$

In this two-dimensional system, the permeability tensor components are related to two principal in-plane permeabilities and a principal coordinate system, which can be seen in Equation 22 where β is the angle between the first principal permeability and x- or warp axis [6].

$$S_{xx} = \frac{S_{11} + S_{22}}{2} + \frac{S_{11} - S_{22}}{2}\cos 2\beta \tag{22a}$$

$$S_{xy} = \frac{S_{11} - S_{22}}{2}\sin 2\beta \tag{22b}$$

$$S_{yy} = \frac{S_{11} + S_{22}}{2} - \frac{S_{11} - S_{22}}{2}\cos 2\beta \tag{22c}$$

This angle β is often of high interest in process modeling as it defines the orientation of principal flow direction, and 90° to this angle is the second principal permeability or direction of highest resistance to flow. This orientation angle can be observed in two-dimensional radial infusions of preforms or it can be determined by a series of one dimensional channel flow experiments as described by Fingerson [45] or by Weitzenböck [61]. Methods of this nature will be discussed in more detail in the Measurement Techniques section.

Commonly in RTM, infusions are made parallel to the direction of the fabric preform, and parts are relatively thin compared to their length. Due to this, resin flow is often assumed to be a two-dimensional problem where in-plane permeabilities are dominant [6]. With thicker parts and complex part geometry, transverse permeability plays a larger role in the description of the mold fill and must be investigated. For this study, in-plane and transverse or through-thickness permeabilities will be investigated for a more robust characterization of the reinforcements of interest.

2.3.1.2 Assumptions

It should be noted that a Darcy's law formulation for permeability is valid upon the assumption of Newtonian fluid and creeping flow or a low Reynolds number [62]. Interpretation of the Reynolds number for fibrous reinforcements varies depending on length scale and fabric type. Engineering judgment must be used when defining the characteristic length used in the Reynolds number calculation. Gauvin et al. [63] defined Re as the Reynolds number for continuous strand mats with a characteristic length of d_f or the roving diameter seen in Equation 23, where ρ is the fluid mass density, μ is the dynamic viscosity and v is the flow velocity.

$$Re = \frac{\rho v d_f}{\mu} \tag{23}$$

Drapier et al. [64], in perhaps a more sensical approach, defined a maximum Reynolds number for their studied biaxial stitched fabric in Equation 24.

$$Re^{max} = \frac{\rho v^{max} d}{\mu} \tag{24}$$

Here, v^{max} is defined as the maximum fluid velocity encountered and d is the largest characteristic length defined as the largest stitching hole that was measured from micrographs of the reinforcement. The authors were able to show a maximum Reynolds number that was far less than 1. Shojaei et al. [65] defined Reynolds number using the square root of preform permeability as the characteristic length in Equation 25.

$$Re = \frac{v^* \rho \sqrt{S}}{\mu} \tag{25}$$

Here, S is the preform permeability and v^* is the average particle velocity, which is related to the Darcy velocity by the relationship

$$v^* = \frac{v}{\varphi} \tag{26}$$

This relation uses the Darcy velocity, v, and the preform porosity, φ, to define the average particle velocity. The significance of non-Darcy flow will be investigated in Chapter 6, as high flow rates or injections pressures have been used in industry during RTM applications and this flow scenario may be applicable.

2.3.2 Measurement Techniques

There is no universally accepted, standard method for permeability measurements of LCM reinforcements. Basic test methods use similar formulation to determine permeability, but have

many variants of fixture types and test parameters. Measurement of reinforcement permeability is known to be notoriously variable in results where variation has been found to be up to an order of magnitude between test methods for the same material [66]. Attempts have been made to standardize methods for collaborative measurement studies where setup consistency and error reduction is of main focus [66]–[69]. Other standardization efforts include a permeability database creation [70], a proposed 3D woven reference fabric [71], and a proposed epoxy-based reference test specimen not of fibrous architecture [18].

Of the myriad of measurement techniques employed to obtain the permeability parameter for preforms used in resin infusion modeling, general formulation is based on Darcy's law. At a most basic level, these techniques generally fall in either 1D channel flow or 2D radial measurement methods, while a few methods [72]–[76] have been developed to measure 3D permeability tensor of a preform. One-dimensional methods involve linearly injecting a test fluid (line-source to line-sink) into a preform placed in a rectangular cavity. Radial measurements are conducted by centrally injecting a test fluid in a preform and observing the resulting propagation of the flow front ellipse in the in-plane directions. Although other methods have also been used to obtain permeability, this research will focus on linear injection and radial methods, as these are most common and are used in this study. Other notable methods researchers have employed include capillary rise techniques to find tow or fiber bundle permeability [77]–[79].

2.3.2.1 1D Linear Techniques

The basis of the 1D channel flow permeability measurement techniques is to isolate one direction of a preform by a linear fluid injection to obtain one component of the permeability tensor. One-

dimensional flow experiments can be made in either a transient or steady-state case. There are benefits and disadvantages to each case. Transient or advancing flow front methods involve a measurement of an unsaturated permeability and reflect the transient nature seen an actual RTM mold fill. Steady-state or saturated permeability methods are conducted after a preform has been completely filled with test fluid. This is at a different physical state than seen in RTM mold fills, but these saturated methods allow the ability to measure permeability at unlimited fiber volume fractions or preform thicknesses with one sample, while transient techniques can only be tested at a single fiber volume fraction [45]. In this respect, saturated methods allow a user to develop a much larger range of data points for a preform than what could be done with an unsaturated experiment on a sample/material amount basis. Methods and fixtures have also been developed to allow an investigation on both unsaturated and saturated flow in a single test sample [11], [45]. This is done by first measuring unsaturated permeability in a transient injection, then taking steady state measurements at the same or higher fiber volume fraction of the original infusion.

In experimental measurements of saturated permeability, a constant flow rate injection is used to permeate the preform and measurements are made after flow has reached a steady-state condition. With this technique, saturated permeability S^{sat} can be determined using a Darcy's law formulation seen in Equation 27.

$$S^{sat} = \frac{Q\mu L}{A\Delta P} \tag{27}$$

This formulation is used for saturated 1D, in-plane permeability measurements, but also can be used successfully in through-thickness or S_{zz} measurements with appropriately designed test fixtures [44], [45]. In steady-state flow experiments, the volumetric flow rate, Q should have a linear relationship with pressure drop across the preform. A researcher can obtain the saturated

permeability over a range of flow rates for a given fiber volume fraction. Any significant nonlinearity seen in pressure versus flow rate curves during these investigations points to possible test discrepancies of fixture leaking, progressive fiber displacement, or presence of inertial effects.

For unsaturated flow methods, either a constant flow rate injection is used and the pressure drop across the preform is measured, or a constant pressure injection is used and the flow front position at a given time after initiation is measured. For 1D, transient or advancing front cases Darcy's law can be expressed on a temporal basis seen in Equation 28 where $x(t)$ represents the flow front position (relative to the inlet) at time, t [60].

$$\frac{dx}{dt} = \frac{S}{\mu\varphi}\frac{\Delta P(t)}{x(t)} \tag{28}$$

Integrating this equation yields a solution for transient, unsaturated permeability, S^{unsat}, for constant pressure injections seen in Equation 29 with initial condition of $x(0) = 0$ [60].

$$S^{unsat} = \frac{x^2(t)\mu\varphi}{2t\Delta P} \tag{29}$$

This formulation is used for in-plane directions. Note that to measure a flow front position at a given time, an unsaturated permeability fixture usually is implemented with a visualization window and the infusion is recorded for analysis or the fixture is outfitted with in-cavity pressure sensors along the flow path. At constant pressure injections, the flow front velocity slows with increasing time and distance from inlet. To account for capillary effects, the capillary pressure should be added to the pressure difference term used in Equation 29 [60]. If a constant flow rate injection is used for measuring unsaturated permeability, the formulation seen in Equation 30 should be used.

$$S^{unsat} = \frac{Q\mu x}{A\Delta P} \tag{30}$$

Here, x represents the length at which the flow front has reached and ΔP is the instantaneous pressure difference between the mold and atmospheric pressure. In constant flow rate, transient experiments, the flow front position should be known for any time given the geometry of the mold cavity, while the pressure varies with time and increasing flow front position.

2.3.2.2 2D Radial Technique

Radial permeability measurement techniques allow the in-plane permeabilities of a fabric to be determined in a single infusion. Test fluid is injected at a circular inlet port at a central location of a preform in a mold. The radially increasing flow front is then tracked over time in a transient case. Generally, radial methods involve a fixture outfitted with a clear top or bottom so that the flow front can be visually tracked, although some radial flow fixtures are designed with in-cavity pressure transducers or sensors to evaluate flow front position [80]. For isotropic preforms, often those of random fiber orientation, flow fronts advance in a circular shape as the permeability is the same in all directions [60]. Weitzenböck et al. [81] defined the unsaturated radial permeability, S^{unsat} for isotropic reinforcements to be that seen in Equation 31 where *t* is the time from initiation, r_f is the radius of the flow front, and r_0 is the radius of the inlet.

$$S^{unsat} = \frac{\mu\varphi}{4t\Delta P}\{r_f^2[2\ \ln(r_f/r_0) - 1] + r_0^2\} \tag{31}$$

Weitzenböck et al. [81] also defined the unsaturated radial permeability for orthotropic materials along both the x- and y- directions seen in Equation 32 and Equation 33 respectively. Here x_f and y_f are flow front position at time *t* of the each respective direction and x_0 and y_0 are the inlet radii.

$$S_{xx}^{unsat} = \frac{\mu\varphi}{4t\Delta P}\{x_f^2[2\ \ln(x_f/x_0) - 1] + x_0^2\} \quad (32)$$

$$S_{yy}^{unsat} = \frac{\mu\varphi}{4t\Delta P}\{y_f^2[2\ \ln(y_f/y_0) - 1] + y_0^2\} \quad (33)$$

When preparing preforms for radial permeability measurements, researchers have center hole-punched their samples at the fixture inlet in order to eliminate any through thickness flow, allowing for purely in-plane fluid propagation [67], [80]. This technique is advisable when using reinforcements with low transverse permeability characteristics. Others have used a radial technique that does not employ a center hole-punch and has the additional ability to measure through-thickness permeability and in-plane flow to create a 3D measurement technique within a single infusion [72].

2.3.3 Modeling and Prediction

Regarding theoretical permeability modeling, Lundström et al. [67] stated that "the theoretical expressions that have been derived for the permeability are based on some specific and simplified fiber arrangement and do not apply to a general case". This fact continues to drive the need for continuing experimental permeability measurement work and leaves a wanting for a robust and adaptive permeability modeling tool. Several types of general models have been used to characterize permeability for reinforcements: empirical, analytical, and numerical. These models are often used to describe preform permeability as a function of fiber volume fraction and geometry. While empirical models may present the most accurate and representative values, they are based on time-consuming experimental characterization. Analytical and semi-analytical models offer a reduction in experimentation but are often too idealized for application to complex geometry preforms. Numerical permeability prediction has gained capability in recent

years and looks to be a promising future alternative to experimental measurements, although added complexity to the numerical simulations can become computationally costly.

2.3.3.1 Empirical Models

Often, it is useful to model experimentally produced permeability over a range of fiber volume fractions. If a suitable fit is found for a range measured permeabilities at several points of fiber volume fraction, an accurate prediction of permeability can be extrapolated at fiber volume fractions that were not tested with the specific preform. Multiple relations have been used to model empirical trends in permeability throughout LCM research. A generalized version of the Carman-Kozeny equation, seen in Equation 34, has been applied by many researchers to fit their permeability measurements over a range of fiber volume fractions where a and b are constants [6].

$$S = \frac{a\left(1 - V_f\right)^{b+1}}{V_f^b} \tag{34}$$

Kim et al. [82] proposed a model of form in Equation 35 where $V_{f\infty}$ is the fiber volume fraction at maximum compression and the model is valid when $V_f \leq V_{f\infty}$ and when $1 \leq b \leq 1/V_{f\infty}$.

$$S = a\left(bV_{f\infty} - V_f\right)^4 \tag{35}$$

Gauvin et al. [63] developed the empirical model seen in Equation 36 for continuous strand mats, where a, b, and c are constants and φ is the mat porosity.

$$S = a + be^{(c\varphi)} \tag{36}$$

Tuncol [44] found good empirical fits for the fiber volume fraction range tested using a similar exponential model in Equation 37.

$$S = ae^{(bV_f)} \tag{37}$$

Several other researchers [36], [37], [43], [45], [83], [84] have found an appropriate fit using a power law regression, seen in Equation 38, over a range of reinforcements.

$$S = a\left(V_f\right)^b \tag{38}$$

Overall, any empirical model can be justified to describe permeability if a good fit is resultant.

2.3.3.2 Semi-analytical and Analytic Models

Analytical and semi-analytical models for permeability prediction have been of interest in the LCM community for decades. The ability to reduce experimental preform characterization or to eliminate it entirely has great time and resource saving potential for LCM process modeling. Researchers have employed method to predict permeability simply from the geometry of the reinforcement alone using the lubrication approach. Due to the complexities of reinforcement architectures and the dependence of permeability on geometry, accurate analytical prediction different reinforcement types can be a difficult.

Many researchers have employed the Carmen-Kozeny equation to predict permeability for unidirectional reinforcements [6]. While the relation was originally used for flow through isotropic media composed of spherical particles, a modified version is used to describe flow through a cylinder bed representative of aligned fibers [7]. This modified version of the Carman-Kozeny relation defines permeability in Equation 39.

$$S = \frac{r_f^2}{4C_k}\frac{\left(1 - V_f\right)^3}{V_f^2} \tag{39}$$

Here, r_f is the fiber radius, C_k is the Kozeny constant, and V_f is the fiber volume fraction. The Kozeny constant then has to be determined and possesses different values for flow parallel and perpendicular to the fiber bed. This relation was modified by Gutowski et al. [85] to account for that fact that the Carman-Kozeny equation predicts a non-zero permeability at fiber volume fractions higher than the theoretical maximum [7]. Gutowski et al. [85] proposed the following modification for transverse permeability in Equation 40.

$$S = \frac{r_f^2}{4C_k{}'} \frac{\left(\sqrt{\frac{V_a{}'}{V_f}} - 1\right)^3}{\left(\frac{V_a{}'}{V_f} + 1\right)} \tag{40}$$

In this equation, $C_k{}'$ and $V_a{}'$ are empirical parameters where $V_a{}'$ is the maximum available fiber volume fraction. Later, Gebart [86] proposed that both the Carman-Kozeny equation and the model from Gutowski et al. [85] lacked in detailed geometric consideration and could be improved upon. Gebart [86] introduced the geometries of quadratic and hexagonal fiber packing arrangements into a model for unidirectional permeability. Permeabilities parallel and perpendicular to the fiber bed then were defined for quadratic and hexagonal fiber packing as seen in Equation 41 and Equation 42.

$$S_{\parallel} = \frac{8r_f^2}{C_{\parallel}} \left(\frac{1 - V_f}{V_f{}^2}\right)^3 \tag{41}$$

$$S_{\perp} = C_{\perp} \left(\sqrt{\frac{V_{fmax}}{V_f}} - 1\right)^{5/2} r_f^2 \tag{42}$$

Here, the maximum fiber volume fraction, V_{fmax}, constant $C_{\parallel}$ and constant $C_{\perp}$ are defined by fiber packing arrangement in Table 2.1.

Table 2.1: Parameters for Permeability Prediction from Gebart [86]

Fiber Arrangement	$C_{\parallel}$	$C_{\perp}$	V_{fmax}
Quadratic	57	$\frac{16}{9\pi\sqrt{2}}$	$\frac{\pi}{4}$
Hexagonal	53	$\frac{16}{9\pi\sqrt{6}}$	$\frac{\pi}{2\sqrt{3}}$

Gebart's [86] models for permeability have continually been used by researchers to define unidirectional permeability. The models have also been found successful in application for prediction of intra-tow permeability in more complex fabrics [87]–[89]. Further models for permeability have also been created, but will not be discussed here. Several more of these resources can be found in [90]–[94]. While the predictions of permeability in aligned fiber beds have been formulated in an analytical fashion, extensions of these predictions to complex geometry reinforcements requires a more robust approach. Here, numerical modeling can play an important role.

2.3.3.3 Numerical/Unit Cell Predictions

In recent years, researchers have begun to find success in numerically predicting preform permeability using the geometrical makeup of a fabric or reinforcement, often using a unit cell [84], [87]–[89], [95], [96]. The modeling is focused at the meso-scale and incorporates the dual-scale porosity of intra-tow and inter-tow domains. Generally, this involves modeling the inter-tow regions with Stokes flow and the intra-tow regions with Darcy flow [88]. With this approach, inputs include fabric geometry and permeability is the desired output. Contrarily, the practice of obtaining an experimental permeability tensor for a bulk preform, applying this tensor to a modeled domain, and solving the fluid equations in this region for a mold fill has been

commonplace in LCM research for many years. The details of this modeling approach, including resin cure kinetics and thermodynamic considerations, will not be discussed in this work. Further background in this area can be found in [29], [97]. Permeability prediction with a unit cell aims to reduce or eliminate the time consuming experimental characterization step of this numerical modeling process.

Zeng et al. [87] used a numerical unit cell approach to predict permeability of the 2x2 twill weave carbon fabric that was widely characterized in an international benchmark study [66], [69]. They first geometrically characterized 9 layers of the fabric using x-ray micro-computed Tomography (μ-CT). These tow and architecture geometries were then used as inputs into the open source TexGen software developed from the University of Nottingham, which created a representative unit cell. The tows were treated as porous media and Gebart's [86] analytical relations were used to define intra-tow permeability. The resulting intra-tow permeabilities were deemed low enough to assume tow impermeability. Multiple simulated infusions were then run on the modeled geometry in a computational fluid dynamics (CFD) package. The researchers also incorporated nesting possibilities into their simulations using a Latin hypercube sampling technique. It was concluded that, given accurate geometrical data, numerically predicted permeability could be more reliable than the experimental data produced in the first round of the benchmark exercise. Luchini et al. [84] used a similar approach to predict permeability in plain weave glass fabric. Fabric geometry was measured from optical microscopy of a finished composite laminate. This procedure took laminate measurements at the tow and intra-tow level. The intra-tow geometry consisting of a fiber packing arrangement, fiber volume fraction, and fiber diameter was characterized. Gebart's [86] analytical expression was also used to find the

intra-tow permeability, and a representative unit cell was created in TexGen. Tows were treated as porous media using the predicted intra-tow permeability and gaps between tows were handled with Stokes flow. CFD simulations were run to produce a unit cell permeability, which compared very well to experimental saturated permeability measurements of the same fabric in both the warp and weft directions.

Tan et al. [89] compared similar CFD permeability predictions of small and large representative unit cells of a biaxial stitched mat to experimental permeability. They also used Gebart's [86] analytical permeability for tow permeability and applied an finite element method (FEM) approach to solve the fluid equations. It was found that the large unit cells over predicted permeability, while the small unit cells under predicted the permeability compared to the experimental results. Even with these results, the researchers stood by their conclusion that unit cell numerical modeling is still an effective method for permeability prediction. Chen et al. [88] also used a similar unit cell method and found acceptable agreement between numerical and published experimental permeability results for several plain weave fabrics.

2.3.4 Other Factors of Consideration

2.3.4.1 Reinforcement Architecture/Fabric Type

Geometry and fiber volume fraction/porosity are the dominant factors affecting the permeability of fibrous reinforcements. Being that there are many different types of complex fiber architecture used to create preforms, the reported values of permeability vary greatly among reinforcement types. Among those types include random fiber mats, unidirectional, woven, braided, stitched, knitted and other architectures. These architecture types offer a wide scatter of potential resin

flow paths, which inherently affects the preform permeability. Also, a different fiber network may be used in the same architecture being carbon, glass or other fiber types, which can further create more possibility for permeability variation. Notably, preforms of natural fibers have been reported to swell upon saturation, reducing porosity and affectively increasing flow resistance [98]. Also, preforms featuring multiple fiber types (e.g. carbon and glass) can create further variability.

As preform geometry as a major consideration, researchers have been able to prescribe some generalities for permeability and flow behavior based on architecture. While random fiber mats are known to be homogeneous in permeability, the presence of tows and gaps between tows in woven fabrics create a heterogeneous medium [99]. Unidirectional reinforcements have been seen to possess a higher permeability in the flow direction parallel to the fibers than that in the perpendicular direction. This relationship has also been observed in Gebart's [86] model for unidirectional reinforcements. Endruweit and Long [100] investigated the in-plane principal permeabilities of triaxial braided carbon fabrics with differing fiber bias angles (angles from the warp axis or 0° line to the bias tow) at 45°, 60°, and 70°. With experimental data and numerical modeling, the authors presented permeability as a function of triaxial fabric tow bias angle. It was suggested that the first principal permeability was at β = 0° for triaxial fabrics with bias fibers up to approximately 55°. With bias fibers greater than 55°, the first principal permeability was seen to shift from β = 0° to β = 90°. This result offers valuable insight for principal flow direction of triaxial fabrics and similar investigations could be applied to other braided fabrics, such as biaxial configurations. Permeabilities for other multiple fabric types are summarized in [60] by preform direction (S_{xx} and S_{yy}). Regarding local preform directions, generally the

transverse or through-thickness permeability is seen to be lower than that of the in-plane directions for most reinforcements [60]. Transverse permeability has been reported to be over two magnitudes lower than the in-plane permeabilities of the same preform [101]. Aside from any previously accepted generalization, understanding how fluid will flow through a specific reinforcement cannot be confidently known without first employing experimental characterization or robust modeling and simulation.

2.3.4.2 Wettability, Fluid and Capillary Effects

The effect of test fluid on experimental permeability measurements has been something of debate in LCM preform characterization. A variety of test fluids have been used in permeability experimentation throughout literature in lieu of actual thermosetting resins for reasons likely of cost and ease of use where presence of similar rheological properties may be found in the alternative fluid. Corn syrup [102]–[104] has commonly been used in experimental permeability measurements, as have mixtures of corn syrup, water, and dye [105]–[107]. Previous research has also justified the use of corn oil [82], hydraulic fluid [108], [109], silicon oil [110], [111], and motor oil [112] in various experimental scenarios. Other notable works have used gaseous fluids for permeability measurements including air [113], [114]. A study by Hammond and Loos [115] concluded that fluid type had little effect on steady-state and advancing front permeability while comparing corn oil, water and EPON 815 resin. Luo et al. [116] also concluded that fluid type had an insignificant effect on permeability compared to the experimental variation when comparing advancing front measurements made with silicone oil and diluted corn syrup. Contrarily, Steenkamer et al. [117] saw large variations in measured permeability with different test fluids of motor oil, diluted corn syrup and vinyl ester resin, and concluded that reinforcement

fabrics should be characterized with the actual resin to be used in the given application. It was concluded that capillary effects were the cause of the discrepancies between fluids.

Altering the test fluid will inevitably alter interactions between the fibrous reinforcement and the permeant. Determining whether this has significance on a preform's permeability is then the goal for obtaining accurate and representative measurements. Bahners [118] described wetting as "the result of simultaneous spreading on a rough surface, penetration, and capillary motion in the multi-porous system". Material and fluid selection play a role in the wettability of a reinforcement as thermodynamic wetting is known to be dependent on the surface free energies (SFE) of the materials involved [119]. Fibers of the reinforcement can be studied for their interaction with test fluid/resin systems through contact angle and surface tension measurements. Low contact angles imply good fiber wetting, while a low permeant surface tension aids in elimination of void formation [115]. Surface treatments are often applied to fiber surfaces to aid in wetting or to optimize other properties like the adhesion characteristics between matrix and reinforcement [118]. The physics of wettability will not be discussed in detail in this review, more background can be found in [120].

Multiple test methods have been adopted to measure the wettability of fibrous reinforcements including drop penetration tests, capillary rise tests, and tests employing the Wilhelmy method. Della Volpe et al. [121] investigated the applicability of using the Wilhelmy plate method, an immersion technique that evaluates the resulting forces, to measure fabric advancing and receding contact angles. They concluded that the method was applicable with reasonable error for stiff fabrics but not for soft fabrics. Bahners [118] concluded that due to complex nature of

textile fabrics geometry, the Wilhelmy method with textiles can only be used for qualitative analysis. The author further investigated other wettability measurement techniques including the sessile droplet, capillary rise methods, and the single fiber micro-Wilhelmy method. Bahners [118] concluded that although the stated methods can be useful for qualitative comparisons, the only reliable technique to measure contact angles and find the polar and dispersive components of SFE is through the single fiber micro-Wilhelmy method. This method is further explained in the Fluid Effects chapter, as it is used for characterization of IM7 fibers.

Fluid selection also affects the capillary pressure/forces seen during infusions, which alongside the viscous forces, comprise the main driving forces of flow through a porous media [122]. Capillary pressure can be defined in terms of the surface tension and contact angle as seen in Equation 43.

$$P_c = \frac{\sigma \cos\theta}{m} \tag{43}$$

Here, P_c is the capillary pressure, σ is the surface tension, θ is the contact angle and r_h is the hydraulic radius which is defined in Equation 44 [123] where d_f is the fiber diameter, V_f is fiber volume fraction, and F is a form factor ($F = 4$ for flow along axial tows and $F = 2$ for transverse flow).

$$r_h = \frac{d_f}{F}\frac{(1 - V_f)}{V_f} \tag{44}$$

The capillary number, C_a, defined in Equation 45 can be used to compare the ratio of viscous forces to the capillary forces where here μ is the fluid viscosity, v is the interstitial fluid velocity and σ again is the fluid surface tension [115].

$$C_a = \frac{\mu v}{\sigma} \tag{45}$$

Advancing front or unsaturated permeability can be compared versus the capillary number, thus displaying if permeability has dependence for a given range of produced data. Permeability was found to be independent of capillary number by Hammond et al. [43] for their tests.. Amico and Lekakou [124] and Lou et al. [116] both stated for injections pressures greater than 1 bar, the capillary effect of capillary pressure on permeability is insignificant and can be neglected.

2.3.4.3 Dual-scale Porosity

Complex fiber reinforcements often can be said to possess dual-scale porosity; a porous zone is defined at the tow level where gaps exist between the weave or braid of the tows, while the tows themselves are porous, composed of a cluster of individual fibers. Researchers observed behaviors of this dual scale porosity through comparisons of infusions with randomly aligned and directional fiber preforms. Parseval et al. [125] found that while plotting transient inlet pressure for a constant flow rate infusion, instead of seeing a linear increase of pressure as predicted by Darcy's law (and also seen in random fiber mat infusions), the resulting pressure curved drooped for directional fabrics. This relationship is reproduced graphically in Figure 2.1.

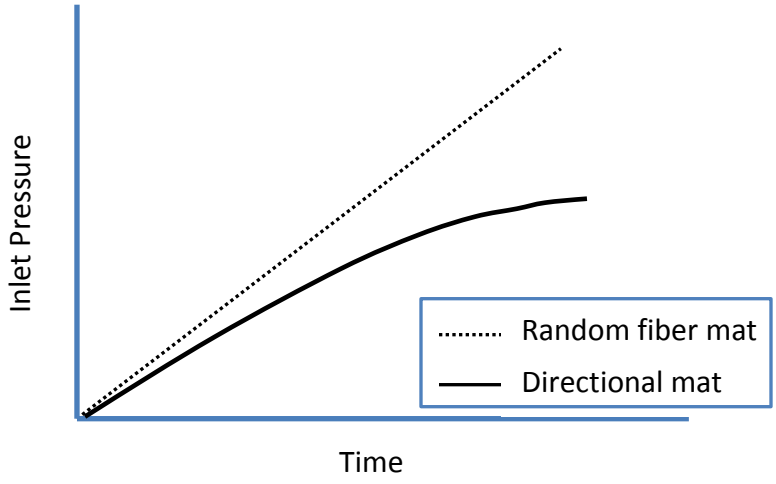

Figure 2.1: Pressure Drooping Effect

Pillai and Advani [126] attributed this drooping effect to the dual scale porous nature of directional fabrics where the permeating fluid first fills the gaps between tows, then lagging tow saturation is seen behind the advancing flow front. They also developed a model that accurately corrected for this pressure drooping by introducing a sink term to the continuity equation as seen in Equation 46, which was substituted directly into Darcy's law.

$$\nabla \cdot \boldsymbol{v} = -\alpha_s \tag{46}$$

Here, *v* is the volume averaged velocity and α_s is the sink term, which the researchers defined as the volumetric rate of liquid absorption. Recently, the sink term has been further employed by researchers to describe the phenomena characteristic of dual-scale porous media in LCM [127]–[129].

Pillai [99] defined a dual-scale fabric by a comparison of characteristic lengths. By comparing the length between tows, L_{tow}, and the length between fibers within a tow, l_{tow}, a dual-scale fabric for LCM considerations will exhibit a relationship of $L_{tow} \gg l_{tow}$. If both characteristic lengths are of similar magnitude, the medium can be considered to possess a single scale of porosity (e.g. a random fiber mat). A later experimental study by Babu and Pillai [130] investigated multiple directional fabrics architectures for inlet pressure drooping and concluded some directional fabrics did not exhibit drooping pressure curves. The authors hypothesized that for a fabric to be considered dual-scale in nature, it then must possess "continuous uninterrupted macro-channels". It is clear that reinforcements of interest should be characterized carefully before applying different models for resin flow and generalizations over entire fabric types.

Dependent on the geometry and fiber volume fraction, the fabric reinforcement of interest may or may not possess a significant state of dual scale porosity.

Due to the transient saturation this dual scale model involves, it can be stated that in steady-state flow scenarios, the permeability will not be affected by this dual scale nature in the same way. Steady-state permeability measurements take place after a fabric reinforcement is fully saturated with fluid. Thus, one would assume that Darcy's law in conjunction with continuity without a sink term would be sufficient to describe this flow, as no lagging saturation will be present. The difference between advancing front and saturated permeability then must be explored.

2.3.4.4 State of Saturation

Steady-state and advancing front permeability measurement techniques involve different flow considerations in porous media, and because of this, there has been much research regarding saturated versus unsaturated permeability in LCM [65], [67], [71], [98], [125], [131]–[136]. Mold fills will naturally occur in an advancing front flow. Due to this, any difference between permeability measurements made at a steady-state or in transient fill should be investigated. One might consider that because of the differences between saturated and unsaturated flow through porous media, advancing front permeability measurements should take priority over steady-state measurements. Although, the benefit of creating permeability values at a full range of fiber volume fractions from a single steady-state sample is attractive for reinforcement characterization. By comparison, unsaturated measurements involve a process of testing a single sample per volume fraction point of interest, which can lead to large material consumption and

labor time for a full volume fraction range of characterization. This aids to the practicality of somehow linking saturated permeability measurements to unsaturated values.

A common comparison that has been made by researchers of LCM processes involves using a ratio of saturated and unsaturated permeability for a specific reinforcement. Review of the reported S^{unsat}/S^{sat} values for multiple fabrics has shown a large scatter of results with ratio values ranging from ¼ to 4 [137]. This range of values are reported as constants, but S^{unsat}/S^{sat} has also been reported to vary during the saturation of a reinforcement [71], [125]. Pillai [137] discussed established techniques in flow through porous media transport theory, and offered a relationship between saturated and unsaturated values. Pillai [137] hypothesized that permeability will reflect the relation of Equation 47, where S^{rel} is the relative permeability.

$$S^{unsat} = S^{rel}S^{sat} \tag{47}$$

In this relationship, s^{rel} is a function of saturation, and can only vary between 0 and 1, thus S^{unsat}/S^{sat} should never be greater than 1. Using this formulation, reinforcement permeability is then defined as a function of saturation. Bréard et al. [138] also explained this permeability relationship based on a function of saturation for purposes of numerical modeling. The researchers defined a geometrical permeability, S_{geo}, which is an intrinsic property of the reinforcement. A relative permeability, $S^{rel}(s)$, which is dependent on the degree of saturation, s was also defined. With these definitions, the permeability of the reinforcement as a function of saturation can then be represented in Equation 48 [138].

$$S(s) = S^{rel}(s)S_{geo} \tag{48}$$

The researchers then presented a mathematical fit allowing the relative permeability to be defined by the degree of saturation based on the ratio of unsaturated and saturated permeability measurements.

In a study by Shih and Lee [139], multiple infusions of stitched, woven, and random fiber mats were conducted where the test fluid was dyed a dark and light color. First, the light color fluid was injected in the reinforcements. Second, the dark dyed fluid was injected after significant sample saturation of the light fluid was attained. During the infusion of a bidirectional stitched mat, the dark dye was seen to preferentially progress in the gaps between the tows quickly, while the light color fluid stayed saturated within the tows due to the low porosity. This behavior was also seen in lesser extent during infusions of a unidirectional and a 4-harness woven mat. This research experimentally displays that saturated flow progresses preferentially through certain fabrics compared to unsaturated flow. Hence, saturated permeability should be higher than unsaturated for these cases. It should be noted that Shih and Lee [139] also performed infusions with a random fiber mat which did not show this preferential advancement of saturated flow as did the directional preforms. This then corroborates with earlier findings from Chick et al. [140] who found the difference of saturated and unsaturated permeabilities for random fiber mats to be negligible.

2.3.4.5 Flow Rate/Injection Pressure Effects

Multiple researchers have investigated flow rate and pressure effects on the permeability of fiber reinforcements for LCM. Introduction of the test fluid in LCM experiments generally are provided by either a constant pressure inlet, or a constant flow rate injection. Studies have identified permeability to increase as the inlet constant flow rate increased [141], [142]. Chan et

al. [141] explained this behavior through a phenomenon of "preferential channeling" where the fluid is pushed through the larger gaps in the reinforcement geometry, avoiding the lower porosity areas as the pressure builds. The authors further added that this preferential channeling may lead to tows not being fully saturated during infusions. Trevino et al. [143] also described a channeling effect while testing directional fiber mats, but noted that it was observed for low fiber volume fractions, below 35% when the preform was not tightly packed. High pressure build ups were not seen until fiber volume fraction was higher than 55%. In comparison, Chen et al. [141] and Young et al. [142] saw increasing of permeability with flow rate while using preforms compacted to 44.8% fiber volume fraction, and lower 30% fiber volume fraction, respectively. These results point to the significance of fiber volume fraction. Significant research in high fiber volume fraction ranges (those at 55% and higher, often of interest in aerospace applications) has not been investigated in this area.

Other researchers have found permeability to be independent of the tested ranges of constant inlet pressures injections [65], [67], [144]. Lundström et al. [67] reported constant permeability over a tested pressure range of 0.5 to 1.5 bars. Kim et al. [144] also corroborated similar results for a pressure range of 1.5 to 2 bars. Shojaei et al. [65] explained that the permeability remained independent over a range of 1 to 3 bars because at those selected pressures, the critical flow rate for the woven E-glass fabric was not achieved at which non-Darcy flow appears. The authors observed this critical fluid velocity to be around 0.2 cm/s through experimental work for their specific fabric type and fiber volume fraction. Also, as stated earlier, with pressure inlet injections made under 1 bar, capillary effects may be significant and permeability could be affected differently at these low pressures [116], [124].

This research involving critical flow rates/velocities for constant permeability or Darcy flow can become of interest when researching high flow rate or velocity flows in LCM. Although most flow in LCM are described to be of low Reynolds number or creeping flow, possibilities of non-Darcy behavior at high flow rates or pressures in industrial is applicable. Forchheimer [145] showed that Darcy's law is flow rate dependent, and described a second order relationship to describe flow through porous media when Darcy's law fails. This study will investigate permeability in high flow rate scenarios with a steady-state, constant flow rate injection fixture. High flow rates may also result in fiber washout or unwanted fabric shear due to high pressure build up within the mold. Further details will be described in Chapter 6 including application of the Forchheimer equation and criteria for defining non-Darcy flow.

2.3.4.6 Reinforcement Deformations: Shear, Nesting, and Fiber Washout

During the preform process of RTM, the packing of a fibrous reinforcement in a mold can result in deformation or shear of the reinforcement, especially when the preform takes a complex shape. Dependent on the type of reinforcement, fabric deformations may take different forms. Shear is considered the dominant form of deformation for woven fabrics in RTM preforming [6], [108], [146]. This in-plane shearing alters the preform geometry including fiber orientation and wrinkling. Due to the change in geometry, the preform permeability is directly affected. This has driven researchers to investigate resin flow in sheared fabric reinforcements due to draping and preforming effects, while fabric shear has also been reported to affect finished laminate mechanical properties [147]. Studies have shown that the fabric shear angle has significant effect on permeability and that the orientation of the first principal permeability, β, is altered to a

generally greater magnitude than the fabric shear angle [148]–[150]. A recent study of reinforcement permeability by Endruweit et al. [151] investigated the effects of a fabric's shear history, which can include multiple deformations per sample during processing. The authors concluded that the "involuntary deformation" that may be subjected to the fabric reinforcement can result in a variation of the principal permeabilities by twofold. With variation of this magnitude, any fabric deformation should be carefully watched and noted during processing.

Not only does fiber reorientation affect permeability, but fabric areal weight and volume fraction are also altered after a shear deformation due to a change in geometry [146], [147]. Heardman et al. [146] presented a relation that is used to define local fiber volume fraction in terms of the shear angle of a fabric as seen in Equation 49.

$$V_f = \frac{V_{f0}}{\cos \alpha} \tag{49}$$

Here, V_f is the sheared fabric fiber volume fraction, V_{f0} is the fiber volume fraction of the unsheared fabric, and α is the fabric shear angle. It should be noted that this relation assumes no yarn or tow slip and no wrinkling. Being that the areal density of fabrics can be directly related to fiber volume fraction, the authors found good agreement between predicted areal densities from Equation 49 to experimental data for multiple fabrics. Depending on the fabric type, different shear angles can be achieved before wrinkling or the lock angle is achieved. Draping properties including the limit deformation angle of multiple glass and carbon fabrics were investigated by Wang et al. [152]. These limits are important as the onset of shear locking and wrinkling has been noted to cause deviation in permeability from the trends measured at angles smaller than the lock angle [146]. Many researchers have applied modeling approaches including the use of fabric unit cells in order to model the permeability of sheared fabric reinforcements

[55], [146], [148], [151], [153]–[158]. These meso-scale approaches generally involve receiving a sheared geometry as given inputs, and solving for the resulting permeating flow. A more robust integration of micro-mechanical unit cell geometries that model shear and permeability have also been discussed [55].

Another reinforcement deformation that influences permeability is nesting. Nesting refers to the reinforcement deformation through the thickness direction induced from compaction pressures. In nesting, upon preform compression, the tows and fibers of the reinforcements are shifted and sit or "nest" together more compactly. This will affect the local fiber volume fraction, where nesting can increase the fiber content. Chen et al. [33] observed experimentally that for a given compaction pressure, the per-ply thickness of 10 and 25 layer preforms was smaller than the thickness of single layer preforms of plain weave, unidirectional, and continuous strand reinforcements. This result displayed the effect of nesting based on layer number. Also, it was noted that the nesting effect was seen to be more prevalent in the woven and unidirectional fabrics than in the continuous strand mat. Endruweit et al. [159] also noted this behavior as they explained that especially in woven fabrics, where large gaps between tows exist, nesting may contribute significantly to variations seen in permeability. Dungan et al. [160] showed a corresponding decrease in in-plane permeability with an increase in preform layers. Hoes et al. [161] reported that nesting between layers was the main source experimental scatter in their permeability measurements of woven glass fabrics. The researchers concluded this by performing permeability measurements on preforms that were restricted from nesting by fusing layers together, and found very little experimental scatter compared to tests of unrestricted samples of the same material. Like fabric shear, nesting can have a significant effect on

permeability and therefore should be in consideration in experimental and modeling environments.

Another mode of reinforcement deformation that can be seen during LCM processes is fiber washout. Fiber washout is caused by high injection pressure or flow rates, where the reinforcement's fibers can be displaced by the permeating fluid. The occurrence of this phenomenon is dependent on the fiber volume fraction, fiber topology, mold surface roughness, fluid viscosity, and inlet pressure/flow rate [162]. If fluid enters a preform at high enough velocity, the surface tension and viscous drag force may prevent the fluid from permeating the reinforcements, resulting in the fibers being moved in the direction of flow [163]. While fiber washout is undesired in LCM, it's occurrence in any permeability measurement experiment must be noted. Richardson and Zhang [164] observed fiber washout while investigating flow through natural fiber composed reinforcements. In their study, fiber washout led to preferential channeling and race tracking, which correspondingly, increases measured permeability. The researchers also found with increase in fiber volume fraction, the fiber washout was gradually reduced. Ultimately, permeability measurements made in presence of fiber washout will not reflect the permeability of an undeformed preform, and permeability should be defined in a pressure/flow rate range below the critical value where washout occurs.

2.3.4.7 Race Tracking and Edge Effects

Race tracking in LCM occurs when infiltrating resin passes through high permeability areas in the mold cavity or preform resulting in quicker flow or so called "racing" [165]. This race tracking often can be produced from edge effects. If space is left between the fibrous

reinforcement and mold edge upon preforming, the infiltrating resin will flow faster through this region, which can result in altered flow patterns, dry-spotting, and can ultimately lead to a poor finished part [6]. Figure 2.2 depicts a gap between the preform and mold wall, which can result in race tracking. Gauvin and Trochu [166] stated that gaps as small as 1 to 2 mm are enough to cause race tracking during an infusion.

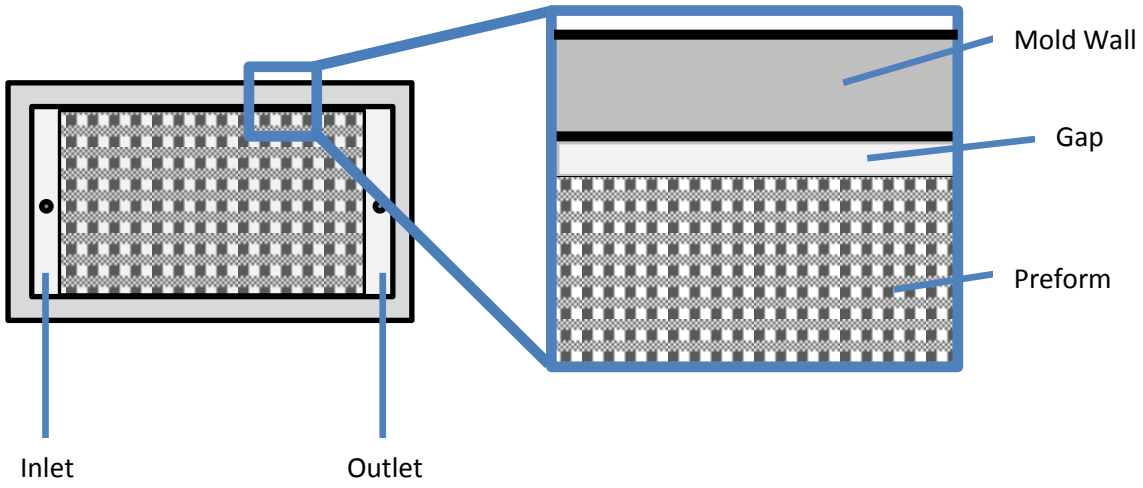

Figure 2.2: Depiction of Edge Effect

A dry spot formation due to race tracking and edge effects is illustrated in Figure 2.3. Initially, the injected fluid is seen to preferentially flow through the high permeability edge gap (A). The flow path then race tracks further along the mold wall (B), and finally results in a dry spot formation (C).

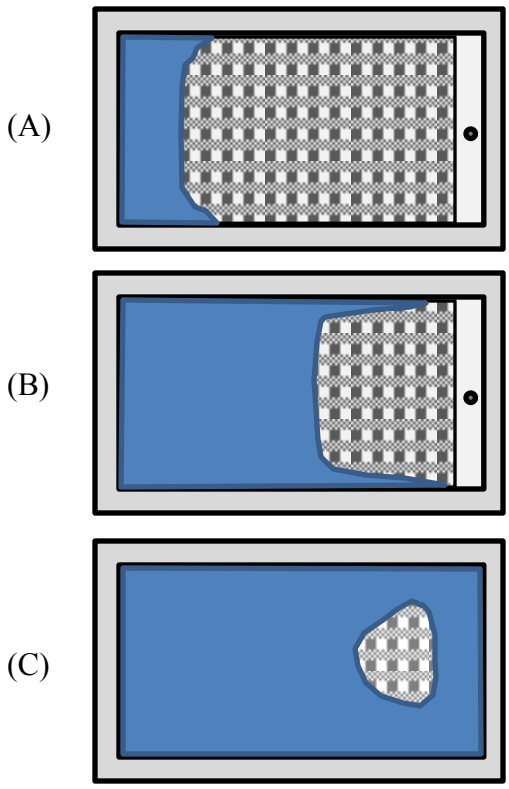

Figure 2.3: Dry Spot Formation from Race Tracking

Edge effects are a major consideration during the experimental measurement of permeability. Due to the high permeability of any present gaps, the average preform permeability derived from channel flow measurements could be artificially high. It should be noted that during radial permeability measurements, the occurrence of race tracking is not typical, and is much more an issue in channel flow or rectilinear measurements [80]. With this in consideration, researchers have offered techniques to mitigate race tracking effects during experimental measurements in 1D, channel flow fixtures. These techniques include the employment of silicone sealant between the preform edge and mold wall [68], the use of O-rings to compress the preform to high fiber volume fractions at the wall and seal from flow [36], and the practice of cutting preforms to precise width and visually observing if race tracking is present during infusions for clear-top fixtures [130], [167]. Dependent on the reinforcement type, some architecture can be more prone

to race tracking than others. Fabrics that are less likely to lose tows or those with secure stitching may be less likely to race track. The loss of a tow at the mold edge or fabric fray can also result in race tracking during infusion [167]. To combat fabric fray upon cutting some researchers have employed tape at the preform edge [71], [124], although Amico and Lekakou [124] found that tape increased the effect of race tracking. Amico and Lekakou [124] also investigated the use of thin strips of extra test fabric at the mold edge, but found that complete flow blockage and other variable results ensued. These researchers found most success in their channel flow experiments by cutting the preform slightly wider than the mold width and employing silicone tubes at the edge. While not attempting to eliminate the edge effect, Lawrence et al. [167] proposed a methodology to correct for experimental permeability in the presence of race tracking for isotropic preforms, and furthered the method for orthotropic preforms using an isotropic scaling method.

As for modeling purposes, the race tracking effects can be significant and thus should be accounted for during mold fill simulations [6]. Researchers have presented multiple methods for handling race tracking and edge effects in mold fill modeling. Several researchers have described relationships to define the equivalent permeability of the gap between preform and mold wall, which can then be used in modeling. This equivalent permeability approach defines the gap air channel as porous media and uses Darcy's law to govern the flow [168]. Ni et al. [165] summarized equivalent permeability formulas for various cross-sections including that of channel flow with one permeable boundary (i.e. a 2D representation of the edge effect). They were able to predict the edge effect using the abovementioned relation, which is seen in Equation 50.

$$S_{gap} = \frac{1}{hd} \sum_{n=1,3,5,\ldots} \left\{ \frac{8}{n\pi {\gamma_n}^3} \left[d - \frac{\sinh(\gamma_n d)}{\gamma_n} - \frac{1 - S{\gamma_n}^2 - \left(\frac{\sqrt{S}}{\alpha}\right)\gamma_n \sinh(\gamma_n d) - \cosh(\gamma_n d)}{\sinh(\gamma_n d) + \left(\frac{\sqrt{S}}{\alpha}\right)\gamma_n \cosh(\gamma_n d)} \frac{\cosh(\gamma_n d) - 1}{\gamma_n} \right] \right\} \tag{50}$$

Here, S_{gap} is the equivalent gap permeability, d is the gap width (the distance between the preform and mold edge), h is the thickness of the gap, $\gamma_n = n\pi/h$, and α is the square root of the ratio between apparent viscosity of the fluid in the fibrous region and the fluid viscosity. Gauvin and Trochu [166] compared two simple relationships for gap permeability seen in Equation 51.

$$S_{gap} = \frac{d^2}{12} \tag{51a}$$

$$S_{gap} = \frac{hd}{8\pi} \tag{51b}$$

The authors, using a range of experimental data and an RTM flow processing software, back calculated the gap permeability that fits the experimental data. The accuracy of the proposed models was found to depend significantly on the ratio of permeability both parallel and perpendicular to the flow direction. Young and Lai [169] found good agreement between experimental values and their proposed relationship for gap permeability seen in Equation 52.

$$S_{gap} = \frac{h^2}{96}\left[1 - \frac{192h}{\pi^5 d}\tanh\left(\frac{\pi d}{2h}\right)\right] \; for \;\; d \leq h \tag{52a}$$

$$S_{gap} = \frac{h^2}{96}\left[1 - \frac{192h}{\pi^5 d}\tanh\left(\frac{\pi h}{2d}\right)\right] \; for \;\; d > h \tag{52b}$$

Bickerton and Advani [168] used a mixed Darcian-Stokes approach to model mold fill simulations with the edge effect. In this approach, Darcy's law is solved in the domain of the preform and 1D Stokes flow is solved in the channel created by the gap.

2.3.4.8 Tackifier/Binder and Particulate Effects

In composite manufacturing, the addition of tackifier to preform alters the total preform geometry and permeability can be affected greatly. The assumption that a fiber preform with and without a tackifier will produce the same permeability and resin flow characteristics is not accurate without validation. Neglecting an investigation of the permeability change could lead to processing issues and failed parts. Furthermore, tackifiers in powdered resin form have been noted to have significant effect on preform permeability depending on the powdered resin type, processing parameters and tackifier location relative to the reinforcement [9]–[11]. Estrada et al. [11] defined locations of tackifier as inter-layer or intra-layer. Inter-layer denoted tackifier placed on the surface of the reinforcement and intra-layer denoted tackifier placement inside fiber tows of the reinforcement.

Inter-layer tackifier has been reported by both Rohatgi and Lee [9] and Estrada et al. [11] to reduce permeability with increasing tackifier content by blocking flow channels between fiber tows that are unobstructed on non-tackified preform counterparts. Tackifier that is distributed within fiber tows has been noted to give little effect to global permeability by Rohatgi and Lee [9] but Shih and Lee [10] reported increasing permeability with increasing tackifier content if intra-layer tackifier was present depending on the processing procedure of the material. Chen et al. [12] investigated the effects of a thermoplastic powered tackifier that were spray-coated onto

glass mats. These researchers saw that during heated mold, one-dimensional infusions, the tackifier was dissolved in injected resin and was seen to increase resin viscosity more than two-fold. Viscosity effects at this magnitude, although will not alter geometrical preform permeability, will change the effective permeability and alter the ease of flow. Work from George [170] saw significant decreases in permeability employing Spunfab, a binder consisting of a web of thermoplastic resin, when the binder was blocking inter-tow channels. Also, difficulty with the infusions, including preferential channeling around rather than through the tackified preforms, was reported in the study.

Similar geometrical additions that affect flow include particulate effects. Manufacturers have used nanomaterials to enhance composite parts' electrical, thermal, and mechanical properties [171]. In these cases, the nanoparticles are either dispersed in the matrix to be injected or are applied directly to the preform before for the LCM infusion. Regarding bulk preform permeability, the effects of nanoparticles should be considered in terms of the alteration of the matrix viscosity rather than in terms of geometrical effects when the nanoparticles are first dispersed in the matrix. The particle type will also play a role in the resulting LCM infusions, as well as particulate washout and reinforcement filtration effects. In a study by Mahrolz et al. [172], silica nanoparticles with loadings up to 25 wt% in epoxy was used to manufacture composite parts. The researchers saw slight changes in resin viscosity and concluded that the injectability for LCM purposes is nearly unaffected. Umer et al. [173] investigated transient permeability of a plain weave S-glass coated with exfoliated graphene nano-platelets (xGnP) at 0.5 and 1.0 wt%. They found that in-plane permeabilities were interestingly increased with the addition of xGnP wt% and attributed this result to a spacer effect where the xGnP coating

increased the resistance to compaction. It should be noted that this study employed a VARTM vacuum bag system to measure permeability. Therefore, the increase in permeability is coupled with the resistance to compaction, which means a lower fiber volume fraction was achieve under the vacuum bad with the addition of xGnP. If these tests were carried out in a closed mold with fixed thickness and fiber volume fraction, a different trend (possibly lower permeability with increase in xGnP) would likely result.

2.3.4.9 Experimental Variability

As reported in literature, preform permeability has been found to be highly variable. The amount of present process variables and the fact that no standard permeability measurement technique exists makes it difficult to maintain consistency across the research area. In a recent large-scale permeability benchmark exercise [66], 11 different institutions participated to characterize a twill weave carbon fabric and a 2x2 twill weave E-glass fabric in in-plane permeability. The participants employed unsaturated and saturated, radial and linear measurements techniques with different test fixtures and varying test fluids. The study found that for each fabric, the reported permeability results from the participants varied by up to an order of magnitude in value. With this significant scatter in data, it was concluded that human error was the main source of variation where sample preparation, consistent equipment operation, and data evaluation could be in question. A sequel benchmark exercise [69] was carried out shortly after. In this exercise, 13 different institutions participated and a common measurement technique with greater parameter control was used throughout. A companion experimental guideline document [68] was also created for this study. The specific guidelines for error reduction will not be mentioned here and can be found therein. For the same materials, this second exercise produced a standard

deviation of ±20%, much smaller than the original study. It was then concluded that differences in experimental procedure were the main cause of the variation and the human factor is negligible.

Lundström et al. [67] performed a previous collaborative permeability study and also compared saturated and unsaturated techniques, albeit on a smaller scale where 3 institutions were involved. Materials characterized included a 3D weave glass fabric, a glass NCF and a plain weave glass fabric. They found that the best repeatability of in-plane permeability measurements is obtained with the unsaturated channel flow technique, which produced standard deviations up to 20%. The researchers stated that material variations and sample preparation were the main causes for deviation among the measurements. With the current state of no permeability measurement standard in the LCM community, the latest collaborative guidelines have produced results with standard deviations of about ±20%. This can then be deemed acceptable variation in permeability measurements. Due to the inherently variable nature of composite reinforcements, especially in complex architecture preforms, this magnitude of scatter should not be unexpected.

3. Compaction

Reinforcement compaction behavior is important to characterize for LCM processes. The applied compaction pressure on a preform can be correlated to thickness and fiber volume fraction. For RTM, the compaction pressure to reach the desired part fiber volume fraction can be used to estimate the needed mold clamping forces. For VARTM, the vacuum, fiber bed, and resin pressures govern the final part fiber volume fraction of the composite being manufactured. The compressibility characteristics of a preform can also be used in conjunction with permeability measurements to better understand the overall processing behavior of the material. This chapter will describe a simple compaction technique and fixture setup for characterization of IM7-4HS preforms. A heated vacuum debulk cycle will also be presented for construction of IM7-4HS preforms. Compressibility will be quantified with focus on the effects of tackifier, debulking, and preform layup. Further investigation will explore the effects of fluid saturated compressibility versus dry compaction. Results of compaction pressure versus fiber volume fraction will be presented, while discussion on these findings will also be made.

3.1 Method

3.1.1 Compaction Setup and Procedure

Measuring the compressibility of fiber preforms in this study involved a simple technique of compacting samples between two steel platens. This technique is similar to that used by Somashekar et al. [38]. The compaction fixture was composed of a bottom steel base plate and a controllable top compression platen that allowed testing of preforms 15.24 cm (6 inch) square in size. The fixture was housed in a 100kN MTS Insight electromechanical testing frame. The fixture, seen in Figure 3.1, was outfitted with a Banner L-GAGE laser gauging sensor to monitor instantaneous sample thickness and a Mitutoyo dial gage indicator was used to confirm the thickness. The compression platen was attached directly to the MTS crosshead, which also possessed a load cell. The MTS crosshead displacement also was used to measure sample thickness. Compaction tests were run with a constant loading and unloading rate. The fixture accepted samples on the base plate, and a loading cycle started when the compression platen was lowered onto the preform at a constant rate of 0.254 mm/min until a user specified load limit was experienced by the load cell. Then, the unloading cycle was started by raising the compression platen at a constant rate of 0.254 mm/min, reducing pressure, until zero load was registered. This entire loading and unloading cycle was programmed into the TestWorks software, which allowed precise control of the MTS and test repeatability.

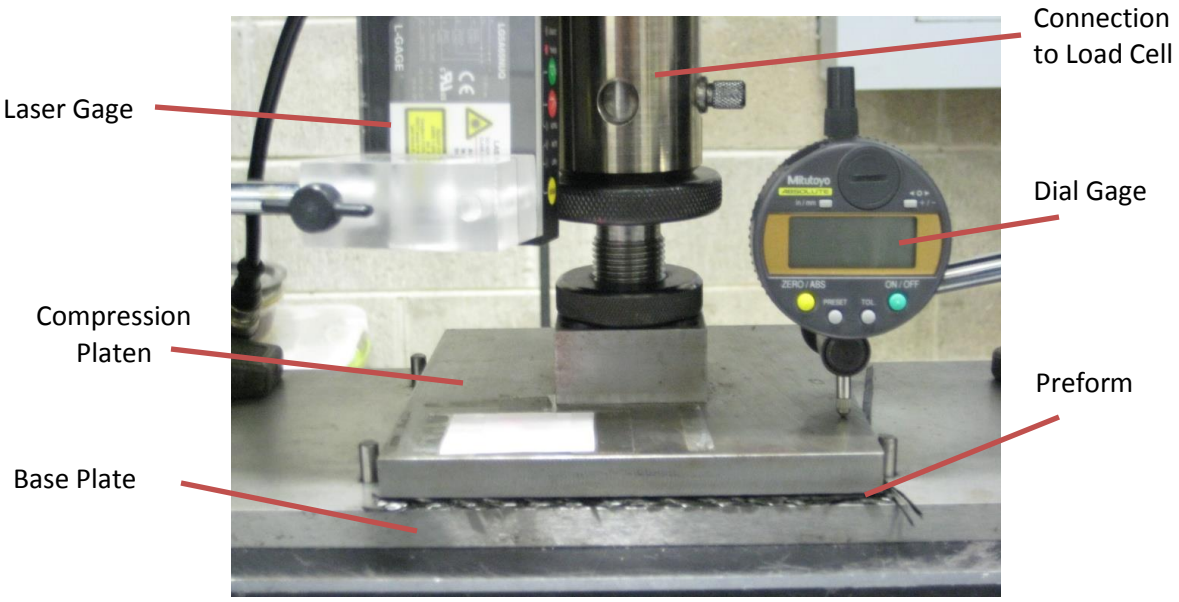

Figure 3.1: Compaction Test Fixture

Before each test, the thickness monitoring devices were calibrated and the load cell was zeroed. This was done by manually lowering the compaction platen until it just touched the base plate and load was registered. This point was specified as the zero location for the laser gage, the dial indicator, and the MTS crosshead displacement. The fixture was then opened to accept a preform. IM7-4HS plies were hand cut with the aid of a cutting die, and laid up in a desired sequence and layer number. The preform was loaded onto the compaction fixture's base plate, and the compaction platen was manually lowered onto the preform until a preload of ~10 N was registered. This was done for each test in attempt to maintain consistency for a starting point of the sample fiber volume fraction. The thickness monitors were read and recorded at this point as the initial preform thickness. The loading/unloading cycle described above was then started and the resulting thickness and load measurements were recorded throughout the test. Using the relation in Equation 53, the measured thickness from the laser gage was converted into fiber volume fraction.

$$V_f = \frac{nA_w}{t\rho_f} \tag{53}$$

Here, V_f is the fiber volume fraction, n is the number of plies, A_w is the fabric areal weight, t is the preform thickness, and ρ_f is the fiber density of the IM7 fibers. The recorded MTS load cell data were converted into applied compaction pressure simply by dividing the measured load by the 15.24 cm (6 inch) square platen area. With this, the preform fiber volume fraction could be plotted as a function of applied compaction pressure, and empirically fitted for modeling purposes. Preforms were also tested in a fluid saturated state, to investigate the effects of wetted compaction. To do this, plies were individually saturated in the SAE 40 motor oil before preform assembly. The compaction tests of wet samples were then carried out using the same method as described above for dry samples.

3.1.2 Material/Preform Preparation

Compaction tests were performed on non-tackified, tackified, and debulked preforms. Non-tackified preforms were cut from supply rolls of IM7-4HS without the low areal weight prepreg tackifier, and tackified preforms were cut from supply rolls with the prepreg. The debulked preforms needed an additional preforming step. They were created from a hot debulk process described in the next subsection. Several preform variations of the IM7-4HS were used to compare compaction effects. These compaction preform variations can be seen in Table 3.1.

Table 3.1: IM7-4HS Preform Variations for Compaction Tests

Variation #	Preform ID	Material	# of Layers	Layup Sequence	Tackifier	Debulked
1	Warp Aligned Non-Tackified	IM7-4HS	6	$[0]_6$	No	No
2	Laminate Non-Tackified	IM7-4HS	6	$[0,+45]_3$	No	No
3	Warp Aligned Tackified	IM7-4HS	6	$[0]_6$	Yes	No
4	Debulked Laminate	IM7-4HS	6	$[0,+45]_3$	Yes	Yes
5	12 ply Laminate Non-Tackified	IM7-4HS	12	$[0,+45]_6$	No	No
6	12 ply Debulked Laminate	IM7-4HS	12	$[0,+45]_6$	Yes	Yes

Also, comparisons were made between certain preform variations and at different compaction pressures. Comparisons between variation #1 and # 3 are made including the effects of wet compaction. These tests were made at high compaction pressures to high fiber volume fractions up to 75%. This level of compaction should be noted to be close to the maximum attainable fiber volume fraction of the material in an RTM process. Focus on the effects of tackifier and lubrication was targeted in these runs. Comparisons were also made between variations #2, #4, #5, and #6. These compaction runs were made at lower pressures so that a maximum fiber volume fraction of around 55% was obtained. The focus of these tests was to investigate the effects of debulking and preform ply number. To conserve material for permeability and flow investigations, an average between two compaction runs was used for each dry compaction data point, while one wet compaction cycle was used for dry vs. wet compaction comparisons.

3.1.2.1 Debulking Process

To create the debulked IM7-4HS samples listed in Table 3.1, a heated vacuum cycle was applied to a laid up stack of the tackified IM7-4HS fabric. The tackified IM7-4HS was laid up in either a

6 or 12 ply stack on a steel plate. A thermocouple was placed midplane in the laminate to monitor part temperature during the debulk process. The preform was sealed under a vacuum bag with sealant tape and pulled to full vacuum using a Welch model 2027 dry vacuum system. The plate was then placed between the platens of a TMP 140 ton heated vacuum press; see Figure 3.2. The TMP press was used only for heating the plate and preform. With increased temperature and pressure, the low areal tackifier was melted, cured, and then cooled to room temperature to unpack. This process effectively "debulked" the preform to a lower thickness than the original layup. Also, the tackifier was cured to firmly hold shape and fiber orientation of the reinforcement. The resulting preform was very stiff or "boardy".

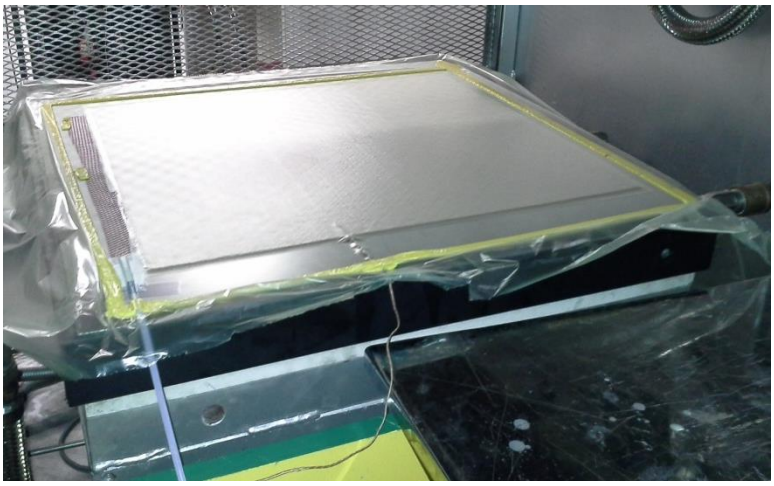

Figure 3.2: IM7-4HS Preform Sealed for Hot Debulking in TMP Heated Press

The press' platen temperatures were computer controlled so a heating cycle was created for debulking purposes. The goal of this cycle was to heat the preform close to 149° C for at least 10 minutes to ensure the tackifier was melted. The heat cycle of the press' platens can be seen Figure 3.3, where the "part" or preform temperature from the midplane thermocouple is also displayed for the first debulk run. After the 10 minute high temperature soak, the press was cooled by a water mist spray inside the platens until 94° C was reached. Then, the platens were

cooled further by flooding their interiors with cold water until they reached 38° C. Vacuum was then halted and the preform was debagged and allowed to reach room temperature before test samples were cut.

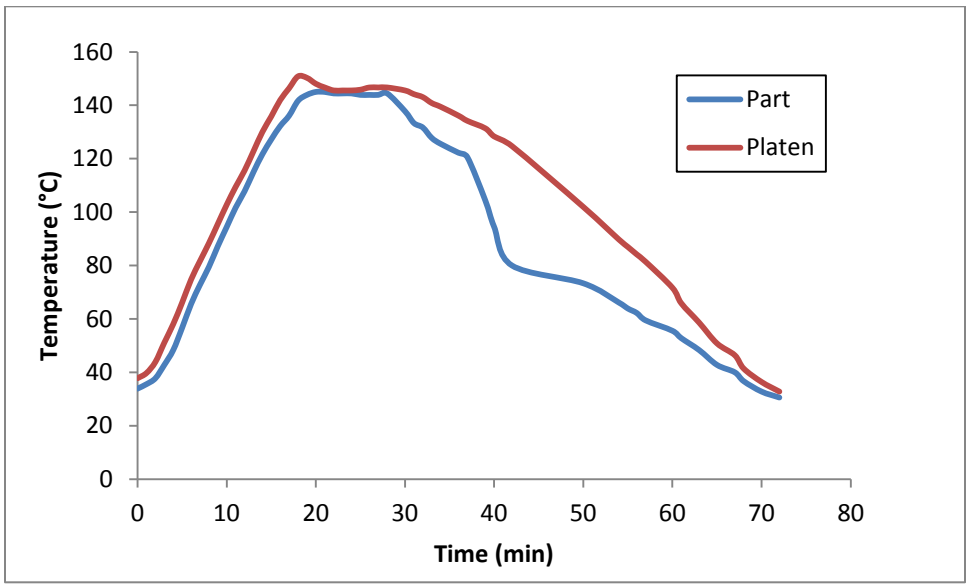

Figure 3.3: TMP Platen Temperature Cycle for Debulking Process

The debulk cycle took roughly 70 minutes to complete and produced stiff preforms that were compacted to roughly 45% to 50% fiber volume fraction with the aid of full vacuum pressure. The interlayer tackifier cured to securely bind together laminate plies. Tackifier melting and rearrangement was expected in the process, including the likelihood of tows absorbing some of the melted tackifier. This debulking process was used for several sets of preforms both for compaction and permeability measurements.

3.2 Results and Discussion

A sample compaction graph is displayed in Figure 3.4. This figure illustrates the general characteristics of the loading and unloading curves. This specific graph was generated from the measurements of a 12 ply, non-tackified IM7-4HS laminate sample. The sample, initially at

about 30% fiber volume fraction, was loaded to 105 kPa of compaction pressure then unloaded until no compaction was present. A maximum fiber volume fraction just under 55% was reached with these compaction pressures. Note the hysteresis of fiber volume fraction starting and ending points. After unloading the sample was roughly 8% higher in fiber volume fraction then initially before the compaction cycle. Although, some of this could be recovered from relaxation over time, this was not studied here, as typically, only the loading curve is needed to characterize preforms for RTM applications. Also, consecutive compaction cycles were not run on the IM7-4HS samples.

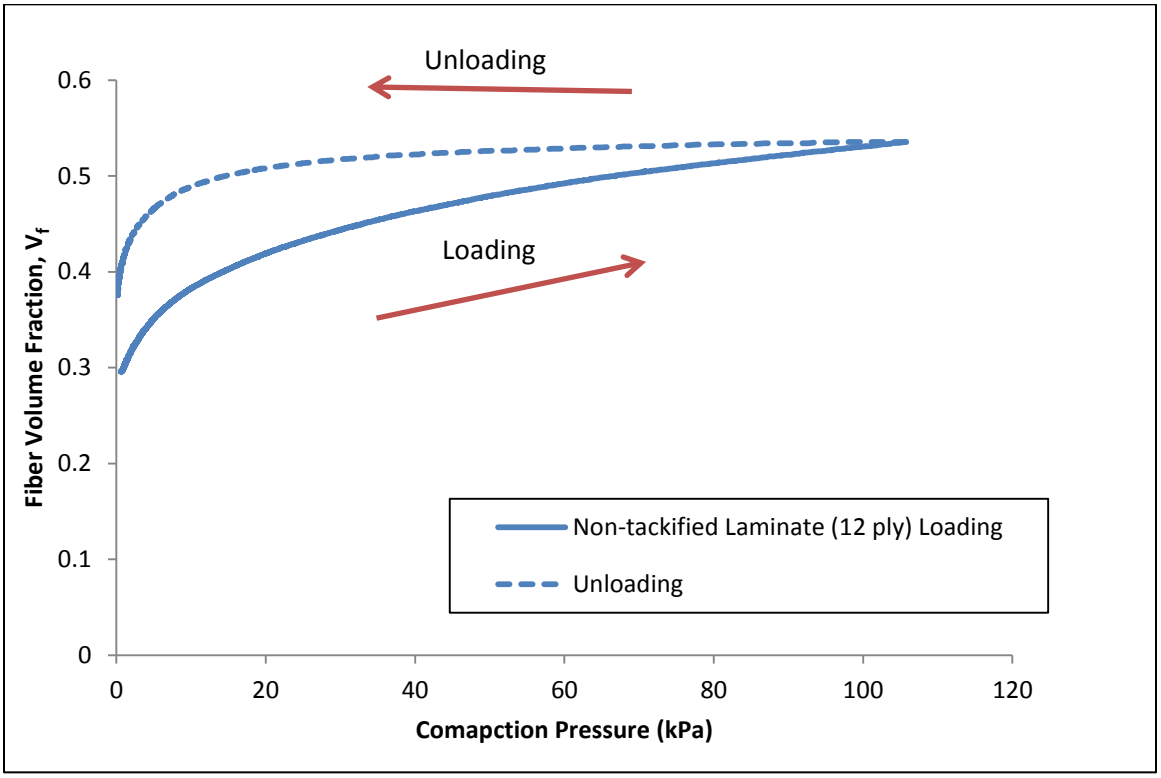

Figure 3.4: Typical Preform Compaction Graph (12 Ply Non-tackified IM7-4HS Laminate)

3.2.1 Debulking and Ply Number Effects

The following few sets of compaction graphs compares non-tackified and debulked laminate preforms at both 6 and 12 ply layups. These curves were loaded to a compaction pressure of 105 kPa. First, results displaying 6 ply non-tackified and debulked laminate (variations #2 and #4 of Table 3.1, respectively) preforms are shown in Figure 3.5. The debulked material's compaction curve is in red, while non-tackified loading and unloading are in blue.

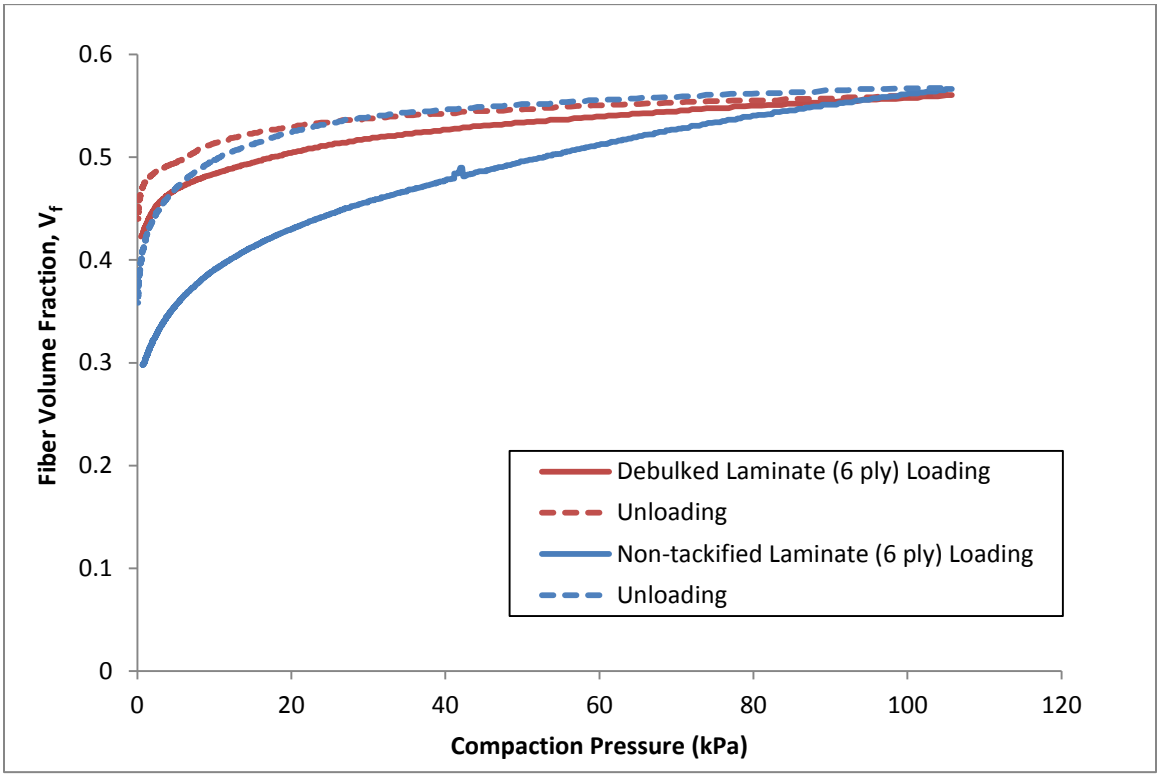

Figure 3.5: Comparison between Non-tackified and Debulked 6 Ply Laminate Compaction

Here, the effects of debulking are evident right away in the shape of the loading and unloading curves compared to that of the non-tackified material. The debulked preform is initially ~12% higher in fiber volume fraction value than the non-tackified due to the heated vacuum consolidation process. The debulked preform also shows much smaller difference between fiber

volume fractions reached during the loading and unloading cycles. The amount of hysteresis seen further shows this, which is nearly negligible for the debulked preform, while the non-tackified material shows the compaction cycle increased the fiber volume fraction roughly 5%. Focusing on the loading portion of each material, it can be seen that the debulked preform shows a shallower slope of fiber volume fraction as compaction pressure increases than the non-tackified. From 0 to 105 kPa of compaction pressure, the non-tackified material was compressed to increase its fiber volume fraction by nearly 25%, while the debulked sample was increased only about 10% from an uncompacted state. This means that the debulked sample possessed a higher resistance to compaction than the non-tackified. Physically, this is because the debulked material possessed the cured inter-layer tackifier, which fused tows together to resist nesting and therefore fiber volume fraction increase. Evidence of this phenomenon is more clearly seen in a comparison of 12 ply preforms of the same laminate stacking sequence. This is seen in Figure 3.6.

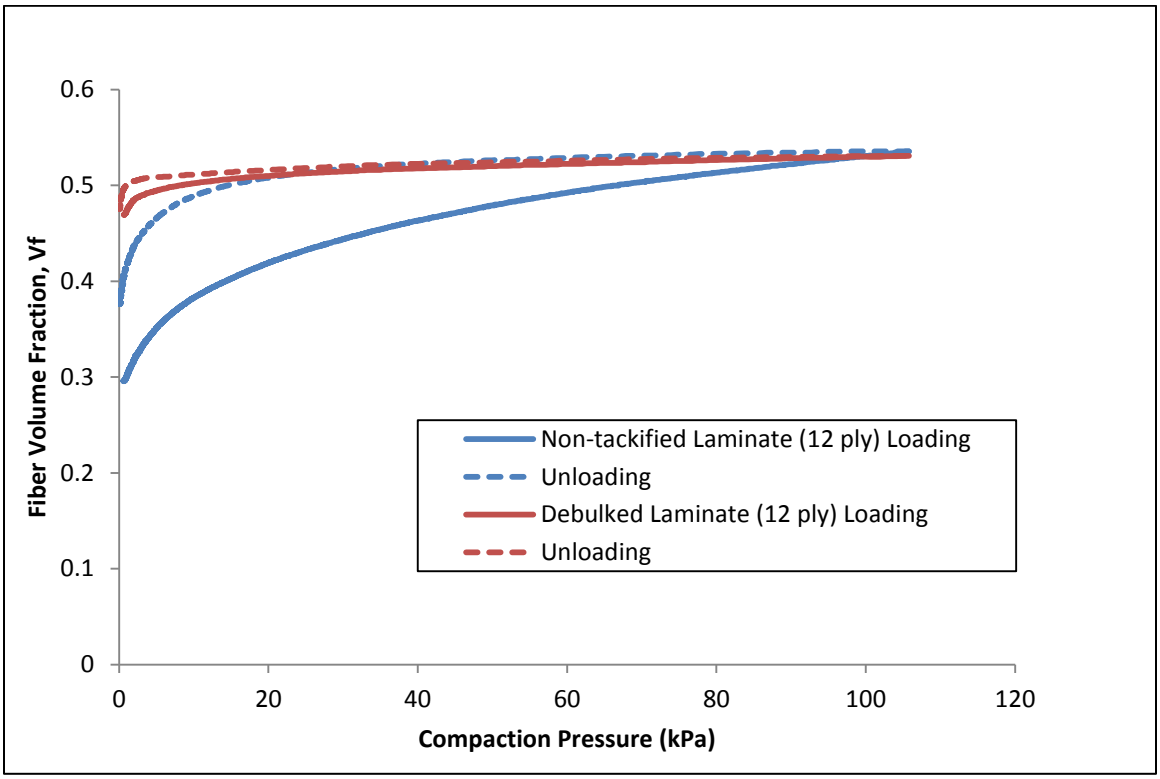

Figure 3.6: Comparison between Non-tackified and Debulked 12 Ply Laminate Compaction

The 12 ply debulked material showed large resistance compaction pressures. Virtually no increase in fiber volume fraction was seen on the loading curve. The debulked sample was also nearly 20% higher in initial fiber volume fraction than the non-tackified material. From these results it can be concluded that reaching higher fiber volume fraction in debulked samples should require very high compaction pressures compared to non-debulked.

Now, an overlay of non-tackified laminate IM7-4HS preform layups is shown in Figure 3.7, where a direct comparison of ply number, 6 versus 12 ply preforms is made. Here, the green curves relates to the 6 ply preform, while black curves represent the 12 ply preform.

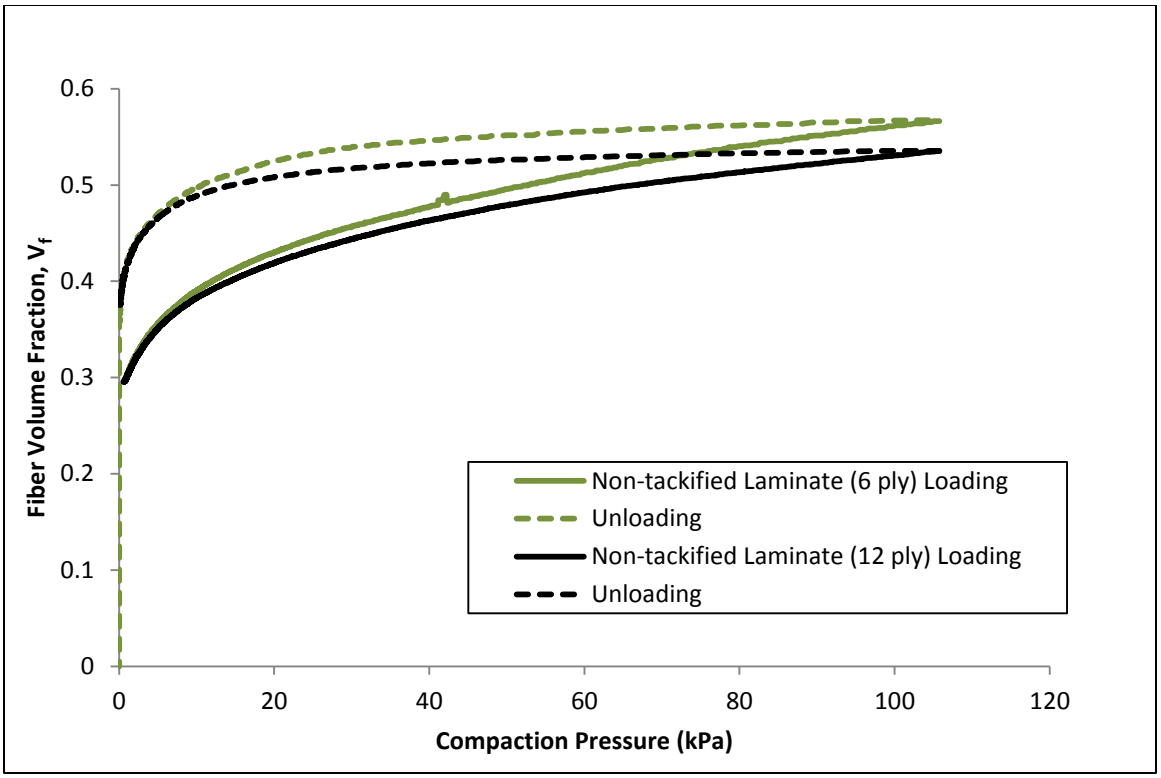

Figure 3.7: Comparison between Non-tackified 6 Ply and 12 Ply Laminate Compaction

Both the 6 and 12 ply loading and unloading curves have similar shape, while interestingly, the 6 ply sample was compacted to a higher fiber volume fraction (~5%) under the same pressure. This is in contradiction to results from Chen et al. [33] and Grimsley [36], who reported decreasing per-ply thickness (increasing fiber volume fraction) with an increase in ply number during compaction experiments. Thus, the results here imply significant nesting is not present at the fiber volume fractions tested.

Figure 3.8 displays the 6 versus 12 ply preform comparison with the debulked IM7-4HS laminate.

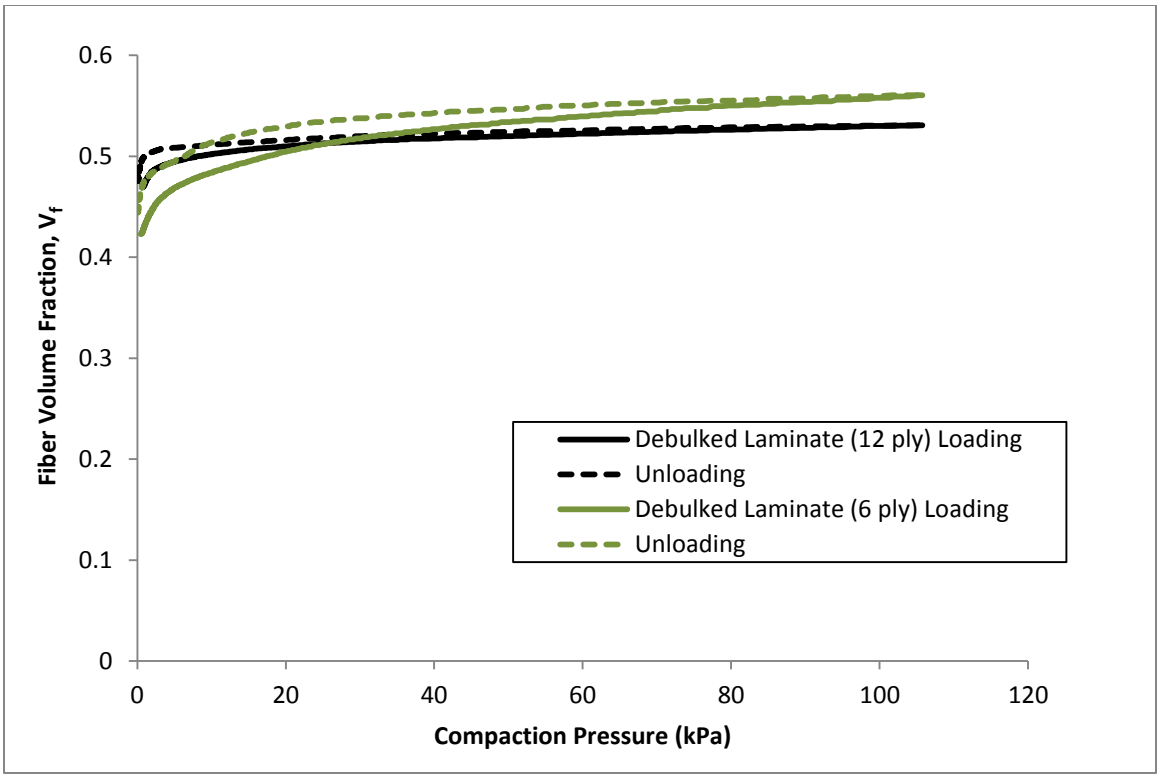

Figure 3.8: Comparison between 6 and 12 Ply Debulked Laminate Compaction

Both the debulked preforms show very flat loading and unloading curves. The cured tackifier provides little give for compaction at these pressures. Again, the 6 ply preform was seen to produce a higher fiber volume fraction than the 12 ply at 105 kPa of compaction pressure. An explanation for this could be that due to the addition of debulked plies in the 12 ply preform, a larger network of the cured tackifier is created and thus produces a stiffer response to the applied pressure. Therefore, little increase in fiber volume fraction is seen compared to that of the 6 ply debulked preform.

3.2.2 Non-Debulked Tackifier and Wetted Compaction Effects

The next set of compaction results reflect those loaded to higher pressures. The curves compare warp aligned non-tackified and tackified (non-debulked) preforms in a 6 ply layup (variations #1

and #3 of Table 3.1, respectively) loaded to 500 kPa. These results also will investigate wet compaction and the lubricative effect. Figure 3.9 displays a comparison between warp aligned non-tackified and tackified preforms. Here, the blue color curves represent preforms constructed of the non-tackified IM7-4HS, whereas the red curves signify the preforms of tackified material, but not debulked.

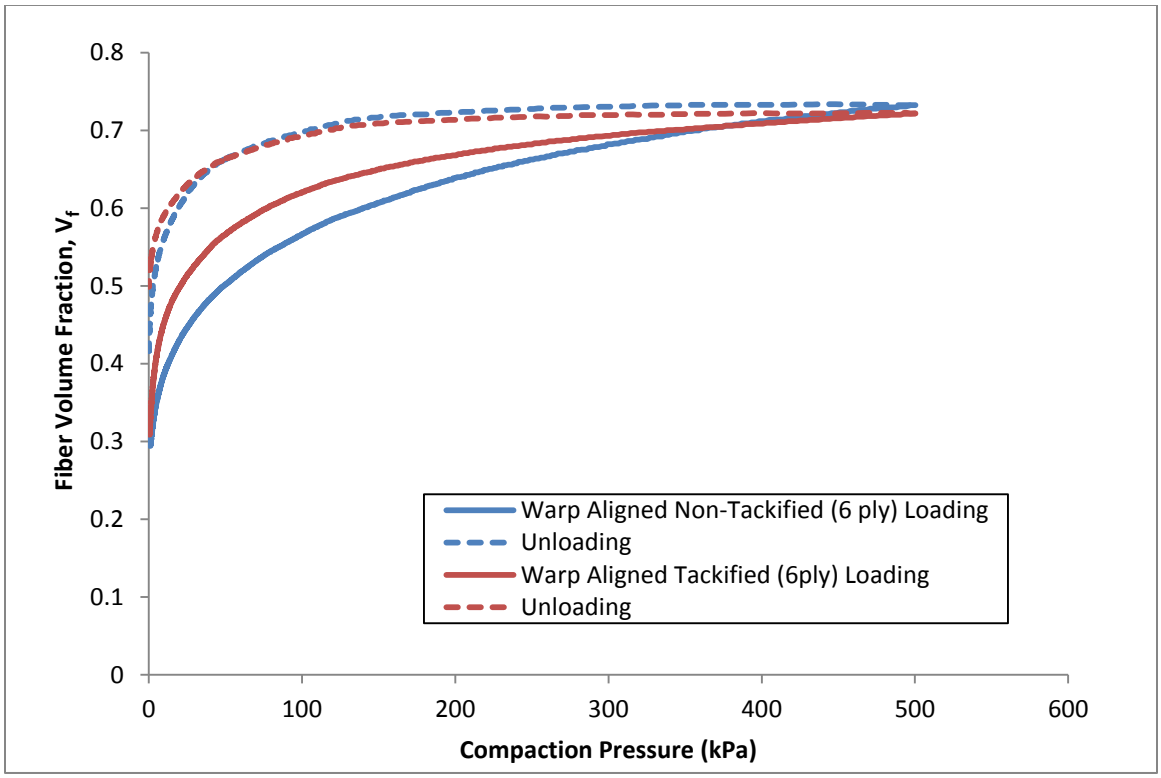

Figure 3.9: Comparisons between Non-tackified and Tackified Warp Aligned 6 Ply IM7-4HS Compaction

Here, both the tackified and non-tackified warp aligned preforms were compacted to a similar fiber volume fraction at maximum pressure. A smaller difference between the loading and unloading curve in fiber volume fraction was seen for the tackified material compared to the non-tackified samples. As compaction pressure increased, the slope of the tackified loading curve became shallower than the non-tackified material. Surprisingly, the loading curve of the

tackified preform was seen to produce higher fiber volume fractions than the non-tackified sample for the same compaction pressure up to roughly 375 kPa.

In Figure 3.10, the warp aligned non-tackified (in blue) is compared to the same preform in a wet compaction condition (orange).

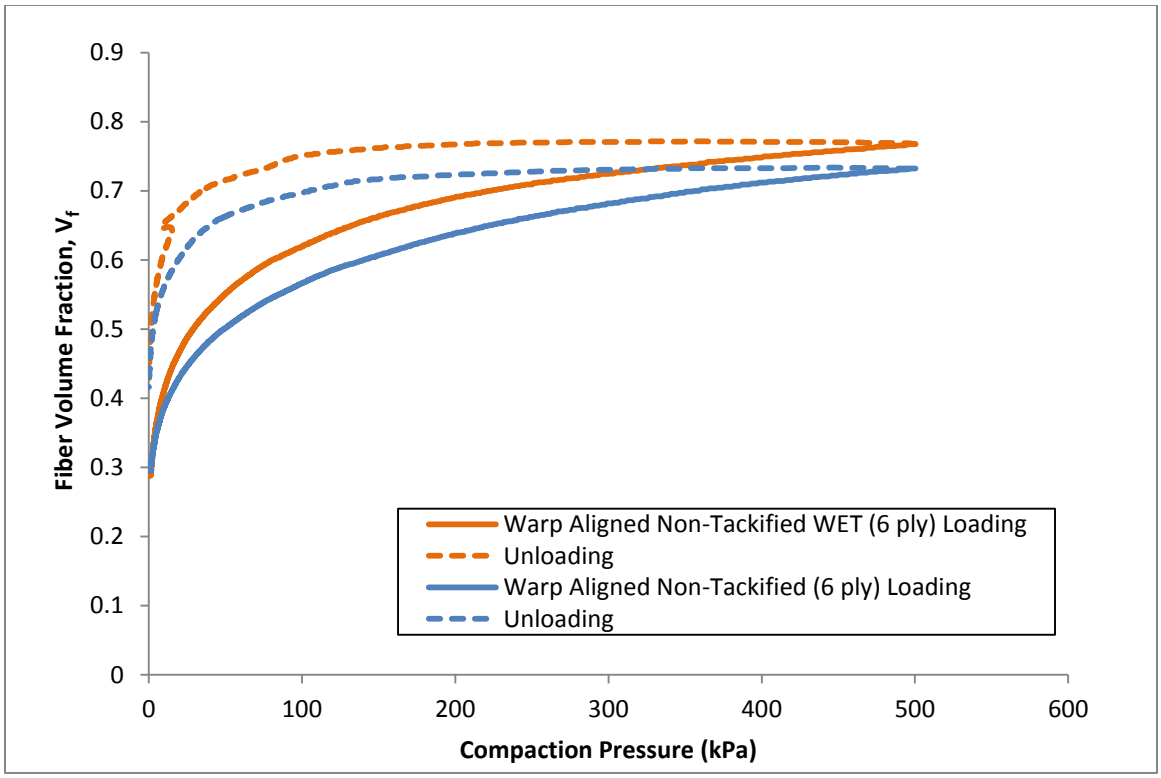

Figure 3.10: Comparisons between Dry and Wet Warp Aligned Non-tackified 6 Ply IM7-4HS Compaction

The wet or SAE 40 oil saturated preform is clearly seen to have a significant effect on the compaction behavior of the reinforcement. The saturated IM-4HS sample was seen to achieve roughly a 5% increase in fiber volume fraction at the end of the loading cycle. This behavior has been documented before by researchers and is attributed to a lubricative effect the fluid supplies, where a rearrangement of fiber network is possible as friction is reduced [36], [46]. Note that the unloading curve of the wet sample showed a discontinuity near complete unloading. This artifact

comes from a suction effect as the interface between preform, fluid, and compaction platen are separated. In Figure 3.11, the same dry verses wet compaction comparison can be seen for the warp aligned tackified IM7-4HS preforms.

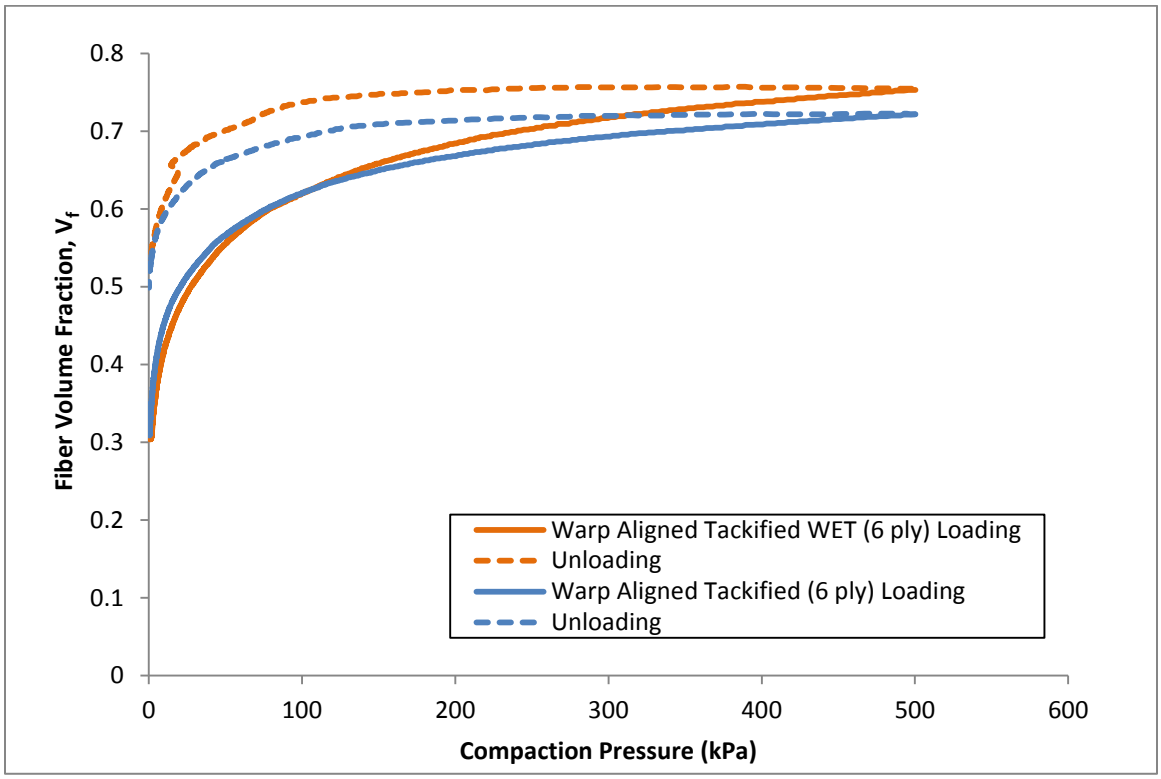

Figure 3.11: Comparisons between Dry and Wet Warp Aligned Tackified 6 Ply IM7-4HS Compaction

Again, the wet compaction showed signs of the lubrication effect and additional nesting (~5% increase in fiber volume fraction) for the tackified material. For VARTM specific applications, wet and dry compaction data can be used together to model the resin infusion under vacuum pressure. For RTM applications, a fixed mold cavity depth or preform thickness is prescribed, and generally a dry preform is closed in the mold before infusion. In this case, wet compaction results are less useful.

Finally, wet compaction curves of non-tackified (green) verses tackified (black) IM7-4HS preforms are presented in Figure 3.12.

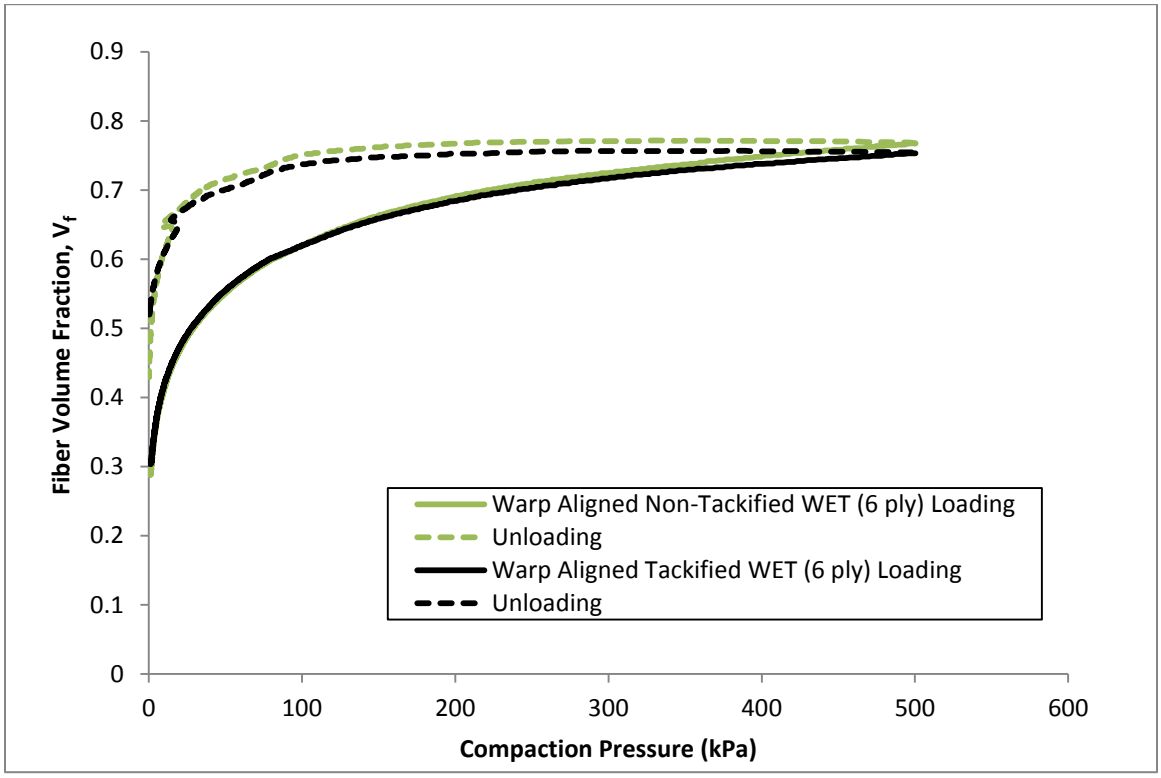

Figure 3.12: Comparisons between Non-tackified and Tackified Warp Aligned 6 Ply IM7-4HS Wet Compaction

Very similar compaction behavior is seen between the wet samples of the non-tackified and tackified IM7-4HS. From this, it may be concluded that the lubrication effect is a dominant feature of the compressibility of the IM7-4HS, and in this case, makes the presence of tackifier negligible.

3.3 Conclusions

In this chapter, simple compressibility experiments were described and results were presented on various IM7-4HS preforms, which correlated applied compaction pressure to fiber volume fraction. The heated vacuum debulk cycle was also presented, which was used to consolidate tackified IM7-4HS preforms. Debulking produced very stiff and boardy preforms. The debulking

process provided pre-compaction to the preforms, where samples were seen to reach between 45% and 50% fiber volume fraction after the cycle was completed. Debulked samples then showed a large resistance to compaction pressures compared to non-debulked preforms. This was attributed the cured tackifier fusing tows together, which resisted fiber rearrangement. 12 ply debulked experiments were seen to resist compaction greater than those of 6 ply. Tackified, but non-debulked samples also displayed some resistance to compaction at high pressures, although not as great as the debulked material. This is because the unprocessed inter-layer tackifier was not cured to fuse tows, so some nesting was still achievable. Further wetted compaction experiments (SAE 40 oil saturated preforms) showed results consistent with literature, where higher fiber content was achievable under the same compaction pressures than dry compaction due to the lubrication effect. Also, the wetted compaction curve comparison between tackified and non-tackified preforms showed nearly identical fiber volume fractions for the same applied compaction pressures. Notably, the wetting effect was deemed to make the presence of tackifier (non-debulked) negligible. Further work could quantify the amount of spring-back obtained among non-tackified, tackified, and debulked IM7-4HS preforms.

Regarding application to LCM, Shih and Lee [10] stated that an ideal tackifier should be able to prevent spring-back to maintain good preform dimension control. While spring-back and relaxation were not explicitly studied in this investigation, it is clear that upon debulking of tackified IM7-4HS, a very stiff and compaction resistant preform is created. For RTM then, debulking may be beneficial in terms of dimensional control. Although if preform fiber volume fractions are desired that are higher than what vacuum compaction can achieve, debulking in rigid molds may be necessary. Compaction experiments at high compaction pressures (like the

ones done in this study) then would become helpful. Care should be taken regarding debulking, to ensure the preform is not compacted to a smaller thickness than what will be obtained in an RTM mold. If this is the case, race-tracking around the preform may occur [10]. Permeability and flow through IM7-4HS preforms including debulked samples will be explored next in Chapter 4.

4. Saturated Permeability

Saturated permeability characterization methods have been used for years to provide input parameters for Darcian flow based process models in LCM. While in some cases, these methods have been noted to produce different flow and permeability than those of unsaturated flow (flow native to the LCM process) [139], their data output per sample is much higher. Saturated measurements allow characterization of permeability across multiple fiber volume fractions with one sample, while unsaturated methods can only produce one data point per sample. Saturated permeability measurements then provide a good baseline method for characterization of the IM7-4HS preforms. This chapter will present the saturated permeability measurement techniques and fixture setup for both in-plane and transverse characterization. The effects of the inter-layer tackifier, sample debulking, layup, and ply number on preform permeability are also presented. Important inferences regarding tackifier effects will be noted in reference to composite manufacturing. The baseline results produced here will be used to compare with unsaturated methods in Chapter 5.

4.1 Methods

4.1.1 In-plane Permeability Fixture Setup

Channel flow or parallel flow permeability fixtures have been commonly employed in LCM literature to measure preform permeability by isolating the permeating fluid flow in one direction. This isolation allows for permeability formulation based on one-dimensional Darcy's law. Known fabric geometry parameters and measured pressure drops across a preform induced from fluid injection are used to define permeability. To obtain these saturated in-plane permeability measurements in this manner, a matching steel mold test fixture was employed, as displayed in Figure 4.1. Preforms 15.24 cm wide by 15.32 cm long, and up to 1.27 cm thick can be accommodated in the test cavity. Two main components comprise the in-plane fixture: 1) the guided plunger on the top half to provide preform compaction, and 2) the bottom half housing the test cavity and pressure transducers. The fixture was loaded into a 100kN MTS Insight mechanical testing frame that allowed for user control of the fixture's cavity thickness by lowering the plunger into the test cavity. The plunger features a groove machined in the head to accommodate a 3.97 mm (5/32 inch), square cross-section O-ring. This O-ring provided a seal during testing to ensure built up pressure was not lost. The O-ring also protruded past the head of the plunger to ensure no race tracking of fluid over the preform was possible at this recess. Preforms were loaded into the test cavity and were compacted to a thickness corresponding to a desired fiber volume fraction using Equation 54.

$$t = \frac{nA_w}{V_f \rho_f} \tag{54}$$

Here, t is the preform thickens, n is the number of fabric layers, A_w is the fabric areal weight, V_f is the desired fiber volume fraction, and ρ_f is the fiber density. Linear variable differential

transformers (LVDT) were positioned at both the ends of the fixture to measure the preform thickness and ensure the compaction was uniform across the sample.

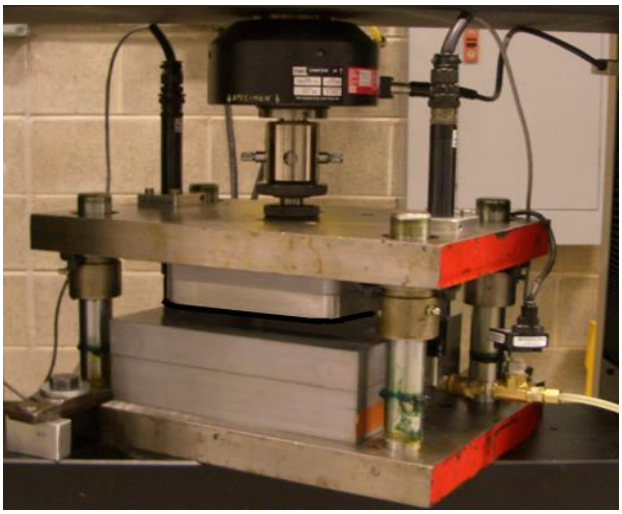

Figure 4.1: In-plane fixture for saturated permeability measurements

After samples were loaded and compacted in the test cavity, SAE 40 motor oil was introduced into the fixture at constant flow rates using a Parker Zenith precision metering pump. The sample was allowed to fully saturate as fluid from a line source permeated the material and exited the fixture at a line sink. This process is visualized through the diagram shown in Figure 4.2.

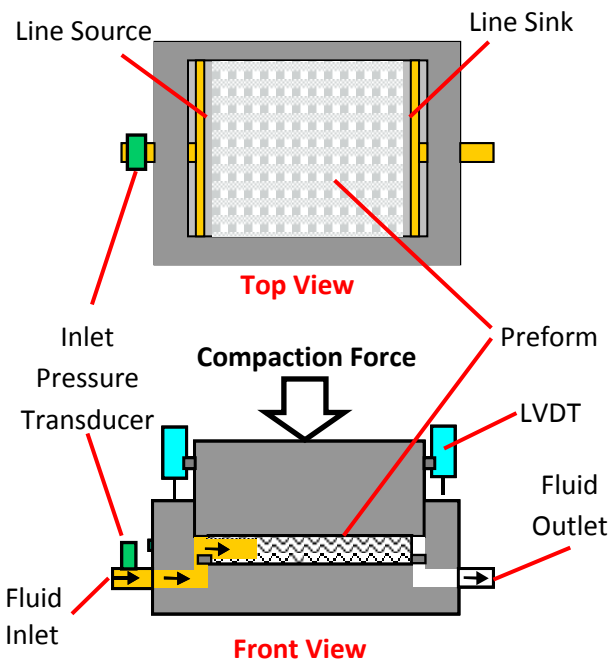

Figure 4.2: In-plane Fixture Test Diagram. Top and Front View.

Steady-state was reached when inlet pressure readouts from the in-line pressure transducer (Omega PX180-100GV) and the outlet digital pressure gage (Omega DPG1000B-15G) remained constant after full preform saturation. Pressure drops across the preform were measured for the set fiber volume fraction at multiple flow rates. These pressure drops are plotted versus the flow rates to attain a slope, m, which can be used in an altered form of Darcy's law (Equation 55) to calculate the average permeability of the preform. Permeability is defined by S while μ is the fluid viscosity, L is the preform length in the direction of the flow, and A is the area normal to the flow.

$$S = \mu m \frac{L}{A} \tag{55}$$

This process can then be repeated with the same sample in the fixture for multiple, higher fiber volume fractions as further compaction can be induced on the preform.

4.1.2 Transverse Permeability Fixture Setup

Similar to the in-plane permeability measurement method, the transverse permeability of IM7-4HS preforms was also characterized. For these measurements, a separate fixture was used that allowed for saturated flow through the thickness of the samples tested. This fixture consisted of a similar setup to that of the in-plane fixture. It possessed both a bottom half with a sample-housing cavity and a user-controlled top half with a compaction plunger. This fixture can be seen in Figure 4.3 and also was housed in the MTS mechanical testing frame.

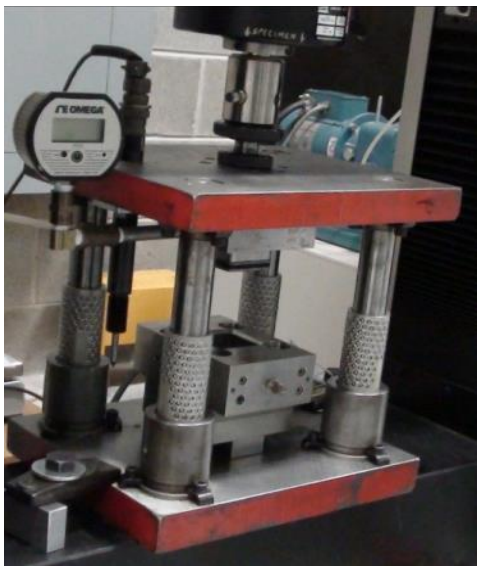

Figure 4.3: Transverse Saturated Permeability Test Fixture

The fixture allowed for the testing of samples in a 5.08 cm square cavity. Samples up to 3.20 cm thick can be accommodated in this fixture. To obtain the pressure drop across the samples, an in-line pressure transducer (Omega PX180-100GV) was outfitted at the inlet to the fixture cavity, while an electronic pressure gage (Omega DPG1000B-15G) was fixed to the outlet of the cavity.

A single LVDT was mounted on the fixture to monitor the sample thickness in the cavity. In this fixture's setup, the fluid flow was introduced underneath the samples. The flow then permeated upward through the sample thickness and exited through the plunger, which featured a porous fluid distribution plate that allowed fluid passage. A groove was machined on the compaction plunger for instillation of a 3.97 mm (5/32 inch) circular cross-section Buna-N O-ring 158 mm in length. Fluid was also introduced at constant flow rates from the Parker Zenith precision gear metering pump. A diagram of this fixture setup can be seen in Figure 4.4.

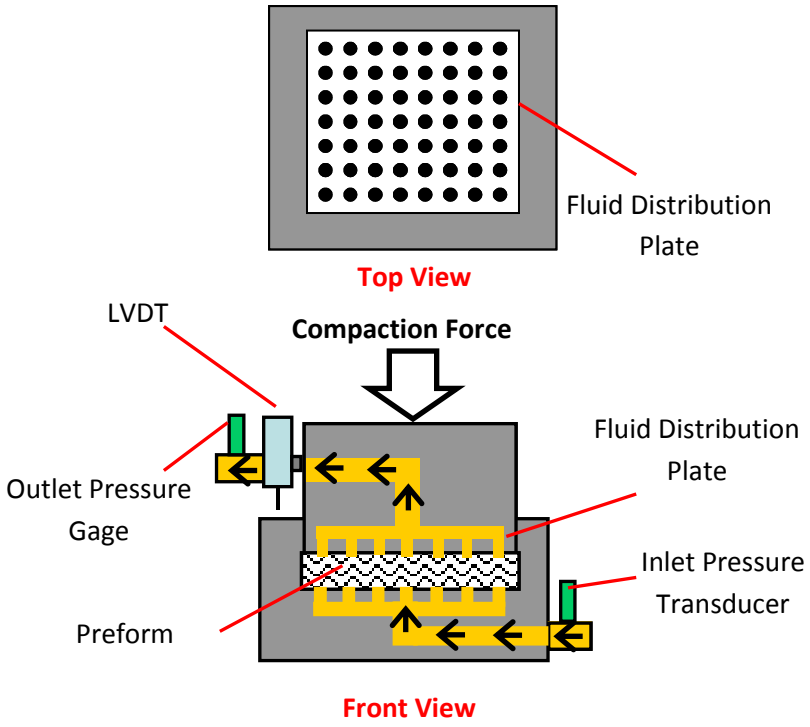

Figure 4.4: Transverse Permeability Fixture Diagram. Top and Front View.

After steady-state was reached (steady-state is defined when the preform is fully saturated and inlet and outlet pressure readouts are constant), pressure drop across the preform was measured for several different flow rates at each target fiber volume fraction. The relation in Equation 55 is then used in the same fashion as described for the in-plane permeability determination to determine the transverse permeability. Note that in the transverse case, the length of the preform

in the direction of flow is the sample thickness. Gravitational effects in this transverse setup were not included in the permeability measurements as they are small compared to the pressure drop produced at the supplied flow rates.

4.1.3 Material/Preform Preparation

Several different preforms of IM7-4HS fabric were constructed for the saturated permeability comparison. These preform variations were used to determine the effects of tackifier, debulking, layup sequence, and ply number on saturated permeability. The in-plane and transverse samples created are summarized in Table 4.1. Preforms were produced by hand cutting individual plies from either tackified or non-tackified rolls of the IM7-4HS with a fabric cutting wheel. Exact cutting templates of the fixture cavity dimensions were machined from aluminum blocks to ensure ply-by-ply consistency and precise in-cavity fit.

Table 4.1: IM7-4HS Preform Variations for Saturated Permeability Tests

Variation #	Preform ID	Material	# of Layers	Layup Sequence	Tackifier	Debulked
1	Warp Aligned Non-Tackified	IM7-4HS	6	$[0]_6$	No	No
2	Laminate Non-Tackified	IM7-4HS	6	$[0,+45]_3$	No	No
3	Warp Aligned Tackified	IM7-4HS	6	$[0]_6$	Yes	No
4	Debulked Laminate	IM7-4HS	6	$[0,+45]_3$	Yes	Yes
5	12 ply Laminate Non-Tackified	IM7-4HS	12	$[0,+45]_6$	No	No
6	12 ply Debulked Laminate	IM7-4HS	12	$[0,+45]_6$	Yes	Yes

Rolls of the tackified IM7-4HS fabric were stored in a freezer to prevent cure of the pre-impregnated resin. To prepare tackified preforms, the rolls of material were taken out of the freezer, allowed to reach room temperature, cut, and then laid up. The debulked preforms were

produced by laying up the cut sheets of tackified IM7-4HS fabric and then exposing the preform to the hot debulk cycle described in Chapter 3. They were also allowed to reach ambient temperature before saturated testing took place.

4.1.4 Permeability Measurement Procedure

Before any in-plane or transverse saturated permeability measurements took place, the Parker Zenith constant flow rate pump was calibrated. To do this, the SAE 40 motor oil was pumped through the equipment at flow rates ranging from 1 cc/min to 20 cc/min into a container placed on Mettler Toledo SB1600 scale. At each flow rate, the oil was pumped into the container for 1 minute, and the weight of the fluid was recorded. Knowing the density of the oil, the weight collected and the elapsed time, an average actual flow rate could be calculated and compared to the pump's setting.

Both the in-plane and transverse fixtures were installed on the baseplate of a 100 kN MTS Insight material testing machine. The plunger of the fixture was connected to the load cell mounted in the crosshead. The crosshead displacement and load cell measurements were recorded the MTS TestWorks controlled system. On a separate lab computer, LabVIEW programs were written specifically for both the in-plane and transverse setup. These LabVIEW programs were used in conjunction with a NI 9219 data acquisition system, which was hard wired to both the LVDTs and the pressure transducers. With this, the instantaneous LVDT readouts were displayed and recorded, and the pressures were be recorded over time and averaged for pressure drop measurements in permeability.

4.1.4.1 In-plane Procedure: Step-by-Step

In-plane IM7-4HS preforms were each tested in 3 different flow direction: along the warp (0°), along the weft/fill (90° and perpendicular to the warp), and at 45° from the warp. This was done by cutting the preforms at different angles so that the apparent flow path was in these directions. The measured permeabilities in the 0°, 90°, and 45° are referred to as S_{xx}, S_{yy}, and $S_{xx}{}'$, respectively. Measuring the in-plane permeability of each of these directions allowed the principal permeabilities (S_{11} and S_{22}) to be determined from a tensor transformation, as well as the orientation of the first principal permeability (β). This was done with a simple MATLAB script, which can be found in Appendix C. The sensitivity of the angle β, as a product of 3 saturated channel flow tests, will be further discussed in the results and discussion portion of this chapter.

To measure each preform of the IM7-4HS material, first the fabric was cut from rolls of IM7-4HS that were either with or without the prepreg tackifier. The samples were laid up according to the stacking sequences given in Table 4.1. Next, the LVDTs on the in-plane fixture were recalibrated. This was done by manually lowering the compaction plunger into the empty cavity of the fixture until significant load was measured on the load cell, meaning that the plunger had made contact with the bottom of the test cavity. This was designated as zero thickness for the LVDTs, as well as, for the MTS crosshead displacement readout. The fixture was then opened to accept the IM7-4HS sample at the appropriate flow angle. A square O-ring, with the dimensions specified earlier was cut from a bulk supply, glued, and placed in the groove machined on the plunger head. The O-ring was then lubricated with Dow Corning's Molykote 111 and the plunger was slowly lowered into the test cavity as the O-ring created a seal. The plunger was

allowed to compact the fiber sample in the cavity until a specific thickness was reached that corresponded with the desired levels of fiber volume fraction. The areal weight relation in Equation 2 was used to do this. The frictional forces from the fixture guide posts entering the couplings were too significant to allow the compaction of the IM7-4HS samples to be defined from compaction pressure measured by the MTS load cell. Once the first level of compaction was reached, the test fluid (SAE 40 motor oil) was supplied from the Parker Zenith metering pump at low flow rates generally in the range of 1 cc/min to 10 cc/min. Low flow rates were used so that fluid pressures generated did not exceed the inlet pressure transducer limit of 690 kPa. In Chapter 6, higher flow rates were used and different measurement equipment was employed, which will be described in detail there. Once full saturation and steady-state were reached for a test sample, the pressure drop across the preform was measured at multiple flow rates (generally 4 to 5 flow rates per fiber volume fraction level). The pump was stopped, further compaction on the sample was applied to achieve a higher desired fiber volume fraction level, and the measurement process was repeated. For each IM7-4HS preform, fiber volume fractions of 50%, 55% and 60% were targeted. This range represents a practical area of interest for RTM manufacturing. If at any point, signs of pressure leakage or if test fluid was seen leaking out from the O-ring seal, the test was halted and data was not used.

4.1.4.2 Transverse Procedure: Step-by-Step

The procedure used for transverse permeability measurements is very similar to the in-plane setup. The transverse fixture included a single LVDT that was recalibrated before each run using the same technique described in the in-plane step-by-step process. Smaller 5.08 x 5.08 cm samples were cut based on the stacking sequence of Table 4.1. Circular O-rings were cut and

lubricated to seal flow on the plunger's head. Also, the same sample target fiber volume fractions were used for through-thickness permeability. Flow rates in the range of 1 cc/min to 10 cc/min were generally used for transverse permeation.

4.2 Results and Discussion

For each saturated data point, a target minimum of 3 tests was made, although a few variations were repeated fewer times due to material supply. This means that for each flow direction (S_{xx}, S_{yy}, S_{xx}', or S_{zz}), and at each fiber volume fraction, multiple tests were made to establish an average and standard deviation. It should also be noted that each saturated test would take approximately 3 hours to complete (this includes sample cutting, lay up, and permeability measurement at the three target fiber volume fractions). This results section will only display graphical representations of a pertinent selection of the entire measurement set because of the large amount of data produced. The entire body of raw saturated permeability results can be found in Appendix A. The results are graphically presented are chosen so that the effects of fiber volume fraction, tackifier, layup, debulking, and ply number on IM7-4HS permeability can be examined.

4.2.1 In-plane Permeability Results

A total of 62 samples were cut and laid up amounting to 174 separate saturated in-plane permeability measurements at the specific fiber volume fractions of interest (50%, 55% and 60%). A typical flow rate versus pressure drop curve for a saturated permeability measurement can be seen in Figure 4.5. The solid lines are linear regressions of each data set. The slope and R-squared value of each regression are also displayed on the graph. These data are from a debulked

IM7-4HS laminate preform (variation #6 in Table 4.1). The slopes of these data were used to calculate the in-plane permeability with the method described in Equation 55. Note the excellent fits of the linear regressions to the experimental data.

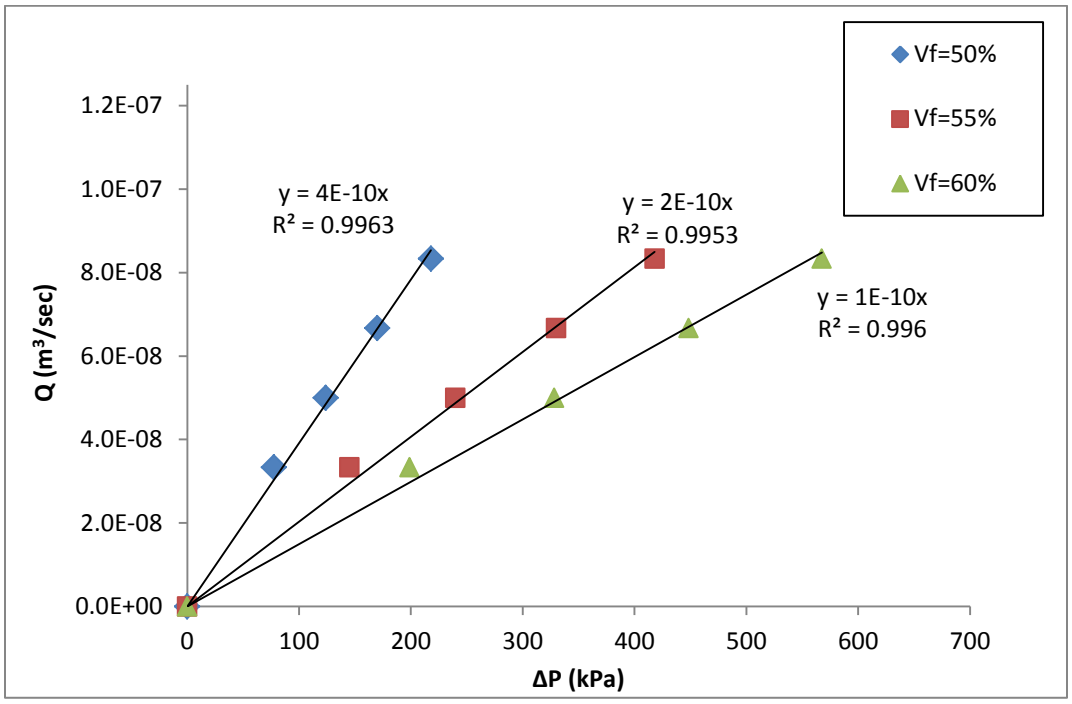

Figure 4.5: Sample In-Plane Permeability Test Data for Flow Rate vs. Measured Pressure Drop

In Figure 4.6, a sample of the average in-plane permeability data as a function of fiber volume fraction for 3 flow directions is displayed. This data is from the warp aligned, non-tackified IM7-4HS fabric (variation #1 in Table 4.1). The permeability of the preform was measured in the warp direction (0°), the off-axis direction (45°), and the weft direction (90°). These data are presented on a semi-log plot and fit to a power law equation (solid lines with respective color to their data points). The permeability is seen to be drastically reduced in value as the fiber volume fraction increases. Of course, this is a well-defined relationship and has been documented for multiple preforms [60].

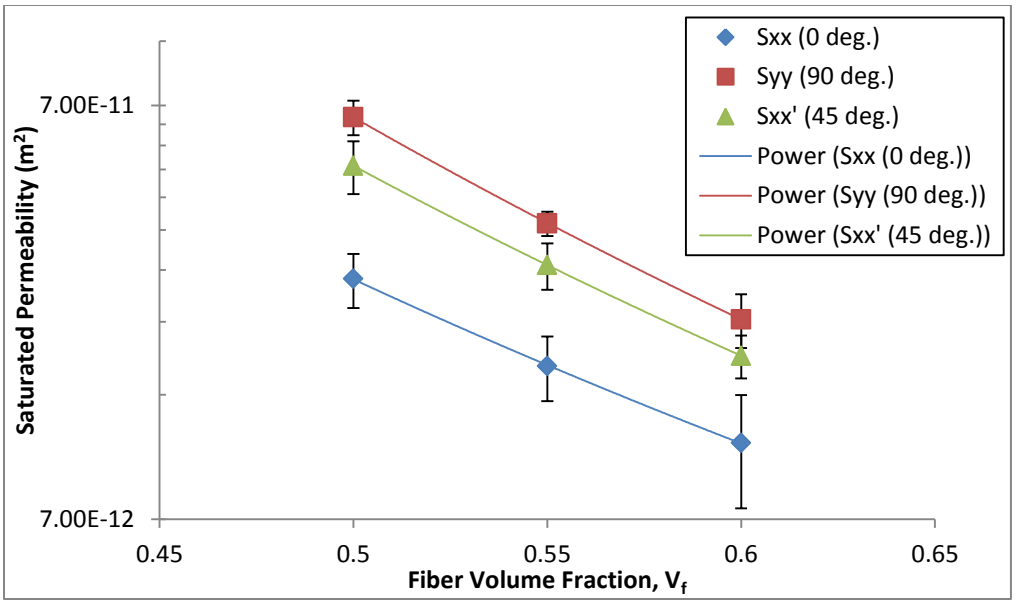

Figure 4.6: Permeability vs. Fiber Volume Fraction for Warp Aligned, Non-tackified IM7-4HS Fabric

With measurements from 3 different flow directions for a single preform, the resulting experimental permeability tensor could then be transformed to produce the first (S_{11}) and second (S_{22}) principal in-plane permeabilities. The principal permeabilities that correspond to data in Figure 4.6 are displayed in Figure 4.7. The principal permeability data are fit to a power law curve. The error bars represent the standard deviation in the data.

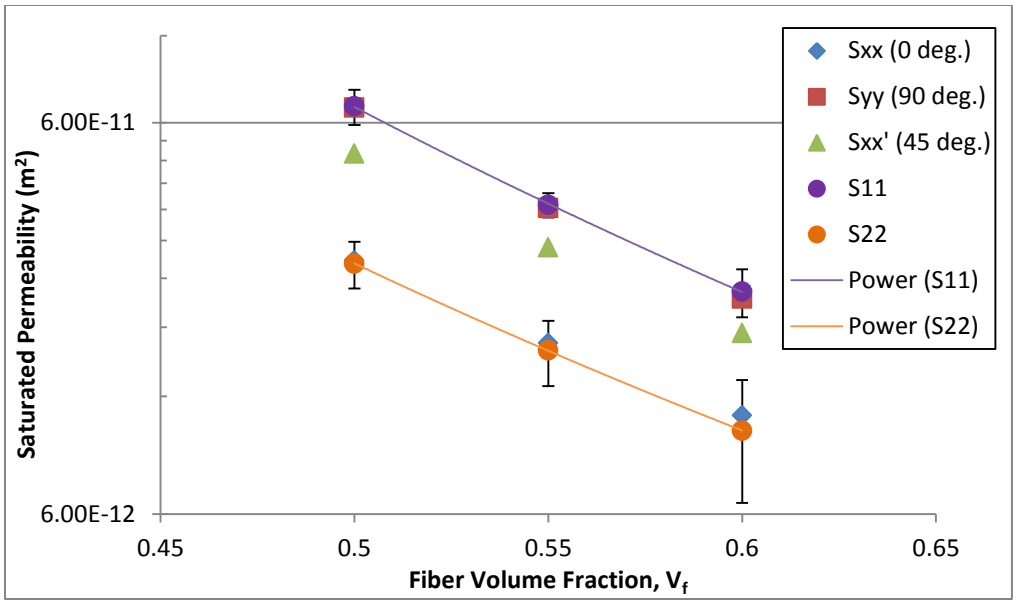

Figure 4.7: Principal Permeability vs. Fiber Volume Fraction for Warp Aligned, Non-tackified IM7-4HS Fabric

For this specific warp-aligned preform, the permeability in along the warp axis (0°) of the material was seen to be much less permeable compared to flow in the weft (90°) direction. The 45° permeability measurements fell between values for the warp and weft. The resulting principal permeabilities were seen to be slightly higher and slightly lower in value than the weft and warp directions, respectively. From this, one can assume that orientation of first principal permeability, or β angle is approximately 90° from the warp. Further discussion on the β angle determination and variability will be made later.

4.2.1.1 Fiber Volume Fraction, Layup, Tackifier, and Debulking Effects

After calculating principal permeabilities for all preforms tested, comparisons among layup, tackifier content, and debulking effects could be made. A comparison of all the 6 ply IM7-4HS layups can be seen at 55% fiber volume fraction in Figure 4.8. This specific fiber volume fraction was used to compare preforms types due to the difficulties and anomalies experienced at

50% and 60% for the debulked samples (this will be explained later). Additionally, the average permeabilities from Figure 4.8 are numerically presented in Table 4.2. Following in Table 4.3, the percent coefficients of variation (CV) by preform and test direction are displayed.

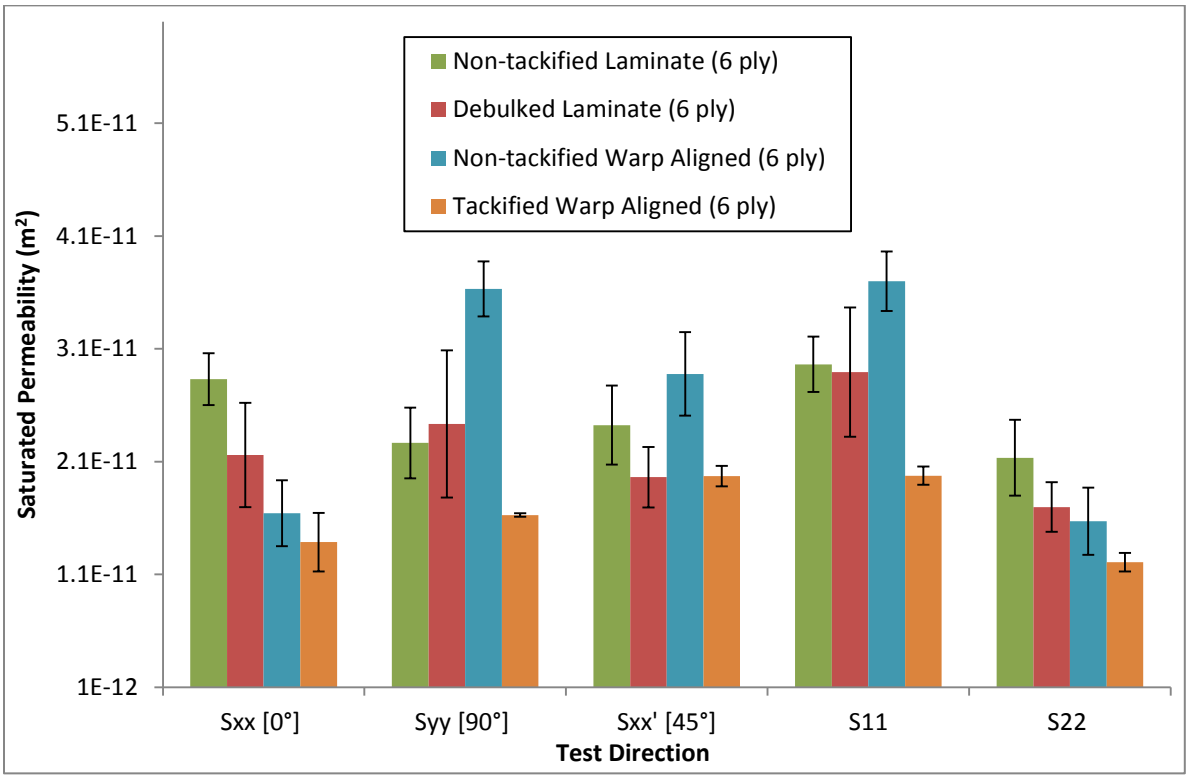

Figure 4.8: Saturated Permeability Comparison of 6 Ply IM7-4HS Layups at 55% Fiber Volume Fraction

Table 4.2: Average Saturated In-Plane Permeabilities of Various IM7-4HS Preforms at 55% Fiber Volume Fraction

Preform Type	Average Saturated Permeability by Test Direction (m^2)				
	S_{xx} [0°]	S_{yy} [90°]	S_{xx}' [45°]	S_{11}	S_{22}
Non-tackified Laminate (6 ply)	2.83E-11	2.27E-11	2.42E-11	2.96E-11	2.13E-11
Debulked Laminate (6 ply)	2.16E-11	2.43E-11	1.96E-11	2.89E-11	1.70E-11
Non-tackified Warp Aligned (6 ply)	1.64E-11	3.63E-11	2.88E-11	3.70E-11	1.57E-11
Tackified Warp Aligned (6 ply)	1.39E-11	1.63E-11	1.97E-11	1.98E-11	1.21E-11

Table 4.3: Saturated In-Plane Permeabilities CVs of Various IM7-4HS Preforms at 55% Fiber Volume Fraction

Preform Type	Saturated Permeability Coefficients of Variations (%)				
	S_{xx} [0°]	S_{yy} [90°]	S_{xx}' [45°]	S_{11}	S_{22}
Non-tackified Laminate (6 ply)	8.09	13.85	14.49	8.26	15.80
Debulked Laminate (6 ply)	21.43	26.78	13.66	19.80	12.93
Non-tackified Warp Aligned (6 ply)	17.77	6.72	12.84	7.13	18.99
Tackified Warp Aligned (6 ply)	18.72	0.93	4.59	4.08	6.80

Multiple inferences can be made from the results displayed in Figure 4.8 and Table 4.2. Firstly, we can see that as displayed earlier in Figure 4.6 and Figure 4.7, the warp aligned non-tackified preforms displayed a large directional bias in permeability. This meaning, the permeability in the 90° direction was seen to be roughly 2.2 times greater than that measured in the 0° direction. Contrarily, the laminate non-tackified measurements showed the difference between 0° and 90° directions to be only 20%, almost within experimental scatter. Across all directions tested, the laminate non-tackified preform showed little difference in permeability. This is likely due to the fact that laminate layup preforms (stacking sequence of $[0, +45]_3$) provides a nearly quasi-isotropic stacking sequence. The nature of the harness satin weave has dominantly featured tows aligned in the warp direction on the top-side of fabric, while the bottom side of has dominantly featured tows aligned in the weft direction. Thus, the preform geometry of the laminate layup will exhibit a more isotropic architecture pattern (where the [0, +45] may resemble a unidirectional layup of [0/90, +45/-45]) compared to that of the warp aligned preforms of stacking sequence of $[0]_6$.

Interestingly, this layup effect is not reflected in the tackified preforms. One might expect that the tackified warp aligned preforms would show preferential flow in one direction, similar to that

of the non-tackified warp aligned preforms (where permeability is much higher in the 90° direction than the other directions tested). As seen in Figure 4.8, the warp aligned tackified preforms showed only a 17% difference between S_{xx} and S_{yy} permeability, which is within the experimental scatter of the S_{xx} measurements. Thus, the inter-layer tackifier appears to aid in creating a more isotropic in-plane permeability by greatly reducing the S_{yy} value (roughly 2.2 times less) compared to the non-tackified warp aligned preforms. Further, the addition of tackifier appears to have little effect on permeability measured in the 0° direction. The presence of tackifier for the warp aligned preforms showed only a 15% drop in permeability, which was well within the experimental scatter for both preforms. Explanation for this effect may be due to the manufacturing process, and how the tackifier is applied.

Effects from the debulk cycle on preform permeability can also be gleaned by comparing the non-tackified laminate preforms to the debulked laminate preforms. It can be seen that, rather surprisingly, no significant difference in permeability was registered between the two laminates. This may be best explained by the solidification that occurs as results of the debulking process. Once the tackifier is heated in the debulk process, it melts and flows through the preform by the vacuum pressure, and then goes through an irreversible chemical change in curing. This essentially fuses the tows in place at roughly 50% fiber volume fraction, producing very stiff preforms. This cured tackifier aids to resist nesting of the fibers and tows upon compression in the permeability fixture. Nesting, of course, reduces local permeability through the increase in local fiber volume fraction. A simple schematic diagram of tows of tackified (non-debulked) and debulked preforms is seen Figure 4.9 to illustrate this point.

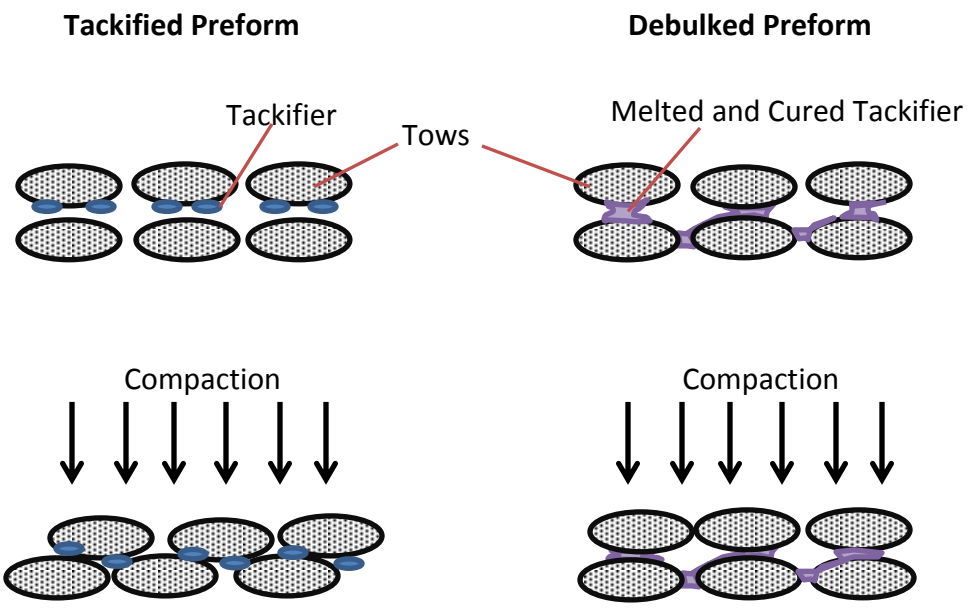

Figure 4.9: Illustration of the Nesting Comparison between Tackified and Debulked Preforms

Here, the figure shows that the tackifier (blue) on the unprocessed preform tows still allows nesting under compaction. On the other hand, the heated and cured tackifier (purple) shown on the debulked preform tows have been distributed throughout the fiber network and fuse the reinforcement together to resist the compaction pressure.

This effect was seen in Chapter 3, where debulked preforms required greater compaction pressure than non-debulked preforms to achieve the same fiber volume fraction. Difficulty compacting the debulked samples in the permeability fixture was also noted during these measurements. While the cured tackifier still blocks some inter-tow flow channels, it is hypothesized here that the resistance to nesting allows these gaps to stay large enough to affect permeability on the bulk scale, producing similar values to that of non-tackified material. This also may explain why the debulked preforms tested higher in permeability than the tackified

preforms. In this case, the tackified preforms, which have not been cured, supply tack and preform stability but still allow fibers and tows to nest under compaction.

Additionally, the tows absorbed some of the tackifier during its low viscosity state before cure in the debulk cycle. Rohatgi and Lee [9] investigated powdered tackifier effects on the in-plane permeability of a four harness satin carbon fabric. They found that if the tackifier was absorbed into the tows during heated debulking, the resulting permeability would be similar to that of non-tackified samples. If tackifier particles were not absorbed into the tows, they would block inter-tow gaps, which results in significant reduction in permeability. Similar results could be happening with the debulked IM7-4HS, where fewer blockages of the inter-tow flow channels are seen. Without further study of debulked IM7-4HS microstructure, the amount of tackifier absorption into the tows cannot be definitively concluded. The extent of this, although, is expected to be relatively significant due to the apparent stiffness of the entire preform upon debulk cycle conclusion. Interesting future work could take multiple debulked cross-sections to determine the amount of tackifier absorption into the tows compared to that remaining in inter-tow gaps at different processing temperatures.

Further comparisons of the debulked preforms can be seen in Figure 4.10, where 6 versus 12 ply in-plane permeabilities are displayed in the warp (S_{xx}) and weft (S_{yy}) directions.

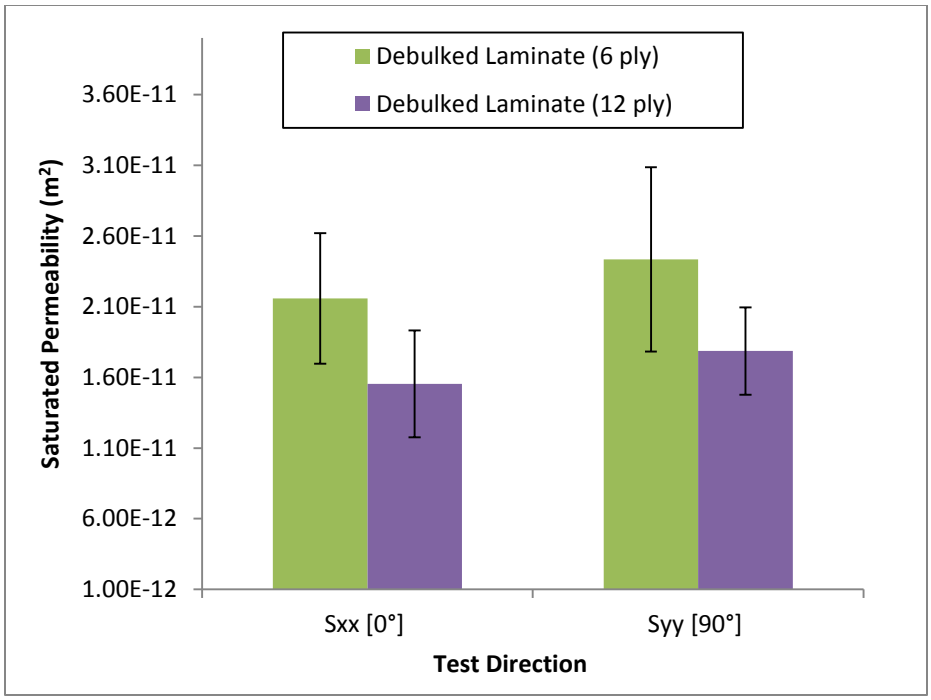

Figure 4.10: Saturated Permeability Ply Number Comparison for Debulked IM7-4HS Laminate Preforms

Here, it is seen that the 12 ply preforms produce in-plane permeability that is ~27% less than the 6 ply preforms for both the warp and weft directions. Although this is a sizeable reduction, the experimental variability for the debulked preforms was large at around 20%, thus the permeability results are within scatter. The large amount of experimental scatter could be due to the variability of melted tackifier movement during the debulk process. Adding an additional processing step to these preforms allowed added geometrical variations. The tackifier was able to rearrange itself within the reinforcement at high temperatures of the debulk cycle. This could possibly result in areas rich in tackifier or regions with little tackifier, thus altering fluid flow paths. This could further add uncertainty to the local compaction of the preform in the permeability fixture. While very large reductions in permeability have been reported from increasing preform ply number [160], the results here, at 55% fiber volume fraction, display only

a slight drop in permeability when number of preform layers is doubled. Thus, the debulking process can be further concluded to resist inter-tow nesting.

Now that the general trends of permeability among different preform variations have been discussed at a single fiber volume fraction, the preforms can be compared over the range of fiber volume fractions. Figure 4.11 shows a comparison of the average S_{xx} permeabilities at 50%, 55%, and 60% fiber volume fraction. The data were fit to a power law equation. Figure 4.12 shows a similar comparison of the S_{yy} permeabilities. The full set of power law fits for every flow direction can be found in Appendix C.

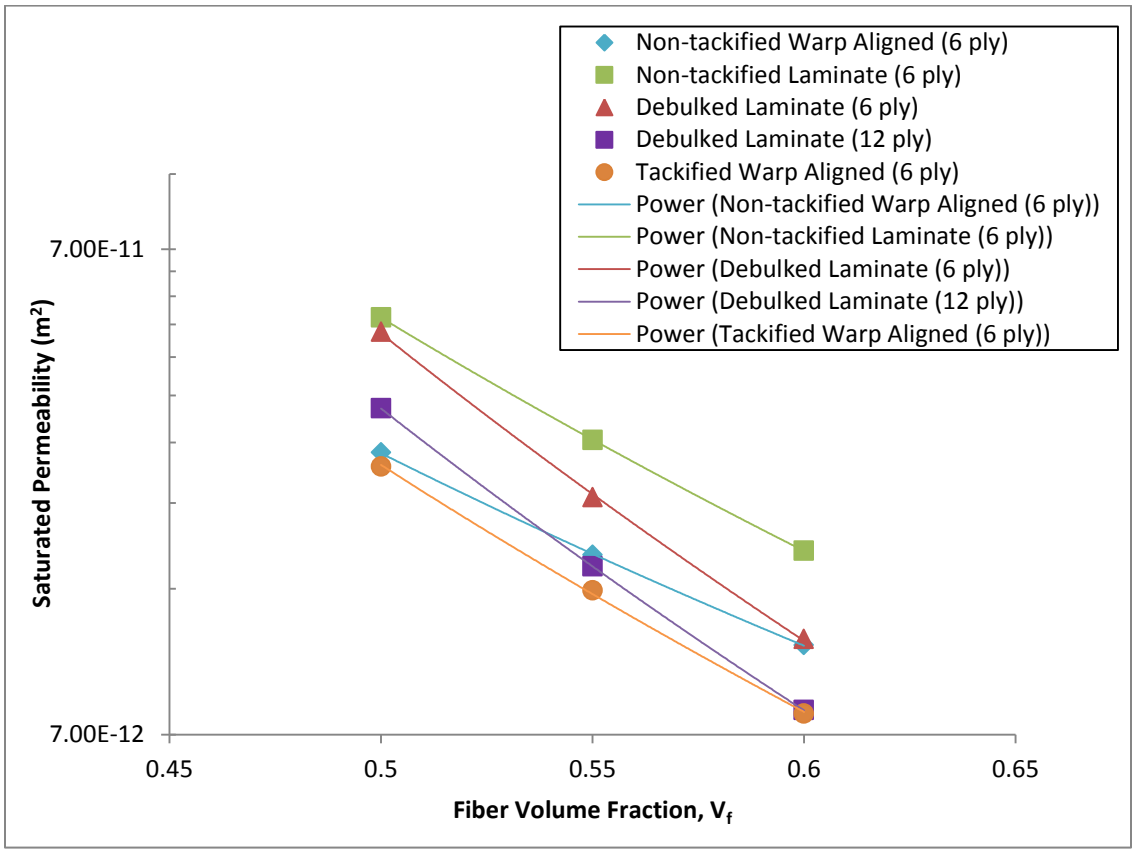

Figure 4.11: Saturated IM7-4HS S_{xx} Permeability versus Fiber Volume Fraction

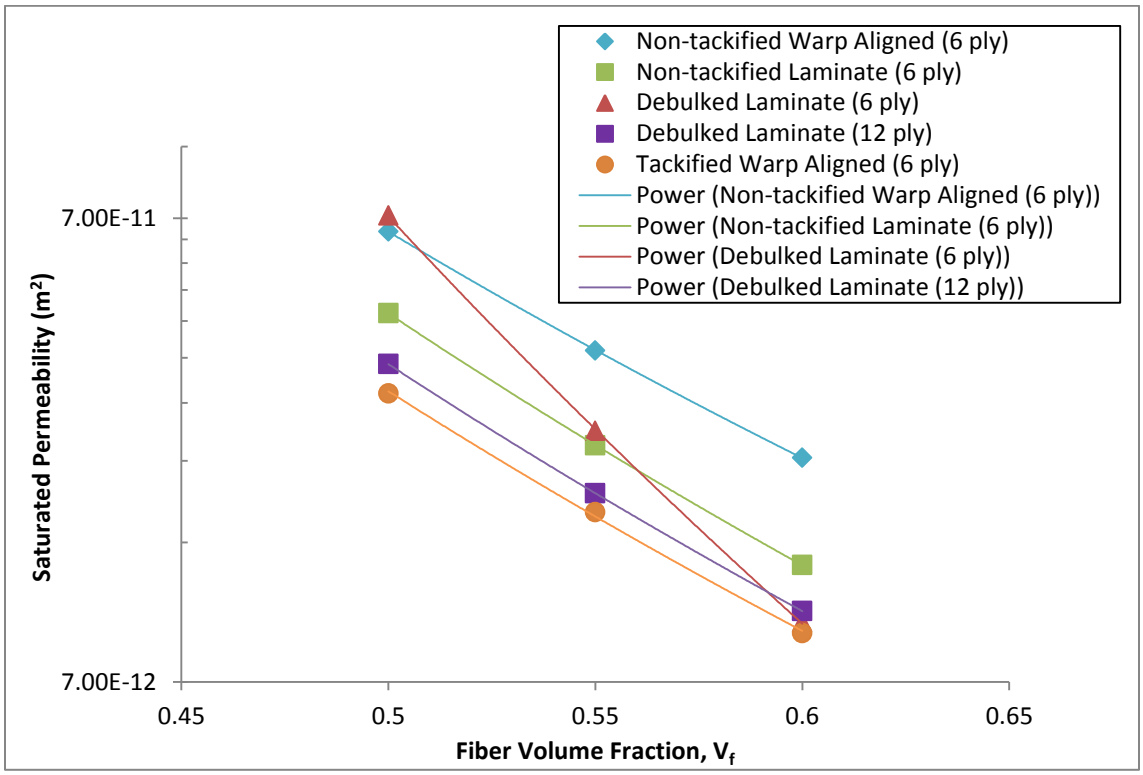

Figure 4.12: Saturated IM7-4HS S_{yy} Permeability Comparison over Fiber Volume Fraction

The trends among preform types discussed earlier at 55% fiber volume fraction are relatively consistent across fiber volume fraction, although some crossover was seen between preform types. The tackified and debulked samples generally tested lower in permeability than the other preform types. The 6 ply debulked samples showed the largest variation in trend across fiber volume fraction. These preforms were seen to drastically reduce in permeability over fiber volume fraction for the S_{yy} measurements. A distinct explanation for this is not known, although it is possible that at high enough compaction pressures, some of the cured tackifier fusing tows together may separate. This would then allow additional nesting to take place and thus explaining the low permeability nature of the debulked samples at 60% fiber volume fraction. To explain the relatively high permeability of the 6 ply debulked samples at 50% fiber volume fraction, the debulk processing must be considered. Shih and Lee [10] noted that tackified

preforms should be compressed to a thickness slightly larger than the target thickness for a permeability test, so the sample can be re-compressed to the desired fiber volume fraction in the measurement fixture to avoid race-tracking over or under the sample. In the vacuum debulk process, the vacuum pressure compacted the 6 ply preforms to a thickness very close or past the 50% fiber volume fraction point. This may allow for some race-tracking over the sample to take place and artificially raise the permeability if the pre-compacted sample was of smaller thickness than the cavity depth set in the permeability fixture. From the compaction experiments in Chapter 3, it was observed that compacting the 6 ply debulked samples to 100 kPa (roughly full vacuum pressure) produced fiber volume fractions just over 50%. Therefore, it may be possible to observe race tracking effects with these samples at the 50% fiber volume fraction thickness set in the permeability measurement cavity. In this case, the saturated permeability testing cavity may be of slightly larger thickness than the sample, allowing the fluid a path of low resistance over the top of the preform. Alternatively, the 12 ply debulked samples showed no artificially high permeability at 50% fiber volume fraction, which corresponds to the trend of more compaction resistance seen in these samples than in the 6 ply preforms in the Chapter 3 results.

4.2.1.2 Principal Permeability Ratios and Orientation

In addition to calculating principal in-plane permeabilities from the tensor transformation, the angle of first principal permeability orientation (β) was also found. It was observed that relatively small changes in permeability measurements resulted in large changes in the β angle. For example, using S_{xx}, S_{yy}, and $S_{xx}{}'$ data for the 6 ply non-tackified laminate, employing a 15% change in the original S_{xx} value returned a change in the β angle of 19° from the original tensor transformation. This is disappointing as average experimental scatter among in-plane

permeability measurements was seen to be roughly 15% for the non-tackified laminate. This 15% change in S_{xx} also resulted in only a 10% change in the S_{11} and a 3% change in S_{22} value. The β angle then appears to be much more sensitive to experimental scatter than the principal permeability. Furthermore, employing a 15% change to the S_{yy} value results in only a 1° change, while a 15% change in S_{xx}' results in an extremely large alteration of 40° in β, all while the principal permeabilities are lightly altered in regards to experimental scatter. Demaría et al. [153] also reviewed how small variations in the measured channel flow permeability measurements make a noticeable change on the angle β. Even a 5% change in S_{xx} permeability was noted to cause up to a 13% change in β by Weitzenböck et al. [61]. Due to this sensitivity, β cannot be confidently reported for the IM7-4HS preforms tested in the saturated permeability fixture. A radial visualization technique was then required to quantify the orientation angle. This is discussed in detail in Chapter 8.

In this case, a more practical approach to quantifying the permeability tensors' directional biases is through comparing permeability ratios. Here, the S_{xx}/S_{yy} and S_{11}/S_{22} ratios can quantify the anisotropy of the permeability of each preform type measured. The S_{xx}/S_{yy} ratio is simply the warp over weft permeability, while the S_{11}/S_{22} shows the maximum ratio of preform anisotropy. When the ratios are close to 1, the in-plane permeability behavior should be close to isotropic. The permeability ratios calculated from average permeabilities for all preforms measured can be seen in Table 4.4. The ratios are displayed over the fiber volume fractions tested. Note that the 12 ply debulked preform was not tested in the S_{xx}' direction, so the principal permeability ratio could not be calculated.

Table 4.4: In-plane Permeability Ratios over Fiber Volume Fraction by IM7-4HS Preform Type

IM7-4HS Preform Type	S_{xx}/S_{yy}			S_{11}/S_{22}		
	50% V_f	55% V_f	60% V_f	50% V_f	55% V_f	60% V_f
6 Ply Warp Aligned Non-tackified	0.41	0.45	0.50	2.52	2.35	2.27
6 Ply Warp Aligned Tackified	0.85	0.85	0.87	1.61	1.63	2.06
6 Ply Non-tackified Laminate	1.16	1.25	1.34	1.49	1.39	1.51
6 Ply Debulked Laminate	0.67	0.89	1.17	2.86	1.71	1.98
12 ply Debulked Laminate	0.97	0.87	0.79	-	-	-

From this data, the warp aligned non-tackified preform shows the greatest anisotropy, with the S_{xx}/S_{yy} ratio showing a very strong bias of high permeability in the weft direction. The addition of tackifier, shows a ratio closer to 1, creating a more isotropic in-plane permeability tensor for the warp aligned preforms. The laminate preforms also showed less directional bias or preferential flow directions, as was described earlier by the more isotropic nature of the layup. Interestingly, for all preforms except the 12 ply debulked, the S_{xx}/S_{yy} ratio increased with increasing fiber volume fraction. Also, it should be noted that the S_{11}/S_{22} ratio was greater than the S_{xx}/S_{yy} ratio for every preform.

4.2.2 Transverse Permeability Results

Saturated permeability measurements made through-the-thickness of the IM7-4HS preforms were conducted on all 6 of the preform variations in Table 4.1. Due to the small sample area (2 inch squares) of the transverse preforms, material supply was not a concern. Similar to the in-plane measurements, linear flow rate versus pressure drop relationships were found for all preforms. Also, low flow rates (1 cc/min to 10 cc/min) again were used to supply the SAE 40. The transverse permeability results are shown in Figure 4.13 over the fiber volume fraction range

tested. Table 4.5 displays the numerical values of these through-thickness measurements including the standard deviations (StDev) and coefficients of variation (CV) from the tests.

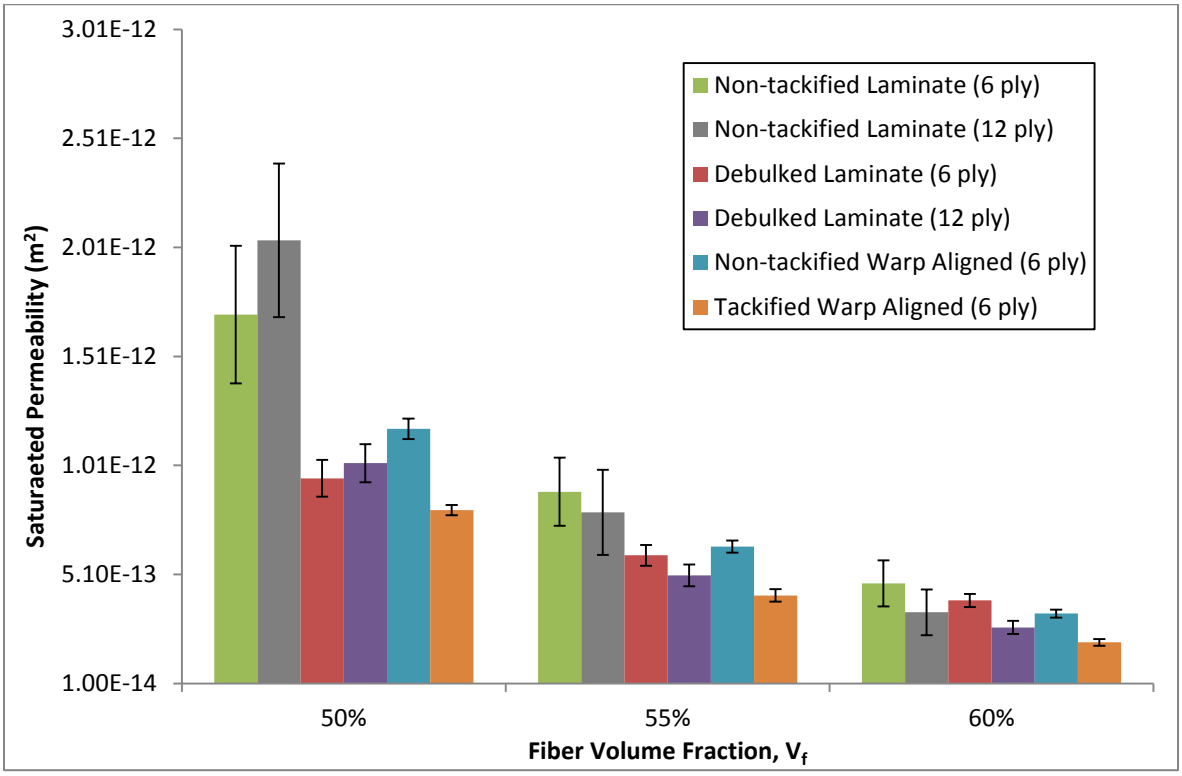

Figure 4.13: Saturated Transverse Permeability by IM7-4HS Preform Type over Fiber Volume Fraction

Table 4.5: Saturated Transverse Permeability Data by IM7-4HS Preform Type over Fiber Volume Fraction

V_f = 50%

Preform Type	Szz (m^2)	StDev (m^2)	CV (%)
Non-tackified Laminate (6 ply)	1.70E-12	3.15E-13	18.53
Non-tackified Laminate (12 ply)	2.04E-12	3.52E-13	17.25
Debulked Laminate (6 ply)	9.51E-13	8.45E-14	8.88
Non-tackified Warp Aligned (6 ply)	1.18E-12	4.71E-14	3.99
Tackified Warp Aligned (6 ply)	8.05E-13	2.30E-14	2.86
Debulked Laminate (12 ply)	1.02E-12	8.76E-14	8.59

V_f = 55%

Preform Type	Szz (m^2)	StDev (m^2)	CV (%)
Non-tackified Laminate (6 ply)	8.89E-13	1.56E-13	17.56
Non-tackified Laminate (12 ply)	7.95E-13	1.96E-13	24.64
Debulked Laminate (6 ply)	5.97E-13	4.80E-14	8.04
Non-tackified Warp Aligned (6 ply)	6.38E-13	2.84E-14	4.46
Tackified Warp Aligned (6 ply)	4.14E-13	2.82E-14	6.82
Debulked Laminate (12 ply)	7.95E-13	5.06E-13	9.89

V_f = 60%

Preform Type	Szz (m^2)	StDev (m^2)	CV (%)
Non-tackified Laminate (6 ply)	3.91E-13	1.06E-13	22.66
Non-tackified Laminate (12 ply)	3.36E-13	1.05E-13	31.28
Debulked Laminate (6 ply)	3.91E-13	3.01E-14	7.70
Non-tackified Warp Aligned (6 ply)	3.30E-13	1.83E-14	5.54
Tackified Warp Aligned (6 ply)	1.98E-13	1.58E-14	7.96
Debulked Laminate (12 ply)	3.36E-13	2.67E-13	11.27

The trend of decreasing permeability with increasing fiber content is dominant in these results. On average across all preform variations, increasing the fiber volume fraction from 50% to 55% resulted in a decrease in permeability by 50%. Correspondingly, an increase from 55% to 60% in fiber volume fraction reduced the across-the-board permeability by 48%. Other general trends show that the non-tackified laminate preforms produced the highest transverse permeabilities out of all the samples measured. This could be due to the altered tortuosity the laminate stacking

sequence provides compared to the warp aligned preform layup, while no tackifier is present to block inter-tow flow channels. Generally, the non-tackified preforms also displayed much more experimental scatter than the other preforms. This is likely because the laminate stacking sequence required more user handling and angled fabric cuts than the warp aligned layups. Also, without tackifier, tow loss and slippage was common. These factors combine to add to the sample-to-sample variation. The transverse permeability data at only 55% fiber volume fraction is highlighted in Figure 4.14 for further discussion.

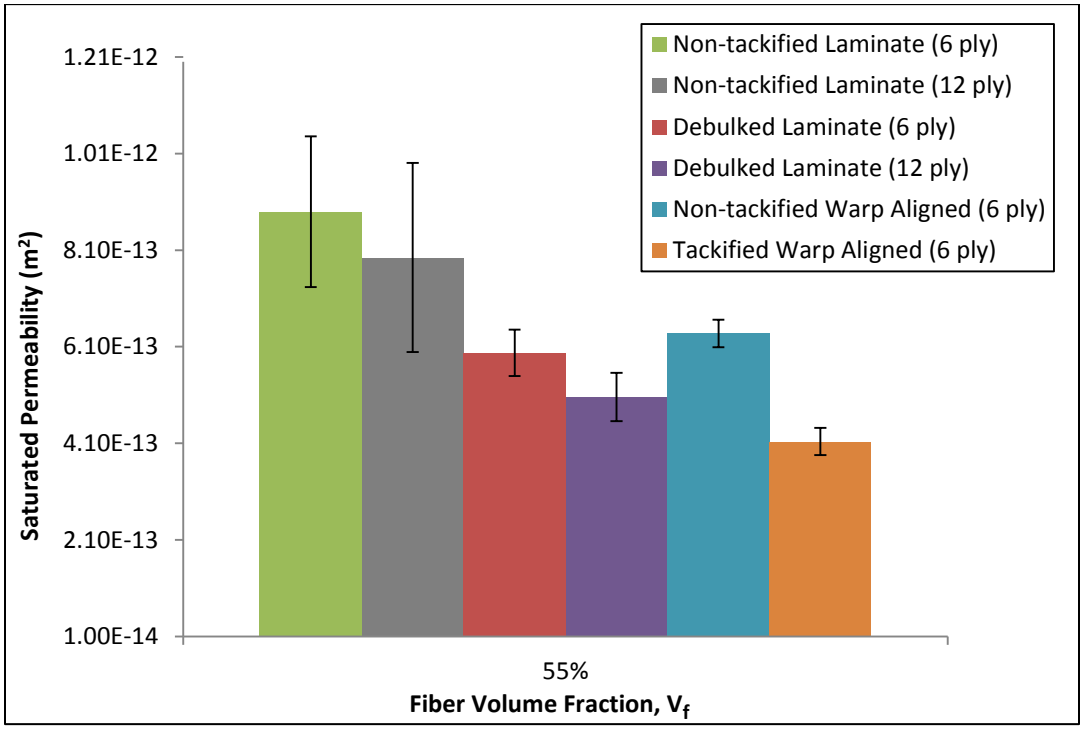

Figure 4.14: Saturated Transverse Permeability by IM7-4HS Preform Type at 55% Fiber Volume Fraction

The tackified warp aligned preforms consistently tested lowest in permeability here and at all other fiber volume fractions. While the debulked samples showed generally low permeability, the tackified preforms (non-debulked) still produced lower values of transverse permeability (30% lower than the 6 ply and 18% lower than the 12 ply debulked sample at 55% fiber volume

fraction). As described earlier in the in-plane permeability discussion, this is likely because the tackifier aids in blocking the inter-tow flow channels, while still allowing nesting to take place where the debulked samples resisted nesting.

Another important result to note is, as a whole, the through-thickness direction of the IM7-4HS preforms was much less permeable than their in-plane counterparts. This is a trend that has been cited and is well known for most reinforcements [60]. Transverse permeability has been reported to be over two magnitudes lower than the in-plane permeabilities of the same preform [101]. Using sample data from the 6 ply non-tackified laminate permeability measurements, the two in-plane principal permeabilities and the S_{zz}, or effectively the S_{33}, can be plotted across fiber volume fraction on one plot. This is seen in Figure 4.15 where the permeability is plotted on a logarithmic scale.

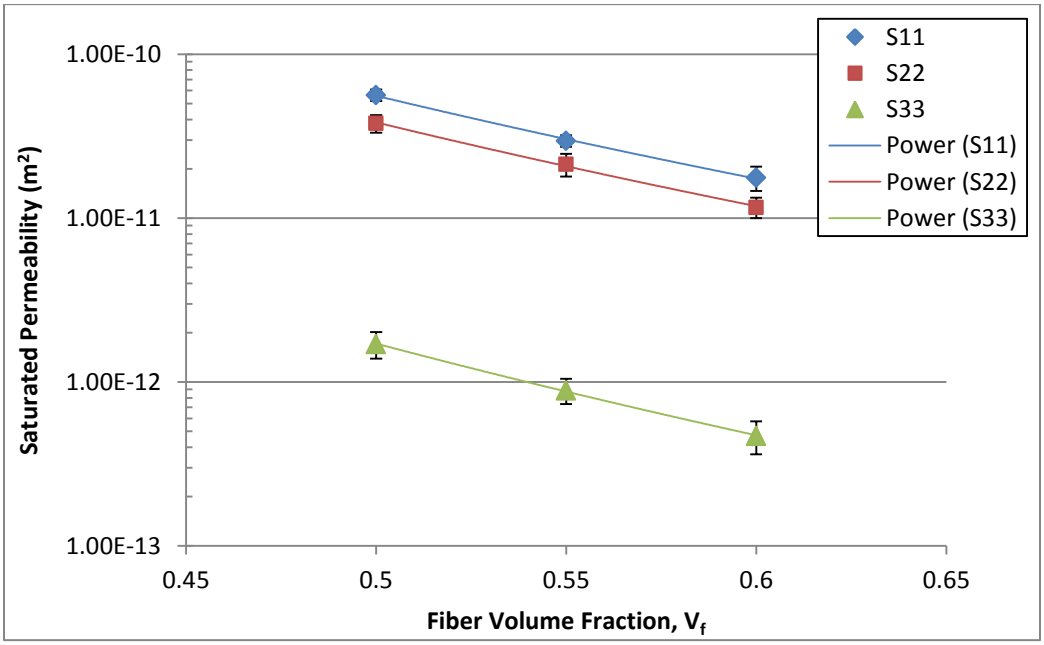

Figure 4.15: Principal Permeabilities over Fiber Volume Fraction for the 6 Ply Non-tackified Laminate IM7-4HS

Here, the in-plane permeabilities are seen to be of the same order of magnitude, while the third principal permeability, deemed through-the-thickness, is roughly a full order of magnitude lower. This relationship can be attributed to the relatively tight weave of the harness satin fabric. Out-of-plane flow then permeates through very small inter-tow gaps and also largely through intra-tow regions, which possess a much higher local fiber volume fraction then the bulk preform. In-plane flow sees much larger inter-tow gaps where comparatively, much less resistance to flow is seen.

4.3 Conclusions

Saturated permeability measurements with various IM7-4HS preform types created a baseline of data for further permeability comparisons. The saturated technique also allowed for quicker characterization across a range of fiber volume fractions than unsaturated tests would. Permeability was seen to decrease largely with the increase of fiber volume fraction for both in-plane and through-thickness measurements. Three different in-plane measurement directions were made per preform so that the permeability tensor could be transformed to define the principal permeabilities and their orientation. The orientation angle proved to be too sensitive to be confidently calculated based on measurement variability, while principal permeabilities were not significantly affected from this variation.

The effects of tackifier, debulking, and preform layup were also highlighted. Layup was seen to play a large role in the in-plane permeability tensor anisotropy. Layups with the warp direction of each ply aligned possessed much higher permeability in the weft direction than the warp, while layups with a more quasi-isotropic stacking sequence delivered similar permeabilities in all

test directions. The presence of inter-layer tackifier was seen to reduce permeability in all test directions due to a blocking of inter-tow gaps, while some directions were more affected than others. Tackified samples in the warp aligned preforms created a much more isotropic in-plane permeability tensor compared to the non-tackified. Debulked samples proved to be most difficult to characterize in permeability. The curing of the tackifier altered the compaction behavior of these samples. Debulked samples resisted inter-ply nesting, and resulted in higher permeability than the tackified, non-debulked samples as fewer inter-tow flow channels were blocked. Transverse measurements showed similar trends, while permeability here was roughly an order of magnitude lower than in the in-plane measurements.

Using the produced permeability data here, Darcian flow based process models can be created to simulate mold fills for RTM. If low permeability is not a concern, tackified IM7-4HS should be used in a manufacturing setting over the non-tackified material, as the tackifier aids in holding fiber orientation and preform shape. Debulking will further hold preform shape, although preform compaction and race-tracking may become a concern inside the mold. Note that the injected resin should be compatible with tackifier used in preforming. Future work for a more robust characterization could include the effect of shear and flow through curved portions of the reinforcement. Further work could develop an in situ permeability measurement system, where the effects of the unique geometrical features of specific molds could be characterized before infusion.

5. Fluid Effects

Understanding how reinforcement fibers interact with a permeating fluid is telling to the degree of compatibility between the reinforcement and matrix. In this study, the majority of permeability measurements was made with SAE 40 motor oil due to the low cost and ease of use with respect to equipment cleanup. For actual LCM infusions, epoxy resins are used that possess different surface chemistry than that of motor oil. Due to differing surface chemistry, the adhesion between the reinforcing fibers and the fluids could be affected. Wettability of the fibers may be altered and a natural inquiry asks if the fluid type affects permeability. As stated in the literature review, the effect of fluid type on permeability has been controversial. Some researchers have found little effect compared to experimental scatter [115], [116], while others found large deviations based on the fluid used [117]. To investigate this fiber/fluid interaction and compare different fluids, measurements of the liquid to fiber contact angle and fluid surface tension can be made. Low contact angles and surface tensions are generally desired for LCM. Lower contact angles promote better fiber wet out while lower fluid surface tensions leads to better adhesion and ultimately fewer voids in the finished part [43]. Contact angle and surface tension measurements can then be implemented to define capillary pressure and a capillary number for unsaturated infusions.

To investigate the fluid type effects on permeability, SAE 40 motor oil was compared to Applied Poleramic's SC-15 epoxy resin system (a VARTM resin with similar viscosity to that of the oil at room temperature) in unsaturated, one-dimensional flow experiments. The resin system, SC-

15, has an epoxy component, Part A, and an amine hardening component, Part B (mixing ratio of Part A:Part B = 100:30). A basic comparison of the fluids' properties can be seen in Table 5.1.

Table 5.1: Basic Properties of Test Fluids

Fluid	SAE 40 Oil	SC-15 Part A (Resin)	SC-15 Part B (Hardener)	SC-15 Mixed (A:B = 100:30)
Viscosity at Ambient (Pa-s)	0.24	0.58	0.045	0.285
Density at Ambient (kg/m^3)	706	1129	961	1085

A direct comparison of permeability produced from SAE 40 oil infusions and permeability produced from SC-15 infusions is made for IM7-4HS preforms with and without the inter-layer tackifier. Both the epoxy and motor oil were also measured for surface tension and contact angle with IM7. This first half of this chapter discusses the experimental approach and results of fluid surface tension and fiber contact angle measurements. The second half of the chapter introduces the unsaturated permeability measurement technique and discusses capillary effects on permeability induced from the interactions characterized in the first half.

5.1 Contact Angle and Surface Tension Measurements

5.1.1 Methods

5.1.1.1 Surface Tension Measurements

To measure fluid surface tensions of the SAE 40 oil and epoxy portion of the SC-15, the Du Noüy ring method was employed. With this measurement technique, a platinum-iridium ring of known surface contact angle is introduced into a test fluid with unknown surface tension. The Du Noüy ring method was carried out on a Thermo Cahn Dynamic Contact Angle (DCA) analyzer model 322, seen in Figure 5.1. The DCA possesses a high-precision balance with sensitivity

rating 0.1 μg. The ring has a circumference of 6.00 cm and is immersed into the test fluid. The wetting force is measured as the ring is pulled out of the fluid. With this, the surface tension of the liquid can be directly calculated. The measurement procedure and data interpretation for surface tension calculations described here are from the DCA's manufacturers tutorial found in [174].

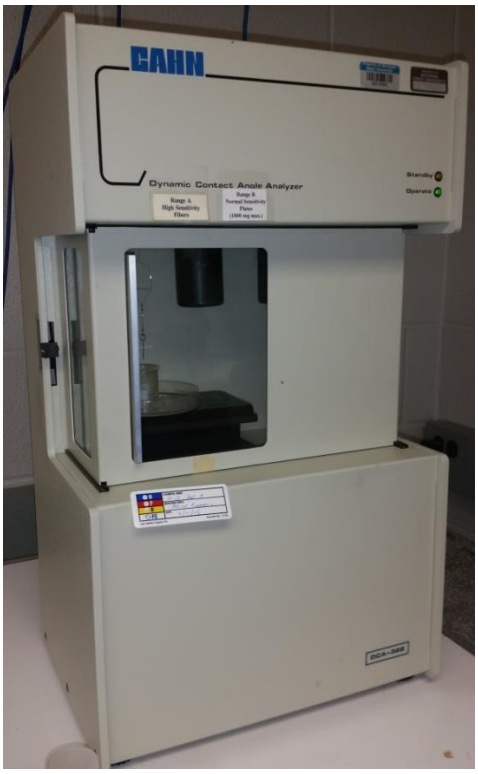

Figure 5.1: Cahn DCA 322

A representation of the Du Noüy ring method can be seen in Figure 5.2. A total of three measurements per test fluid were measured (SAE 40 motor oil and SC-15 Part A). Test fluids were housed in a 50 mL beaker. The ring was introduced into the test fluids at 20 μm/s, and once fully immerged, it was pulled out at the same rate until the fluid broke from the ring surface. The ring was cleaned with acetone and flame from a propane torch between each measurement. The

ring was allowed to fully cool to room temperature before subsequent testing. Also, between each measurement of the same liquid, a fresh liquid surface was introduced by pipet injection.

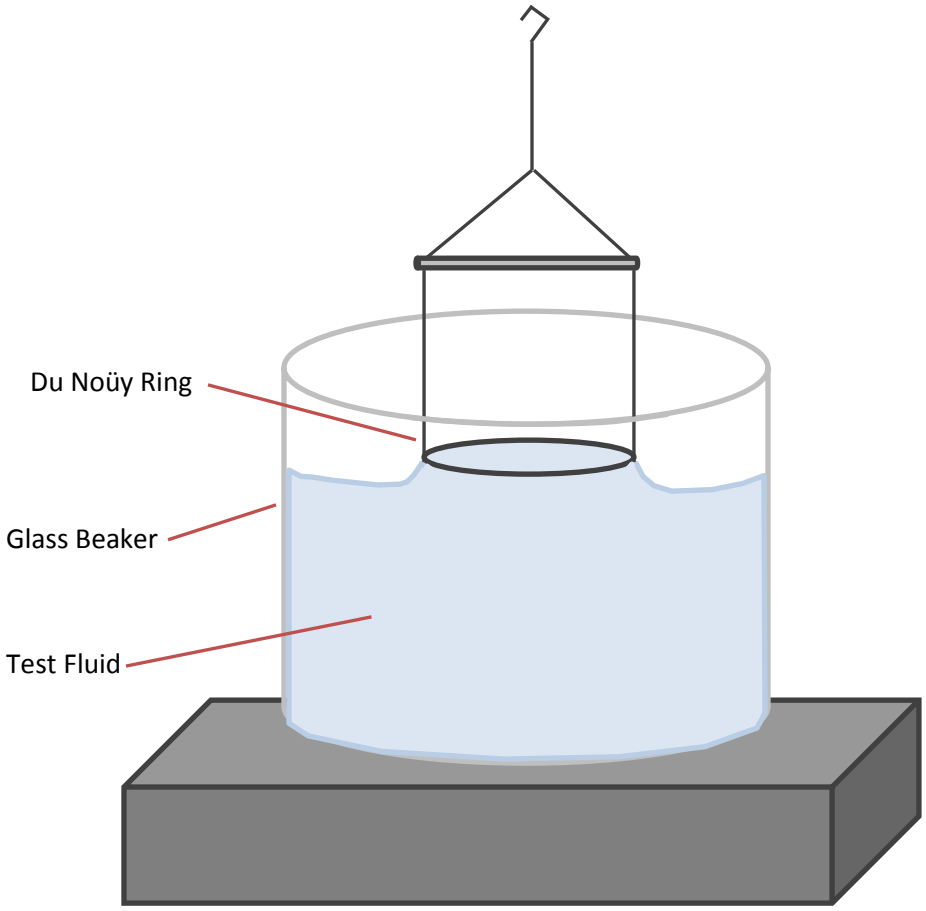

Figure 5.2: Du Noüy Ring Representation

Using the relation seen in Equation 56, the surface tension of the fluid, σ, can then be determined where σ' is the raw surface tension reading from the wetting force measurement and c_f is the correction factor

$$\sigma = \sigma' c_f \tag{56}$$

The raw surface tension is then defined as

$$\sigma' = \frac{F_w}{p} \tag{57}$$

Here, F_w is the measured wetting force during the ring pullout and p is the wetted perimeter ($p = 4\pi R$ where R is the radius of the ring). As recommended from the DCA manufacturer [174], the Deutsches Institut für Normung (DIN) standard of using the max pull point (point of maximum wetting force during ring pullout) for the surface tension calculation was used rather than the American Society for Testing and Materials (ASTM) standard of using the break point. The break point (the point during the test at which the fluid breaks away from the Du Noüy ring as it is pulled from the fluid) may be altered from vibrations or other outside interferences [175]. The correction factor is used to account for the liquid that is attached to the bottom of the Du Noüy ring during pullout. The correction factor is defined in Equation 58, where C is the mean circumference of the ring, ρ_{fluid} is the density of the test fluid, ρ_{air} is the density of the surrounding air, R is the radius of the ring, and r is the radius of the wire composing the Du Noüy ring. The density of the oil was provided by the manufacturer, while the density of the epoxy was referenced from the resin system material data sheet in [176].

$$c_f = 0.7250 + \sqrt{\frac{1.452\sigma'}{C^2\left(\rho_{fluid} - \rho_{air}\right)} + 0.04534 - \frac{1.679}{R/r}} \tag{58}$$

5.1.1.2 Contact Angle Measurements

To measure the advancing and receding contact angles of the SAE 40 motor oil and epoxy resin on the IM7 carbon fibers, the micro-Wilhelmy method was used. This method is similar to the Du Noüy ring method as it also employs the Cahn DCA, although single carbon fibers, attached to wire hangers, are introduced into the test fluid. A representation of the micro-Wilhelmy setup using the Cahn DCA 322 can be seen in Figure 5.3.

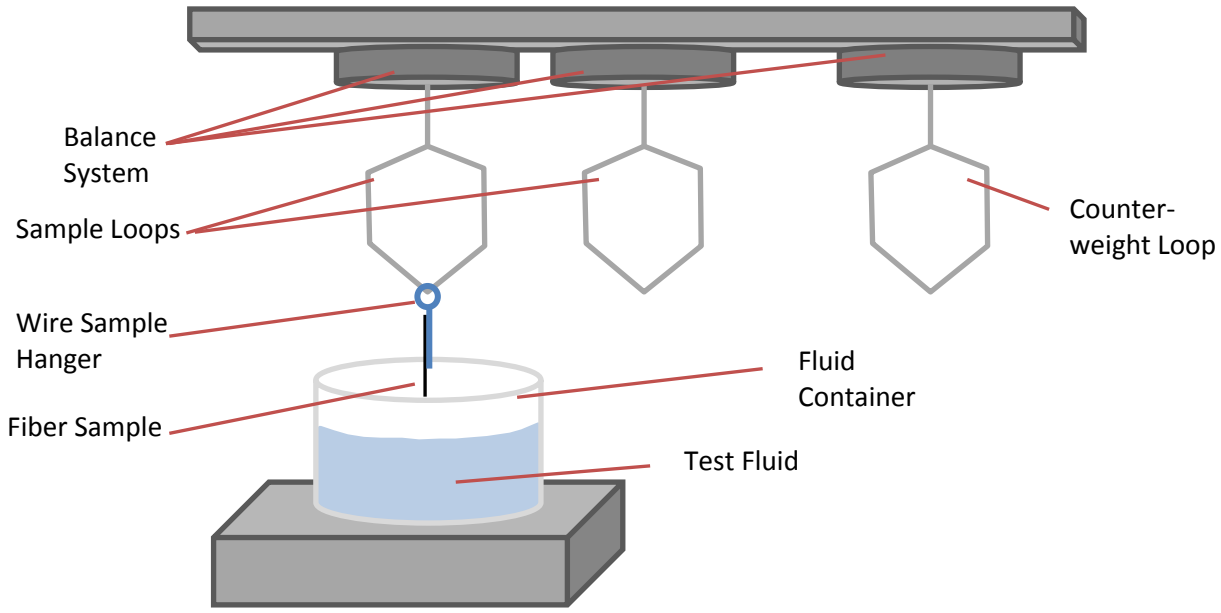

Figure 5.3: Micro-Wilhelmy Setup using the Thermo Cahn DCA 322

Using the relation in Equation 59, the advancing and receding fiber contact angles, θ, can be determined for each test fluid.

$$\cos\theta = \frac{F_w}{\sigma p} \tag{59}$$

The wetted perimeter, p, in this case refers to the fiber's circumference, while θ is the fiber contact angle, and F_w is the measured wetting force. Also, the work of adhesion between fiber and liquid can be determined from these measurements. The work of adhesion is defined as the total attraction between two phases, and is produced from both chemical and physical factors [177]. The work of adhesion, W_A, can be calculated from the measured quantities of fluid surface tension and contact angle as seen in Equation 60 [177], [178].

$$W_A = \sigma(1 + \cos\theta) \tag{60}$$

To obtain these wetting force measurements, micro-Wilhelmy samples were first laid up. To assemble the fiber samples, single carbon fibers were selected from a tow of the IM7-4HS fabric.

The fibers were then carefully glued to the wire hangers roughly 1.59 cm in length. The fibers were attached to be as straight as possible along the shaft of the hangers with about a 1 cm length of the fibers protruding past the end of the hanger. This left a length of the fibers free to contact with the test fluids. Sample layup was done under the aid of magnification. A total of 29 samples were produced. Each individual micro-Wilhelmy fiber sample was measured in diameter with a laser scan micrometer at 3 different points over the fiber's length. The average fiber diameter was calculated from these 3 points. Assuming a circular cross-section for carbon fiber, the wetted perimeter was calculated for each sample. A laid up micro-Wilhelmy sample is shown in Figure 5.4 (due to the carbon fiber size, it is not easily seen in this figure).

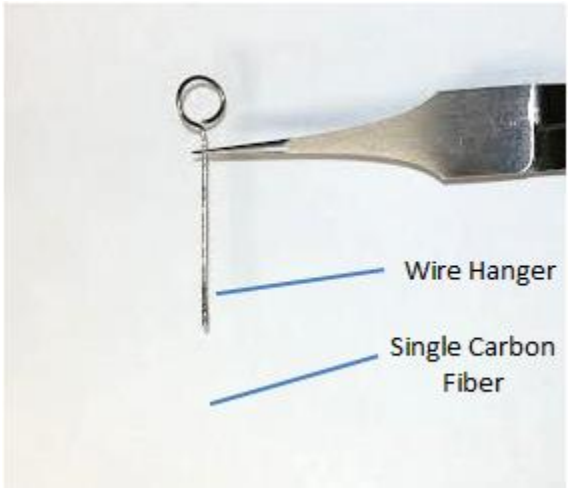

Figure 5.4: Micro-Wilhelmy Test Specimen

Micro-Wilhelmy contact angle tests were run with the IM7 samples with the SAE 40 oil, the SC-15 resin system (a ratio of epoxy to hardener of 100:30), and with epoxy portion only of the SC-15 (Part A only). The SC-15 resin system and the Part A only samples were vacuum degassed for 10 minutes before the contact angle measurements were conducted to reduce the presence of air bubbles, which are detrimental to the micro-Wilhelmy tests. Elapsed time after mixture of the SC-15 system was recorded in reference to when fiber samples were introduced. Advancing and

receding contact angles were found by introducing the fibers into the test fluids at 20 μm/s to an immersion depth of 3 mm, and then allowed to recede at the same speed until the fibers were pulled out of the liquid. The test fluids were housed in 10 mL glass beakers during these measurements. The wetting force during advancement and recession of the fibers were recorded from the DCA high precision balance and were used to find the contact angles. To do this, the advancing and receding portions of the curve were fit separately to linear regressions to account for the buoyancy effect. The advancing and receding wetting forces were then solved from these regressions at the point of zero depth of immersion (ZDOI) and used for the contact angle calculation.

5.1.2 Results and Discussion

5.1.2.1 Surface Tension Measurements

A total of 3 surface tension calculations were made for each test fluid using the Du Noüy ring method. Surface tension tests were made after the fiber contact angle measurements, and due to unsuccessful micro-Wilhelmy measurements with the full SC-15 system (Part A and Part B), only the epoxy portion (Part A) of the SC-15 and the SAE 40 motor oil and were measured. The surface tension calculations from each run of both tested liquids are listed in Table 5.2 along with the average, standard deviation (StDev), and percent coefficient of variation (CV). Note that the surface tension measurements for both fluids were made at room temperature in air.

Table 5.2: Surface Tension Measurement Results by Test Fluid

Surface Tension by Test Fluid (dyne/cm)		
Run #	SAE 40 Motor Oil	SC-15 Part A
1	29.18	32.36
2	29.12	32.41
3	29.14	32.46
Average	**29.15**	**32.41**
StDev	0.03	0.05
CV (%)	0.11	0.16

The surface tension results were very consistent for both fluids as seen in the table. Also, both the epoxy and motor oil were measured to possess a very similar surface tension value. Due to the small difference between surface tensions of the motor oil and epoxy, it is difficult to make an inference towards the determination of a better wetting fluid. Contact angle and work of adhesion results will aid in this. Literature values for the SC-15 epoxy could not be found for a comparison. The SAE 40 motor oil compares close to reported value of 35 dyne/cm for SAE 30 and SAE 50 oils [179]. A full list of surface tension measurement run data, including values for raw measurement surface tension, correction factors, and maximum pull out weights can be found in Appendix B. Also, sample wetting force graphs for both oil and epoxy in the Du Noüy ring measurements can be found in Appendix B.

5.1.2.2 Fiber Diameter Measurements

Of the 29 micro-Wilhelmy fiber samples measured, the average diameter of one sample was significantly higher than the remaining samples, so it was concluded that this was actually 2 fibers still twisted together from the tow. That left 28 samples of single fibers diameters. Each

fiber diameter was averaged over three points. The average IM7 fiber diameter, perimeter, standard deviation (StDev) and coefficient of variation (CV) are listed in Table 5.3.

Table 5.3: IM7 Fiber Diameter Statistics

Average Data from 28 Fiber Samples	
Fiber Diameter (μm)	5.59
Diameter StDev (μm)	0.27
Diameter CV (%)	4.86
Fiber Perimeter (From Average) (μm)	17.55

Compared to the manufacturer's supplied average fiber diameter of 5.2 μm shown in Table 1.1, the experimental average was about 7% higher. It should be noted that the sample body average diameter was not used for each contact angle measurement. Each individual fiber diameter was used for more accuracy. The entire data sample set can be seen in Appendix B.

5.1.2.3 Contact Angle Measurements

During micro-Wilhelmy testing for fiber contact angles, 13 IM7 fiber samples were designated for tests with the oil, 8 samples were designated for the SC-15 resin system, and 8 samples were designated for SC-15 Part A measurements. Due to fiber irregularities, bubbles in test fluids, and other effects, not all samples test data was used. Also, for some samples, only the advancing contact angle data was produced. A full list of the micro-Wilhelmy fibers and their data status can be found in Appendix B. Successful measurements were taken from 10 out of the 13 fiber samples used with the oil, all 8 fibers samples used with the SC-15 Part A, and none of the 8 samples measured with the full SC-15 system produced usable data for advancing contact angles. The advancing and receding contact angle results can be seen in Table 5.4. A complete list of individual fibers and their test data can be found in Appendix B.

Table 5.4: Advancing and Receding Contact Angle Measurement Results by Fluid

Fluid	SAE 40 Oil		SC-15 Part A (Epoxy only)	
Contact Angle Type	Advancing	Receding	Advancing	Receding
Sample Size	10	9	8	7
Average θ (degrees)	45.34	56.36	37.54	47.81
StDev θ (degrees)	5.92	3.96	5.63	6.91
CV (%)	13.06	7.03	14.99	14.46

These results infer that the epoxy is a better wetting liquid with the IM7 fiber because the advancing contact angle is smaller than that of the oil. While this comparison has been made by some researchers [43] to indicate a better wetting fluid, Miller [177] argues that only in a comparison of a single fluid does an increase in attraction confidently result in a decrease in contact angle. Therefore, the work of adhesion should be examined. While the epoxy possesses a lower average contact angle, both sets of fluid produced advancing contact angles with standard deviations of about 6 degrees. With this variation and a difference between the fluids averages of about 7 degrees, the difference of wettability between the fluids may not be statistically relevant. Other results show that the advancing contact angles for both fluids is less than their receding counterparts implying that a dry fiber is more attracted to the test fluids than a pre-wetted fiber. The calculated work of adhesion for these fluids with the IM7 will further investigate these inferences.

The work of adhesion for both advancement and recession were calculated for the motor oil and epoxy. The results are displayed in Table 5.4. This table also includes values of a hysteresis ratio, which is the ratio of between the work of adhesion of advancement over recession (hysteresis ratio= W_A^r / W_A^a). This was done for each full micro-Wilhelmy measurement (including both advancing and receding portions of the wetting force curve). The hysteresis ratio is clear

indication of whether the liquid is more attracted to a dry solid or the solid in a pre-wetted state [177].

Table 5.5: Work of Adhesion of Test Fluids with IM7 Fibers

Fluid	SAE 40 Oil			SC-15 Part A (Epoxy only)		
	Advancing	Receding	Hysteresis Ratio	Advancing	Receding	Hysteresis Ratio
Sample Size	10	9	9	8	7	7
Average W_A (erg/cm^2)	49.53	45.26	0.92	58.00	54.04	0.92
StDev W_A (erg/cm^2)	2.08	1.64	0.03	2.02	2.91	0.03
CV (%)	4.21	3.62	3.60	3.48	5.38	3.23

As seen in Table 5.5, the work of adhesion for the epoxy is higher than that of the oil (15.75% higher for the advancing portion). This shows that the total attraction between the IM7 fiber and epoxy is stronger than interaction between the IM7 and oil, which means that better wetting will result. Also, the coefficients of variation of these results is lower than that of the contact angle results, creating a more clear indication of the better wetting fluid. The hysteresis ratio for both the oil and epoxy is 0.92. While being close to a value of 1 (meaning there is no difference in attraction between a dry and pre-wetted surface), the hysteresis ratios for both fluids indicates that there is stronger attraction to the dry IM7 fiber surface than the pre-wetted fiber. Note that a full set of work of adhesion calculations can be found in Appendix B.

Similar work was produced by Hammond et al. [43], where surface tension and contact angle measurements were reported for IM7 and E-glass fibers with corn oil and EPON 815, a low viscosity epoxy resin. The researchers used the advancing contact angles alone to designate that the epoxy was better wetting for both the E-glass and IM7. Although the authors did not report the work of adhesion, their stated surface tension and contact angle results were used to generate

the data in Table 5.6. The fluid and fiber results are compared here with the IM7 fiber results from this current study. Note that the IM7 fibers from Hammond et al. [43] were from a 8-harness satin weave fabric, and due to possible differences with surface treatments, sizing, or other manufacturing variables, these results cannot be compared to the current study in a direct, quantitative sense, although the general trends of the comparison are relevant.

Table 5.6: Fluid Surface Tension, Contact Angle and Work of Adhesion Comparison with Hammond et al. [43] for IM7 Fibers

	Current Study Results		Results from Hammond et al. [43]	
Fluid	SAE 40 Oil	SC-15 Part A (Epoxy only)	Corn Oil	EPON 815
Surface Tension (dyne/cm)	29.1	32.4	26.5	37.2
Average Advancing θ (degrees)	45.3	37.5	36.1	28.5
Advancing W_A (erg/cm^2)	49.5	58.0	48.0	69.9

The comparison between these results is strikingly similar. Both results indicate that the epoxy was better wetting than their oil counterparts through lower contact angles and higher work of adhesion. Also, in both sets of results, the epoxy possessed higher surface tension than its oil equivalent. Overall, it can be concluded that the SC-15 epoxy is a better wetting fluid than the SAE 40 oil, while these similar results in literature [43] have produced concurring testimony.

Regarding the results of the SC-15 Part A and Part B mixture, the likely causes of the low success rate of the micro-Wilhelmy measurements could be due to air bubbles present after degassing and the chemical reactions taking place. Even after degassing, some air was still entrapped in the SC-15. Since the resin surface properties were time sensitive, extended

degassing cycles were not pursued. Also, upon placement of the resin supply in the DCA measurement chamber, a thin film or skin would start to form on the surface of resin (in a matter of minutes) due to the interaction with the atmosphere. This skin would cause the fiber samples to bend upon contact and ruin sampling data. To prevent this, the surface film was manually broken up with a sterile glass pipet, although the complete elimination of these highly viscous formations could not be confirmed before each test. It should be noted that the low success rate of the contact angle measurements made with the SC-15 Part A and Part B system are due to the fluid rather than fiber inconsistencies.

A sample graph of fiber contact angle measurement data is shown in Figure 5.5 displaying the wetting force being tracked as a function of the fiber immersion depth. This sample was immersed in SC-15 Part A. The significant features of the immersion and recession curve are noted in the figure. Fiber surface irregularities also can be seen on the advancing portion of the curve. The following graph in Figure 5.6 displays the advancing and receding portion of the wetting force transient. These curve potions were fitted to linear regressions. The fitted points at zero depth of immersion (ZDOI) are also marked, which are used for the fiber contact angle calculations to account for the buoyancy effect as described earlier.

Fiber irregularities are also found as spikes in the wetting force curve [180] as seen in Figure 5.7. Tests that produced unusable data show results typical to those in Figure 5.8. Throughout testing, the IM7 fiber samples produced moderately consistent wetting force readouts, which correlate to a fairly smooth surface. This smoothness could be a product of the sizing or surface treatment placed on the fibers by the fabric manufacturer. Hammond et al. [43] also mentioned this

regarding the apparent smoothness of their IM7 fibers seen in scanning electron micrographs. Irregularities in the form of spikes on the advancing and receding curves were excluded in the buoyancy correction linear regressions. Some of the irregularities could be due to fiber sizing inconsistencies or from deformations experienced when the fibers were manually separated from the tow.

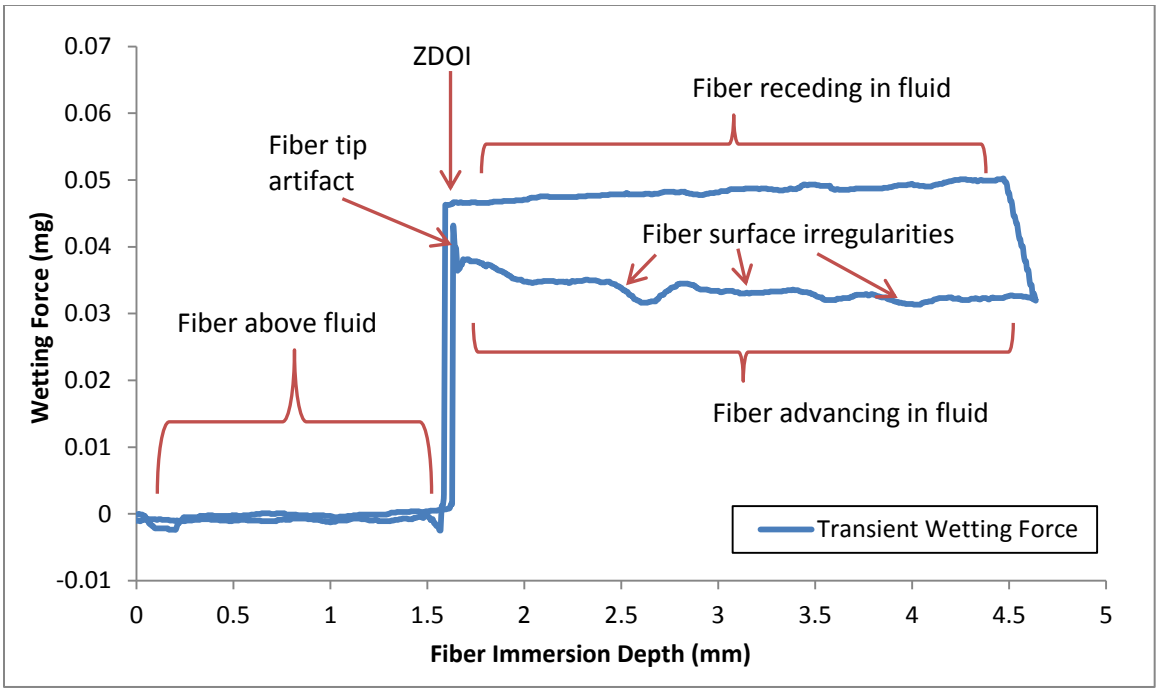

Figure 5.5: Sample Micro-Wilhelmy Test Data

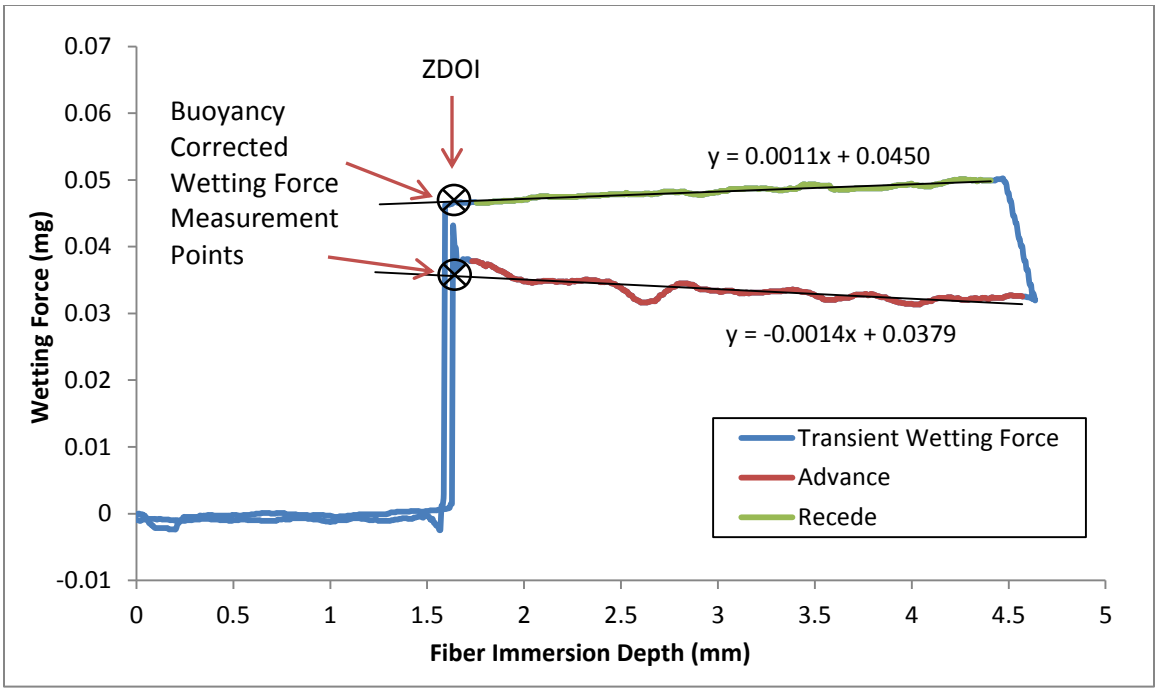

Figure 5.6: Sample Micro-Wilhelmy Test Data with Buoyancy Correction

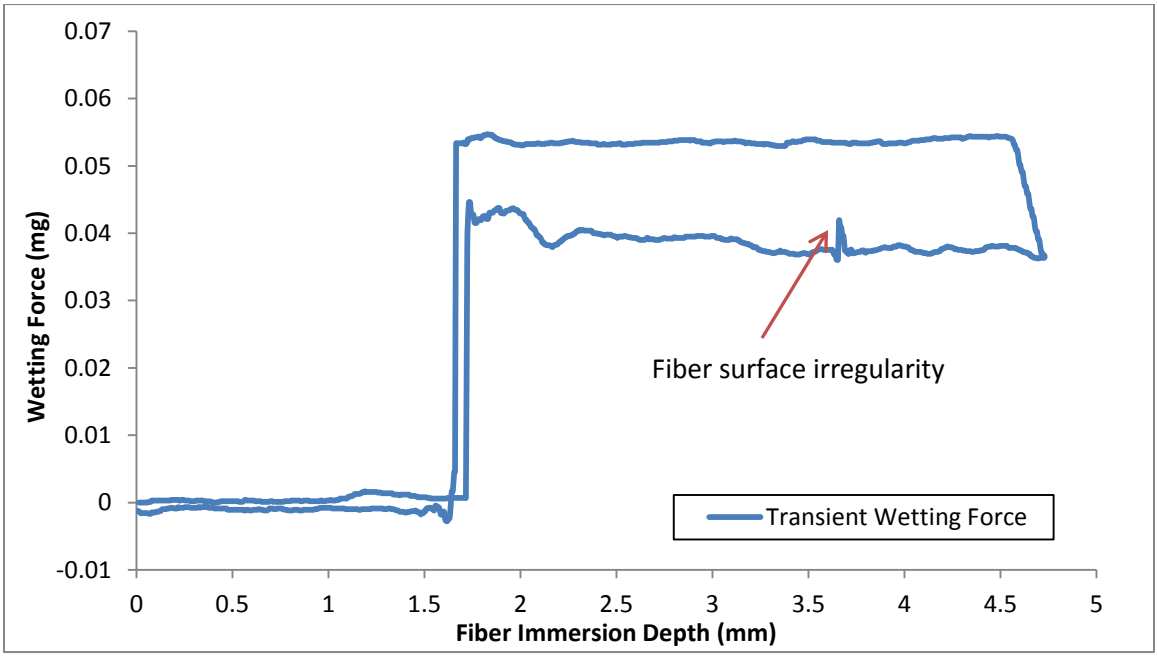

Figure 5.7: Sample Micro-Wilhelmy Test Data

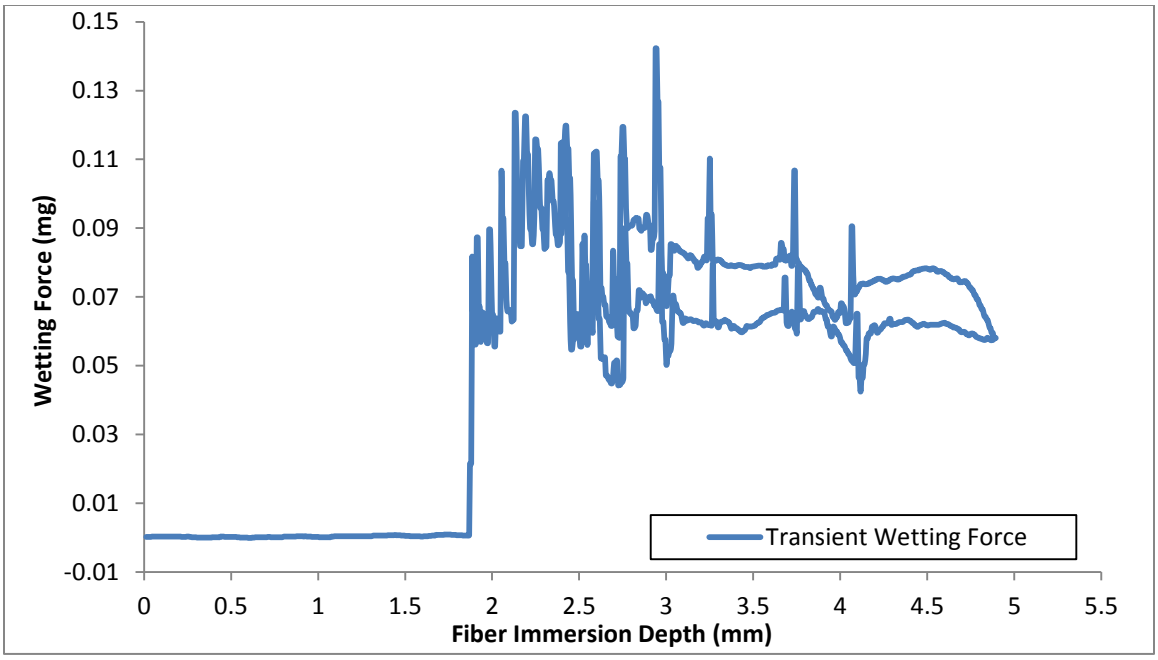

Figure 5.8: Sample Micro-Wilhelmy Unusable Test Data

From the results of fluid and fiber interactions, it was then necessary to determine if these fluid properties would produce significant effects in the determination of experimental preform permeability. To do this, the surface tension and contact angle results were used to quantify capillary effects and direct comparisons of SC-15 epoxy and SAE 40 motor oil infusions were made. This work will be discussed in detail in the next section of this chapter.

5.2 Unsaturated Channel Flow Measurements with Differing Fluids

5.2.1 Methods

5.2.1.1 Experimental Setup

Advancing front permeability measurements for both SAE 40 oil and SC-15 Part A were obtained using a channel flow visualization fixture. The full SC-15 resin system (Part A and B mixture) was not used here due to the unsuccessful micro-Wilhelmy characterization discussed earlier. This permeability fixture provided the ability to visually observe flow fronts progressing through preforms of IM7-4HS. The fixture is constructed of aluminum and allows a preform 15.13 cm in width, 17.11 cm in length, and 6.35 cm in thickness. A line source and line sink lay on either side of the fixture's preform cavity, which produces a rectilinear, in-plane flow. An Airtech pressure pot was used to supply constant pressure injections of the test fluids with the aid of a pressure regulator. The fixture was outfitted with an Omega PX-180 in-line pressure transducer, which monitored the precise supplied injection pressure. Using a camera positioned over the visualization window, advancing flow front locations were recorded while the elapsed time was monitored with a stopwatch. An exploded view schematic of the fixture can be seen in Figure 5.9.

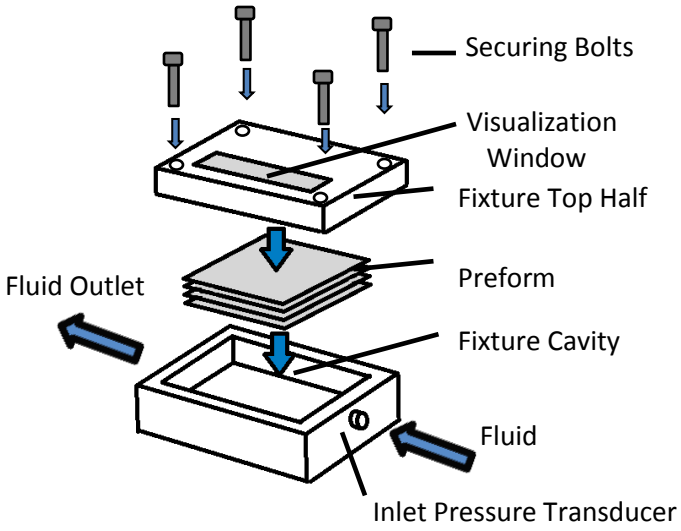

Figure 5.9: Exploded View Schematic of the Channel Flow Unsaturated Permeability Fixture

The channel flow fixture has two visualization windows, one on the top and one oriented on the side to allow for viewing the preform's cross-section. Due to the dark color of the IM7-4HS preforms, only the flow front view through the top visualization window was recorded by the camera and clear differentiation could be made between saturated and unsaturated regions of the reinforcement.

The nature of advancing front permeability measurements restricts the number of permeability data points to one per preform. As opposed to saturated measurements, permeability at only one fiber volume fraction can be calculated in unsaturated experiments. Once a preform is saturated in an advancing front test, it cannot be measured again under the same conditions. Due to this limitation, IM7-4HS preforms of a single layup, fiber volume fraction, and flow direction were tested in order to maximize material supply. The focus of the unsaturated permeability experiments were to determine the effects of capillary pressure, fluid type, tackifier, and injection pressure on permeability. This means that layup orientation and ply number effects

were not investigated as they were studied in the saturated experiments. Two aluminum shims were carefully cut and sealed with silicone into the unsaturated test fixture to produce a cavity depth of 1.68 mm, resulting in an IM7-4HS preform fiber volume fraction of 54.6% with 8 plies. A warp direction aligned preform layup was used for each sample producing a stacking sequence of $[0]_8$. Multiple measurements were made at 69, 138 and 276 kPa (10, 20 and 40 psi) target constant inlet pressure set points. These unsaturated test parameters and others can be seen in Table 5.7.

Table 5.7: Unsaturated Channel Flow Test Setup Parameters

Material	Layup	V_f	Constant Inlet Pressures Set Points (kPa)	# Runs per Inlet Pressure Set Point	Flow Direction
Non-tackified IM7-4HS	$[0]_8$	54.6%	69, 138, 276	3	Warp or S_{xx}
Tackified IM7-4HS	$[0]_8$	54.6%	69, 138, 276	3	Warp or S_{xx}

Each infusion experiment was recorded and post-processed to determine the unsaturated, advancing front permeability. The visualization fixture window was graduated every 6.35 mm (0.5 inch) so that location and time of the flow front was easily distinguished at these points. The flow front locations were recorded over time and the method described by Hammond et al. [43] was used to derive the permeability. Beginning with Darcy's law of form in Equation 61, substitutions of $\frac{Q}{A} = \frac{dx}{dt}\varphi$ and $\frac{dP}{dx} = -\frac{\Delta P}{x}$ can be made to derive an altered form of Darcy's law in Equation 62. Recall that in Darcy's law, Q is the flow rate, A is the cross-sectional area normal to flow, μ is the fluid viscosity, S is the permeability, and $\frac{dP}{dx}$ is the pressure gradient.

$$\frac{Q}{A} = -\frac{S}{\mu}\frac{dP}{dx} \tag{61}$$

$$\frac{dx}{dt}\varphi = \frac{S}{\mu}\frac{\Delta P}{x} \tag{62}$$

Here, ΔP is the pressure drop over the preform length, or essentially the injection pressure if gage pressure is used, φ is the preform porosity, and t is the time elapsed at the flow front location, x. Then, by integrating Equation 62 with an initial condition of $x(0) = 0$, one can derive the relationship seen in Equation 63.

$$x^2 = \left(\frac{2S\Delta P}{\mu\varphi}\right)t \tag{63}$$

By using a linear pressure drop versus flow front location assumption, the measured flow front location squared (x^2) versus time can be fit to a linear regression where $\left(\frac{2S\Delta P}{\mu\varphi}\right)$ is the slope (say, m, with units of length squared per second) of the experimental data. Then, the unsaturated permeability of the preform can be determined directly from the slope of the x^2 verses time curve with Equation 64. Note that this derives average unsaturated preform permeability over the infusion by taking the slope of all experimental points on the curve.

$$S^{unsat} = \frac{m\mu\varphi}{2\Delta P} \tag{64}$$

The linear pressure drop assumption is valid if a good linear regression fit can be made for the experimental flow front location squared versus time data. If this is not the case, then the assumption cannot be used and permeability must be calculated separately per flow front location or time of interest.

5.2.1.2 Capillary Pressure Determination

If capillary pressure is to be accounted for during the calculation of experimental unsaturated permeability, then this value can be added with the injection or mechanical pressure term [123], [133]. This gives

$$\Delta P = P_{inj} + P_c \tag{65}$$

Here, P_{inj} is the constant injection pressure of the infusion and P_c is the capillary pressure. Note that this formulation neglects gravitational pressure, which is assumed to have little influence on the entire pressure drop. This pressure drop can then be directly substituted back into Equation 63 and Equation 64. To define the capillary pressure, experimental or theoretical techniques can be used. In this study, analytical formulations will be used to define capillary pressure contributions, as well as, an experimental technique based on constant injection pressure infusions, and a dynamic capillary pressure model based on capillary number. These methods will be described next.

5.2.1.2.1 Analytical Methods

Ahn et al. [123] gave a theoretical expression (also, see Equation 43 and Equation 44 in Chapter 2) for defining capillary pressure in one-dimensional flow through fiber bundles. This is seen in Equation 66 where d_f is the average fiber diameter, φ is the porosity, σ is the fluid surface tension, θ is the fiber contact angle, and F is the form factor, which is based on the geometry and flow direction.

$$P_c = \frac{F}{d_f}\frac{(1-\varphi)}{\varphi}\sigma\cos\theta \tag{66}$$

For fluid flow parallel to the fiber bundle, $F = 4$ and for transverse flow, $F = 2$. For complex architecture preforms, a precise shape factor can only be obtained through experimental capillary measurement [124]. Amico and Lekakou [124] found through their experiments form factors in the range of 3.79 to 3.84 for their plain weave fabric, which was in the expected range between 2 and 4. Considering that the four-harness satin material used in this study has a combination fiber bundles of both parallel and transverse to any induced one-dimensional flow, a representative

form factor would also be expected to be between 2 and 4. Due to this, formulation from Ahn [123] in Equation 66 was used in this study to estimate capillary pressure in the SAE 40 and SC-15 infusions, where the limits prescribed from the range of possible form factors is also discussed. Verrey et al. [181] defined a similar theoretical relationship to model capillary pressure including the effect of fiber volume fraction. This formulation is seen in Equation 67.

$$\Delta P_c = -\frac{A_{1fiber}}{V_{1fiber}} \sigma \cos\theta \frac{V_f}{1 - V_f} \tag{67}$$

In this geometrical formulation, A_{1fiber} is the surface area of one fiber and V_{1fiber} is the volume of one fiber, while V_f is the fiber volume fraction of the fiber packing. Relationships from both Ahn et al. [123] and Verrey et al. [181] were modeled over multiple fiber volume fractions and compared to constant flow rate measurements of capillary pressure from SAE 40 experiments.

Further, Ahn et al. [123] also defined a capillary number seen in Equation 68. The capillary number relates the relative effects of viscous forces over the surface tension forces.

$$Ca = \frac{\mu v}{\sigma} \tag{68}$$

Here, v is the interstitial velocity, which is defined as

$$v = \frac{q}{\varphi} \tag{69}$$

In this relationship, q is the Darcy flux, which can be defined from Darcy's law by

$$q = -\frac{S}{\mu}\frac{dP}{dx} \tag{70}$$

5.2.1.2.2 Constant Injection Pressure Method

Several researchers [123], [124], [181] have used an experimental approach where results from constant pressure infusions were used to define capillary pressure. By including capillary

pressure in the pressure drop term of Darcy's law and integrating in the same fashion to the formulation of Equation 64, the relationship seen in Equation 71 is formed where the slope, m, is now represented in Equation 72 [181].

$$x^2 = mt \tag{71}$$

$$m = -\frac{2S}{\mu\varphi}\left(\Delta P_c - P_{app}\right) \tag{72}$$

Here, P_{app} is the applied pressure and ΔP_c is the capillary pressure drop. Simply by plotting m against the applied pressure for multiple experiments at different injection levels, the capillary pressure drop can be found by fitting a linear regression curve to the plot and extrapolating it to $m = 0$ [181]. This technique was used to determine the capillary pressures with SAE 40 oil and SC-15 Part A in the unsaturated IM7-4HS infusions. It should be noted that this technique provides a constant value of capillary pressure.

5.2.1.2.3 Dynamic Capillary Pressure Method

A similar approach can be applied using constant flow rate experiments where upon consideration of the capillary contributions the relationship in Equation 73 is formed [181].

$$-P_{app} = \frac{Q^2\mu}{A^2S\varphi}t + \Delta P_c \tag{73}$$

Here, Q is the constant flow rate, and A is the area normal to flow. By plotting the pressure difference at the inlet versus the elapsed time, the capillary pressure can be determined by extrapolating the linear portion of the curve to $t = 0$ [181]. Recently, Verrey et al. [181] used this technique as a basis for developing a more robust, dynamic capillary pressure determination method for LCM infusions. This method will be described here and was also employed with the non-tackified IM7-4HS material. To do this, constant flow rate infusions with the non-tackified

IM7-4HS preforms were performed. The transient inlet pressure was recorded during resin infusion from initiation to preform saturation, producing a pressure verses time curve for multiple fiber volume fractions.

Verrey et al. [181] reasoned that the fluid/fiber contact angle is a dynamic function that is dependent on capillary number, and therefore, the capillary pressure should also be a function of capillary number. The Hoffman-Voinov-Tanner law shows the relationship between the dynamic contact angle and the capillary number, and is seen in Equation 74 [181].

$$\theta_{dyn}{}^3 - \theta_0{}^3 \cong c_T Ca \tag{74}$$

Here, θ_{dyn} is the dynamic contact angle, θ_0 is the contact angle at thermodynamic equilibrium, Ca is the capillary number and c_T is an experimental constant. Based on the slow speed of micro-Wilhelmy experiments, the measured contact angle was considered to be close to thermodynamic equilibrium. The experimental constant, c_T, was defined by fitting the constant flow rate experiment results, described in Chapter 4, to the Hoffman-Voinov-Tanner law. Verrey et al. [181] then used the relation in Equation 74 and combined it with the capillary pressure drop definition of Mortensen and Wong [182] shown in Equation 75.

$$\Delta P_c = -S_f \sigma \cos\theta_{dyn} \tag{75}$$

In this relation, σ is the fluid surface tension between fiber, fluid, and surrounding air, and S_f is the surface area of the interface per unit volume of the fluid. Similar to Ahn et al.'s [123] theoretical formulation for capillary pressure, S_f can also be defined from idealized geometrical fiber packing considerations with [181]

$$S_f = \frac{2}{r_f}\left(\frac{V_f}{1 - V_f}\right) \tag{76}$$

Here, r_f is the fiber radius and V_f is the fiber volume fraction. This S_f value has also been determined experimentally through Brunauer–Emmett–Teller (BET) techniques [181], [182]. By combining Equation 74 and Equation 75, the capillary pressure was directly related to the capillary number, and thus a critical capillary number could be found where fluid behavior changes from wetting flow (enhancing the flow) to non-wetting flow (forced flow). This method was employed in this current study to define capillary pressures in the IM7-4HS preforms as a function of capillary number. Note that this technique was employed only with the non-tackified IM7-4HS due to material supply. Later in the results, permeability correction based on this technique will also be explored.

5.2.2 Results and Discussion

Unsaturated infusions were made for both SAE 40 oil and SC-15 (Part A only) resin at 3 constant injections pressures of 69, 138 and 276 kPa. A total of 3 runs were made for each test fluid, at each of the 3 injection pressures, totaling 18 infusions with non-tackified IM7-4HS and 18 infusions with the tackified IM7-4HS. A typical example of flow front advancement over time is shown in Figure 5.10 with SAE 40 oil as the permeating fluid. To define permeability measured in the infusions, capillary pressure estimations were considered first and are discussed next.

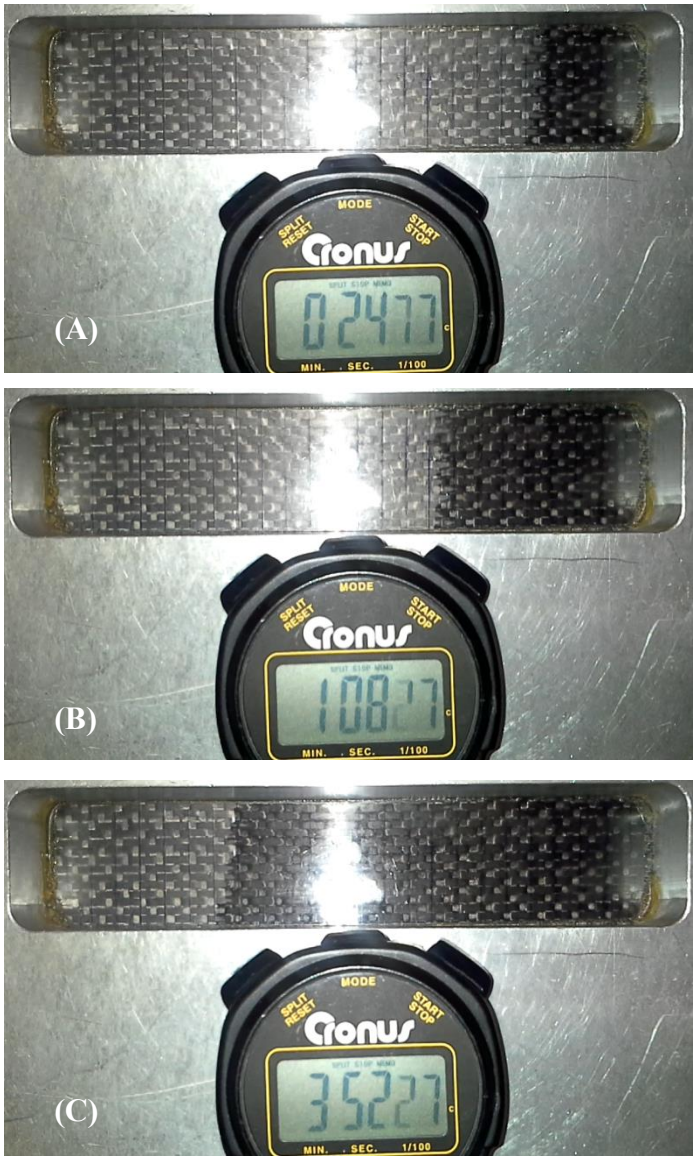

Figure 5.10: Linear Flow Front Advancement through Non-Tackified IM7-4HS. (A) Flow front at 24 sec. (B) Flow front at 1 min. 8 sec (C) Flow front at 3 min. 52 sec.

5.2.2.1 Capillary Pressure Determination

This study employs three different techniques for capillary pressure determination as described in the Methods section: 1) analytical, 2) experimental with constant injection pressure infusions, and 3) a dynamic capillary determination based on capillary number. Permeability was also

determined by neglecting capillary pressure contributions. The results from these methods are described in detail.

5.2.2.1.1 Analytical Capillary Pressure

Using the analytical formulation in Equation 66, it can be seen that capillary pressure varies linearly with the form factor. In Figure 5.11, the capillary pressure is plotted against form factors ranging from 2 to 4 for both test fluids.

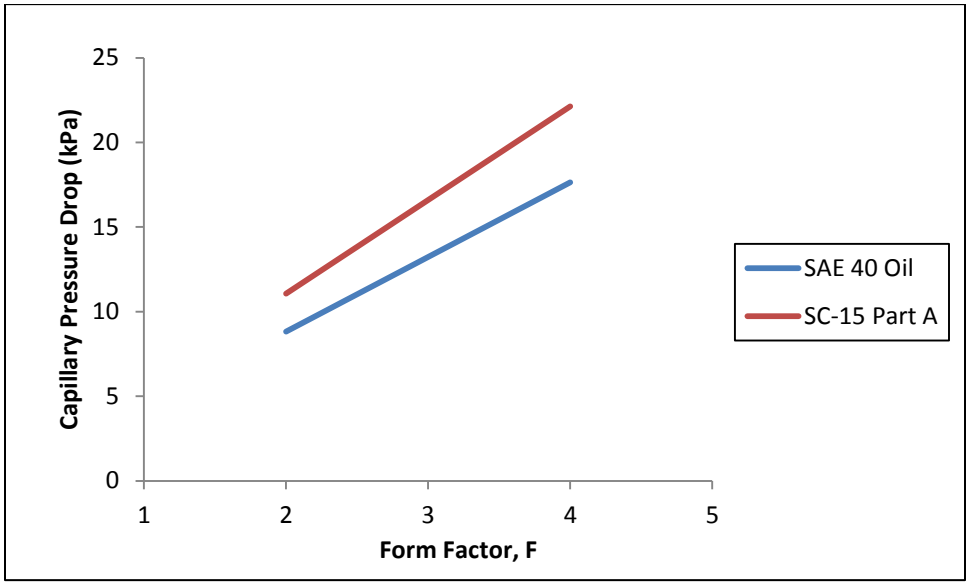

Figure 5.11: Capillary Pressure versus Form Factor

Capillary pressure ranges from 8.8 to 17.6 kPa (1.3 to 2.6 psi) for the SAE 40 oil and 11.0 to 22.1 kPa (1.6 to 3.2 psi) for the SC-15 Part A. Using the limits of these ranges, the unsaturated permeability can be corrected for capillary pressure for each infusion made. Note that these capillary pressure drops are assumed to be flow enhancing, or opposite in value (negative) to the applied pressure.

5.2.2.1.2 Constant Injection Pressure Method

Using the experimental procedure for capillary pressure determination from constant pressure injection pressure tests [123], [124], [181], [182], the m versus pressure difference for all advancing flow front experiments can be fit to a linear regression curve. As explained in the methods section, this regression is extrapolated to $m = 0$, which corresponds directly to the capillary pressure value. This can be seen in Figure 5.12 for both test fluids in conjunction with the non-tackified IM7-4HS preforms. Similar data can be seen plotted for the tackified IM7-4HS preforms in Figure 5.13. Note that each data point represents the average values of 3 constant pressure injections with error bars the vertical direction (representing scatter in m values) The repeatability of injection pressure was excellent for each set, and therefore horizontal error bars are not evident for the majority of data points.

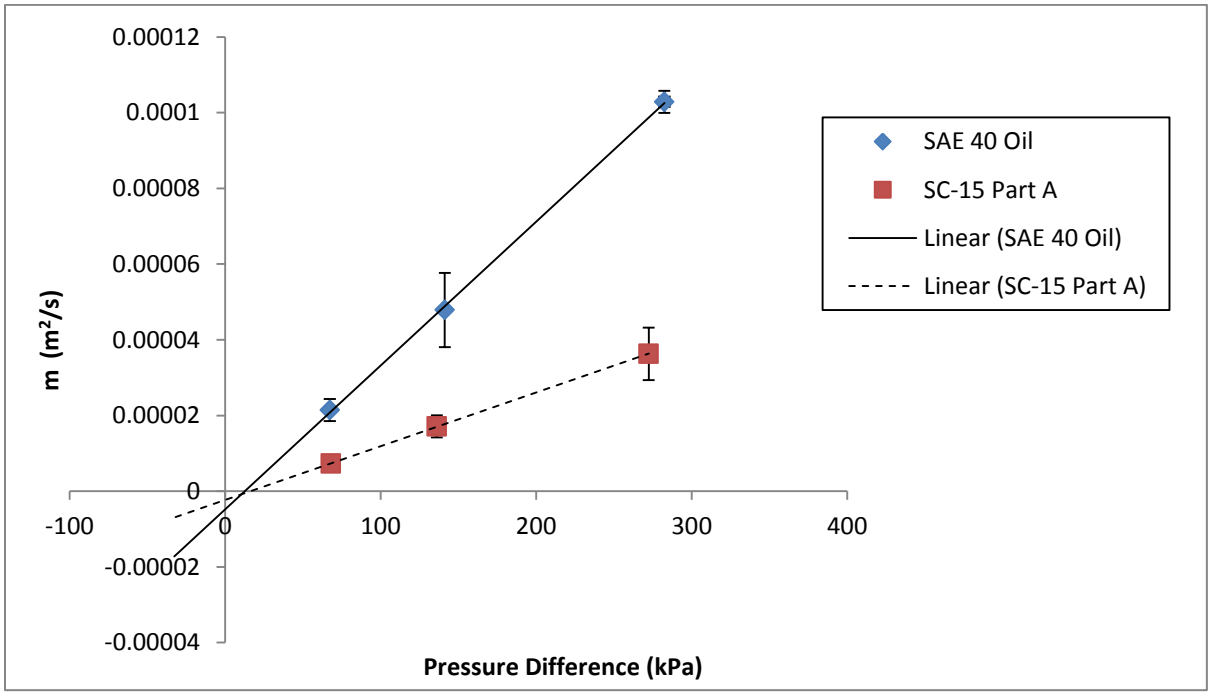

Figure 5.12: Capillary Pressure Determination from Constant Injection Pressure Experiments for Non-tackified IM7-4HS

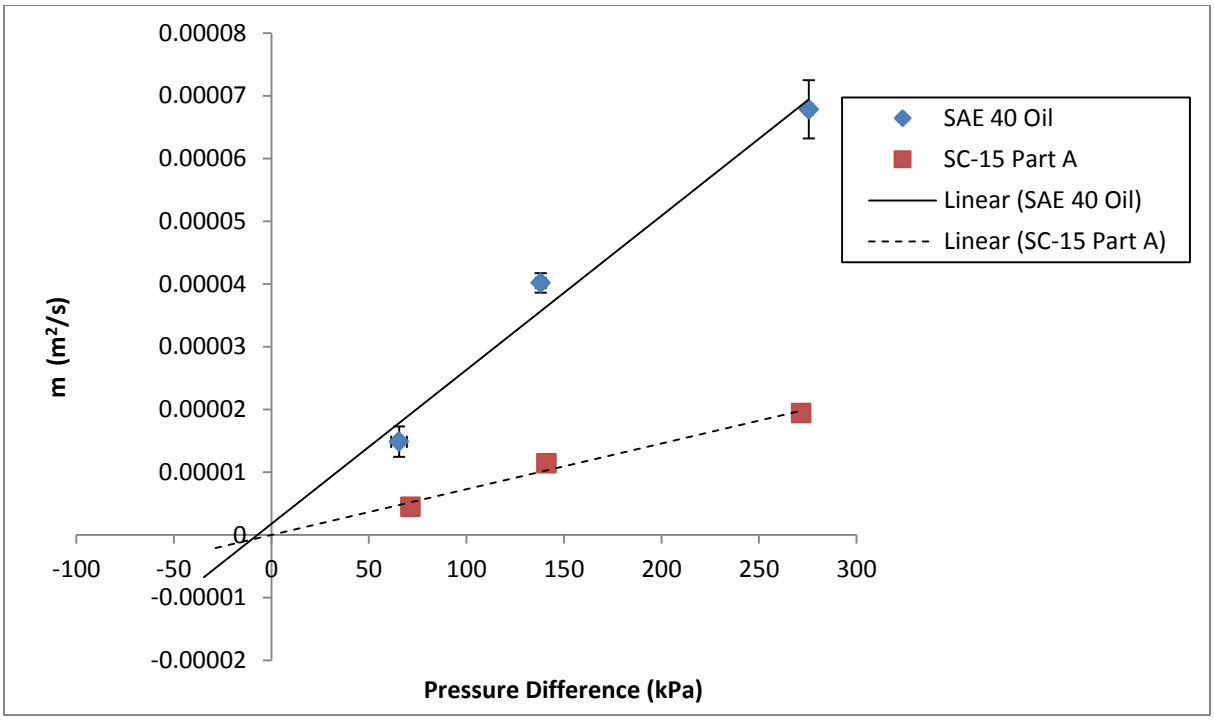

Figure 5.13: Capillary Pressure Determination from Constant Injection Pressure Experiments Tackified IM7-4HS

These linear regressions can be seen extrapolated to zero, where interestingly, positive capillary pressures are the result for the non-tackified experiments, while negative pressures are the result for the tackified IM7-4HS preforms. Hence, both the SAE 40 oil and SC-15 Part A resisted fiber wetting in the non-tackified preforms rather than permit wicking, as a negative capillary pressure would allow. The presence of tackifier appears to encourage wicking flow compared to non-tackified preforms, as negative capillary pressure values resulted for both test fluids. The values of the extrapolated pressures are shown in Table 5.8. It should also be noted that the tackified preforms produced less scatter than their non-tackified counterparts. This is likely due to the fact that the tackifier aided in holding fiber orientation and helped reduce the loss of tows during sample preparation.

Table 5.8: Capillary Pressures Determined from Constant Pressure Injection Method

Preform Type	P_c (kPa) by Test Fluid Type	
	SAE 40 Oil	SC-15 Part A
Non-tackified	12.64	16.23
Tackified	-7.12	-0.21

This effect on the sign of the capillary pressure term may be explained by the inter-layer tackifier presence in the inter-tow gaps of the tackified preforms. The blocking of inter-tow gaps encourages permeating fluid to flow more through the intra-tow regions. This result was verified by the low permeability results of tackified preforms in Chapter 4 compared to non-tackified material. It is then hypothesized that by increasing the flow through the intra-tow pores, capillary action is encouraged. The non-tackified fabric allows greater flow through inter-tow gaps, so that fluid preferentially flows first around the low-permeability tows and then slowly saturates them. The positive capillary pressure results have been noted in previous research. Verrey et al. [181] found similar results with a Diglycidyl Ether of Bisphenol A (DGEBA) epoxy, where the experimental capillary pressure was determined to be positive 17.9 kPa when injection pressures over a range of roughly 25 to 175 kPa were fit to a linear regression curve. This study used a similar, yet slightly larger pressure range from roughly 69 kPa to 275 kPa. Mortensen and Wong [182] also found similar results of positive capillary pressures up to 1.5 MPa, although these researchers were investigating capillary effects of molten aluminum permeating alumina/silica fibers. Considering the fiber contact angles presented earlier, both the oil and epoxy possessed values less than 90 degrees, which in contradiction, infers wetting. Verrey [181] explained that the dynamic contact angle should depend on the capillary number, and the capillary pressure, in turn, depends on the capillary number. Being that constant pressure experiments have variable velocity, the capillary number also varies from high at the inlet to low at the exit of the fixture; the higher the fluid velocity, the higher the viscous effects. This being said, the measurements of

fiber contact angle and surface tension should be considered close to equilibrium if the capillary number is below 10E-5, and thus capillary numbers experienced higher than this value should be regarded to be in the dynamic regime [181]. Regarding the tackifier effect, the non-tackified preforms tested here allow for more preferential flow through the inter-tow gaps compared to the tackified preforms. This allows for higher fluid velocity, and therefore higher capillary numbers. In turn, this increases the possibility of capillary numbers to be over the threshold value considered to mark the start of the dynamic flow regime. On the contrary, the tackified preforms reduced flow in the inter-tow channels, which results in reduced fluid velocity and fill times.

To further interpret these results, the capillary numbers for the constant injection pressure experiments were investigated. Figure 5.14 shows the averaged capillary number per target injection pressure versus flow front location for the non-tackified IM7-4HS oil infusions. Alternatively, Figure 5.15 shows the same relationship with the tackified material. Both sets of data are fitted with power law relationships, while the error bars represent the standard deviations of the 3 experiments per target inlet pressure set point. Both the non-tackified and tackified infusions show high capillary numbers at the start of the infusions, while as the flow front reaches the mold outlet, the capillary numbers drop significantly. Also, note that the non-tackified infusion capillary numbers are higher than their tackified counterparts for the same injection pressure. This is because the inter-layer tackifier reduces the apparent porosity of the preform and subsequently reduces the fluid velocity.

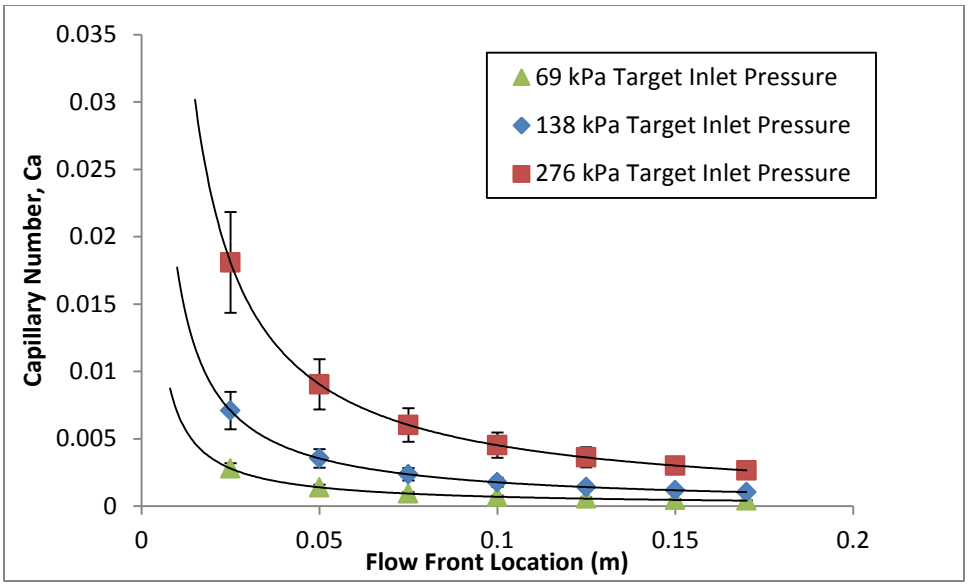

Figure 5.14: Capillary Number vs. Flow Front Location for Non-Tackified IM7-4HS Oil Infusions

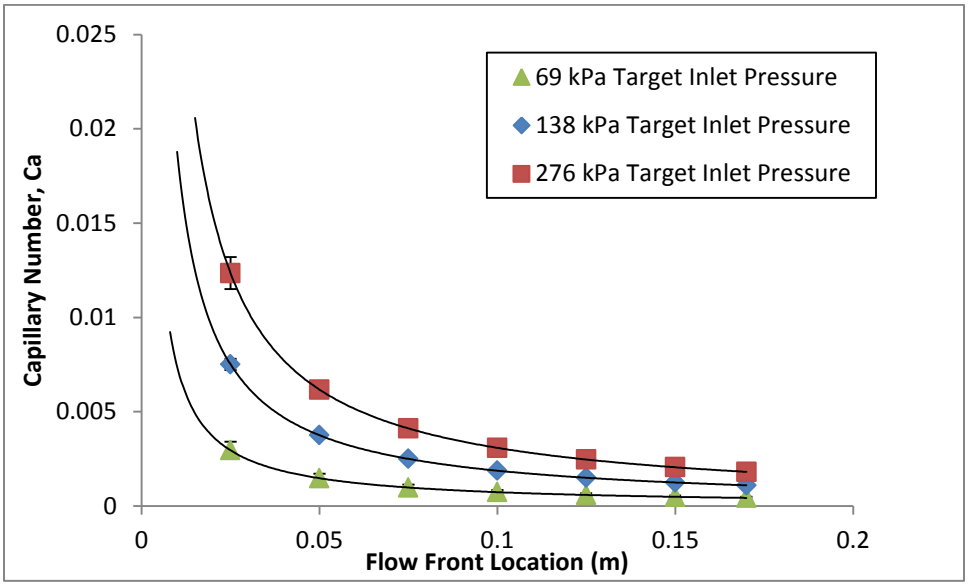

Figure 5.15: Capillary Number vs. Flow Front Location for Tackified IM7-4HS Oil Infusions

Using Equation 75 and data from the constant pressure capillary experiments, Mortensen and Wong [182] found the apparent dynamic contact angles during molten aluminum infusions into fibrous preforms. They found apparent contact angles of over 100 degrees, which correlated with

their positive capillary pressure finding stated earlier. Using this method, the apparent contact angles for both the SAE 40 and SC-15 Part A can be determined from the results shown in Figure 5.12 and Figure 5.13. These apparent values are displayed in Table 5.9.

Table 5.9: Experimental Capillary Pressure and Apparent Contact Angles

	Non-Tackified		Tackified	
Fluid	SAE 40 Oil	SC-15 Part A	SAE 40 Oil	SC-15 Part A
P_c (kPa)	12.64	16.23	-7.12	-0.21
Apparent θ	92.89°	93.34°	73.50°	89.56°

These apparent contact angles were found to be just over 90 degrees for the non-tackified material, implying non-wetting behavior. The tackified preforms produced apparent contact angles below 90 degrees for both fluids. While these are interesting results, they are limited by a constant capillary pressure and apparent fiber contact angle for an entire infusion. It was shown in Figure 5.14 and Figure 5.15 that capillary numbers are not constant over constant injection pressure infusions, and based on work by Verrey et al. [181], the capillary pressure contribution should then also be variable for such scenarios. A more robust dynamic model for capillary pressure determination based on flow rate or capillary number is presented next.

5.2.2.1.3 Dynamic Capillary Determination

Using Verrey et al.'s [181] capillary pressure determination method for constant flow rate experiments, the capillary pressure versus fiber volume fraction for SAE 40 oil was determined over a small range of fiber content. The epoxy was not used in these set of experiments, and also only non-tackified preforms were used due to material supply. Multiple constant flow rate experiments were conducted over a range of fiber volume fractions of ~45% to ~55% where inlet

pressure was monitored versus time. A typical result of a constant flow rate IM7-4HS infusion can be seen in Figure 5.16.

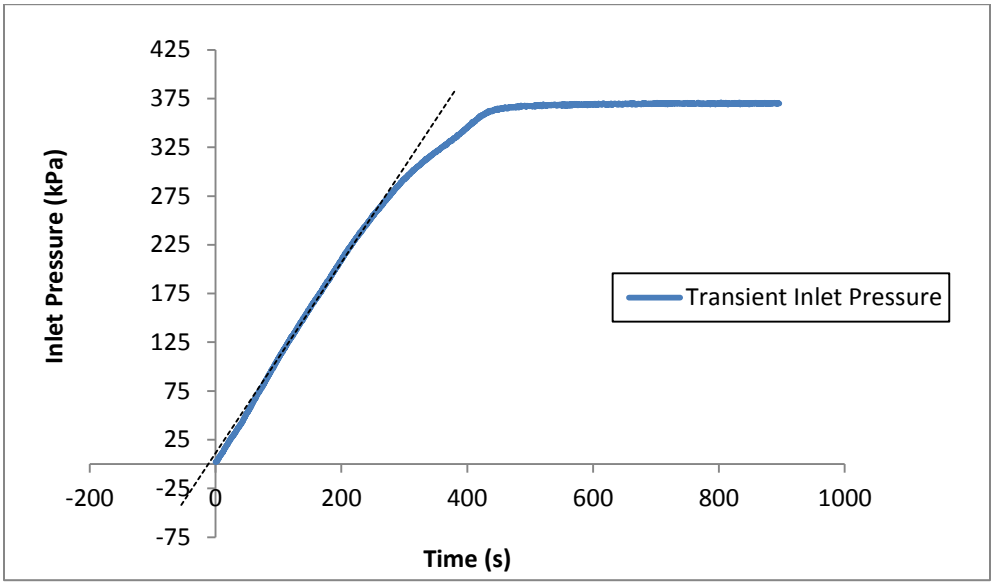

Figure 5.16: Sample Inlet Pressure vs. Time for Constant Flow Rate IM7-4HS Injection

As explained in the Methods section, the linear portion of the constant flow rate curve is selected and extrapolated to $t = 0$ where the capillary pressure is then defined. The capillary number for the flow rate is determined from the constant flow rate prescribed and the porosity of the medium. In Figure 5.17, the measured capillary pressures verses fiber volume fraction are displayed. Note that all constant flow rate tests (made at 3 cc/min and varying porosities) produced small positive capillary pressures. Also in Figure 5.17, are the plots of the calculated capillary pressure versus fiber volume fraction using the methods of Ahn et al. [123] (Equation 66 with $F = 2$ and $F = 4$) and Verrey et al. [181] (Equation 67). A favorable agreement is seen between experimental data and Ahn et al.'s [123] theoretical fit with a shape factor between 2 and 4.

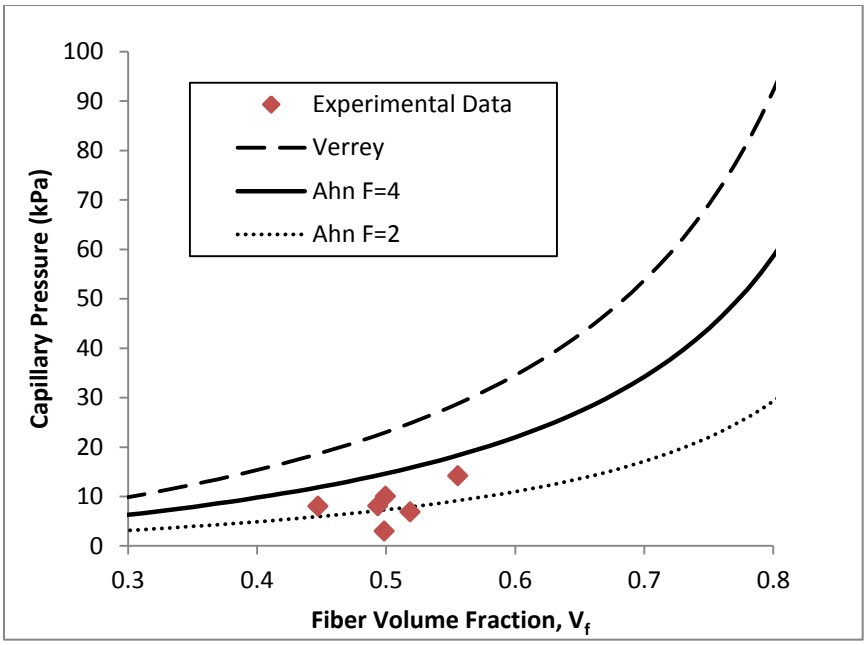

Figure 5.17: Experimental and Theoretical (Assumed Positive) Capillary Pressures by Fiber Volume Fraction

Using the constant flow rate experiments to determine the constant c_T in the Hoffman-Voinov-Tanner law, the theoretical SAE 40 oil dynamic contact angle versus capillary number can be plotted for the non-tackified IM7-4HS fabric. This is shown in Figure 5.18.

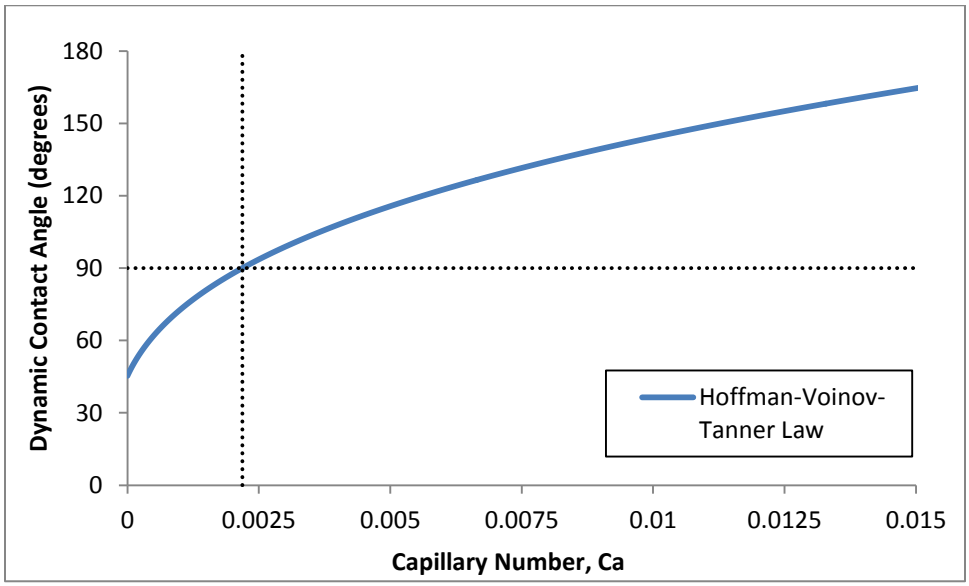

Figure 5.18: Dynamic Contact Angle vs. Capillary Number using Hoffman-Voinov-Tanner's Law

A critical capillary number of 0.0022 is found from this plot. Beneath this value, the SAE 40 oil contact angle is less than 90 degrees and capillary effects are seen to enhance flow, while above this value, the flow becomes forced and the oil behaves as a non-wetting fluid. Verrey et al. [181] saw similar results with their epoxy, as they found a critical capillary number of 0.014, where the epoxy changed from wetting to non-wetting. The critical value of 0.0022 found from the constant flow rate experiments, although small, compares well with the constant-pressure-produced capillary pressure data, in which low capillary numbers (seen in Figure 5.14), were found to a produce positive capillary pressures. The capillary numbers for all SAE 40 constant pressure infusions were averaged over the flow distance to produce a value of 0.005. Using this average capillary number and the constant flow rate data, the experimental capillary pressure drop versus capillary number can be displayed and compared to the theoretical values. This comparison is made in Figure 5.19.

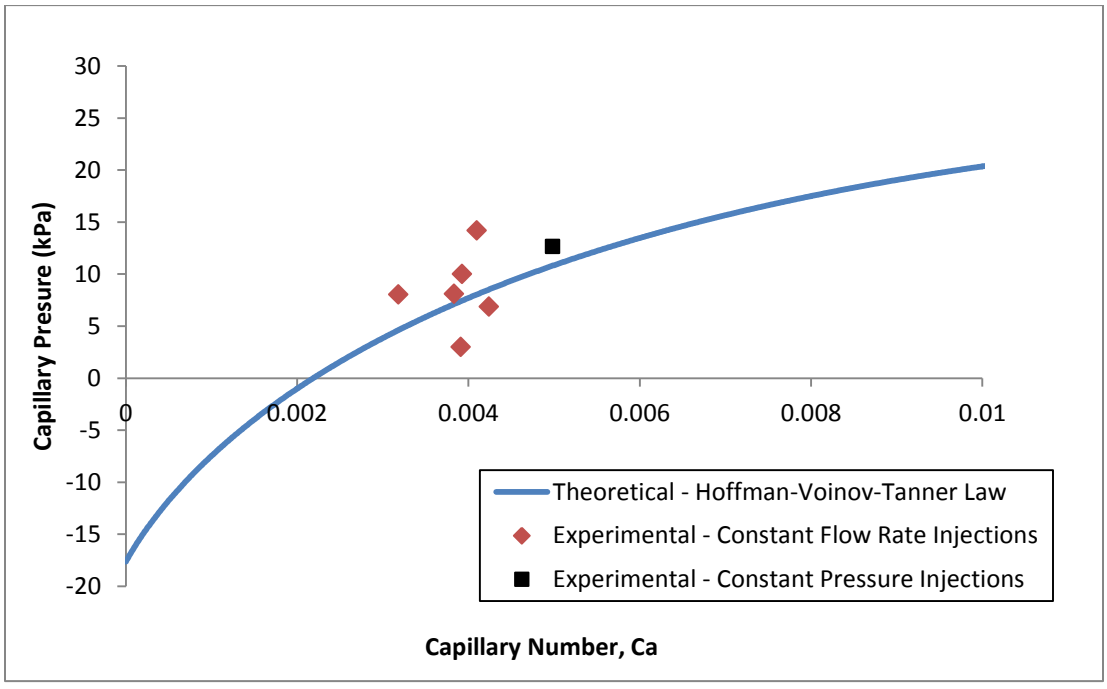

Figure 5.19: Theoretical and Experimental Capillary Pressures vs. Capillary Number for IM7-4HS with SAE 40 Oil

The experimental data produces a favorable fit with the theoretical formulation. It can also be seen here that capillary numbers lower than the critical 0.0022 value produce negative capillary pressures, while the numbers higher than the threshold produce positive values. Hence, flow is enhanced beneath the critical capillary number and resisted above it. This will then inevitably alter the preform permeability, and permeability could be expressed a function of capillary number (which is a function of fluid velocity). The magnitude of capillary the effect then comes into consideration, as the experimentally determined capillary pressures are generally seen to be small compared to normal LCM injection pressures. The significance of this capillary effect in terms of preform permeability is explored next.

5.2.2.2 Permeability Correction for Capillary Effects

This study compares four different methods for correcting permeability for capillary pressure. These methods include: 1) a dynamic correction described earlier using the Hoffman-Voinov-Tanner law paired with constant flow rate experiments, 2) a constant capillary pressure correction derived from constant pressure injection experiments, 3) a theoretical capillary pressure correction described by Ahn et al. [123], and 4) neglecting capillary effects altogether (i.e. no correction). The dynamic correction method from the Hoffman-Voinov-Tanner law was only produced for the SAE 40 oil infusions with non-tackified preforms, and is not used for the SC-15 Part A tests. A comparison of the four correction methods and capillary values is shown in Table 5.10 for the SAE 40 oil experiments for both tackified and non-tackified preforms.

Table 5.10: Capillary Pressure Correction Method Comparison for SAE 40 Oil and IM7-4HS

Method	Hoffman-Voinov-Tanner	Constant Pressure Injections Experiments	Ahn's Theoretical Formulation, F=4	Ahn's Theoretical Formulation, F=2	Neglecting Capillary Effects
Correction Value Type	Dynamic	Constant	Constant	Constant	Constant
P_c (kPa) for Non-tackified Preforms	Function of Ca	12.64	-17.64	-8.82	0
P_c (kPa) for Tackified Preforms	N/A	-7.12	-17.64	-8.82	0

Due to the variable capillary number in the constant pressure infusions, the Hoffman-Voinov-Tanner method gives a dynamic range of capillary pressures during the infusion. This is difficult to consider without employing numerical models in terms of permeability correction. In this study, the capillary number over the entire infusion length was averaged so a simple correction could be applied based on the injection pressure. The average capillary numbers and resulting capillary pressures from the Hoffman-Voinov-Tanner fit can be seen in Table 5.11 for all nine SAE 40 oil infusions with the non-tackified preforms.

Table 5.11: Average Capillary Numbers and Pressure from the Hoffman-Voinov-Tanner Correction for non-tackified IM7-4HS and SAE 40 Oil

Target Injection Pressure (kPa)	Run #	Actual Injection Pressure (kPa)	Average Ca Over Length (-)	P_c from Hoffman-Voinov-Tanner Fit (kPa)
69	1	67.2	0.00134	-5.0
	2	66.9	0.00142	-4.6
	3	68.0	0.00173	-2.6
138	1	141.1	0.00295	3.6
	2	141.3	0.00406	7.9
	3	141.3	0.00436	8.9
276	1	280.0	0.00869	18.6
	2	284.9	0.00835	18.1
	3	278.2	0.01196	22.3

For the 69 kPa (10 psi) injection pressure range, the resulting capillary pressures were negative, while at the 138 and 276 kPa (20 and 40 psi) ranges the capillary pressures were positive and increasing in magnitude, respectively. Figure 5.20 shows a comparison of the capillary correction methods and their effect on the unsaturated permeability of non-tackified IM7-4HS with SAE 40 oil.

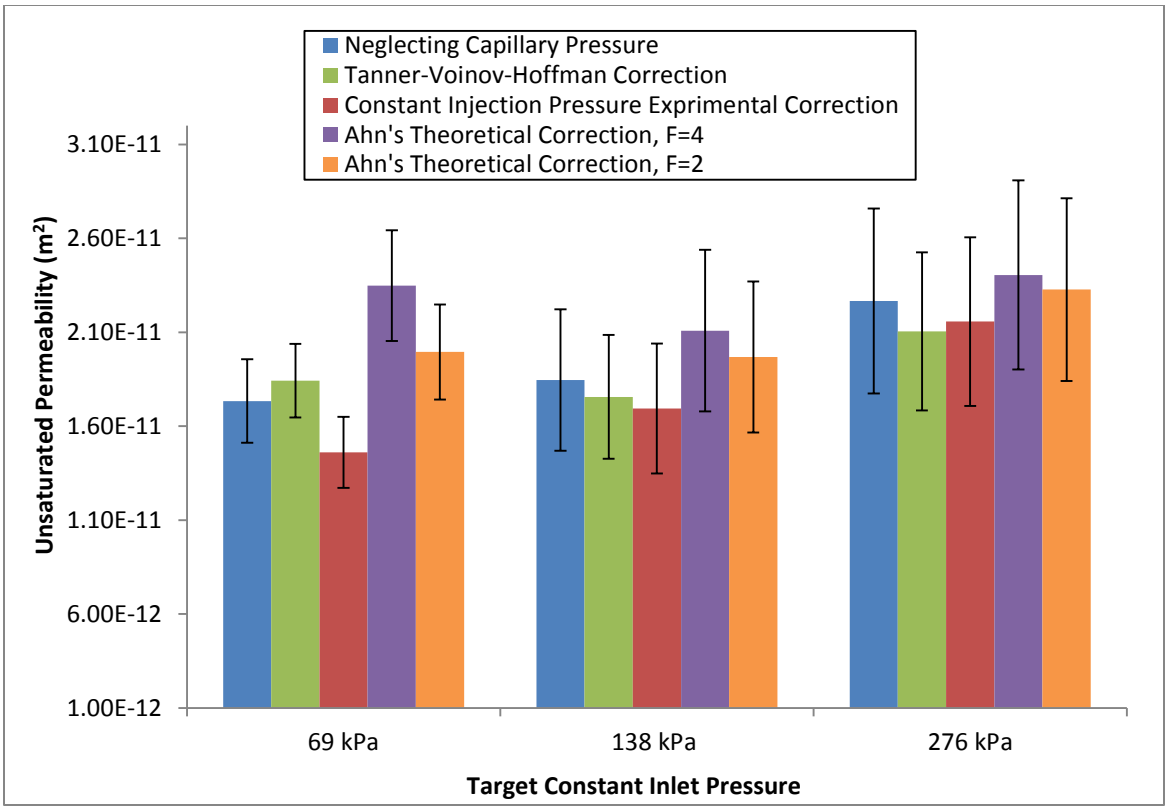

Figure 5.20: Capillary Correction Comparison for Non-tackified IM7-4HS with SAE 40 Oil

For the majority of capillary corrections made with the SAE 40 oil, the difference in permeability was not substantial compared to the experimental scatter. At the 69 kPa injection range, however, significant difference is seen when comparing Ahn's theoretical model to the other methods. This is due to the fact that this theoretical formulation assumes close-to-equilibrium capillary numbers, and thus large negative capillary pressures. Also, the 69 kPa injection range, the capillary correction from the constant pressure experiments is seen to give a permeability value 20% less than the Hoffman-Voinov-Tanner method, and about 16% less than the value from neglecting capillary effects. This constant pressure injection capillary correction, was also employed by Amico and Lekakou [124], and led the researchers to conclude that capillary effects are significant at low injection pressures. Interestingly, in this study, similar results may be concluded using the same correction method, although the dynamic correction from the

Hoffman-Voinov-Tanner method showed no significant difference from neglecting capillary effects at all injection pressures. It is assumed here that the Hoffman-Voinov-Tanner correction is more accurate than the constant pressure injection value as it accounts more robustly for changes in capillary number. Thus, this constant pressure method to determine capillary pressure may lead to inaccurate conclusions in terms of permeability correction. Verrey et al. [181] also noted that the constant pressure method should not be used to correct for capillary effects as the velocity in these experiments changes strongly throughout testing. Regardless of sign on the capillary pressure term, these effects are seen to become negligible as injection pressure increases. This is because the capillary pressure drop accounts for less of the total pressure drop used to determine permeability as injection pressure increases. The permeability comparison with capillary correction methods for the tackified IM7-4HS tested with SAE 40 oil is shown in Figure 5.21.

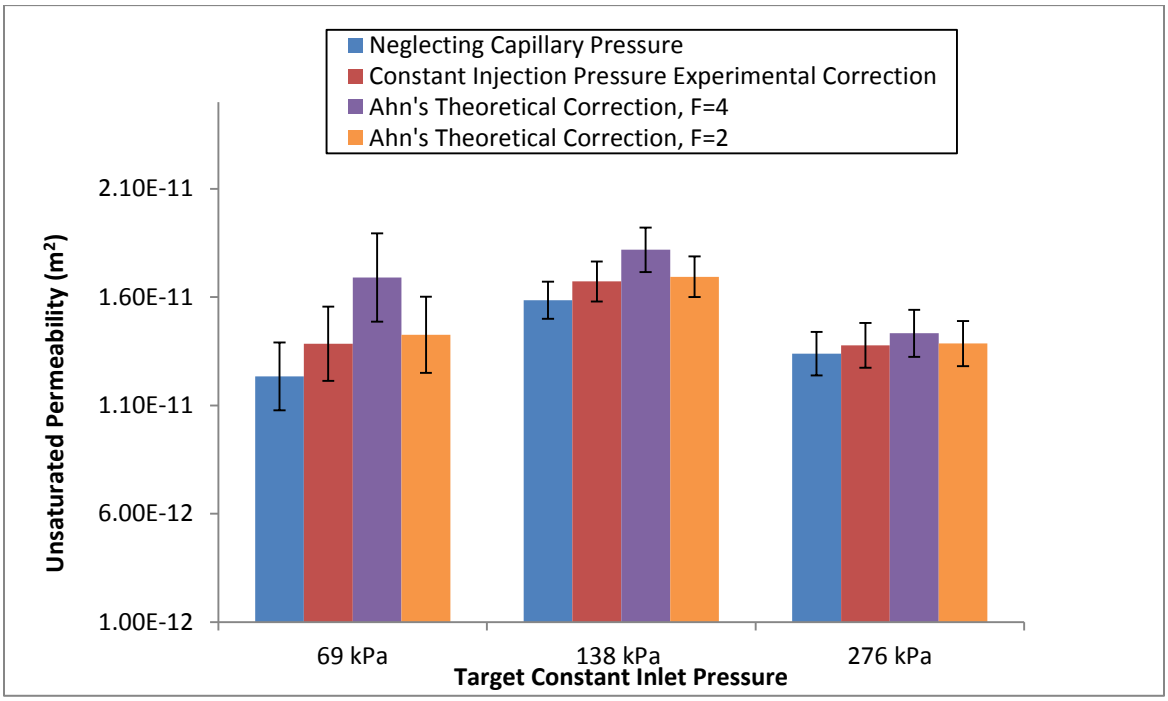

Figure 5.21: Capillary Correction Comparison for Tackified IM7-4HS with SAE 40 Oil

Note that the Hoffman-Voinov-Tanner dynamic correction model was not produced for the tackified samples. Compared to the non-tackified data, the tackified unsaturated permeability measurements produced less experimental scatter. This is because the presence of tackifier holds fiber and tow orientation stable throughout sample preparation, while the non-tackified preforms were more likely to be subject to tow loss and preform deformation. At the 69 kPa target injection pressure range, the permeability was much more sensitive to the correction method than at the higher injection pressures. This again points to the importance of capillary pressure at low injection pressures, while the higher pressures showed no statistical difference in permeability was observed.

Overall from the IM7-4HS testing with the oil, it can be concluded that the capillary correction method from the Hoffman-Voinov-Tanner law described in this study is the most robust method presented. While being hypothesized as the most accurate, this method still did not show any significant difference from neglecting capillary effects altogether in the unsaturated permeability calculation at any injection pressure tested. A comparison of the capillary correction methods and their values for the SC-15 infusions in preforms with and without tackifier are shown in Table 5.12.

Table 5.12: Capillary Pressure Correction Method Comparison for SC-15 Part A and IM7-4HS

Method	Hoffman-Voinov-Tanner	Constant Pressure Injections Experiments	Ahn's Theoretical Formulation, F=4	Ahn's Theoretical Formulation, F=2	Neglecting Capillary Effects
Correction Value Type	Dynamic	Constant	Constant	Constant	Constant
P_c (kPa) for Non-tackified Preforms	N/A	16.23	22.13	11.06	0
P_c (kPa) for Tackified Preforms	N/A	-0.21	22.13	11.06	0

Again, note that the Hoffman-Voinov-Tanner correction for capillary pressure is not shown here, as it was not determined for the SC-15. In Figure 5.22, the capillary correction permeability comparison for the non-tackified IM7-4HS tests with SC-15 Part A is shown.

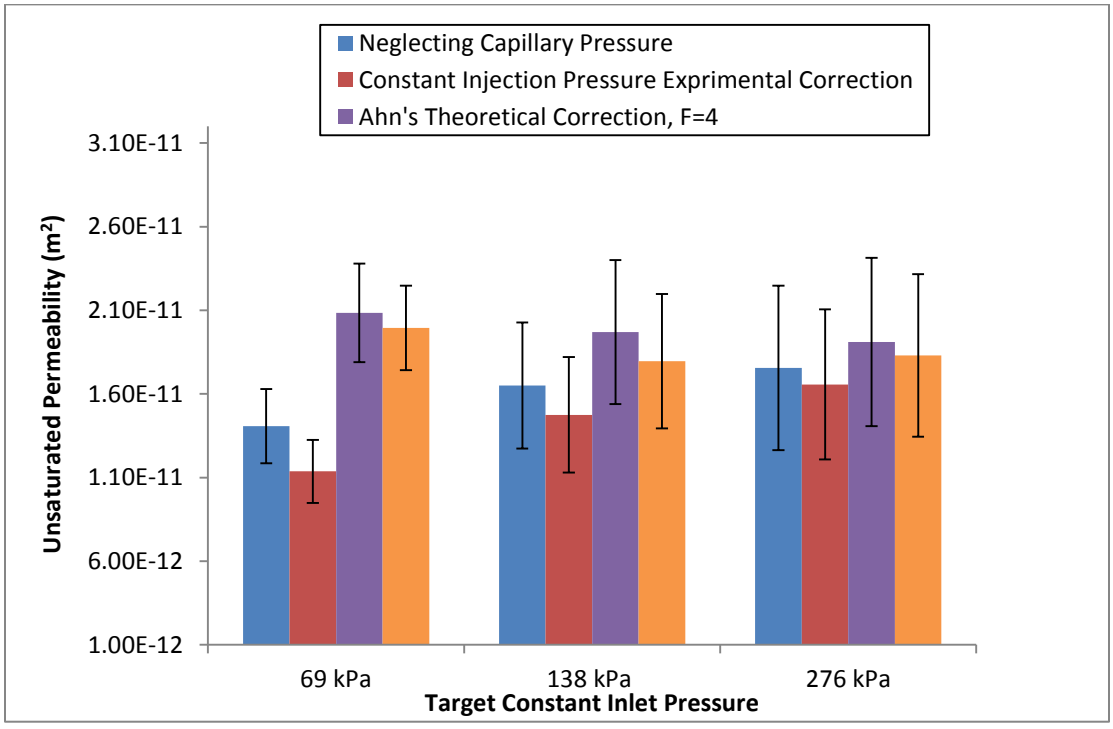

Figure 5.22: Capillary Correction Comparison for Non-tackified IM7-4HS with SC-15 Part A

Here, large variations in permeability are seen between the analytical expressions for capillary correction and experimental methods. Although, the dynamic correction for capillary pressure based on capillary number is not used, from the SAE 40 oil results, it may be assumed that they will offer similar trends in the SC-15 tests. Therefore, further comparisons between SAE oil and SC-15 unsaturated permeabilities will be made while neglecting capillary pressure. Again, as injection pressure increases, the differences between capillary correction methods become negligible. At the 138 and 276 kPa injection ranges, no significant differences outside of experimental scatter in permeability may be seen among the correction methods. The unsaturated permeability comparison for the tackified IM7-4HS tests with SC-15 Part A is shown in Figure 5.23.

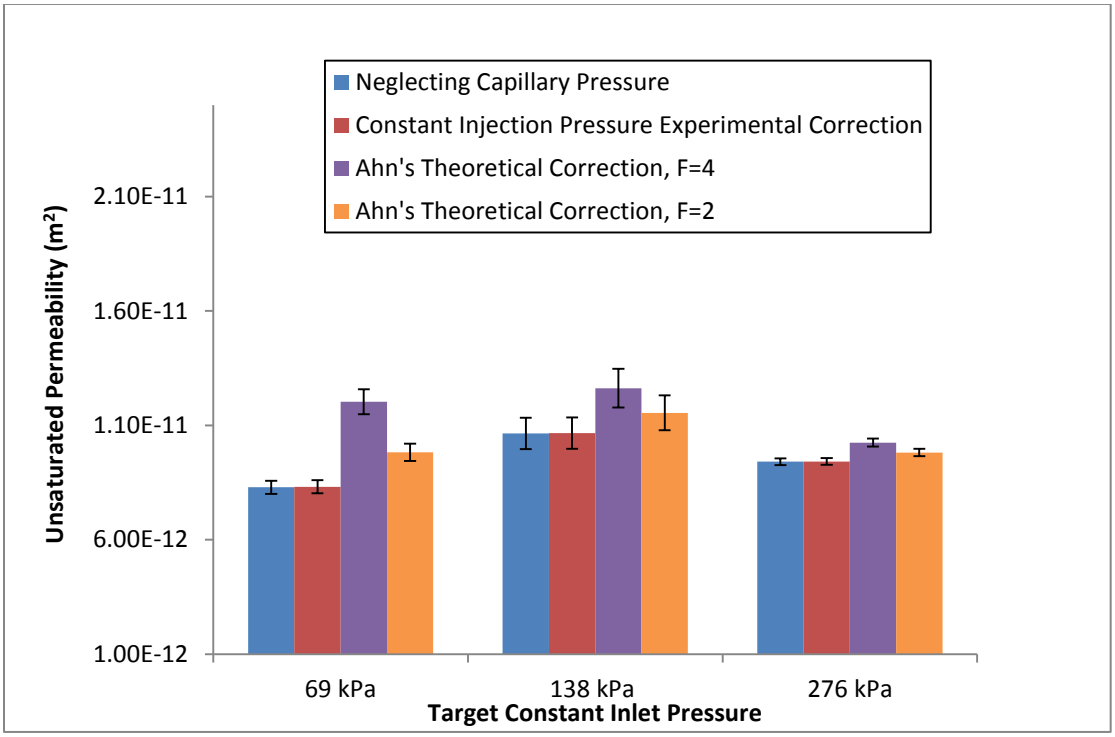

Figure 5.23: Capillary Correction Comparison for Tackified IM7-4HS with SC-15 Part A

Large variations in the permeability correction again are seen at the lowest injection pressure. As the injection pressure increases, the difference between correction methods is seen to diminish drastically. The tackifier again shows aid in reducing test-to-test scatter.

For both test fluids employed, it can be concluded that large variations between permeability are seen only at the lowest injection pressure range (69 kPa) depending on the capillary correction method chosen. It can then be concluded that capillary pressures may only be significant for these IM7-4HS preforms when injections are made at 69 kPa or less. The permeability determined using the dynamic method for capillary correction has been shown to be very close to the permeability determined by neglecting capillary pressure. Also, depending on the injection pressure used, infiltrating flow may result in forced or wicking flow as capillary pressure is a function of capillary number.

5.2.2.3 Fluid Type Effects

A comparison of unsaturated permeability with fluid type is shown in Figure 5.24 for the non-tackified. Capillary pressure effects are neglected in this comparison. The data from Figure 5.24 are tabulated following in Table 5.13.

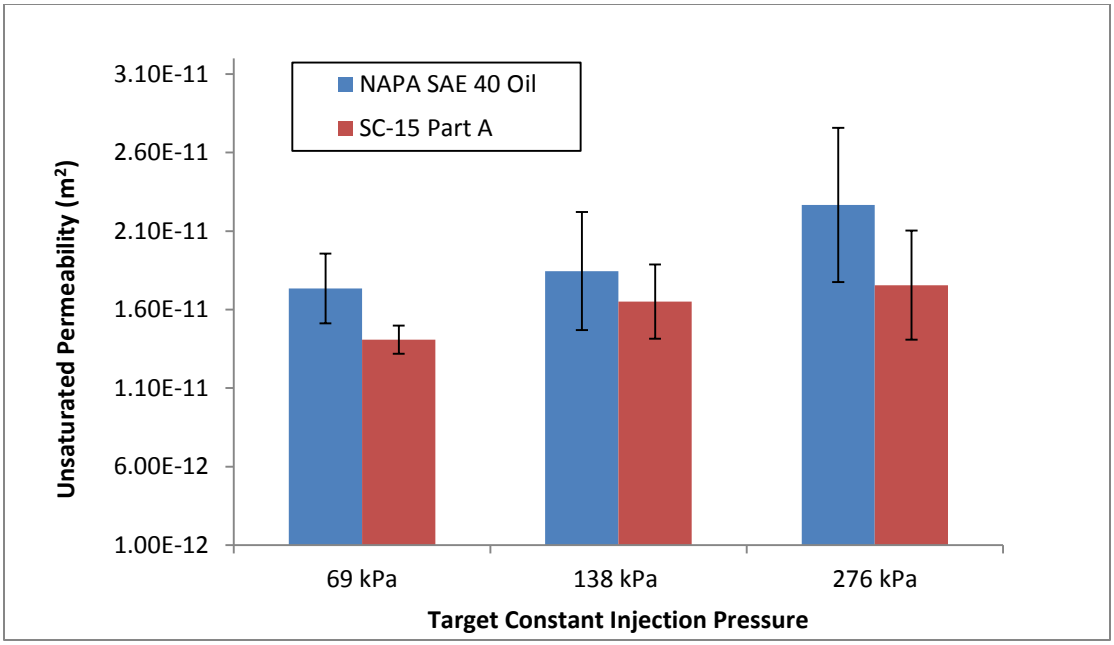

Figure 5.24: Unsaturated Permeability of Non-tackified IM7-4HS by Test Fluid

Table 5.13: Non-tackified IM7-4HS Unsaturated Permeability by Target Constant Inlet Pressure

Sxx Permeability by Test Fluid and Target Inlet Pressure (m^2)						
Run #	**69 kPa**		**138 kPa**		**276 kPa**	
	SAE 40 Oil	SC-15 Part A	SAE 40 Oil	SC-15 Part A	SAE 40 Oil	SC-15 Part A
Run 1	1.56E-11	1.31E-11	1.42E-11	1.39E-11	2.04E-11	1.39E-11
Run 2	1.66E-11	1.48E-11	2.00E-11	1.86E-11	1.93E-11	2.08E-11
Run 3	1.98E-11	1.43E-11	2.12E-11	1.70E-11	2.83E-11	1.79E-11
Avg.	**1.73E-11**	**1.41E-11**	**1.85E-11**	**1.65E-11**	**2.27E-11**	**1.76E-11**
StDev	2.22E-12	8.95E-13	3.77E-12	2.37E-12	4.92E-12	3.47E-12
CV (%)	12.8	6.4	20.4	14.3	21.7	19.8

The fluid type comparison for the tackified IM7-4HS unsaturated permeability measurements is shown in Figure 5.25, and following in Table 5.14 are the numerical data of this plot.

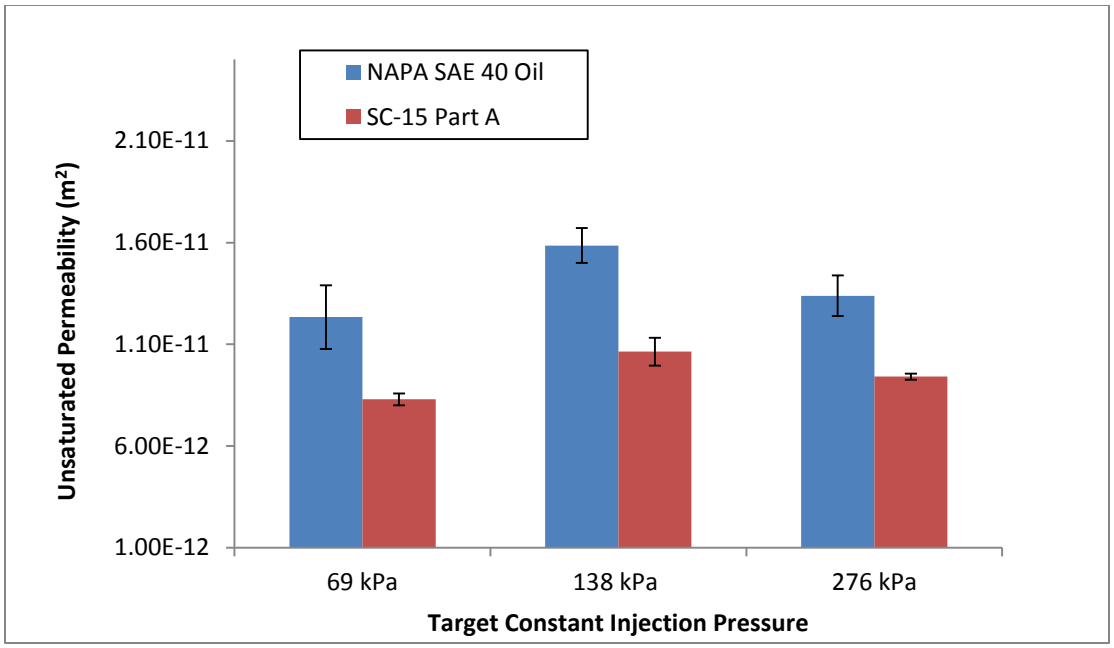

Figure 5.25: Unsaturated Permeability of Tackified IM7-4HS by Test Fluid

Table 5.14: Tackified IM7-4HS Unsaturated Permeability by Target Constant Inlet Pressure

Sxx Permeability by Test Fluid and Target Inlet Pressure (m^2)						
Run #	**69 kPa**		**138 kPa**		**276 kPa**	
	SAE 40 Oil	SC-15 Part A	SAE 40 Oil	SC-15 Part A	SAE 40 Oil	SC-15 Part A
Run 1	1.06E-11	8.62E-12	1.66E-11	1.02E-11	1.35E-11	9.25E-12
Run 2	1.27E-11	8.11E-12	1.49E-11	1.14E-11	1.43E-11	9.54E-12
Run 3	1.37E-11	8.15E-12	1.61E-11	1.03E-11	1.23E-11	9.45E-12
Avg	**1.23E-11**	**8.29E-12**	**1.59E-11**	**1.06E-11**	**1.34E-11**	**9.41E-12**
StDev	1.56E-12	2.87E-13	8.56E-13	6.86E-13	1.00E-12	1.48E-13
CV (%)	12.6	3.5	5.4	6.4	7.5	1.6

In a basic comparison of permeability versus fluid type, the average unsaturated permeability measured with SC-15 Part A produce lower values than that of the SAE 40 oil. Interestingly, the non-tackified preform comparison showed little to no statistically significant difference in permeability between the fluid types. It is likely that the chemical makeup of the inter-layer

tackifier alters the wettability between the resin and the IM7 fibers. It may also be possible that the tackifier causes more intra-tow flow and therefore the influence of capillary effects are magnified compared to the non-tackified samples. Capillary effects have been noted by researchers to produce significant difference in permeability among fluid types [117]. Other reasoning could be that with the addition of tackifier, the test-by-test variation significantly reduced, so that less change in permeability is needed to produce statistically significant differences. This allows the possibilities of other test inconsistencies (e.g. user variations, small ambient temperature changes, etc.) to have larger influence on test outcome.

Researchers including Hammond et al. [43], [133] and Luo et al. [116] have concluded that different test fluids had little effect on measured permeability. Although, it should be noted that Hammond's [43], [133] studies directly compared measurements of saturated permeability with different fluids and did not directly compare unsaturated measurements of varying fluids. This is important to note as saturated permeability experiments involve single phase flow, while unsaturated scenarios inherently involve a multi-phase flow. From these current results it can be concluded that unsaturated non-tackified IM7-4HS permeability does not depend on test fluid when the injection pressure is high enough for capillary effects to be neglected, while tackified IM7-4HS permeability is sensitive to the test fluid employed. With this in consideration, future preform permeability characterization should be conducted with the resin that will be employed during actual manufacturing. Also, at low injection pressure or flow rates, capillary effects may cause significant differences in permeability depending on the test fluid. At the high pressures/flow rates (often seen in RTM processing), viscous forces dominate and permeability

should scale with the viscosity of the fluid. At low pressures, permeability may be affected by both fluid viscosity and surface tension (capillary pressure) effects.

5.2.2.4 Injection Pressure Effects

A plot of unsaturated permeability (neglecting capillary pressure) versus injection pressures is displayed in Figure 5.26 for the non-tackified IM7-4HS constant pressure injection experiments. The actual injection pressure was measured by the fixture in-line pressure transducer and averaged over the infusion time. A linear regression curve was also fit to the data for both fluids. The same plot for the tackified material is presented in Figure 5.27.

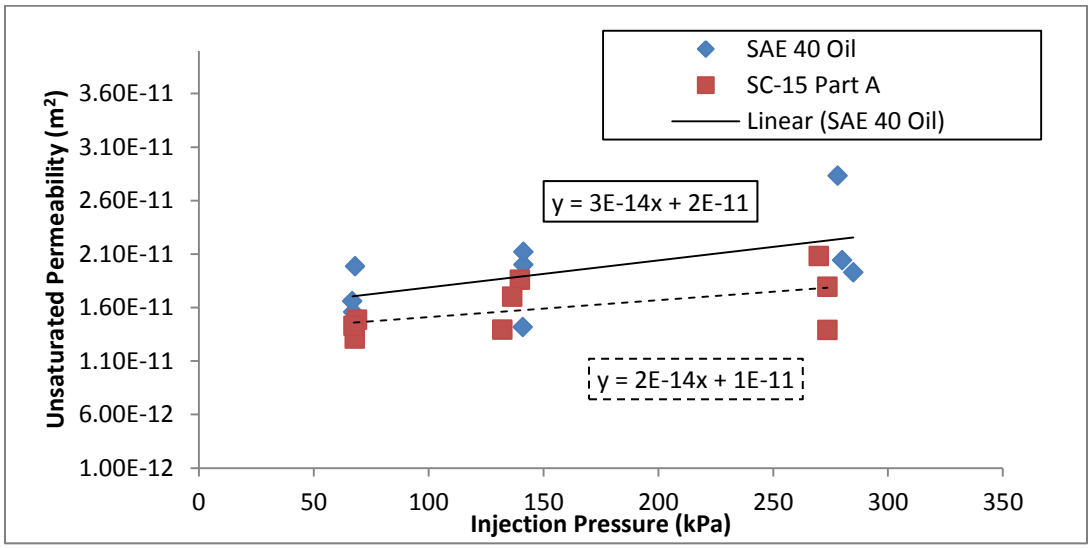

Figure 5.26: Unsaturated Permeability of Non-tackified IM7-4HS versus Injection Pressure

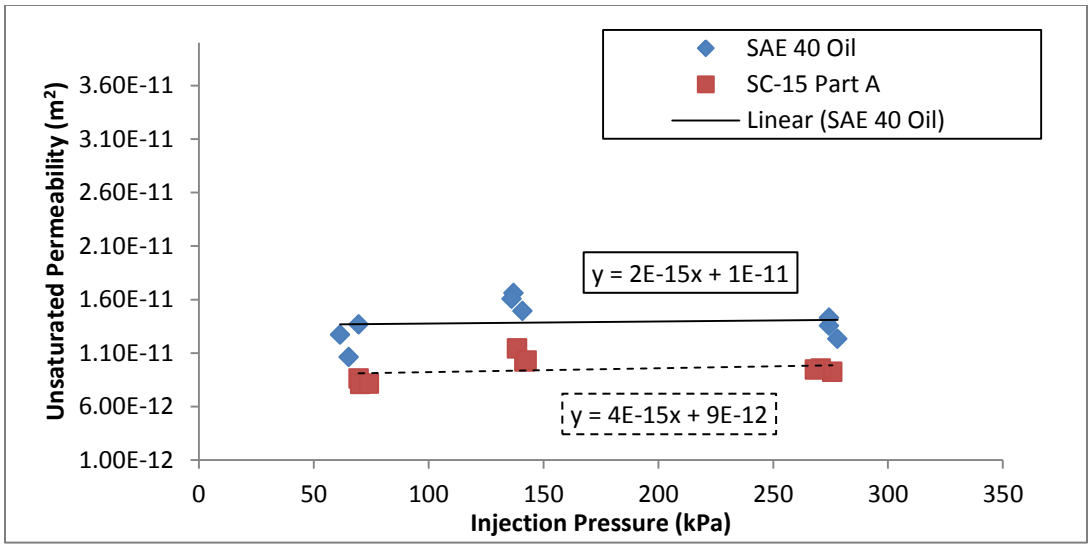

Figure 5.27: Unsaturated Permeability of Tackified IM7-4HS versus Injection Pressure

It is evident that there is a slight increase in permeability as injection pressure increases for the non-tackified preforms, although with considerable data scatter. This relationship was also seen by Shojaei et al. [65], albeit in small magnitude. The tackified IM7-4HS permeability showed no dependence on injection pressure.

In Figure 5.28, the unsaturated permeability (neglecting capillary pressure) is plotted against the average infusion capillary number for the non-tackified IM7-4HS constant pressure injections. In this graph, the 3 runs for each target inlet pressure (69, 138, and 276 kPa) for both oil and resin are fit separately to linear regression curves. The blue data points represent SAE 40 oil infusion results, while the red data points represent SC-15 Part A infusion data. The solid-line linear regression curves relate to the oil fits, while the dashed regression curve lines correspond to the SC-15 Part A. The regression equations and R^2 values are also displayed on the graph. Following in Figure 5.29, the same relationship is plotted for the tackified IM7-4HS measurements. Due to the capillary number's dependence on flow front location for the constant pressure injections, an

average capillary number was determined over the preform length before being plotted against the corresponding permeability.

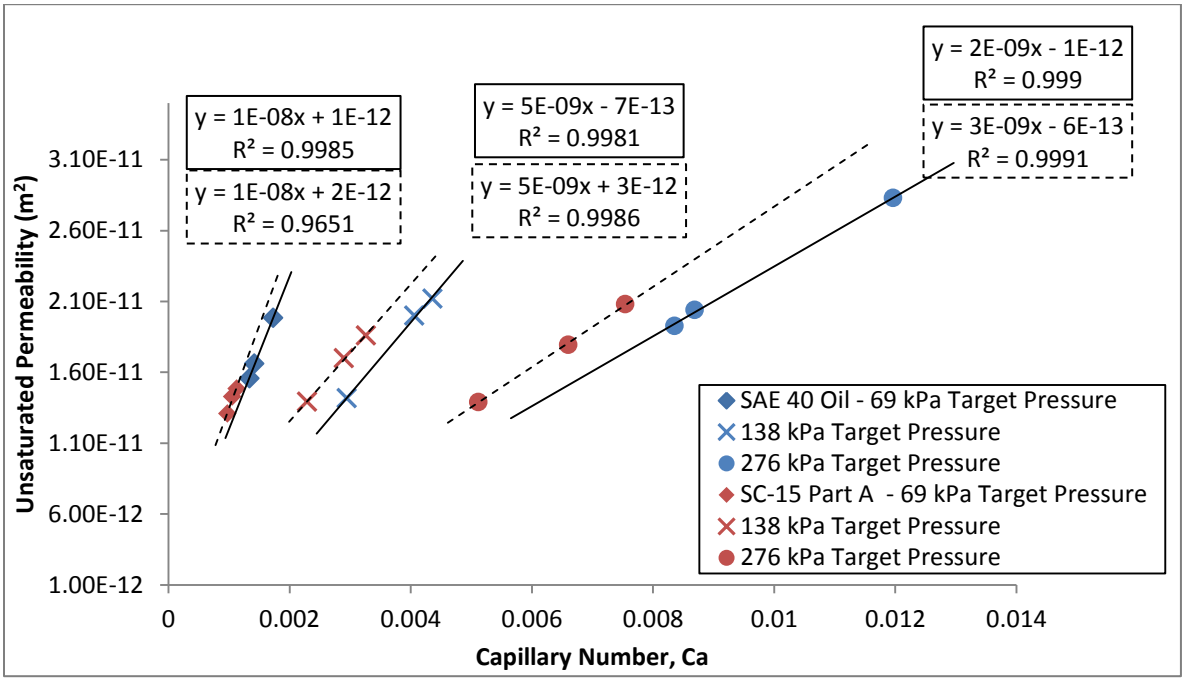

Figure 5.28: Unsaturated Permeability of Non-tackified IM7-4HS versus Capillary Number

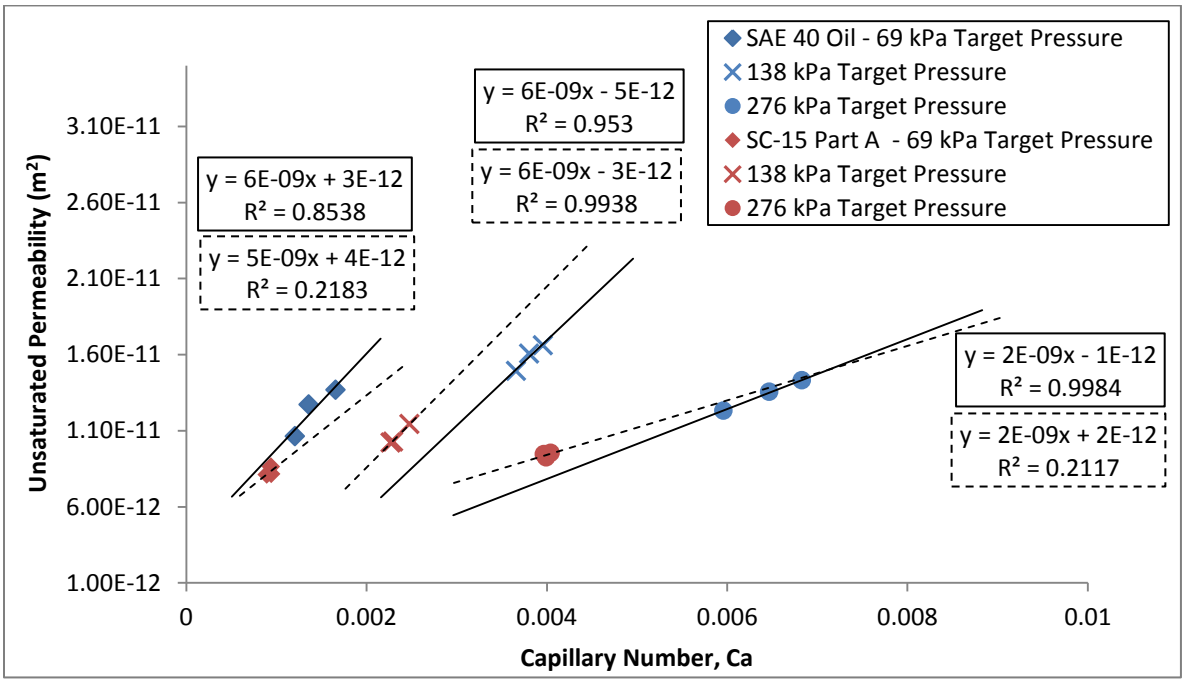

Figure 5.29: Unsaturated Permeability of Tackified IM7-4HS versus Capillary Number

Within each injection pressure range, the permeability increases with capillary number for both fluids in preforms with and without tackifier. The majority of these linear regression curves show a high value of fit. Also, the oil and resin regression curves for each corresponding target injection pressure range are similar in slope, which alludes to the fact that this behavior is likely characteristic to the fabric architecture, not the fluid. Interestingly, no clear trend in permeability versus capillary number can be seen across all injection pressure ranges, which corroborates with the findings of Figure 5.26 and Figure 5.27. Hammond et al. [43], [133] found permeability to be independent of capillary number, while Young et al. [142] saw large increases in permeability with fluid velocity for random fiber and bidirectional fiber mats. Although the velocities used were high at 1 to 11 cm/s. In a study by Shojaei et al. [65], a critical velocity of only 0.2 cm/s was calculated for the glass fabric used. Velocities over this were hypothesized to produce permeability values that increased with increasing flow rate, which is induced by increasing pressure. Being that within each injection pressure range, an increase in permeability over capillary number was seen, it is possible that this may be due to the fluid passing a critical velocity barrier similar to that reported by Shojaei et al. [65].

5.2.2.5 Tackifier Effects

A comparison of unsaturated IM7-4HS permeability measurements with and without the inter-layer tackifier is shown in Figure 5.30. This is shown with both test fluids, while capillary pressure is neglected in the permeability formulations.

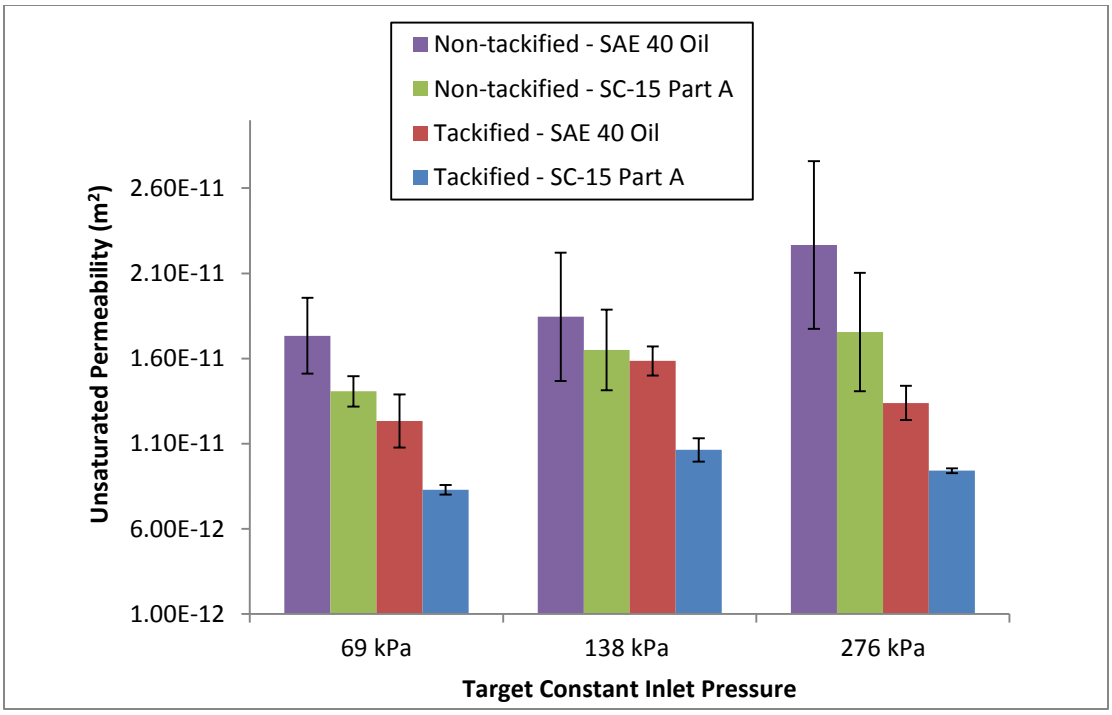

Figure 5.30: Tackifier Effects on Unsaturated Permeability

On average, the tackified samples produced permeability that was 34% less than their non-tackified counterparts. This is attributed to the tackifier blocking the inter-tow flow channels and forcing more flow through low porosity, intra-tow regions. The tackifier also appears to be more sensitive to fluid type, which is likely due to a change in the surface chemistry, and ultimately an alteration of reinforcement wettability.

5.2.2.6 Saturation Effects

Finally, a comparison between unsaturated and saturated permeabilities of the warp aligned IM7-4HS preforms at different target injection pressures is made. This comparison includes saturated permeability values from SAE 40 oil experiments, and unsaturated permeability from both the SAE 40 oil and SC-15 Part A constant pressure infusions (neglecting capillary effects). This comparison for the non-tackified preforms is shown in Figure 5.31, and the permeability

comparison for the tackified material is shown in Figure 5.32. The saturated values were presented in Chapter 4 and were obtained from the power law fit at the 54.6% fiber volume fraction of the unsaturated experiments.

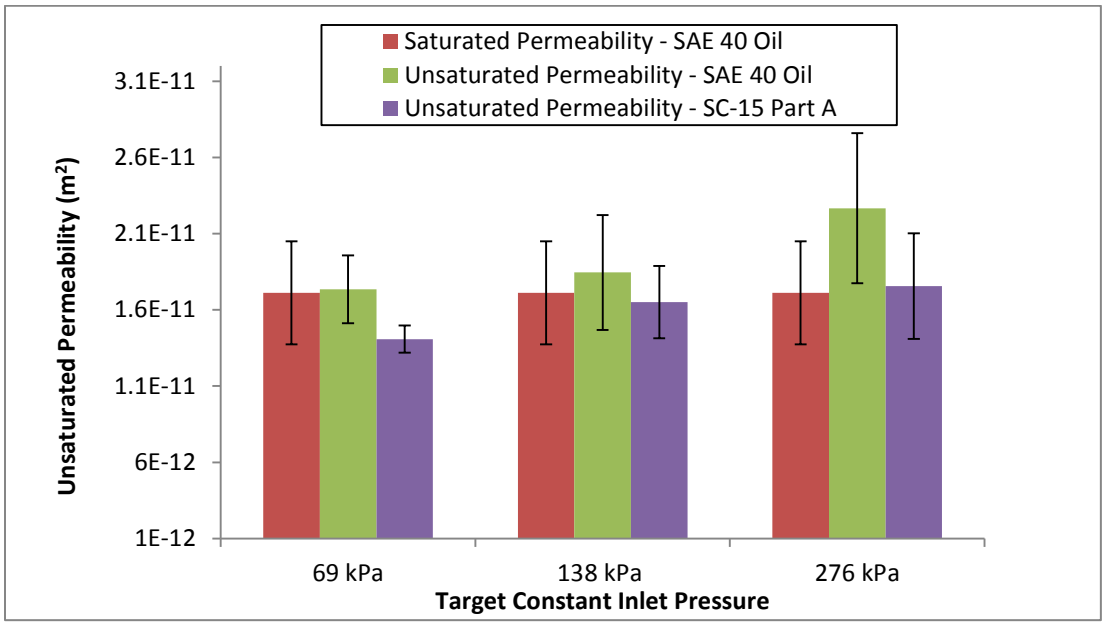

Figure 5.31: Saturated vs. Unsaturated S_{xx} Permeability for Warp-Aligned Non-tackified IM7-4HS at 54.6% V_f

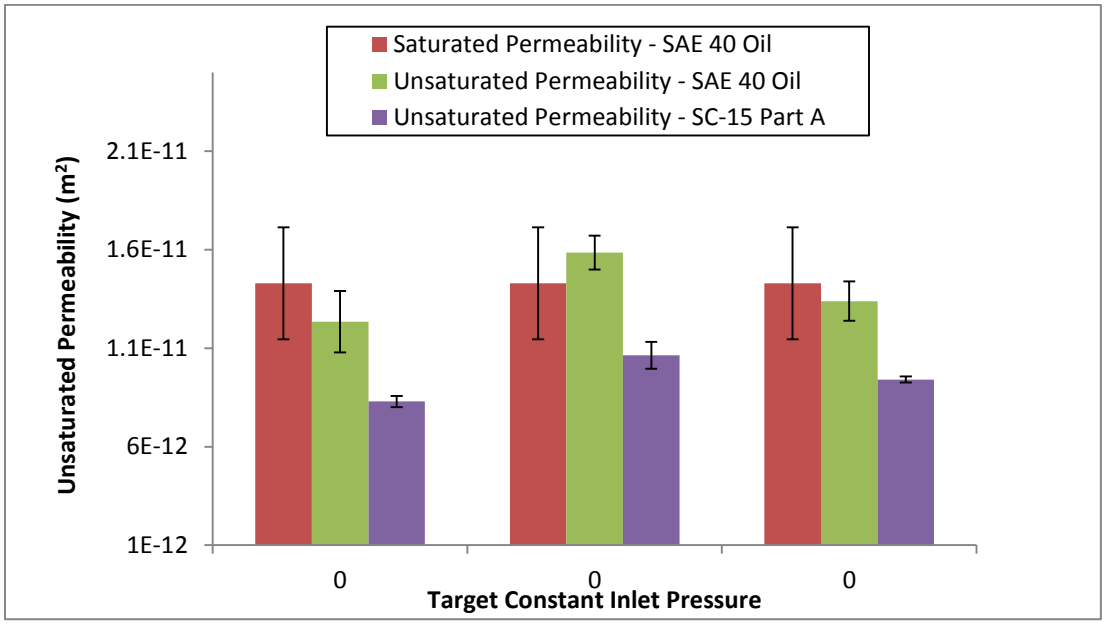

Figure 5.32: Saturated vs. Unsaturated S_{xx} Permeability for Warp-Aligned Tackified IM7-4HS at 54.6% V_f

Permeabilities of saturated and unsaturated measurements are well within experimental scatter of each other for the all the non-tackified measurements. For the tackified material, both the saturated and unsaturated permeabilities measured using a SAE 40 oil were also well within experimental scatter of each other for all injection pressure ranges. Interestingly, the unsaturated permeability of the tackified IM7-4HS measured with SC-15 Part A tested significantly lower than the saturated and unsaturated cases measured with oil. As discussed earlier, it is likely that the addition of the tackifier significantly alters the wetting behavior between the oil and resin. It is then concluded that for the non-tackified IM7-4HS, fluid type does not affect permeability, while the addition of tackifier creates significant difference in permeability depending on the fluid type used. Other researchers have found the difference between saturated and unsaturated permeability to be negligible depending on the preform type [43], [133]. This could be due to the fact that certain fabric architectures may mitigate the role of the dual scale porosity, which has been stated to have larger effects when uninterrupted flow channels are present in the reinforcement [130]. The dual scale porosity is a function of saturation, while capillary effects can cause differences in flow front evolution [138]. By comparing saturated and advancing front permeability measurements directly, one is essentially neglecting saturation effects. If this simplification can be justified, material characterization can become more efficient as saturated flow tests, which can deliver more data per sample, can be used. For this study, saturated measurements made in a separate test fixture have produced values within scatter of the advancing front tests at a single volume fraction (the environment more native to actual LCM infusions) for the non-tackified IM7-4HS. Extending this relationship to other fiber volume fractions is not completed in this thesis due to material constraints, but the assumption is reasonable. On the contrary, the tackified IM7-4HS saturated versus unsaturated permeability

results show significant difference. It is hypothesized that the addition of tackifier may encourage more intra-tow flow and capillary effects due to the inter-tow channel blockages. Also, the addition of tackifier may result in enough flow channel geometry change to create a more severe dual-scale porosity compared to the non-tackified architecture, resulting in the significant unsaturated versus saturated permeability difference.

5.3 Conclusions

Fluid surface tension and IM7 fiber contact angle measurements were performed with SAE 40 motor oil and SC-15 Part A epoxy resin. The epoxy was found to be a better wetting fluid with the IM7 fiber. Then, constant pressure unsaturated permeability experiments were conducted to investigate fluid effects on the permeability of IM7-4HS preforms. Capillary pressures were calculated with theoretical models and experimental measurements and used in calculation of unsaturated permeability. The theoretical expression for capillary pressure was found to affect the unsaturated permeability calculations at low injection pressures. The theoretical formulation was determined to be a poor representation of capillary effects, as it was based on idealized fiber packing arrangements and close-to-equilibrium fiber contact angle values. A constant injection pressure experimental technique was used to determine capillary pressure and produced positive capillary pressures, inferring non-wetting behavior during infusion for the non-tackified preforms. The tackified preforms, on the contrary, produced negative capillary pressures. It was hypothesized that the presence of inter-layer tackifier forces more flow through the intra-tow capillaries, and encourages wicking flow. Further, constant flow rate experiments were run to determine capillary pressure over a range of capillary numbers. Positive capillary pressures were also found here for the non-tackified preforms. Starting with the formulation proposed by Verrey

et al. [181] and the constant flow rate data, a dynamic capillary correction method was employed based on average infusion capillary number. The resulting capillary pressures showed little effect on the unsaturated permeability calculation. Significant differences between the SAE 40 motor oil and the SC-15 Part A epoxy were only seen at low injection pressures (<69 kPa) for the non-tackified preforms, while the tackified fabric showed significant differences in permeability depending on the test fluid. It was concluded that the resin used in manufacturing should be also be used in preform characterization. Unsaturated permeability data were also compared with saturated permeability data and the values were within experimental scatter of each other for the non-tackified fabric. The tackified fabric, however, showed difference between saturated permeability and unsaturated permeability measured with differing test fluid. This provides that accurate characterization for LCM mold fill models can be produced from saturated permeability measurements for the non-tackified four-harness satin fabric, while tackified fabric should be characterized in unsaturated infusions with the resin that is used in manufacturing.

Although in earlier discussions, specific test parameters and effects are highlighted for their influence on preform permeability, these effects are closely tied to each other and their relationships should be noted. Preform permeability is a function of saturation. In saturated flow, a single phase of fluid propagates through the porous media that is already fully saturated with the permeant. In advancing front or unsaturated scenarios, the flow will be a multiphase where the permeating fluid displaces an existing fluid of different properties (e.g. air in most LCM systems). The difference between saturated and unsaturated flow have been shown experimentally to be significantly different dependent on the reinforcement type [139]. For preforms with a dual scale porous nature, the difference in saturated and unsaturated flow is

notable, where low permeability zones act as sinks and lag the preform saturation [99]. Multiphase flow will also involve the consideration of capillary and surface tension forces. As shown in this study and in others [116], [124], the significance of capillary effects is then dependent on the injection pressure or flow rate induced. Furthermore, if capillary numbers of an infusion are in the dynamic regime, fluid contact angle and capillary pressures may vary. Here, a critical capillary number may be determined where the fluid can be defined as transitioning from wetting to non-wetting or forced flow [181]. Additionally, Darcy's law itself is known to accurately define flow only for low flow rates [145]. Then, another critical velocity or Reynolds number may be defined where Darcy's law no longer holds and preform permeability alone may not accurately represent the flow [65]. Figure 5.33 shows these critical points on a scale of general dependency of unsaturated flows on velocity for dual scale fibrous reinforcements.

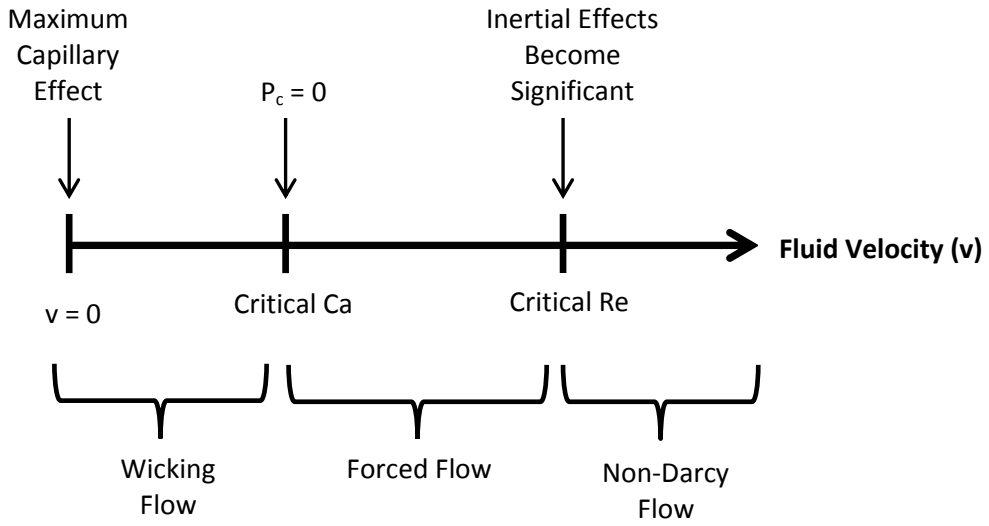

Figure 5.33: Flow Dependency on Velocity for Dual-Scale Fibrous Reinforcements

Here, the two critical points can be seen in the flow. The critical capillary number defines the point at which capillary pressure (P_c) equals zero and flow changes from wicking to forced flow.

The critical Reynolds number shows where inertial effects become significant and non-Darcy flow initiates. Note that it is possible that the region of non-Darcy flow may overlap with the regions of wicking and forced flow. The specific critical values of capillary number and Reynolds number are highly dependent on the preform geometry and makeup, as well as the infiltrating fluid properties.

6. Non-Darcy Flow

Generally in LCM, the infiltrating resin has been assumed to have low velocity and low Reynolds number, where Darcy's law can accurately describe the flow. In this creeping flow regime, viscous interactions are the dominant sources of pressure gradients, but in high velocity flows, an inertial pressure loss is produced from the acceleration and deceleration of the fluid [183]. When the relationship between pressure and flow rate is nonlinear, additional pressure loss warrants the need for amendment of Darcy's law. This additional, second order term, describes the flow driven through porous media in such regimes. To investigate the possibilities of non-Darcy flow during permeability testing, previous saturated measurements made in this study were reviewed. Also, high flow rate permeability experiments were conducted with tackified and non-tackified IM7-4HS preforms in effort to quantify any observed non-Darcy effects. In this chapter, background on non-Darcy flow will be reviewed and criteria will be selected for defining the point at which Darcy's law is no longer valid. This criterion would also be useful in a manufacturing setting where process models could alert if non-Darcy flow may result during mold fill. The method used for this will be described as well as the technique employed to investigate high flow rate effects in the saturated permeability test fixture. The applicability and results of non-Darcy flow will also be presented.

6.1 Background

Resin impregnation in LCM has long been represented by Darcy's law, where the flow rate of fluid through a porous media is linearly proportional to pressure drop across reinforcement. This is further related by the reinforcement's permeability, geometry, and the permeating fluid's viscosity. This law is an empirical relationship, which was derived while Darcy [59] observed the flow of water through beds of sand in 1856, and later was derived from homogenization from first principles. Darcy's law represents a linear relationship between pressure drop and applied flow rate. This relationship describes the influence of viscous forces on the observed pressure drop. Forchheimer [145] showed that this relationship can be flow rate dependent. At low flow rates, Darcy's law accurately describes the pressure drop across a porous media, but at high flow rates, the pressure drop exceeds that predicted by Darcy's law. Forchheimer described a more general relationship of flow through a porous media as seen in Equation 77.

$$-\frac{dP}{dx} = \frac{\mu}{S}v + \rho\gamma v^2 \tag{77}$$

Here, P is the pressure, x is the distance, μ is the fluid viscosity and ρ is the fluid density, while v is the superficial fluid velocity, S is the media permeability, and γ is the non-Darcy coefficient. Determining the permeability and non-Darcy coefficient then requires experimental work where Equation 77 can be fit to data. Cornell and Katz [184] expressed the Forchheimer equation for gas permeability experiments using a constant flow rate pump seen in Equation 78.

$$\frac{M_w A(p_1^2 - p_2^2)}{2zRT\mu l\rho_p Q_p} = \frac{1}{S} + \gamma\left(\frac{\rho_p Q_p}{\mu A}\right) \tag{78}$$

Here, M_w is the molecular weight of the gas, A is the sample cross-sectional area, p_1 and p_2 are the pressure at the sample inlet and outlet, z is the gas compressibility factor, R is the universal gas constant, T is sample temperature, μ is the gas viscosity, l is the length of the sample, ρ_p is

the density of the gas in the constant flow rate pump, and Q_p is flow rate in the pump. While this may be appropriate for gas permeability measurements, which have been applied for preform characterization [113], [114], a different formulation should be applied for non-gaseous flows. For non-gaseous, fluid driven LCM permeability experiments (like those of one-dimensional saturated flow), an experimental data set of velocity versus pressure drop can be created. Fitting this data to a polynomial trendline will yield an expression of form seen in Equation 79 where ΔP is pressure drop, v is the superficial velocity, m_1 is the first coefficient and m_2 is the second [185].

$$\Delta P = m_1 v^2 - m_2 v \tag{79}$$

The non-Darcy or inertial loss coefficient can then be found from the first coefficient of Equation 79. The permeability can be derived from the second coefficient of the quadratic using Equation 80 and Equation 81 where ρ is the fluid density, μ is the fluid viscosity, L is the length of the sample in the direction of flow, and α is viscous resistance, which can also be defined as the inverse of permeability [185].

$$m_1 = \gamma \frac{1}{2} \rho \tag{80}$$

$$-m_2 = \frac{\mu}{\alpha} L \tag{81}$$

A natural question is, at what flow rates do non-Darcy flows begin, or what are the criteria needed to consider non-Darcy flow? Chilton and Colburn [186] first described the criteria for non-Darcy flow through packed particles using a modified Reynolds number of form shown in Equation 82 where d_p is the particle diameter.

$$Re = \frac{\rho v d_p}{\mu} \tag{82}$$

Using this criterion, the critical Reynolds number was then experimentally found for non-Darcy flow. Green and Duwez [187] then redefined critical Reynolds number for non-Darcy flow shown in Equation 83 where permeability and the non-Darcy coefficient are used in place of a characteristic length.

$$Re = \frac{S\beta\rho v}{\mu} \tag{83}$$

Due to the difficulty in determining the particle diameters, Equation 83 was developed. Similar alterations of critical Reynolds numbers have also been created [188]–[190]. Recently, Zeng and Grigg [191] have revisited the criteria for non-Darcy flow in porous media and defined variations of these critical Reynolds number as either Type-I or Type-II. Type-I criterion was defined as that similar to what was proposed by Chilton and Colburn and takes form in Equation 84 where here, d, is the characteristic length of the porous media.

$$Re = \frac{\rho d v}{\mu} \tag{84}$$

Type-II criterion was then defined as the Forchheimer number, which has been adopted to represent the form originally described by Green and Duwez [187]. Type-II criterion is seen in Equation 85 where Fo is the Forchheimer number.

$$Fo = \frac{S\gamma\rho v}{\mu} \tag{85}$$

Zeng and Grigg [191] summarized that researchers using different forms of these criteria have found critical values for non-Darcy flow of similar media to be in range from 1 to 100 for Type-I and 0.005 to 0.2 for Type-II. Due to the large scatter in critical values, the researchers then argued for using one single criterion, Type-II, which possesses clear definition and applicability over any type of porous media. They further defined this Type-II criterion based on the non-Darcy error, E_{nD}, and the Forchheimer number in Equation 86.

$$E_{nD} = \frac{Fo}{1 + Fo} \tag{86}$$

The critical Forchheimer number, Fo_c, for non-Darcy flow could then be determined based on the amount of acceptable error, E_c, by Equation 87.

$$Fo_c = \frac{E_c}{1 - E_c} \tag{87}$$

The amount of acceptable error must be a carefully considered quantity and needs engineering judgement for the specific situation.

6.2 Methods

6.2.1 Non-Darcy Criteria Definition

Previously measured permeability results presented in Chapter 4 were reviewed to study the implementation of non-Darcy flow criteria. Obviously, these measurements were made at relatively low flow rates (1-10 cc/min), and generally, linear relationships were observed in the flow rate versus pressure drop data. It was expected that this data would show no signs of inertial effects and nonlinearities, but using the previously defined criteria, inferences can be made as to when non-Darcy flow may appear in the IM7-4HS fabric. It was then hypothesized that additional high flow rate testing (to be described in the next subsection) could verify these assumptions and produce non-Darcy flows.

Zeng and Grigg's [191] formulation for critical Forchheimer number (Equation 87) was used as the non-Darcy flow criterion. Based on the average scatter from all saturated permeability testing, the amount of acceptable error, E_c, was defined. Using the critical Forchheimer number and experimental data, an estimation of the critical velocity or flow rate could then be made for

the IM7-4HS preforms. Also, reduction of previously measured IM7-4HS data was carried out using the Forchheimer based fit from Equation 79 through Equation 81.

6.2.2 High Flow Rate/Pressure Testing

To investigate the applicability and effects of non-Darcy flow, high flow rate tests using the saturated permeability fixture described in Chapter 2 were conducted. In these experiments, the constant flow rate supplied from the metering pump was gradually increased until nonlinearity in the pressure versus flow rate curves was observed. These tests were conducted with preforms of IM7-4HS with and without tackifier over a range of fiber volume fractions at 50%, 55%, 60%, and 65%. These fiber volume fractions were selected to fit a range of practical interest in RTM. It should be noted that high flow rate testing was carried out with one preform per fiber volume fraction. This was done to ensure that any preform deformation that may be induced from high pressure at one volume fraction level of testing would not be carried into the next volume fraction and artificially skew the measurements. The permeating fluid was SAE 40 motor oil. The saturated permeability fixture was re-outfitted with high pressure equipment to handle these aggressive test requirements. A high-pressure, in-line pressure transducer (Omega PX180-500GV) with a limit of 500 gage psi was employed. The injection tubing linking the flow rate pump and the inlet of the fixture was highly pressure resistant up to 800 psi (McMaster-Carr high-pressure nylon tubing 9685T3). These precautions insured that at high pressures, any nonlinearity between flow rate and pressure drop would not be due to a leak at the inlet side. The test parameters can be seen summarized in Table 6.1.

Table 6.1: Test Parameters for Saturated High Flow Rate Permeability Tests

Material	Layup Orientation	V_f Range Tested	Test Fluid
Non-Tackified IM7-4HS	$[0]_6$	50%, 55%, 60%, 65%	SAE 40 Oil
Tackified IM7-4HS	$[0]_6$	50%, 55%, 60%, 65%	SAE 40 Oil

It was hypothesized that as the injection flow rate increases, a critical value would be reached where the flow rate and pressure drop relationship would become nonlinear, i.e. non-Darcy flow would occur. Depending on the slope of the flow rate versus pressure drop curve, the type of non-Darcy effect could be speculated, whether it was inertial effects playing a role or race tracking and other leaking events. Figure 6.1 displays these possibilities relative to the linear fit described by Darcy's law relating pressure drop and flow rate.

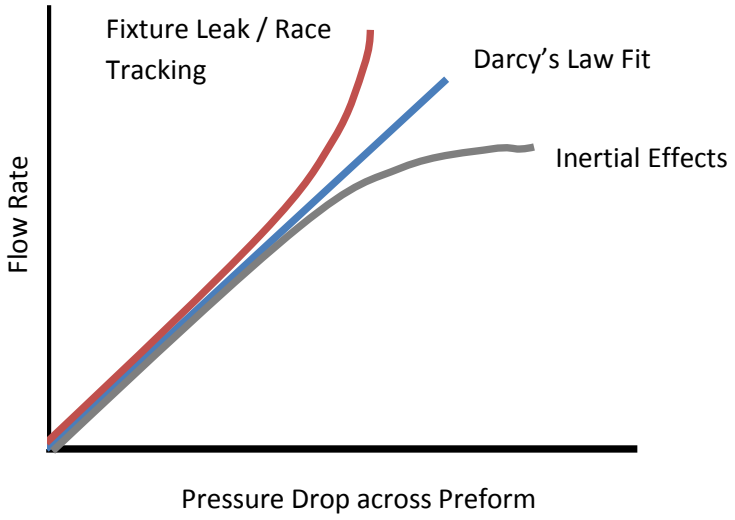

Figure 6.1: Non-Darcy Flow Possibilities

As the fluid velocity increases, inertial effects may be present if the flow rate versus pressure begins to curve downwards. In this case, Darcy's law will under predict the resulting pressure drop based on flow rate while the Forchheimer equation may be a more appropriate fit. If the flow rate/pressure drop relationship begins to curve upward from a linear trend, then Darcy's law

will over predict the pressure based on flow rate. This may be the result of a pressure leak from the fixture or fiber washout to the extent of race tracking. These interpretations were used to describe the result of the IM7-4HS high flow rate tests.

6.3 Results and Discussion

6.3.1 Data Reduction of Previously Measured Permeability

To define an acceptable error value for determination of the critical Forchheimer number, coefficients of variation of all saturated permeability measurements (including all fiber volume fractions) from Chapter 4 were averaged. This average coefficient of variation (CV) was 17.43%. Note that the CV did not change significantly with fiber volume fraction. This amount of scatter, although high in value, is common in permeability measurements. A recent large-scale effort to benchmark a permeability measurement procedure produced scatter of ±20% among multiple researchers' results for the same preform [69]. Therefore critical error of 17.43% is a reasonable quantity for the non-Darcy criterion, and any error greater than this this will result in significant difference from the standard measured scatter. Implementation into Equation 87 resulted in a critical Forchheimer number of 0.210. Thus, infusions producing Forchheimer numbers higher than this value should result in a significantly measured non-Darcy effect.

Flow rate versus pressure drop data from the measurements of Chapter 4 for warp aligned, tackified and non-tackified IM7-4HS were fit to the second-order, Forchheimer equation to investigate non-Darcy flow. From these re-fits, the Forchheimer permeability and non-Darcy coefficient were determined, thus ultimately allowing for a critical superficial velocity and flow rate to be determined. The Forchheimer fit values of the warp aligned non-tackified IM7-4HS

preform tests can be seen in Table 6.2, including the average (Avg.), standard deviation (StDev), and coefficient of variation (CV). Also, displayed is the ratio of Darcy permeability over permeability from the Forchheimer fit ($S^{Darcy}/S^{For.}$). Ratio values close to 1 show that no significant difference exists between the Darcy and Forchheimer fit.

Table 6.2: Warp Aligned Non-Tackified IM7-4HS Forchheimer Fit Values

V_f	Value	γ (m^{-1})	Forchheimer Permeability (m^2)	$S^{Darcy}/S^{For.}$
50%	Avg.	3.61E+09	2.67E-11	1.00
	StDev	1.70E+09	3.44E-12	0.07
	CV (%)	47.13	12.88	7.35
55%	Avg.	1.96E+10	1.98E-11	0.90
	StDev	2.34E+10	4.52E-12	0.09
	CV (%)	119.32	22.84	9.66
60%	Avg.	7.76E+10	1.46E-11	0.78
	StDev	6.23E+10	2.46E-12	0.13
	CV (%)	80.34	16.84	17.16

As expected, the permeability from the Forchheimer fit was generally similar to that of the Darcy fit. This is because these tests were made at low flow rates. Although, the permeability between fits was seen to be close in value, as fiber volume fraction increased, an increase in difference was seen between Darcy and Forchheimer permeabilities. The 60% fiber volume fraction range produced a permeability ratio to be 0.78, which shows a significant difference. This is may be due to the fact that non-Darcy behavior is more severe in low permeability porous media [191]. Further explanation could be that, at higher fiber volume fractions, less data points could be measured experimentally on the flow rate versus pressure drop curve due to the rapid in-cavity pressure build-up. This resulted first and second order fits to be calculated from only 3 data points, compared to the 4 or 5 data points of lower fiber volume fraction measurements. The

Forchheimer fit results for the warp aligned, tackified IM7-4HS saturated permeability tests can be seen in Table 6.3.

Table 6.3: Warp Aligned Tackified IM7-4HS Forchheimer Fit Values

V_f	Value	γ (m^{-1})	Forchheimer Permeability (m^2)	$S^{Darcy}/S^{For.}$
50%	Avg.	6.32E+09	2.59E-11	1.09
	StDev	9.02E+09	4.98E-12	0.15
	CV(%)	142.81	19.20	13.81
55%	Avg.	2.70E+09	1.84E-11	0.99
	StDev	2.42E+09	3.56E-12	0.03
	CV(%)	89.48	19.31	3.04
60%	Avg.	1.59E+10	1.02E-11	0.97
	StDev	2.21E+10	1.89E-12	0.06
	CV(%)	139.51	18.46	6.51

Here, the Darcy over Forchheimer permeability ratios are close to 1 for all fiber volume fractions tested. For both tackified and non-tackified IM7-4HS, a Forchheimer (second order) fit is not needed to accurately define permeability. With all tests, the linear regression fits of Darcy's law capture the flow rate vs. pressure drop data well with the one described exception, but as discussed earlier, these Forchheimer coefficients (γ and Forchheimer permeability) can be used to estimate critical superficial velocities. These, in turn, were used to find the critical pump-supplied constant flow rates, which are shown in Table 6.4 for multiple fiber volume fractions.

Table 6.4: Critical Velocity and Flow Rate Estimations for Non-Darcy Flow in IM7-4HS with and without Tackifier

V_f = 50%

Flow Rate Value	Avg. (cc/min)	StDev (cc/min)	CV (%)
Non-Tackified IM7-4HS	12.19	9.17	75.21
Tackified IM7-4HS	21.60	19.53	90.42

V_f = 55%

Flow Rate Value	Avg. (cc/min)	StDev (cc/min)	CV (%)
Non-Tackified IM7-4HS	6.22	6.90	110.98
Tackified IM7-4HS	29.90	26.82	89.68

V_f = 60%

Flow Rate Value	Avg. (cc/min)	StDev (cc/min)	CV (%)
Non-Tackified IM7-4HS	0.97	0.60	61.78
Tackified IM7-4HS	27.18	29.44	108.32

For the non-tackified material, the critical flow rates drop as the fiber volume fraction increases. This is likely because that non-Darcy behavior is becomes more prevalent in low permeability porous media, as mentioned earlier. However, for the tackified fabric, no clear relationship is seen between critical flow rate and fiber volume fraction. Regardless of observed trends, the experimental scatter of the critical flow rates were so large that no reasonable estimation can be made regarding a critical value. This scatter may best be explained by the experimental variability seen in the non-Darcy coefficient. This coefficient showed large scatter for both tackified and non-tackified material, over 100% in some cases (see Table 6.2 and Table 6.3). The non-Darcy coefficients proved to be very sensitive to the experimental data compared to the Forchheimer permeability, which was seen to possess standard values of scatter (<20%).

Zeng and Grigg [191] argued for the use of a critical Forchheimer number as a criterion for non-Darcy flow in porous media. As described by the researchers, the definition of this criterion is

simple and can be based on critical error. Unfortunately, the applicability of this method did not prove consistent, as very large experimental variations were seen in the critical flow rate estimations. Due to the sensitivity of the calculation of the non-Darcy coefficient, this criterion cannot be used confidently to find the critical flow rate or velocity values for IM7-4HS preforms. Nonetheless, further permeability measurements at high flow rates were conducted in attempt to observe non-Darcy flow. The results of these measurements are discussed next.

6.3.2 High Flow Rate/Pressure Experiments

A total of 8 high flow rate experiments were conducted with tackified and non-tackified IM7-4HS preforms. These tests were run from 50% fiber volume fraction to 65%. A sample relationship of the flow rate (Q) versus pressure drop (ΔP) for a non-tackified IM7-4HS at 50% fiber volume can be seen in Figure 6.2. It is seen that as the flow rate increases, deviation from a linear fit was found. This nonlinearity curves upward, as a result of a pressure leak. It was seen that for this sample, nonlinearity began around flow rate of 7 cc/min and pressure drop of roughly 690 kPa. At a certain point during testing, when the flow rate was increased over 1.6E-7 m^3/s, the measured pressure drop across the preform actually reduced.

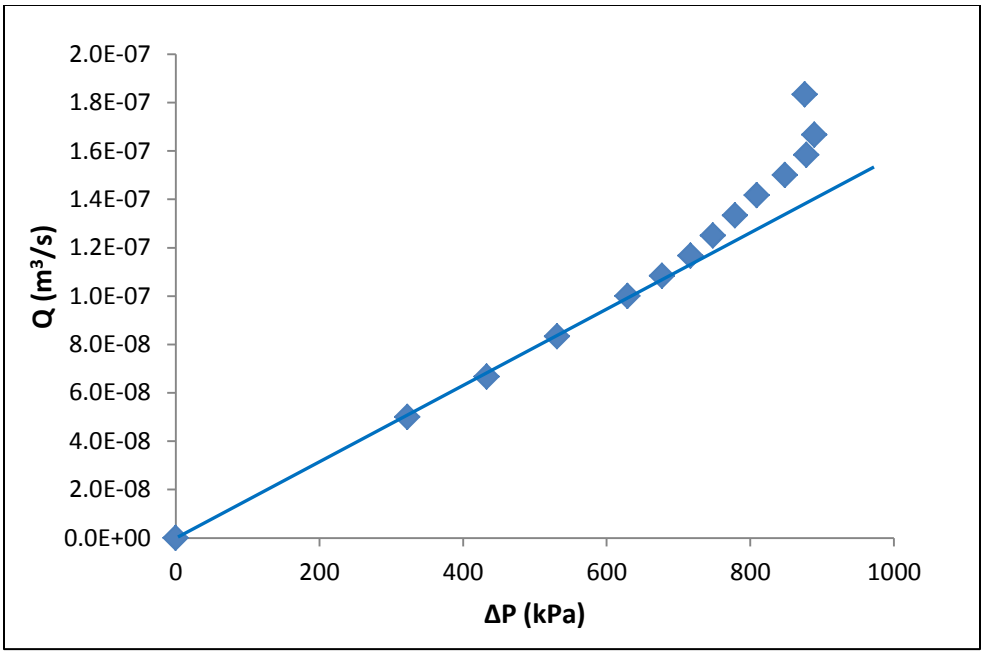

Figure 6.2: High Flow Rate Effects of Non-Tackified IM7-4HS at 50% Fiber Volume Fraction

Upon further testing, this nonlinearity was found to be systematic. At every fiber volume fraction tested, both non-tackified and tackified IM7-4HS were found to result in a lower measured pressure drop than calculated from Darcy's law at the corresponding flow rate. The flow rate versus pressure drop for the non-tackified IM7-4HS preforms are shown in Figure 6.3. Additionally, the same data for the tackified IM7-4HS can be seen in Figure 6.4.

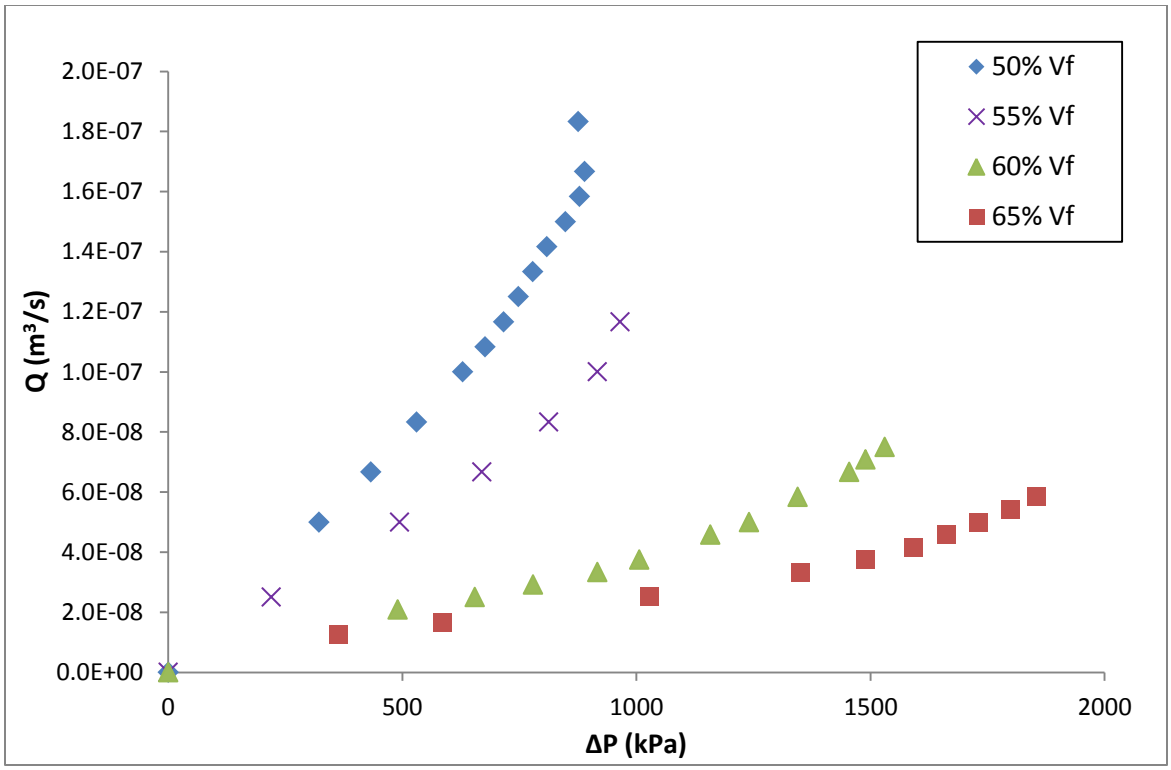

Figure 6.3: Flow Rate versus Pressure Drop for Non-Tackified IM7-4HS

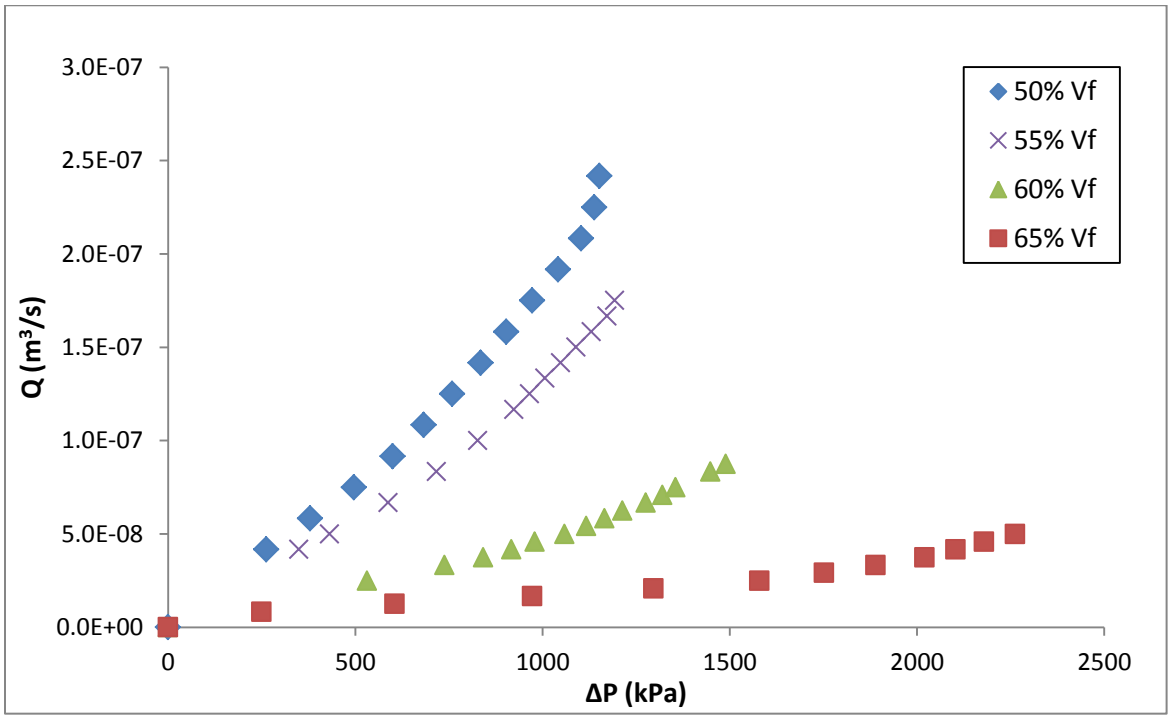

Figure 6.4: Flow Rate versus Pressure Drop for Tackified IM7-4HS

While these results were interesting, they were not expected from the experiments. Rather than an appearance of inertial effects, the tests produced signs of fixture leak and race tracking at high flow rates. The reason for this will be discussed, but notable trends can also be taken from these figures. For both the non-tackified and tackified preforms, as the fiber volume fraction increased, higher pressure drops could be achieved before nonlinearity occurred. This results show that high fiber volume fractions can withstand higher pressures before nonlinearity occurs than low fiber content preforms. Also, at high fiber volume fractions, low flow rates produce very high pressure drops compared to high flow rates at low fiber volume fractions.

Further investigation revealed that the non-Darcy flow regime could be attributed to a combination of the preform type, fiber volume fraction, and the robustness of the fixture. While running the high flow rate tests, the fixture's inlet and outlet side cavity thicknesses were monitored by two LVDTs. It was seen that depending on the fiber volume fraction, the inlet side of the fixture was pushed upwards once oil pressure increased high enough from flow rate injection (Figure 6.5). This fixture displacement proved to be significant, and the initiation point for the nonlinearities seen.

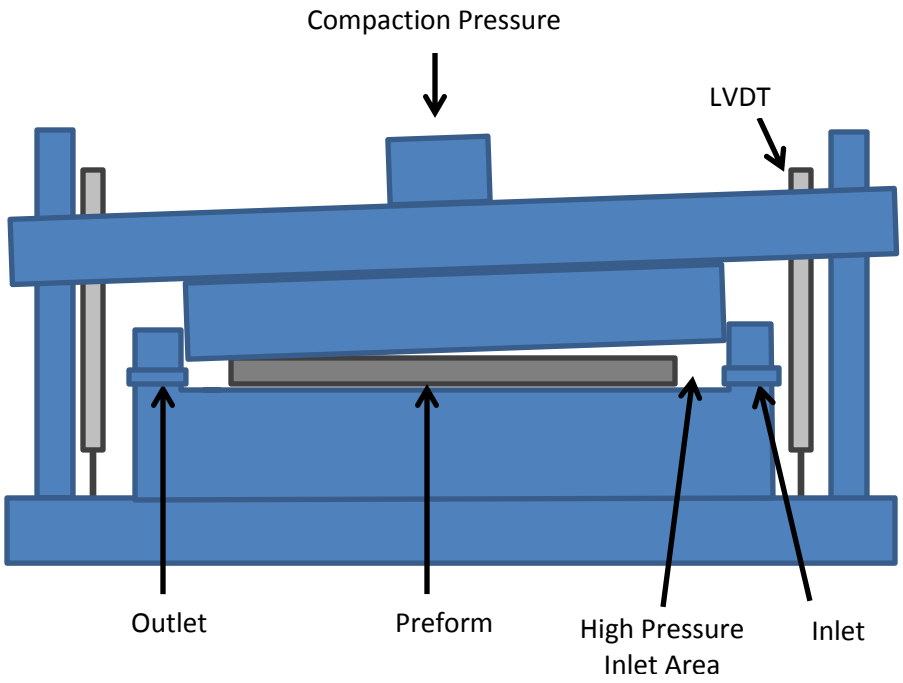

Figure 6.5: Fixture Displacement Representation from High Pressure/Flow Rate Testing

A sample LVDT readout of the tackified IM7-4HS high flow rate test at 50% fiber volume fraction can be seen in Figure 6.6. Here, the LVDT measured cavity depth versus inlet pressure is plotted over the entire test.

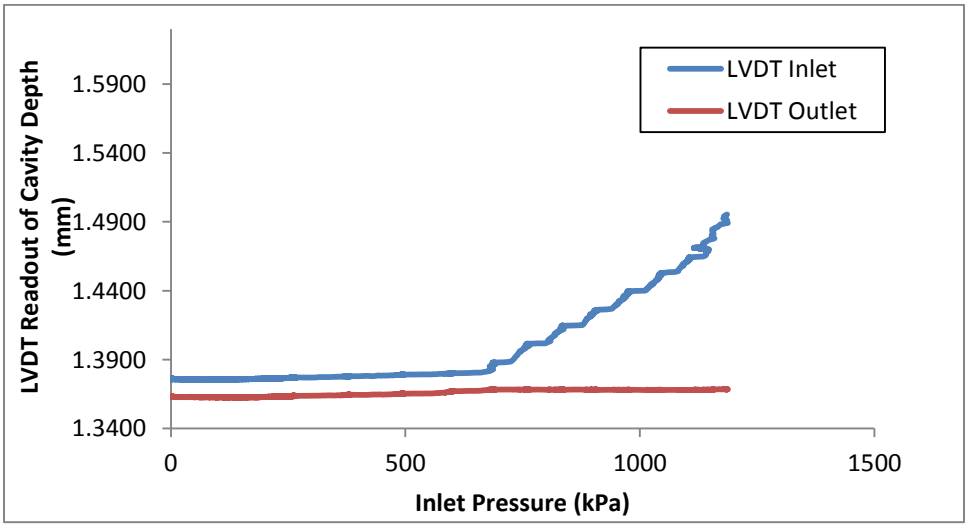

Figure 6.6: Sample LVDT Readout vs. Inlet Pressure for High Pressure/Flow Rate Test at 50% V_f

It can be seen that after the inlet pressure reached roughly 690 kPa (100 psi), the inlet side of the fixture was displaced upward a significant amount, increasing cavity depth, while the outlet side of the fixture remained constant. For this specific test, cavity depth at the inlet side increased a total of 8.9%, which corresponds to a fiber volume fraction decrease of 4%. With this result, inertial effects are impossible to explore as the apparent robustness of the saturated permeability fixture is not great enough to withstand high pressure while maintaining constant preform fiber volume fraction. This critical point of 690 kPa can be seen as the starting point for nonlinear behavior in the measured flow rate versus pressure drop curve. The corresponding flow rate versus pressure drop curve for the tackified IM7-4HS preform at 50% can be seen in Figure 6.7. In this graph, the data points measured before the critical 690 kPa value are marked separately and are seen to fit well to a linear regression. After this value, Darcy's law no longer holds as pressure leaking is observed. Again, this trend was seen for all experiments conducted.

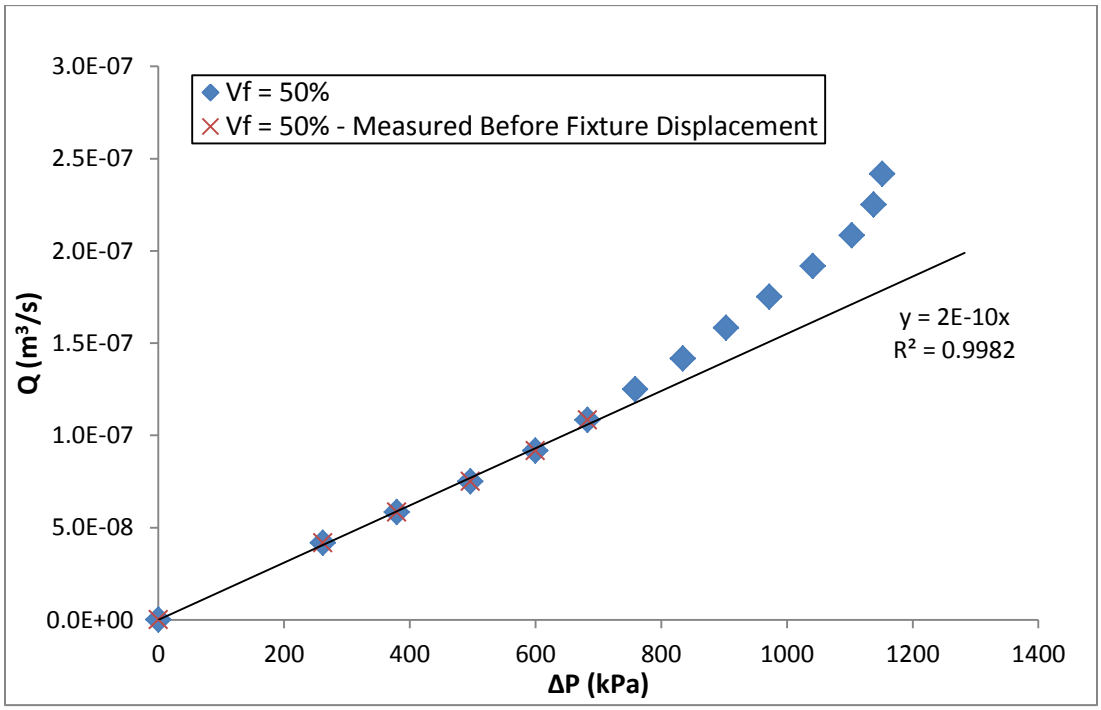

Figure 6.7: Tackified IM7-4HS Flow Rate vs. Pressure Drop with Fixture Displacement Consideration

After the high flow rate tests, fiber washout was also seen for the non-tackified preforms. As the inlet side of the fixture was displaced from oil pressure, the compaction of the preforms (and fiber volume fraction) was greatly reduced. With low levels of compaction pressure at the inlet side of the fixture, the non-tackified preforms were loosely held and easily deformed by the infiltrating flow. Interestingly, the tackified preforms did not exhibit significant signs of fiber washout. This can be attributed to the added tack and fiber-hold the inter-layer tackifier provided. Sample post-test state preforms with and without tackifier can be seen in Figure 6.8.

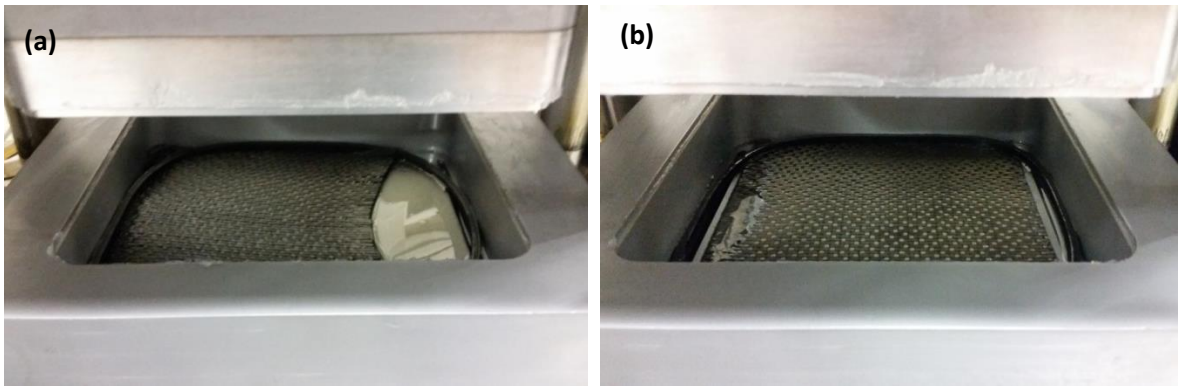

Figure 6.8: Post-test Preform Deformation for (a) Non-Tackified and (b) Tackified IM7-4HS

The addition of tackifier (non-debulked) effectively resists the event of fiber washout and deformation in the IM7-4HS compared to non-tackified fabric, while also decreasing the permeability. It should be noted that even without fiber washout, the fixture displacement became great enough during tackified preform testing to create pressure leaking and non-Darcy flow. This leads to the conclusion that while tackifier resists fiber washout, the nonlinearities due to pressure leaking are highly dependent on the fixture's displacement. Interestingly, at higher fiber volume fractions, especially at 60% and 65%, higher inlet pressures could be reached

before the fixture was displaced. This can be seen in Figure 6.9, where the inlet LVDT readout for a tackified preform at 65% is plotted versus the measured inlet pressure.

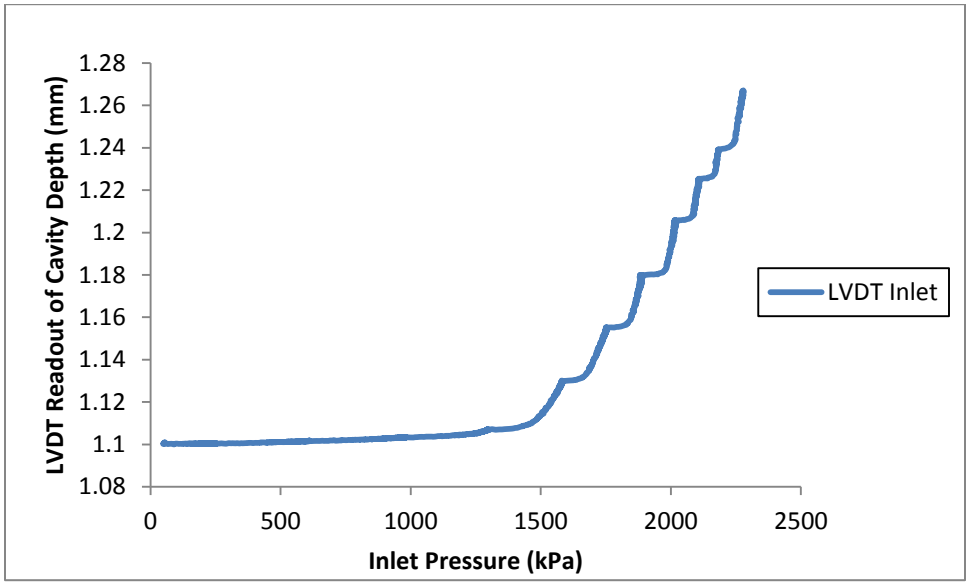

Figure 6.9: Sample LVDT Readout of Tackified IM7-4HS High Flow Rate Test at 65% V_f

It is clear that significant fixture displacement at the inlet is not measured until the inlet pressure is over 1400 kPa. Thus, the nonlinearities seen are a function of the inlet pressure reached, the fixture's robustness and the applied compaction pressure. It is hypothesized that at the higher compaction pressures needed to compress the preforms to high volume fractions, the added compaction aids to resist oil pressure produced at the inlet. Table 6.5 summarizes the critical inlet pressures reached before fixture displacement occurred at each volume fraction for the materials tested.

Table 6.5: Critical Inlet Pressure before Fixture Displacement and non-Darcy Flow

Critical Inlet Pressure (kPa)		
V_f	IM7-4HS Preform Type	
	Non-Tackified	Tackified
50%	717	689
55%	818	717
60%	1007	979
65%	1351	1400

This data also show no significant critical pressure difference between tackified and non-tackified preforms.

6.4 Conclusions

Overall, it can be concluded that the high flow rate tests did produce non-Darcy flow, although this is attributed to pressure leaking due to fixture displacement under high pressure. Unfortunately, the test equipment used was not robust enough to investigate the possibility of inertial effects. However, the experiments did reveal that tackified preforms were able to resist fiber washout on all tests where the non-tackified preforms succumbed to deformation under the high pressures produced. Also, using a Forchheimer fit with low flow rate measurement data produced very similar permeability to that of Darcy's law, as expected. Critical flow rates were then defined from these experiments, although large scatter in the non-Darcy coefficient proved to give little confidence in the criteria defined. Therefore, the Forchheimer criterion recommended by Zeng and Grigg [191] cannot be used to accurately predict critical flow rates where non-Darcy flow should appear in IM7-4HS preforms. For future studies, test fixtures that employ more heavy-duty and robust design should be used to investigate high flow rate infusions. If inertial effects could be characterized in future permeability measurements, criteria should be implemented into process modeling. Then, a Forchheimer relationship could be used

to govern the flow in a mold fill simulation to account for the additional pressure loss. Further interesting work would compare non-Darcy flow in saturated versus unsaturated test cases. The effects of two-phase flow may result in significant difference from that of a saturated case.

7. Radial Flow Measurement and Simulation

Infusion visualization methods offer much insight into the flow and permeability characteristics of reinforcements that closed-mold methods lack. Although closed-mold methods can be used to determine the principal flow direction with multiple experiments, the sensitivity of the permeability tensor transformation is high. As discussed in the Saturated Permeability chapter, slight changes in experimental values produce large swing in the β angle determination. Due to this, a radial visualization fixture was created to verify optically the IM7-4HS fabric principal in-plane flow directions, while also observing the effects of fabric direction and tackifier. The following chapter will describe the radial fixture design, method, and results including tackified vs. non-tackified infusions, β angle determination, and transient permeability values. This chapter will also present simulation results of tackified and non-tackified radial mold fills produced from the measured permeability data. Inferences can then be made regarding basic mold fills and the effects of the inter-layer tackifier on preform permeability. This fixture's description and infusion results with IM7-4HS preforms can also be found in an earlier published work by Sommerlot et al. [192].

7.1 Visualization Method

7.1.1 Experimental Method and Fixture Setup

To produce transient in-plane permeability infusions, a radial visualization fixture was designed and machined. This fixture was created to allow a constant pressure inlet at the fixture's center, which produced a propagating flow front ellipse. The radial fixture features a base plate to house IM7-4HS preforms and a clear, cast acrylic top plate, which allows visualization of the transient infusions. An exploded view rendering of this fixture can be seen in Figure 7.1.

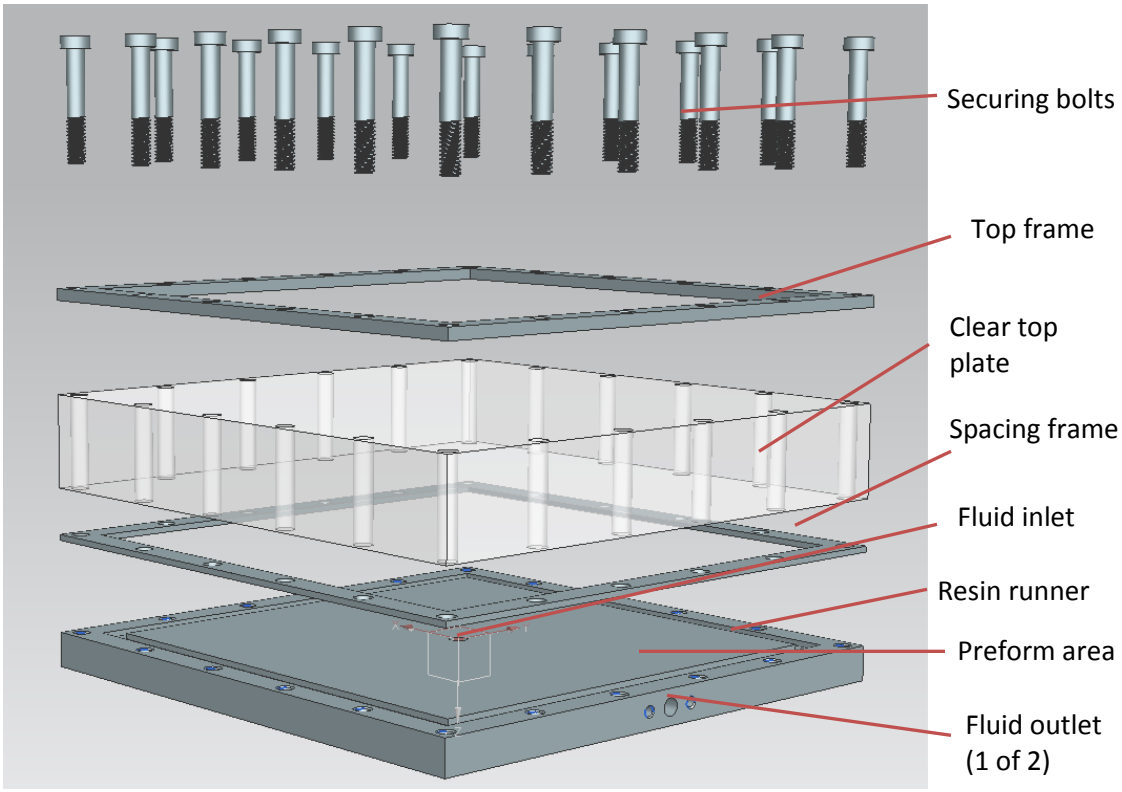

Figure 7.1: Radial Visualization Fixture Exploded View

To hold tight tolerances in the vertical direction, the fixtures base plate was machined from precision ground aluminum and was designed to contain a 25.4 x 25.4 cm preform. The base plate has a 3/8 inch diameter, centrally located inlet to allow fluid initiation. The base plate also contains a resin runner groove around the outside of the preform area that is 9.53 mm in width

and 3.18 mm deep. The resin runner allows fluid to easily flow to the fixture's outlets once the preform area is traversed. This eliminates the unwanted pressure build ups in the fixture and controls the outer-edge race-tracking. A precision ground aluminum spacing frame sits on the base plate, which controls the preform thickness. Above that, the 5.08 cm thick, clear acrylic top plate sits, which is used to compress the preform to the spacing frame thickness. The thickness of the acrylic top plate ensures little to no flex during compaction and infusion, and therefore holds a consistent fiber volume fraction throughout testing. A top frame is bolted on to the clear top plate for added rigidity with 20 equally spaced bolts.

An Airtech Advanced Materials Group pressure pot was used to supply constant pressure injections to the radial fixture. Injections were set to a target pressure on the pressure pot regulator, and an in-line pressure transducer (Omega PX180-GV) monitored the exact pressure at the fixture inlet. The in-line transducer was connected with NI 9219 DAQ board, which was controlled from a laptop outfitted with LabVIEW. The test fluid used here, again was the SAE 40 motor oil. A Samsung Galaxy Note 10.1 was employed to record infusion from a top viewpoint, while infusion time was monitored with a stopwatch. After infusions were recorded, the video images were processed with MATLAB. The MATLAB script allowed the user to manually select the best fit ellipse of the advancing flow front over time. This allowed calculation of the radial wet length and orientation (β angle), which were then used to determine the radial, unsaturated in-plane permeabilities following the formulation of Weitzenböck et al. [81], [193] for anisotropic media. The processed images of the advancing ellipses were averaged over the infusion time for principal orientation and in-plane permeabilities. The MATLAB script used for this processing can be found in Appendix C. Constant pressure injections were made at a target

of 138 kPa (20 psi) using the SAE 40 motor oil. From earlier work of Chapter 5, it can be concluded that using SAE 40 oil as the permeant will not produce a significant difference in permeability than from using a resin (SC-15 Part A). Also, the capillary pressure can be neglected in the permeability formulation based on the previous experiments at similar injection pressure ranges.

7.1.2 Material Preparation

Preforms of IM7-4HS with and without tackifier were prepared for the radial infusions by cutting individual plies in 25.4 x 25.4 cm squares. For these infusions, warp aligned preform layups were used. Based on the precision ground spacing frame in the fixture, 14 plies of the IM7-4HS fabric were needed to achieve a fiber volume fraction of 50%. The tackified IM7-preforms were stored on roll in a freezer until the preform plies were cut. The tackified preforms were allowed to reach room temperature before testing and no additional processing was used (i.e. no debulking). Both preforms, with and without tackifier, were center-hole punched with a 9.53 mm (3/8 inch) diameter hole to produce a purely in-plane infiltration. The material, layup, and other test parameters can be seen in Table 7.1 that were prescribed for the radial infusions.

Table 7.1: Radial Infusion Experiment Setup Data

Material	Layup	V_f (%)	# Runs	Target Inlet Pressure (kPa)
Non-tackified IM7-4HS	$[0]_{14}$	50	4	138
Tackified IM7-4HS	$[0]_{14}$	50	2	138

7.1.3 Numerical Method

Numerical models were also produced for the radial infusions with a computational fluid dynamics (CFD) method. This modeling routine took the basic approach of implementing

experimental permeability values into a prescribed modeled preform region. The entire domain consisted of the 3D preform and resin runner regions. The preform was designated as a porous media with in-plane permeabilities defined from the experimental radial infusion results, and a through-thickness permeability defined from the saturated experimental results described in Chapter 4. The resin runner region was prescribed as general void space. Boundary conditions matched those of the experiments including a central pressure inlet, atmospheric outlets, and wall boundaries around the resin runner. A volume of fluid (VOF) method was employed where modeled fluid was injected into the domain, displacing the initially prescribed air-filled mold. With this approach, the fluid volume fraction is tracked as the flow front progresses in time steps. The he equations are solved in this case using the VOF method. The model is composed of the continuity equation given by Equation 88, where ρ is density, t is the time and v is the local velocity.

$$\frac{\partial \rho}{\partial t} + \nabla \cdot (\rho v) = 0 \tag{88}$$

The permeating fluid volume fraction is given by Equation 89, where V_f is the volume fraction.

$$\frac{\partial V_f}{\partial t} + \nabla \cdot \left(V_f v\right) = 0 \tag{89}$$

The momentum equation for each volume is given by Equation 90, where τ_{ij} is the stress tensor, μ is the fluid viscosity, g is the gravity, P is the pressure, and F is an external source vector that can be used to incorporate the resistive force from the porous media.

$$\frac{\partial (\rho v)}{\partial t} + \nabla \cdot (\rho v v) = -\Delta P + \nabla \cdot \left(\mu \tau_{ij}\right) + \rho g + F \tag{90}$$

A simple mesh refinement study was also performed, as meshed domains of both 1,225 and 390,000 elements were solved with the described VOF method.

7.2 Results and Discussion

7.2.1 Experimental Results

A sample MATLAB processed image of an advancing flow front is shown in Figure 7.2. Here, the IM7-4HS preform's warp (0°) and weft (90°) directions are noted and the best fit ellipse can be seen, which was created from the user defined points. The first and second principal axes are also defined, while β is shown as the angle between the warp and S_{11} direction. The major and minor axes of the flow front also can be seen, as well a principal orientation based on the fabric 0° or warp direction. These axes lengths were scaled and inputted as radial wet lengths for the radial permeability calculation from Weitzenböck et al. [81], [193]. The recorded stopwatch time in the image was also inputted into the formulation. The exact values of the parameters including S_{xx}, S_{yy}, the principal permeabilities, and β angle are then outputted from the MATLAB script.

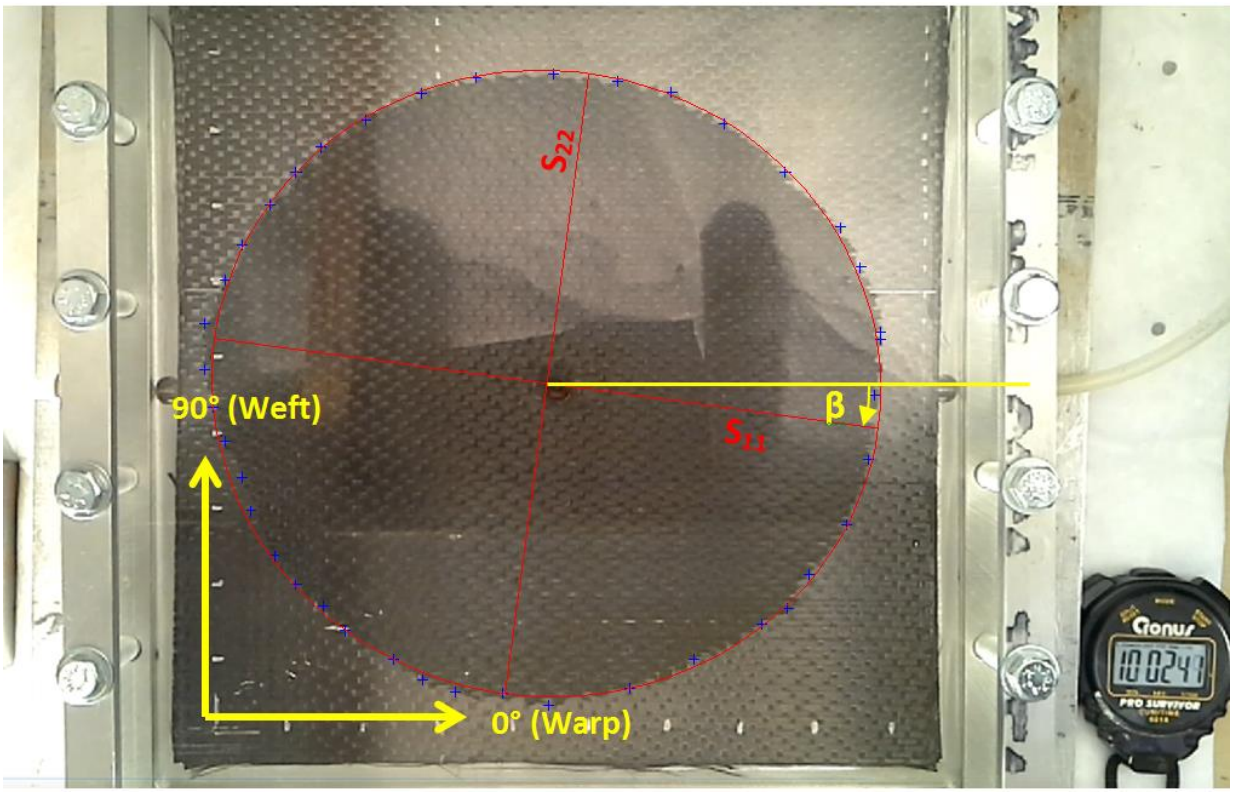

Figure 7.2: Sample MATALB Processed Radial Infusion Image

Although the permeability and β angle were averaged over the entire infusion for each run, the image processed results can be plotted over time. In Figure 7.3, sample data from a non-tackified preform is seen where both the S_{11} and S_{22} permeabilities and β are plotted on the same graph over time.

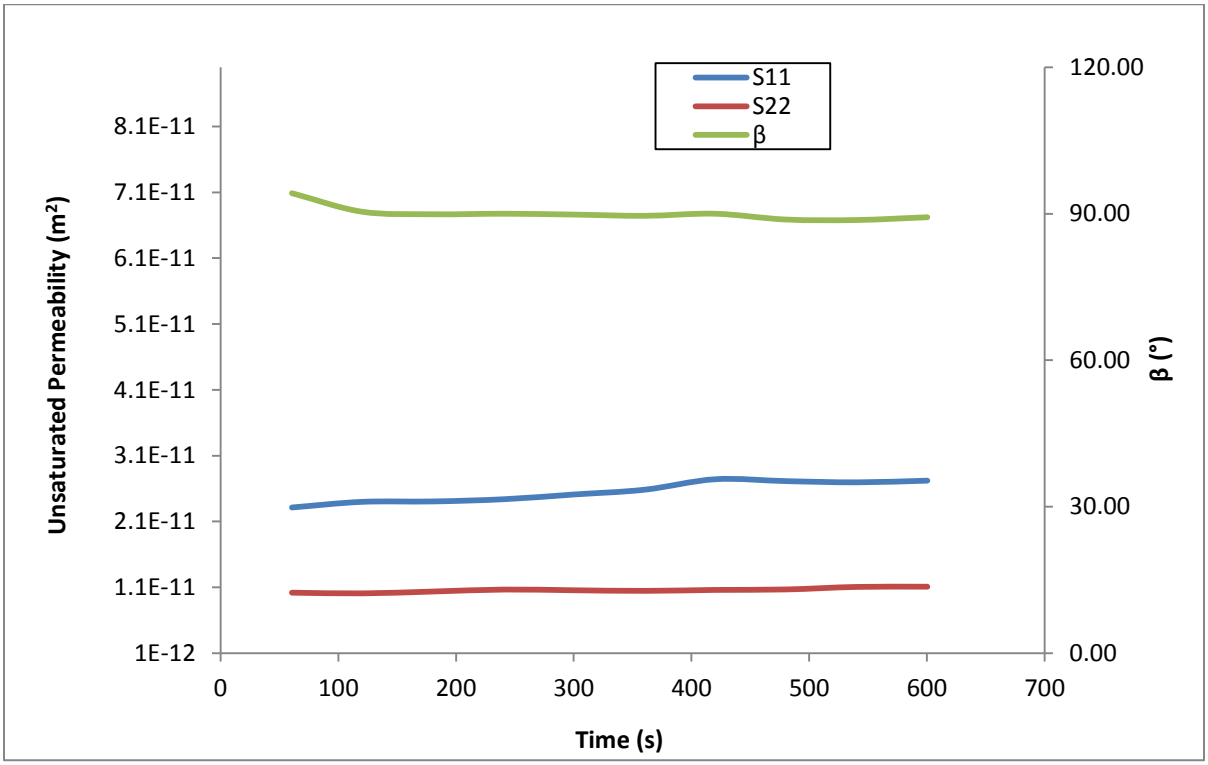

Figure 7.3: Sample Unsaturated Radial Permeability and β Angle over Infusion Time

Here, the calculated permeabilities and orientation angle all show stability over time. This can be attributed to consistent preform geometry and test parameters. The averaged values from all the runs are displayed in Table 7.2. This includes the first and second principal permeabilities as well as the angle of orientation of first principal permeability. Following in Table 7.3, the warp, weft, and 45° off-axis permeabilities can be seen. These permeabilities were calculated from rotations of the best fit ellipse of each run.

Table 7.2: Radial Unsaturated Principal Permeability Results

Run	S_{11} (m^2)		S_{22} (m^2)		β (°)	
	Non-tackified	Tackified	Non-tackified	Tackified	Non-tackified	Tackified
1	6.51E-11	2.56E-11	1.83E-11	2.05E-11	91.23	-7.52
2	2.71E-11	7.01E-12	1.48E-11	6.55E-12	92.68	113.68
3	2.05E-11	-	1.22E-11	-	98.84	-
4	2.55E-11	-	1.06E-11	-	90.07	-
Avg.	3.46E-11	1.63E-11	1.40E-11	1.35E-11	93.21	53.08
StDev	2.06E-11	-	3.38E-12	-	3.91	-
CV (%)	59.48	-	24.16	-	4.19	-

Table 7.3: Radial Unsaturated Warp, Weft, and Off-axis Permeability Results

Run	S_{xx}		S_{yy}		S_{xx}'	
	Non-tackified	Tackified	Non-tackified	Tackified	Non-tackified	Tackified
1	1.83E-11	2.55E-11	6.50E-11	2.06E-11	2.93E-11	2.34E-11
2	1.48E-11	6.60E-12	2.71E-11	6.95E-12	1.97E-11	7.01E-12
3	1.23E-11	-	2.02E-11	-	1.66E-11	-
4	1.06E-11	-	2.55E-11	-	1.50E-11	-
Avg	1.40E-11	1.60E-11	3.44E-11	1.38E-11	2.01E-11	1.52E-11
StDev	3.36E-12	-	2.06E-11	-	6.41E-12	-
CV (%)	23.97	-	59.82	-	31.87	-

Interestingly, the first run for both the tackified and non-tackified preforms showed much higher permeabilities than the subsequent runs. A specific reason for this is not certain. Aside from this artifact, important inferences can be made. Even with the first runs producing higher permeability, the shape of the flow front ellipses remained constant. The non-tackified warp aligned IM7-4HS preforms were seen to show a strong bias in permeability in the weft direction. This is seen as the β angle was calculated to be nearly 90° for every run made. Alternatively, the tackified warp aligned preforms showed little directional bias, with warp, weft, and off-axis permeability measurements all being similar in value. The β values here showed very scattered

results between Run 1 and Run 2. This is explained by the nature of the tackified flow front ellipse. As the flow front becomes more isotropic, the angle of first principal permeability becomes less important in describing the flow front ellipse. This may be better explained by comparing the warp over weft (S_{xx}/S_{yy}) permeability ratio with the β angle for non-tackified and tackified results. This comparison can be seen in Table 7.4.

Table 7.4: Radial Permeability Warp/Weft Ratio and $\boldsymbol{\beta}$ Angle Comparison

Run #	$\boldsymbol{\beta}$ (°)		S_{xx}/S_{yy}	
	Non-tackified	Tackified	Non-tackified	Tackified
1	91.23	-7.52	0.28	1.24
2	92.68	113.68	0.55	0.95
3	98.84	-	0.61	-
4	90.07	-	0.42	-
Average	93.21	53.08	0.46	1.09
StDev	3.91	-	0.15	-
CV (%)	4.19	-	31.51	-

It is very clear here that the addition of tackifier has a strong effect on the orientation of principal permeability. The tackified preforms display a warp over weft permeability ratio average close to 1, which implies a near isotropic advancing front, while the non-tackified ratio average is 0.46. This non-tackified ratio shows the average warp direction permeability is over half that of the weft direction. Physically, the inter-layer tackifier is blocking some of the inter-tow flow channels and reduces permeability to create a more isotropic flow front. This inter-tow gap blockage has been cited by several researchers to attribute to permeability reduction [9]–[11]. These tackifier effects were also observed in the saturated, channel flow permeability measurements of Chapter 4. There, it was found that the addition of tackifier created similar in-plane permeability values in all directions, creating a more isotropic medium. A graphical

comparison of the average saturated, channel flow measurements of the warp aligned IM7-4HS is made with the average radial unsaturated permeabilities in Figure 7.4.

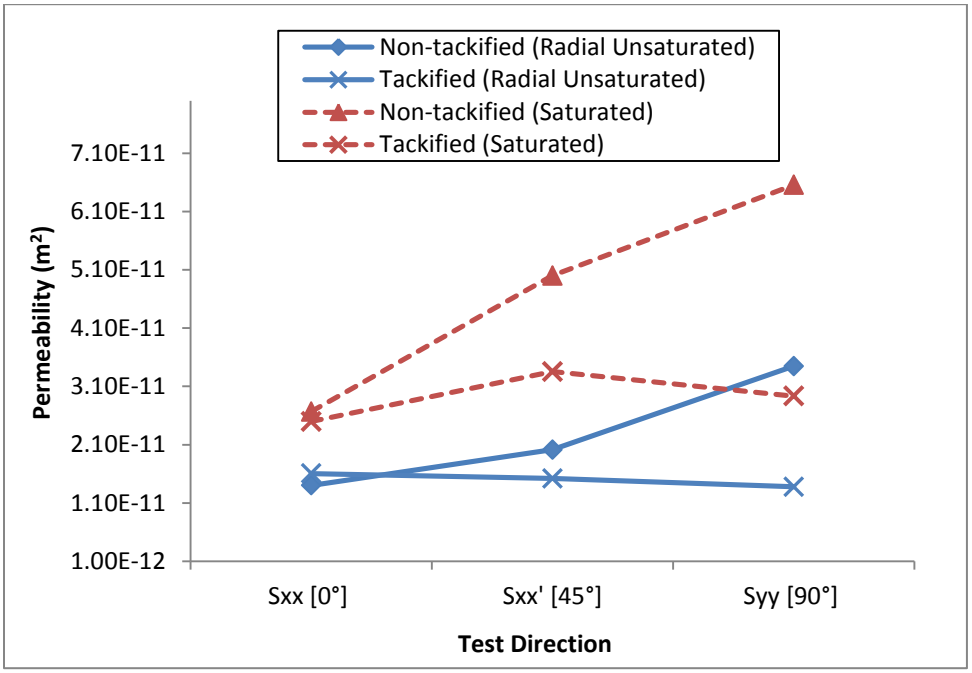

Figure 7.4: Average IM7-4HS Permeability Comparison of Radial Unsaturated and Saturated Channel Flow Measurements

Very similar relationships between the radial and channel flow measurements can be seen over the test direction. Tackified preforms showed little change over test direction in both saturated and radial unsaturated experiments, while the non-tackified preforms show an increasing bias towards the 90° direction. It should be noted that the radial unsaturated permeabilities tested 40% to 50% lower than their saturated counterparts. This relationship has also been noted by Estrada et al. [11], who found up to ~45% reduction in unsaturated permeability compared to saturated test cases with 4 wt% tackified preforms. This, although, is in contradiction from the channel flow unsaturated results of Chapter 5, where no significant difference was seen between unsaturated and saturated permeabilities. Explanation for this must then be placed on the difference between radial and channel flow test parameters. Lundström et al. [67], in a round

robin permeability study, reported that radial flow methods produced permeability values up 23% lower than parallel flow techniques for the same preform. They also explained that radial flow techniques suffers from several sources of error that are not present in channel flow tests, including deviations of the inlet hole shape, the inlet hole radius, and the local permeability near the inlet. With this in consideration, radial flow measurement techniques may represent a higher probability of experimental scatter compared to parallel flow techniques. This may also explain why both the saturated and unsaturated channel flow measurements of Chapter 5 produced very similar permeabilities for the IM7-4HS preforms, while the current radial technique produced very different results.

7.2.2 Comparison with Numerical Solution

To demonstrate the applicability of permeability measurements to simulate mold fills, the permeability results from the first run of the experiments with and without tackifier were used to generate numerical mold fill solutions. A three-dimensional model was constructed of the mold geometry as described in the methods section of this chapter. Numerical simulations results were produced with two in-plane permeability experimental measurements (S_{xx} and S_{yy}) and a transverse permeability measurement, which was presented in Chapter 4. Numerical simulation results are compared against actual infusions images at the same time step for both non-tackified and tackified IM7-4HS preforms in Figure 7.5 and Figure 7.6, respectively. The results are divided in three columns: (A) experimental advancing flow fronts that are image processed displaying the best fit ellipse, (B) numerical flow fronts found from a coarsely meshed domain of 1,225 elements, and (C) numerical flow fronts from a refined domain meshed with 390,000 elements. Each column of results represents the flow front ellipse at the infusion time displayed

in the bottom left of the images in column (A). Four time intervals images were selected to be displayed.

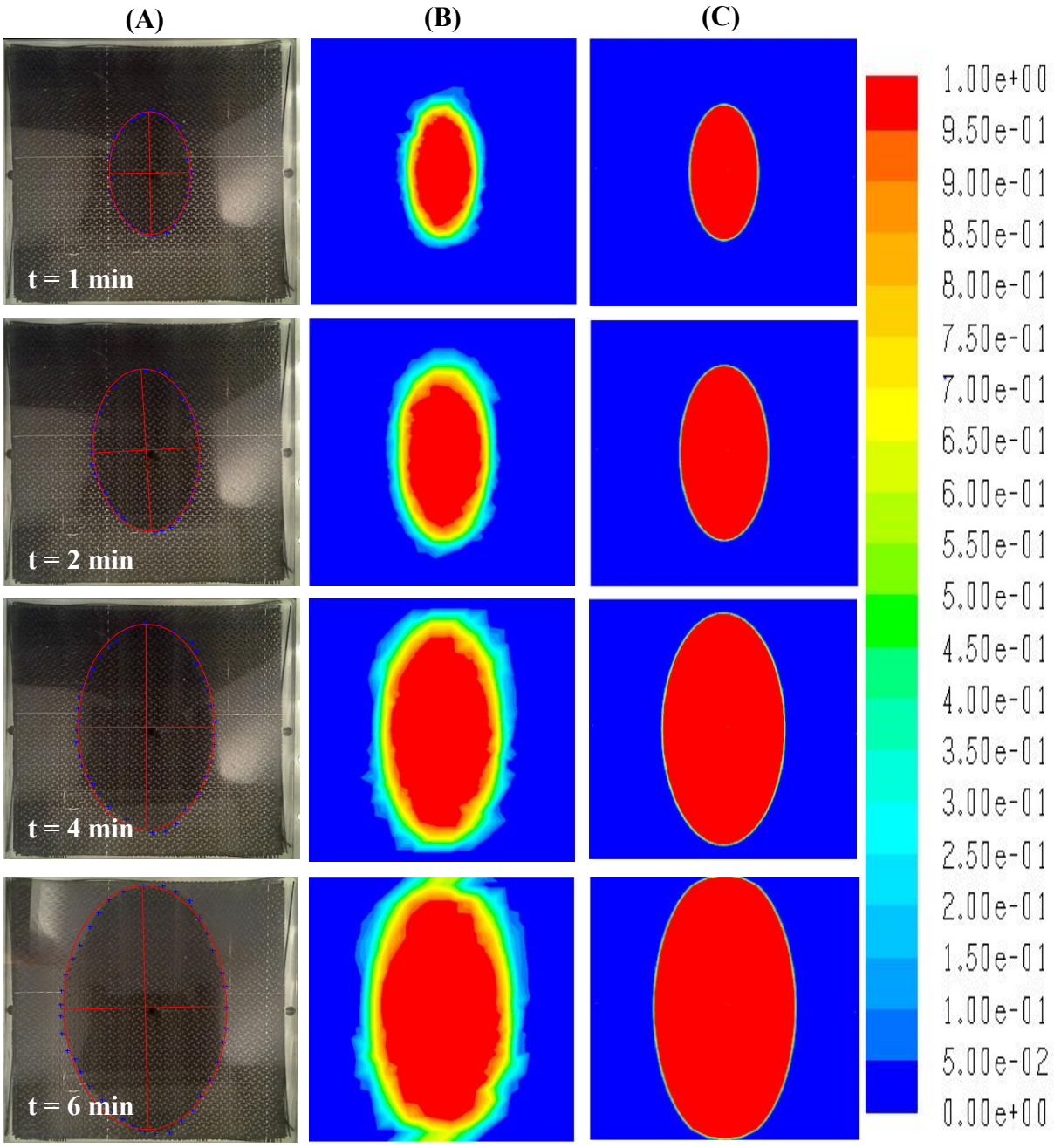

Figure 7.5: Non-Tackified IM7-4HS Advancing Flow Front Comparisons. (A) MATLAB processed experimental flow front propagation with best fit ellipse. (B) Rough mesh numerical advancing front solutions. (C) Fine mesh numerical advancing front solutions. Numerical solutions display volume fraction of the test fluid, SAE 40 oil (red) displacing air (blue).

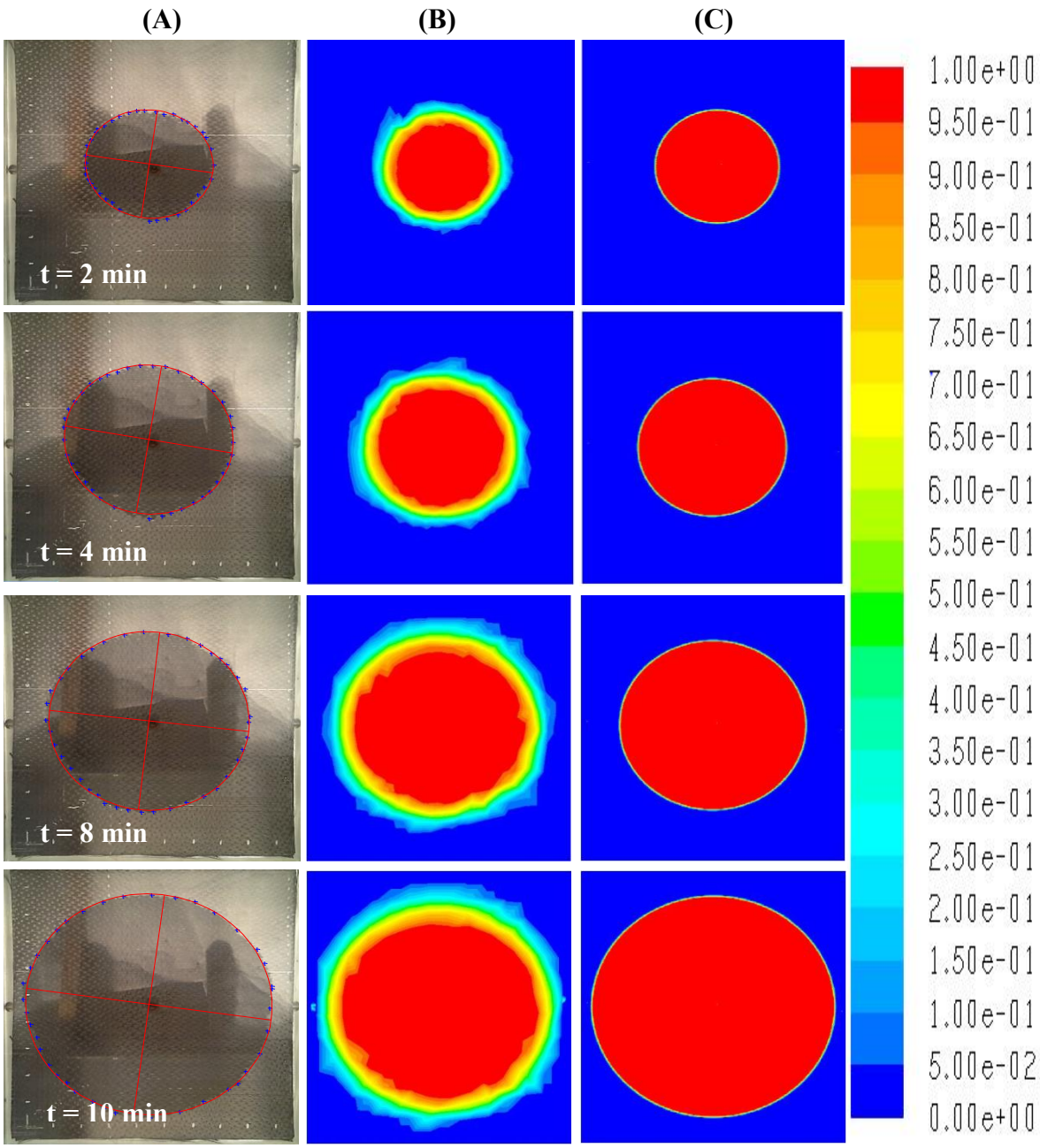

Figure 7.6: Tackified IM7-4HS Advancing Flow Front Comparisons. (A) MATLAB processed experimental flow front propagation with best fit ellipse. (B) Rough mesh numerical advancing front solutions. (C) Fine mesh numerical advancing front solutions. Numerical solutions displaying volume fraction of the test fluid, SAE 40 oil (red) displacing air (blue).

As expected, the numerical results match well with the experimental results. During actual infusions, the flow front was seen to have some "fingering" characteristics due to the variable

porosity produced from the fabric geometry (including inter-tow and intra-tow porosities). These results are not seen in the numerical simulations, as the preforms were modeled as porous media of known permeability rather than geometrical representations of the fabric architecture.

A simple numerical mesh refinement study was conducted and the results were shown. Coarsely meshed geometries were run with 1,225 elements and compared with a fine mesh refinement of 319,000 elements. The total fill time was mostly time step dependent and not iteration dependent, so the simulation time was similar for the coarse and fine mesh cases. The resolution of the flow front boundary was much better for the fine mesh because of the ability to more accurately position the volume fraction of fluid in a smaller computational cell. The time step was chosen as 1E-3s to start the simulation and once the simulation was advancing steadily an adaptive time step was adopted to simulate the advancing flow front more rapidly while continuing to keep good convergence.

The simulations for both non-tackified and tackified cases were also run to investigate the resin runner effect on each mold fill case. Numerical solutions displaying these results can be seen for the non-tackified IM7-4HS sample in Figure 7.7, while Figure 7.8 shows a similar set of results for the tackified IM7-4HS sample. Both figures contain 4 images labeled (A)-(F) showing the volume fraction of the permeating test fluid displacing air in the mold at selected time steps.

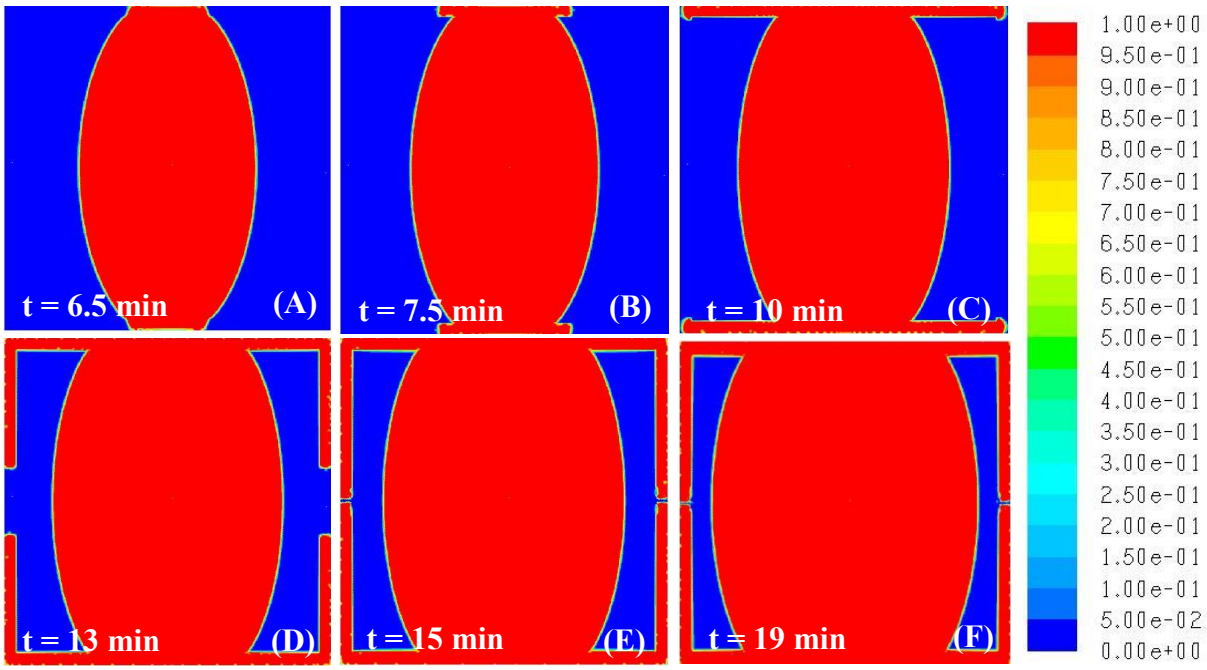

Figure 7.7: Numerical Solution of Non-tackified IM7-4HS Mold Fill Including Resin Runner Effect. Volume fraction of test fluid (red) displacing air (blue) at advancing time steps (A)-(F).

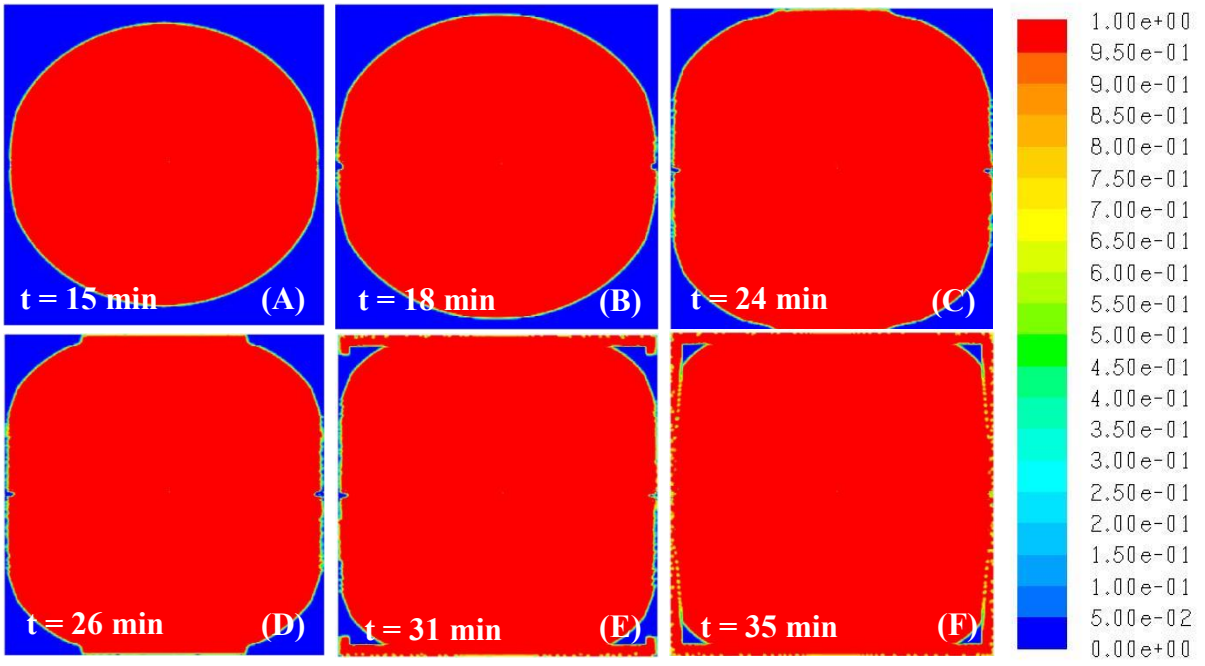

Figure 7.8: Numerical Solution of Tackified IM7-4HS Mold Fill Including Resin Runner Effect. Volume fraction of test fluid (red) displacing air (blue) at advancing time steps (A)-(F).

The simulated effects of the resin runner for non-tackified and tackified fabrics matched the experimental cases well. The channel acted as a low resistance to flow region when the oil had reached that part of the geometry. Once the resin runner was reached, the oil flow race tracked around the outside of the mold to the pressure outlets. In a closed mold process, this would give the illusion of a filled mold because resin would be leaving the outlet but the preform would not be fully saturated at this point. Further, the corners of the preform take a significantly long time to fill because of the pressures present there and it is indicative of optimization that could have been done before the mold was created, if this was designed for actual RTM application.

7.3 Conclusions

In this chapter, a radial flow fixture was described and experiments were conducted on warp aligned IM7-4HS preforms with and without tackifier. In these experiments, advancing elliptical flow fronts were visually tracked in an unsaturated mold filling scenario. Image analysis code was prepared that allowed the orientation of first principal permeability (β) to be visually determined and the in-plane permeabilities to be calculated from formulation from Weitzenböck et al. [81], [193]. The inclusion of an inter-layer tackifier was seen to have similar effects to those reported by Rohatgi and Lee [6] and Estrada et al. [11], where permeability was reduced with increasing tackifier content and mold filling times increased. For the non-tackified IM7-4HS, the orientation of the first principal permeability was close to 90° for each run, displaying permeation was fastest in the weft fabric direction. However, with tackified samples, the orientation of principal permeability was not found to be variable for each measurement, but the warp/weft permeability ratio was found to be close to 1, creating less significance for the β

angle. Notably, this effect was also seen from the saturated parallel flow experiments presented in Chapter 4. Also, the tackified IM7-4HS exhibited more isotropic flow front ellipses (more circular) than the non-tackified samples. This effect is attributed to the tackifier blocking the flow channels between tows throughout the fabric, creating a more uniform advancing flow front than those that are subject only to the anisotropic fabric architecture (i.e. non-tackified flow fronts). Interestingly, much like the results in Chapter 4, the permeability was reduced more significantly in the weft fabric direction than the warp. It should be noted that the radial unsaturated measurements produced permeabilities much lower than saturated and unsaturated parallel flow measurements of Chapter 4 and 5, respectively. Permeability measurements from radial flow techniques have also been reported by researchers to be lower compared to parallel flow measurements of the same preform, while additional sources of error have been discussed to be at play in the radial technique [67]. Thus, the radial flow method, while being very useful in quickly defining the full in-plane permeability tensor and β angle, may be less reliable than the channel flow techniques for determining permeability.

Numerical mold fill models of both the tackified and non-tackified IM7-4HS were also produced using the experimentally measured permeability values. The models displayed good correlation between experimental and numerical mold fills and also were used to display effects seen from resin runners. The effect of tackifier points to need for characterization of such materials for accurate mold fill modeling in LCM. The presence of tackifier can not only change preform permeability, it can significantly alter the advancing front shape or flow profile of the infiltrating resin. Future work would involve validating these measurements and conclusions for the IM7-4HS material on a complex geometry mold fill. Also, to expand this work further for composite

manufacturing modeling, a method of geometrical characterization of the tackified fabric should be developed so that CFD can be used to predict the permeability through a known geometry, alleviating the need for experimental work.

8. Summary and Conclusions

8.1 Summary and Conclusions

In this study, a compaction and permeability characterization of a four harness satin carbon fabric (IM7-4HS) with and without a unique low areal weight inter-layer tackifier (Cytec CYCOM PR 520-1) was conducted. Characterization included dry and wetted compaction experiments, saturated in-plane and through-thickness permeability measurements, high flow rate saturated measurements, unsaturated parallel flow measurements, and radial flow unsaturated measurements. These characterization methods were used to investigate the effects of tackifier, preform debulking, preform layup, saturation, flow rate, capillary pressure, and fluid type on the processing for LCM and RTM applications. Further novel contributions in this study include results on the effect of tackifier on principal permeability orientation, a modified experimental capillary pressure technique for permeability correction, and an investigation on the applicability of a specific criterion for defining non-Darcy flow in high flow rate permeability measurements.

Specifically, the investigations revealed that the addition of the inter-layer tackifier significantly reduced the permeability of IM7-4HS preforms compared to non-tackified samples, while compaction was less affected. Tackifier also significantly altered the orientation of the principal in-plane permeabilities. Additional processing of tackified fabric under heat and pressure cured the tackifier to produce debulked preforms. These debulked samples were very stiff and provided large resistance to compaction pressures and nesting. Consequently, debulked preforms produced an interesting behavior in permeability, where the resisted fiber nesting characteristic provided

larger inter-tow flow channels than unprocessed tackified samples. This resulted in permeabilities generally higher than the unprocessed tackified samples and similar to the non-tackified material for both in-plane and transverse flow directions. Additionally, it was found that the directional biases of the in-plane permeability tensor could be tailored by altering the preform layup stacking sequence.

Further investigations compared unsaturated parallel flow permeability measurements with oil and a low-viscosity epoxy resin. It was found that fluid type had little effect on permeability on the non-tackified preforms, unless injection pressure was very low where capillary pressures are significant. However, the tackified preforms showed a large sensitivity to the fluid type, and it was hypothesized that the addition of tackifier alters the wettability of the fiber reinforcement depending on fluid type, and also encourages more intra-tow flow, which increases capillary action. Additional high flow rate testing showed the possibility of non-Darcy flow during infusions. From these results, it was concluded that all LCM infusions should be considered based on fluid velocity or flow rate. Depending on the velocity, capillary pressures may be significant or neglected, inertial effects may require a Forchheimer relationship to describe the flow, or Darcy's law may fit the application well.

For consideration of RTM and other LCM applications, the use of tackifier strongly aids in preforming, holding fiber orientation and part shape, and resisting deformation in high pressure or flow rate infusions. Although, the addition of tackifier will also reduce permeability and increase mold fill times. Debulking can further hold preform shape as the cured tackifier fuses the reinforcement fiber network together. However, the mold used must be robust enough to

overcome the large resistance to compaction the debulked preform provides. Also, if debulking is considered, the injection resin should be chemically compatible, if not the same, as the tackifier system to avoid void formations, poor fiber/matrix interfaces, and ultimately low part performance.

8.2 Future Work

For a more robust characterization of the IM7-4HS preforms, specialized test fixtures should be produced to measure permeability of deformed geometry native to complex molds, including sheared and curved portions of the reinforcement. Further investigations should be made to quantify the void formation in IM7-4HS preforms with and without the inter-layer tackifier, as well as in the debulked preforms after infusions. Aside from the tackifier showing aid in preform creation, the addition of tackifier, especially pre-cured in the debulk process, may result in irregular flows and local blockages leading to possible void formations. To further investigate the high flow rate experiments, unsaturated infusions should be investigated with a robust fixture that will not permit displacement or race-tracking. Also, a visualization window should be introduced so that the precise pressure or flow rate can be defined where fiber shift and washout initiate for non-tackified and tackified preforms. This would be of very practical interest for RTM applications and material selection consideration.

While this study has shown the applicability of permeability measurements to simple numerical mold fill solutions, further work should look to predict permeability based on geometry and other infusion parameters. This would alleviate the need for expensive, time consuming manual characterization techniques. Furthermore, the physical geometry of tackifier should be modeled

to predict the altered flow and permeability through tackified fabrics. These permeability solutions could then be implemented into Darcian flow based solver for mold fill solutions.

Ultimately, a unified reinforcement draping and resin flow simulation tool would create an efficient and ideal approach to process modeling. Here, reinforcement geometry could be used as the input while nesting, shear, and other deformations induced from preforming could be solved mechanically. Then, with the altered preform geometry and infusion parameters known, the permeating flow could be simulated with computational fluid dynamics. This would be a powerful tool for process modeling, although further manual characterization must be done before this technology is computationally available.

APPENDICES

Appendix A: Additional Saturated Permeability Measurement Data

A.I Non-tackified Laminate (6 ply) Permeability

Table A. 1 Non-tackified Laminate (6 ply) Warp and Weft Direction Saturated Permeability

	0 deg. (S_{xx} in m^2)			90 deg. (S_{yy} in m^2)		
Run \Vf	50%	55%	60%	50%	55%	60%
1	4.05E-11	2.48E-11	1.58E-11	4.73E-11	2.30E-11	1.19E-11
2	5.17E-11	2.86E-11	1.66E-11	4.16E-11	1.94E-11	9.62E-12
3	5.73E-11	3.00E-11	1.66E-11	3.86E-11	2.23E-11	1.36E-11
4	5.56E-11	2.76E-11	1.46E-11	3.81E-11	2.09E-11	1.21E-11
5	4.81E-11	3.06E-11	2.02E-11	5.28E-11	2.77E-11	1.53E-11
Avg	**5.06E-11**	**2.83E-11**	**1.68E-11**	**4.37E-11**	**2.27E-11**	**1.25E-11**
StDev	6.70E-12	2.29E-12	2.09E-12	6.28E-12	3.14E-12	2.11E-12
CV (%)	13.22	8.09	12.47	14.37	13.85	16.90

Table A. 2: Non-tackified Laminate (6 ply) Off-axis Direction Saturated Permeability

	45 deg. (S_{xx}' in m^2)		
Run \Vf	50%	55%	60%
1	3.99E-11	2.25E-11	1.33E-11
2	3.74E-11	1.94E-11	1.07E-11
3	4.58E-11	2.43E-11	1.37E-11
4	5.91E-11	2.84E-11	1.45E-11
5	5.59E-11	2.66E-11	1.35E-11
Avg	**4.76E-11**	**2.42E-11**	**1.31E-11**
StDev	9.59E-12	3.51E-12	1.44E-12
CV (%)	20.13	14.49	10.94

Table A. 3: Non-tackified Laminate (6 ply) Principal Saturated Permeability

	S_{11} (1st Principal Permeability in m^2)			S_{22} (2nd Principal Permeability in m^2)		
Run \Vf	50%	55%	60%	50%	55%	60%
1	4.92E-11	2.56E-11	1.59E-11	3.87E-11	2.22E-11	1.18E-11
2	5.72E-11	3.05E-11	1.74E-11	3.61E-11	1.75E-11	8.87E-12
3	5.75E-11	3.04E-11	1.72E-11	3.84E-11	2.19E-11	1.30E-11
4	6.19E-11	2.96E-11	1.50E-11	3.18E-11	1.89E-11	1.17E-11
5	5.64E-11	3.21E-11	2.27E-11	4.45E-11	2.62E-11	1.28E-11
Avg	**5.64E-11**	**2.96E-11**	**1.76E-11**	**3.79E-11**	**2.13E-11**	**1.16E-11**
StDev	4.60E-12	2.45E-12	2.97E-12	4.61E-12	3.37E-12	1.67E-12
CV (%)	8.16	8.26	16.86	12.17	15.80	14.33

Table A. 4: Non-tackified Laminate (6 ply) Through-thickness Saturated Permeability

Through-thickness (S_{zz} in m^2)								
Vf	Run 1	Run 2	Run 3	Run 4	Run5	**Avg.**	StDev	CV (%)
50%	1.43E-12	1.49E-12	1.51E-12	2.08E-12	2.01E-12	**1.70E-12**	3.15E-13	18.53
55%	7.71E-13	8.40E-13	7.31E-13	1.01E-12	1.09E-12	**8.89E-13**	1.56E-13	17.56
60%	3.76E-13	4.40E-13	3.78E-13	5.26E-13	6.24E-13	**4.69E-13**	1.06E-13	22.66

A.II Debulked Laminate (6 ply) Permeability

Table A. 5: Debulked Laminate (6 ply) Warp and Weft Direction Saturated Permeability

	0 deg. (S_{xx} in m^2)			90 deg. (S_{yy} in m^2)		
Run \Vf	50%	55%	60%	50%	55%	60%
1	3.39E-11	2.24E-11	1.54E-11	9.42E-11	2.67E-11	8.45E-12
2	6.15E-11	2.45E-11	1.06E-11	5.55E-11	2.24E-11	9.76E-12
3	7.39E-11	2.72E-11	1.09E-11	6.07E-11	1.69E-11	5.25E-12
4	3.51E-11	1.62E-11	7.99E-12	9.46E-11	3.42E-11	1.35E-11
5	3.20E-11	1.76E-11	1.02E-11	4.95E-11	2.15E-11	1.00E-11
Avg.	**4.73E-11**	**2.16E-11**	**1.10E-11**	**7.09E-11**	**2.43E-11**	**9.39E-12**
StDev	1.92E-11	4.63E-12	2.70E-12	2.18E-11	6.52E-12	2.98E-12
CV (%)	40.61	21.43	24.53	30.75	26.78	31.69

Table A. 6: Debulked Laminate (6 ply) Off-axis Direction Saturated Permeability

	45 deg. (S_{xx}' in m^2)		
Run \Vf	50%	55%	60%
1	3.13E-11	1.51E-11	7.74E-12
2	4.18E-11	2.05E-11	1.07E-11
3	3.86E-11	2.21E-11	1.33E-11
4	3.69E-11	2.08E-11	1.23E-11
5	3.45E-11	1.96E-11	1.17E-11
Avg.	**3.66E-11**	**1.96E-11**	**1.11E-11**
StDev	3.97E-12	2.68E-12	2.13E-12
CV (%)	10.83	13.66	19.07

Table A. 7: Debulked Laminate (6 ply) Principal Saturated Permeability

	S_{11} (1st Principal Permeability in m^2)			S_{22} (2nd Principal Permeability in m^2)		
Run \Vf	50%	55%	60%	50%	55%	60%
1	1.09E-10	3.42E-11	1.74E-11	1.95E-11	1.49E-11	6.49E-12
2	7.55E-11	2.66E-11	1.08E-11	4.15E-11	2.03E-11	9.51E-12
3	9.67E-11	2.72E-11	1.40E-11	3.79E-11	1.69E-11	2.14E-12
4	1.06E-10	3.52E-11	1.39E-11	2.40E-11	1.52E-11	7.58E-12
5	5.15E-11	2.15E-11	1.17E-11	3.00E-11	1.76E-11	8.50E-12
Avg.	**8.76E-11**	**2.89E-11**	**1.36E-11**	**3.06E-11**	**1.70E-11**	**6.84E-12**
StDev	2.40E-11	5.73E-12	2.53E-12	9.19E-12	2.19E-12	2.86E-12
CV (%)	27.38	19.80	18.65	30.05	12.93	41.78

Table A. 8: Debulked Laminate (6 ply) Through-thickness Saturated Permeability

Through-thickness (S_{zz} in m^2)								
Vf	Run 1	Run 2	Run 3	Run 4	Run5	**Avg.**	StDev	CV (%)
50%	9.44E-13	8.56E-13	9.20E-13	9.47E-13	1.09E-12	**9.51E-13**	8.45E-14	8.88
55%	5.76E-13	5.44E-13	5.92E-13	6.01E-13	6.74E-13	**5.97E-13**	4.80E-14	8.04
60%	3.67E-13	3.60E-13	3.95E-13	3.97E-13	4.36E-13	**3.91E-13**	3.01E-14	7.70

A.III Non-Tackified Warp Aligned (6 ply) Permeability

Table A. 9: Non-Tackified Warp Aligned (6 ply) Warp and Weft Direction Saturated Permeability

	0 deg. (S_{xx} in m^2)			90 deg. (S_{yy} in m^2)		
Run \Vf	50%	55%	60%	50%	55%	60%
1	2.32E-11	1.32E-11	7.89E-12	6.28E-11	3.36E-11	1.89E-11
2	2.57E-11	1.89E-11	1.43E-11	6.11E-11	3.82E-11	2.49E-11
3	3.10E-11	1.71E-11	9.95E-12	7.28E-11	3.71E-11	2.01E-11
Avg.	**2.67E-11**	**1.64E-11**	**1.07E-11**	**6.56E-11**	**3.63E-11**	**2.13E-11**
StDev	3.98E-12	2.92E-12	3.26E-12	6.31E-12	2.44E-12	3.15E-12
CV (%)	14.92	17.77	30.48	9.62	6.72	14.81

Table A. 10: Non-Tackified Warp Aligned (6 ply) Off-axis Saturated Permeability

	45 deg. (S_{xx}' in m^2)		
Run \Vf	50%	55%	60%
1	4.63E-11	2.61E-11	1.55E-11
2	4.54E-11	2.72E-11	1.70E-11
3	5.84E-11	3.30E-11	1.96E-11
Avg.	**5.00E-11**	**2.88E-11**	**1.74E-11**
StDev	7.27E-12	3.69E-12	2.06E-12
CV (%)	14.53	12.84	11.86

Table A. 11: Non-Tackified Warp Aligned (6 ply) Principal Saturated Permeability

	S_{11} (1st Principal Permeability in m^2)			S_{22} (2nd Principal Permeability in m^2)		
Run \Vf	50%	55%	60%	50%	55%	60%
1	6.31E-11	3.40E-11	1.93E-11	2.29E-11	1.28E-11	7.50E-12
2	6.12E-11	3.83E-11	2.55E-11	2.56E-11	1.88E-11	1.37E-11
3	7.38E-11	3.87E-11	2.19E-11	3.00E-11	1.55E-11	8.19E-12
4						
5						
Avg.	**6.60E-11**	**3.70E-11**	**2.22E-11**	**2.62E-11**	**1.57E-11**	**9.80E-12**
StDev	6.79E-12	2.64E-12	3.12E-12	3.58E-12	2.98E-12	3.40E-12
CV (%)	10.28	7.13	14.05	13.67	18.99	34.66

Table A. 12: Non-Tackified Warp Aligned (6 ply) Through-thickness Saturated Permeability

Through-thickness (S_{zz} in m^2)					
Vf	Run 1	Run 2	**Avg.**	StDev	CV (%)
50%	1.21E-12	1.14E-12	**1.18E-12**	4.71E-14	3.99
55%	6.58E-13	6.18E-13	**6.38E-13**	2.84E-14	4.46
60%	3.43E-13	3.17E-13	**3.30E-13**	1.83E-14	5.54

A.IV Tackified Warp Aligned (6 ply) Permeability

Table A. 13: Tackified Warp Aligned (6 ply) Warp and Weft Direction Saturated Permeability

	0 deg. (S_{xx} in m^2)			90 deg. (S_{yy} in m^2)		
Run \Vf	50%	55%	60%	50%	55%	60%
1	1.99E-11	1.04E-11	5.73E-12	2.934E-11	1.614E-11	8.915E-12
2	2.51E-11	1.34E-11	7.59E-12		1.624E-11	
3	3.14E-11	1.84E-11	1.13E-11		1.64E-11	
4	2.56E-11	1.35E-11	7.49E-12			
5	2.55E-11	1.39E-11	8.04E-12			
6		1.64E-11				
7	2.22E-11	1.12E-11	6.25E-12			
8		1.36E-11				
Avg.	**2.50E-11**	**1.39E-11**	**7.74E-12**	**2.93E-11**	**1.63E-11**	**8.92E-12**
StDev	3.88E-12	2.60E-12	1.97E-12	-	1.51E-13	-
CV (%)	15.54	18.72	25.44	-	0.93	-

Table A. 14: Tackified Warp Aligned (6 ply) Off-axis Direction Saturated Permeability

	45 deg. (S_{xx}' in m^2)		
Run \Vf	50%	55%	60%
1	3.354E-11	1.871E-11	1.138E-11
2		2.044E-11	
3		2E-11	
Avg.	**3.35E-11**	**1.97E-11**	**1.14E-11**
StDev	-	9.05E-13	-
CV (%)	-	4.59	-

Table A. 15: Tackified Warp Aligned (6 ply) Principal Saturated Permeability

	S_{11} (1st Principal Permeability in m^2)			S_{22} (2nd Principal Permeability in m^2)		
Run \Vf	50%	55%	60%	50%	55%	60%
1	3.383E-11	1.887E-11	1.142E-11	2.101E-11	1.120E-11	5.535E-12
2		2.045E-11			1.224E-11	
3		2E-11			1.28E-11	
Avg.	**3.38E-11**	**1.98E-11**	**1.14E-11**	**2.10E-11**	**1.21E-11**	**5.54E-12**
StDev	-	8.06E-13	-	-	8.22E-13	-
CV (%)	-	4.08	-	-	6.80	-

Table A. 16: Tackified Warp Aligned (6 ply) Through-thickness Saturated Permeability

Through-thickness (S_{zz} in m^2)					
Vf	Run 1	Run 2	**Avg.**	StDev	CV (%)
50%	8.21E-13	7.89E-13	**1.18E-12**	4.71E-14	3.99
55%	4.34E-13	3.94E-13	**6.38E-13**	2.84E-14	4.46
60%	2.09E-13	1.87E-13	**3.30E-13**	1.83E-14	5.54

A.V Debulked Laminate (12 ply) Permeability

Table A. 17: Debulked Laminate (12 ply) Warp and Weft Direction Saturated Permeability

	0 deg. (S_{xx} in m^2)			90 deg. (S_{yy} in m^2)		
Run \Vf	50%	55%	60%	50%	55%	60%
1	3.94E-11	1.91E-11	9.82E-12	4.43E-11	2.25E-11	1.21E-11
2	4.07E-11	1.85E-11	9.03E-12	3.03E-11	1.63E-11	9.26E-12
3	2.64E-11	1.17E-11	5.53E-12	3.05E-11	1.64E-11	9.29E-12
4	2.51E-11	1.29E-11	7.06E-12	3.05E-11	1.63E-11	9.15E-12
Avg.	**3.29E-11**	**1.55E-11**	**7.86E-12**	**3.39E-11**	**1.79E-11**	**9.95E-12**
StDev	8.27E-12	3.79E-12	1.94E-12	6.94E-12	3.09E-12	1.44E-12
CV (%)	25.15	24.36	24.65	20.46	17.29	14.47

Table A. 18: Debulked Laminate (12 ply) Through-thickness Saturated Permeability

Through-thickness (S_{zz} in m^2)						
Vf	Run 1	Run 2	Run 3	**Avg.**	StDev	CV (%)
50%	9.89E-13	9.53E-13	1.12E-12	**1.02E-12**	8.76E-14	8.59
55%	4.79E-13	4.75E-13	5.63E-13	**5.06E-13**	5.00E-14	9.89
60%	2.47E-13	2.52E-13	3.01E-13	**2.67E-13**	3.00E-14	11.27

A.VI Non-tackified Laminate (12 ply) Permeability

Table A. 19: Non-tackified Laminate (12 ply) Warp Direction Saturated Permeability

	0 deg. (S_{xx} in m^2)		
Run \Vf	50%	55%	60%
1	4.70E-11	2.95E-11	1.92E-11
Avg.	**-**	**-**	**-**
StDev	-	-	-
CV (%)	-	-	-

Table A. 20: Non-tackified Laminate (12 ply) Through-thickness Saturated Permeability

Through-thickness (S_{zz} in m^2)					
Vf	Run 1	Run 2	**Avg.**	StDev	CV (%)
50%	1.79E-12	2.29E-12	**2.04E-12**	3.52E-13	17.25
55%	6.56E-13	9.33E-13	**7.95E-13**	1.96E-13	24.64
60%	2.62E-13	4.11E-13	**3.36E-13**	1.05E-13	31.28

A.VII In-Plane Permeability Power Law Fits

Table A. 21: Power Law Fits for Saturated In-plane Permeability Measurements

IM7-4HS Preform Type	**S_{xx}**		**S_{yy}**		**S_{xx}'**	
	a	**b**	**a**	**b**	**a**	**b**
6 Ply Warp Aligned Non-tackified	8.28E-13	-5.00	9.11E-13	-6.17	9.01E-13	-5.79
6 Ply Warp Aligned Tackified	2.94E-13	-6.42	3.21E-13	-6.53	5.59E-13	-5.29
6 Ply Non-tackified Laminate	7.55E-13	-6.07	3.75E-13	-6.86	3.56E-13	-7.06
6 Ply Debulked Laminate	1.84E-13	-7.99	3.24E-14	-1.11	3.98E-13	-6.52
12 ply Debulked Laminate	1.43E-13	-7.85	3.20E-13	-6.73	-	-

IM7-4HS Preform Type	**S_{11}**		**S_{22}**	
	a	**b**	**a**	**b**
6 Ply Warp Aligned Non-tackified	1.05E-12	-5.98	6.25E-13	-5.39
6 Ply Warp Aligned Tackified	5.51E-13	-5.95	1.40E-13	-7.29
6 Ply Non-tackified Laminate	6.65E-13	-6.39	4.36E-13	-6.46
6 Ply Debulked Laminate	6.89E-14	-1.03	1.12E-13	-8.18
12 ply Debulked Laminate	-	-	-	-

Appendix B: Additional Fluid Effects Measurement Data

B.I Fluid Surface Tension Measurement Data

Table B. 1: SAE Oil and SC-15 Part A Fluid Surface Tension Measurement Data

Fluid: SAE 40 Motor Oil

Run #	Maximum Wt. (mg)	σ' (mg/mm)	c_f	σ (mg/mm)	σ (dyne/cm)
1	421.71	3.51	0.847	2.98	29.18
2	420.81	3.51	0.847	2.97	29.12
3	421.19	3.51	0.847	2.97	29.14
Average	**421.24**	**3.51**	**0.847**	**2.97**	**29.15**
StDev	0.45	0.00	0.000	0.00	0.03
CV (%)	0.11	0.11	0.001	0.11	0.11

Fluid: SC-15 Part A (Epoxy only)

Run #	Maximum Wt. (mg)	σ' (mg/mm)	c_f	σ (mg/mm)	σ (dyne/cm)
1	469.03	3.91	0.844	3.30	32.36
2	469.73	3.91	0.844	3.30	32.41
3	470.52	3.92	0.844	3.31	32.46
Average	**469.76**	**3.91**	**0.844**	**3.30**	**32.41**
StDev	0.75	0.01	0.000	0.01	0.05
CV (%)	0.16	0.16	0.001	0.16	0.16

B.II Du Noüy Ring Sample Wetting Graphs

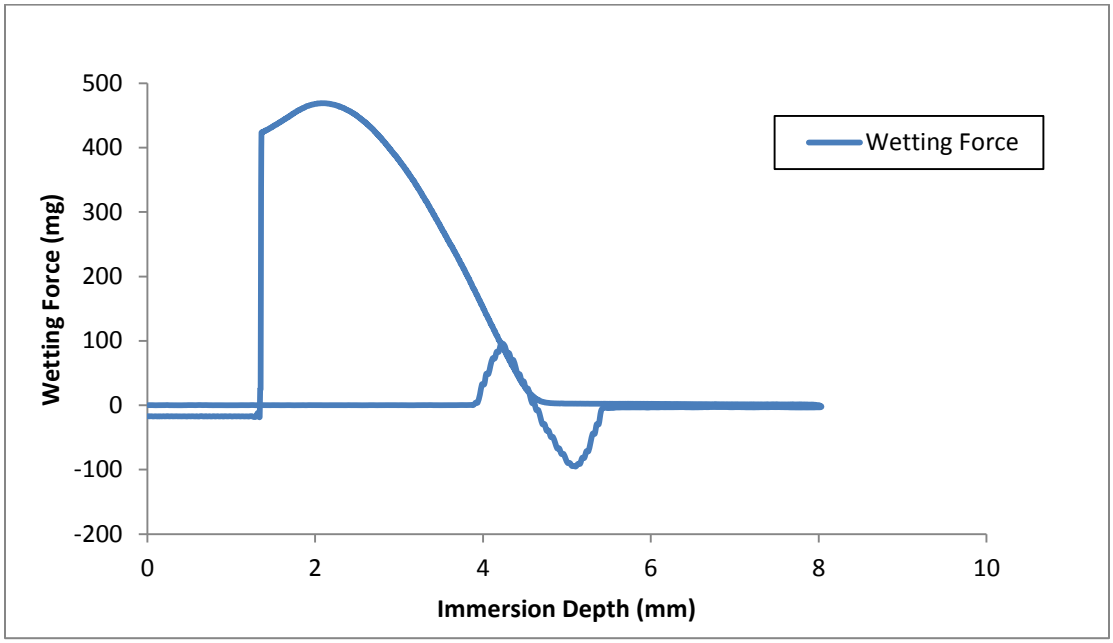

Figure B. 1: Wetting Force versus Immersion Depth of Du Noüy Ring in SC-15 Part A

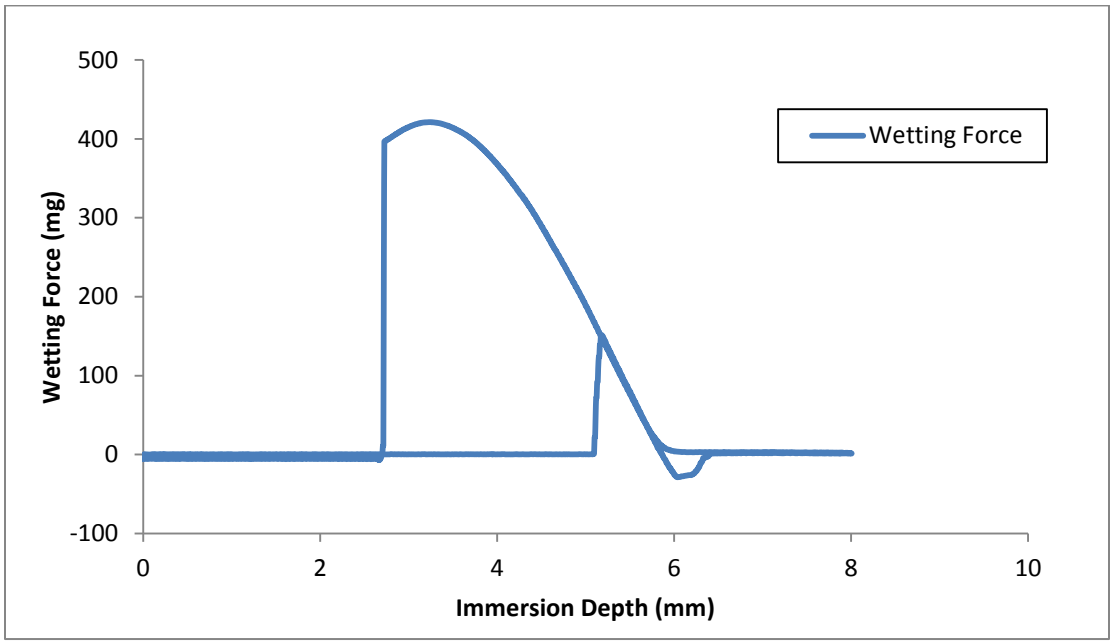

Figure B. 2: Wetting Force versus Immersion Depth of Du Noüy Ring in SAE 40 Oil

B.III Fiber Diameter Measurement Data

Table B. 2: IM7 Fiber Diameter Data from Laser-scan Micromemeter Measurements

IM7 Fiber Diameter Measurements (µm)							
Sample #	**Point 1**	**Point 2**	**Point 3**	**Sample Avg.**	**Sample StDev Among 3 Pts.**	**CV (%) Among 3 Pts.**	**Perimeter (from Avg.)**
1	5.22	5.27	5.38	5.29	0.08	1.55	16.62
2	5.22	5.25	5.2	5.22	0.03	0.48	16.41
3	8.35	7.98	7.82	8.05	0.27	3.38	25.29
4	5.63	5.73	5.71	5.69	0.05	0.93	17.88
5	6.21	5.52	5.6	5.78	0.38	6.53	18.15
6	5.44	5.38	5.65	5.49	0.14	2.58	17.25
7	5.35	5.44	5.29	5.36	0.08	1.41	16.84
8	5.68	5.61	6.8	6.03	0.67	11.07	18.94
9	5.64	5.58	5.58	5.60	0.03	0.62	17.59
10	5.51	5.75	5.69	5.65	0.12	2.21	17.75
11	5.59	5.47	5.38	5.48	0.11	1.92	17.22
12	5.69	6.63	6.71	6.34	0.57	8.94	19.93
13	5.8	5.7	5.94	5.81	0.12	2.07	18.26
14	5.51	5.44	5.41	5.45	0.05	0.94	17.13
15	5.59	5.5	5.41	5.50	0.09	1.64	17.28
16	5.22	5.15	5.19	5.19	0.04	0.68	16.29
17	5.38	5.49	5.39	5.42	0.06	1.12	17.03
18	5.54	5.59	5.77	5.63	0.12	2.15	17.70
19	5.55	5.58	5.58	5.57	0.02	0.31	17.50
20	5.5	5.65	5.6	5.58	0.08	1.37	17.54
21	5.35	5.37	5.4	5.37	0.03	0.47	16.88
22	5.51	6.14	5.34	5.66	0.42	7.44	17.79
23	5.92	5.89	5.92	5.91	0.02	0.29	18.57
24	5.4	5.35	5.45	5.40	0.05	0.93	16.96
25	5.38	5.32	5.3	5.33	0.04	0.78	16.76
26	5.65	5.64	5.67	5.65	0.02	0.27	17.76
27	6.06	5.94	6.07	6.02	0.07	1.20	18.92
28	5.72	5.66	5.83	5.74	0.09	1.50	18.02
29	5.19	5.24	5.23	5.22	0.03	0.51	16.40
Average	5.65	5.66	5.70	5.67	0.13	2.25	17.82
Average without #3	5.55	5.58	5.62	5.59	0.13	2.21	17.55

B.IV Micro-Wilhelmy Sample Status List

Table B. 3: Micro-Wilhelmy Sample Usage Statuses

Sample ID	Test Fluid	Advancing Data	Receding Data
Fiber-1	SAE 40 Oil	Used	Used
Fiber-2	SAE 40 Oil	Used	Used
Fiber-3	SAE 40 Oil	Unused	Unused
Fiber-4	SAE 40 Oil	Used	Used
Fiber-5	SAE 40 Oil	Used	Used
Fiber-6	SAE 40 Oil	Used	Used
Fiber-7	SAE 40 Oil	Used	Used
Fiber-8	SAE 40 Oil	Unused	Unused
Fiber-9	SAE 40 Oil	Unused	Unused
Fiber-10	SAE 40 Oil	Used	Unused
Fiber-11	SAE 40 Oil	Used	Used
Fiber-12	SAE 40 Oil	Used	Used
Fiber-13	SAE 40 Oil	Used	Used
Fiber-14	SC-15	Unused	Unused
Fiber-15	SC-15	Unused	Unused
Fiber-16	SC-15	Unused	Unused
Fiber-17	SC-15	Unused	Unused
Fiber-18	SC-15	Unused	Unused
Fiber-19	SC-15	Unused	Unused
Fiber-20	SC-15	Unused	Unused
Fiber-21	SC-15	Unused	Unused
Fiber-22	SC-15 Part A only	Used	Used
Fiber-23	SC-15 Part A only	Used	Used
Fiber-24	SC-15 Part A only	Used	Used
Fiber-25	SC-15 Part A only	Used	Used
Fiber-26	SC-15 Part A only	Used	Used
Fiber-27	SC-15 Part A only	Used	Used
Fiber-28	SC-15 Part A only	Used	Used
Fiber-29	SC-15 Part A only	Used	Unused

B.V Micro-Wilhelmy Fiber Contact Angle Measurement Data

Table B. 4: IM7 Fiber Contact Angle Data from Micro-Wilhelmy Measurements with SAE 40 Oil

Sample ID	Avg. Adv. Wt. (mg)	Avg. Recd. Wt. (mg)	Diameter (µm)	Perimeter (cm)	Advance cos(θ)	Advance θ (deg.)	Recede cos(θ)	Recede θ (deg.)
Fiber-22	0.036	0.051	5.663	1.779E-03	0.823	34.638	0.645	49.827
Fiber-23	0.032	0.040	5.910	1.857E-03	0.866	29.976	0.798	37.019
Fiber-24	0.035	0.044	5.400	1.696E-03	0.812	35.666	0.711	44.713
Fiber-25	0.036	0.047	5.333	1.676E-03	0.800	36.833	0.664	48.385
Fiber-26	0.036	0.045	5.653	1.776E-03	0.818	35.129	0.716	44.296
Fiber-27	0.040	0.056	6.023	1.892E-03	0.806	36.323	0.628	51.069
Fiber-28	0.046	0.062	5.737	1.802E-03	0.718	44.136	0.510	59.353
Fiber-29	0.045	NA	5.220	1.640E-03	0.674	47.595	NA	NA
Avg.	**0.038**	**0.049**	**5.618**	**1.765E-03**	**0.790**	**37.537**	**0.667**	**47.809**
StDev	0.005	0.008	0.281	8.837E-05	0.062	5.626	0.090	6.912
CV (%)	13.101	15.409	5.008	5.008E+00	7.882	14.987	13.437	14.458

B.VI Work of Adhesion Measurement Data

Table B. 5: Work of Adhesion Data for IM7 Fibers and SAE 40 Oil

SAE 40 Motor Oil			
Fiber ID	Work of Adhesion (erg/cm^2)		Hysteresis Ratio
	Advancing	Receding	
Fiber-1	46.12	45.62	0.99
Fiber-2	49.85	45.40	0.91
Fiber-4	47.30	44.60	0.94
Fiber-5	49.13	43.73	0.89
Fiber-6	49.78	44.02	0.88
Fiber-7	48.58	43.29	0.89
Fiber-10	50.92	NA	NA
Fiber-11	48.90	45.49	0.93
Fiber-12	53.53	48.65	0.91
Fiber-13	51.24	46.55	0.91
Avg.	**49.53**	**45.26**	**0.92**
StDev	1.98	1.55	0.03
CV(%)	3.99	3.42	3.39

Table B. 6: Work of Adhesion Data for IM7 Fibers and SC-15 Part A

SC-15 Epoxy (Part A only)			
Fiber ID	**Work of Adhesion (erg/cm^2)**		**Hysteresis Ratio**
	Advancing	**Receding**	
Fiber-22	59.07	53.32	0.90
Fiber-23	60.48	58.29	0.96
Fiber-24	58.74	55.44	0.94
Fiber-25	58.35	53.93	0.92
Fiber-26	58.92	55.61	0.94
Fiber-27	58.52	52.77	0.90
Fiber-28	55.67	48.93	0.88
Fiber-29	54.27	NA	NA
Avg.	**58.00**	**54.04**	**0.92**
StDev	1.89	2.69	0.03
CV(%)	3.25	4.98	2.99

Appendix C: MATLAB Scripts

C.I Principal Permeability Calculator

```
%Principal Permeability Calculator
%Stephen Sommerlot 3/29/13
%CVRC
%Code takes input from in-plane permeability testing data to find principal
%permeabilities S11 and  S22 and direction. Uses Mohr type transformation
%~~~~~~~~~~~~~~~~~~~~~~~~~~~~~~~~~~~~~~~~~~~~~~~~~~~~~~~~~~~~~~~~~~~~~~~~

%clears the workspace
clear all

%prompts user for permeability data input
Sxx = input('Enter Sxx permeability value: ');
Syy = input('Enter Syy permeability value: ');
Sxx_prime = input('Enter Sxx_prime permeability value (45 deg): ');

%computes off-axis permeability tensor component
Sxy = Sxx_prime - (.5*Sxx) - (.5*Syy)

%disaplys 2-D permeability tensor
S_bar = [Sxx, Sxy; Sxy, Syy]

%rotates S_bar to get S'_bar
deg = pi/4; % 45 deg
%deg = 0.523598776; % for 30 deg.
a_bar_T = [cos(deg), sin(deg); -sin(deg), cos(deg)];
a_bar = [cos(deg), -sin(deg); sin(deg), cos(deg)];

S_prime_bar = a_bar_T * S_bar * a_bar;

%finds principal permeabilities
prinicpal_permeabilities = eig(S_prime_bar)

S11 = max(prinicpal_permeabilities)
S22 = min(prinicpal_permeabilities)

%finds principal direction vector
[V,D] = eig(S_prime_bar)

%calculates angle of rotation (degrees), this is a very sensitive calculation
to %experimental scatter
beta_from_S_bar = (atan(2*S_bar(1,2)/(S_bar(1,1)-S_bar(2,2)))*180/pi)/2
```

C.II Image Processing Script for Radial Infusions

```
% Stephen Sommerlot
% CVRC
% 3/5/14
% Script for ellipse detection in radial-visual fabric flow fronts
% Uses ellipse calculations for unsaturated permeability determination
% based on paper: radial flow permeability measurement. Part A and B by
% Weitzenboeck
% Note: constant pressure injection formulation

% Prompt to get test data from user
material =  input('Enter Material Name: ', 's'); %'Non-Tackified IM7-4HS' OR
Tackified IM7-4HS
ply_num = 14; %input('Enter Ply Number: ');
Vf_in = 50; % input('Enter Material Vf(%): ');
Vf = Vf_in/100;
porosity = 1- Vf;
inlet_diameter = 3/8; % = input('Enter Punch Diameter (in.) Used for Inlet
(can be a fraction): ');
inlet_rad_m = (inlet_diameter*.0254)/2;
x0 = inlet_rad_m;
y0 = inlet_rad_m;
t0 = 0; %27;    % = input('Enter Initial Starting Time(s) Seen on Stopwatch
for Flow Propagation: '); % 27s for SS2
% t_cutoff = input('Enter Cutoff Time of Time for Pressure Data: '); %  1200s
for SS2

% Read test pressures from file, get average and StDev of inlet pressure
cd('C:\Users\sommerl4\Documents\MATLAB\Edge
Detect\coderdemo_edge_detection\Radial_Perm_Data')

psig_in_file = load('Pressure_Inlet_0-6PSIG_tack2.txt');
psig_in_full = psig_in_file(:,2);
time_in_full = psig_in_file(:,1);
% Uncomment for manual truncation
% time_diff = abs(time_in_full - t0);
% [idx idx]  = min(time_diff);
% closest_time_to_t0 = time_in_full(idx);
% time_diff2 =abs(time_in_full - t_cutoff);
% [idx2 idx2] = min(time_diff2);
% time_in = time_in_full(idx:idx2);
% psi_in = psig_in_full(idx:idx2);
avg_psi_in = mean(psig_in_full);
Pressure_StDev_psi = std(psig_in_full);
kpa_in = 6.89475729*psig_in_full;
avg_kpa_in = mean(kpa_in);
avg_pa_in = avg_kpa_in*1000;
Pressure_StDev = std(kpa_in);
pressure_CV = Pressure_StDev*100/avg_kpa_in;

cd('C:\Users\sommerl4\Documents\MATLAB\Edge
Detect\coderdemo_edge_detection\Radial_Perm_Data')

% load image
```

```
image = imread('IM7_tack_run2_3-7-14_10min.png');
imshow(image)

% gives user points to outline ellipse (10 in each quadrant)
[x,y] = ginput(40);

imshow(image)
hold on
plot(x,y, '+')
h = gca; % get current axis handle

% call ellipse finding function
% outputs structure of ellipse props
ellipse_t = fit_ellipse(x,y,h)

% break structure into numerics using ellipse function defs
ellipse_cell = struct2cell(ellipse_t);
a = cell2mat(ellipse_cell(1)); % sub axis (radius) of the X axis of the non-
tilt ellipse
b = cell2mat(ellipse_cell(2)) ; % sub axis (radius) of the Y axis of the non-
tilt ellipse
phi = cell2mat(ellipse_cell(3));  % orientation in radians of the ellipse
(tilt)
X0 = cell2mat(ellipse_cell(4));    % center at the X axis of the non-tilt
ellipse
Y0 = cell2mat(ellipse_cell(5));  % center at the Y axis of the non-tilt
ellipse
X0_in = cell2mat(ellipse_cell(6)); % center at the X axis of the tilted
ellipse
Y0_in = cell2mat(ellipse_cell(7));   % center at the Y axis of the tilted
ellipse
long_axis = cell2mat(ellipse_cell(8));  % size of the long axis of the
ellipse
short_axis = cell2mat(ellipse_cell(9)); % size of the short axis of the
ellipse

% beta angle (just phi converted to degrees)
beta = phi*(180/pi);

%for 45 deg. radius based on non-tilted ellipse (radius should be same just
%not rotated)
deg45 = pi/4;
x45 = a*cos(deg45);
y45 = b*sin(deg45);
r45 = sqrt(x45^2 + y45^2);

% get reference measurement
imtool(image)
distance = 9.1160e+01; %input('Enter Reference Distance Pixel Length: ');
uncomment this to user define distance
refdist = distance;

t_min_current = input('Enter Current Stopwatch Minutes on Image: ');
t_sec_current = input('Enter Current Stopwatch Seconds on Image: ');
t = ((t_min_current)*60 + t_sec_current) - t0;
```

```
n = .0254;
xf = ((a/refdist) * n); %m, radius of front in 1 direction
yf = ((b/refdist) * n); %m, radius of front in 3 direction
rf = ((r45/refdist) * n); %m radius of front in 2 direction

% Calculate Ns,Fs,A,D,phi2, C according to Weitzenboeck
N1 = (xf^2*(2*log(xf/x0) -1) + x0^2);
N2 = (rf^2*(2*log(rf/x0) -1) + x0^2);
N3 = (yf^2*(2*log(yf/y0) -1) + y0^2);

F1 = N1/t;
F2 = N2/t;
F3 = N3/t;

A = (F1 + F3)/2;
D = (F1 - F3)/2;

u=.24; %pa.s

C = ((u*porosity)/(4*avg_pa_in));

phi2 = .5*atan( (A/D) - ((A^2 - D^2)/(F2*D)) );
phi2_deg = phi2*180/pi

% find K1 and K1 unsaturated permeabilities at time
K1 = F1*((A-D)/(A - (D/cos(2*phi2))))*C
K2 = F3*((A+D)/(A + (D/cos(2*phi2))))*C

K1fromBeta = F1*((A-D)/(A - (D/cos(2*phi))))*C
K2fromBeta = F3*((A+D)/(A + (D/cos(2*phi))))*C

% from aligned ellipse
K1align = F1*C
K2align = F3*C
K45degalign = F2*C
%find Keff
zeta_deg = [0 15 60 90 105];
zeta = zeta_deg*pi/180;

Keff = (K1*K2) ./ (K1.*sin(zeta).^2  + K2.*cos(zeta).^2 )

% create vector at time(s) with both S11 and S22 perms for data storage
% purposes
Ks_per_t = [t;
            K1;
            K2];

%clc
disp('~~~~~~~~~~~~~~~~~~~~~~~~~~~~~~~~~~~~~~~~~~~~~~~~~~~~~~~~~~~~~~~~~~~~~~~~~~~~')
% Create test data output structure
Radial_Permeability_Test_Data = struct( ...
        'Test_Material',material,...
        'Ply_Number',ply_num,...
```

```
'Fiber_Volume_Fraction_Vf',Vf,...
'Preform_Inlet_Diameter_in',inlet_diameter,...
'Average_Inlet_Pressure_psi',avg_psi_in,...
'Standard_Deviation_of_Inlet_Pressure_psi',Pressure_StDev_psi,...
'Fluid_Viscosity_Pa_s',u,...
'Beta_Angle',beta,...
'K1', K1, ...
'K2', K2, ...
'Time_at_Measurement_s', t)
```

REFERENCES

REFERENCES

[1]J. Hale, "Boeing 787 from the Ground Up," *AERO*, no. QTR_04 2006, pp. 17–23.

[2]G. Marsh, "Composites get in deep with new-generation engine," *Reinf. Plast.*, vol. 50, no. 11, pp. 26–29, Dec. 2006.

[3]C. Soutis, "Carbon fiber reinforced plastics in aircraft construction," *Mater. Sci. Eng. A*, vol. 412, no. 1–2, pp. 171–176, Dec. 2005.

[4]M. W. Hyer, *Stress Analysis of Fiber-Reinforced Composite Materials*, Updated Edition. Lancaster, PA: DEStech Publications, Inc., 2009.

[5]C.-L. Lee and K.-H. Wei, "Effect of material and process variables on the performance of resin-transfer-molded epoxy fabric composites," *J. Appl. Polym. Sci.*, vol. 77, no. 10, pp. 2149–2155, 2000.

[6]S. Abrate, "Resin flow in fiber preforms," *Appl. Mech. Rev.*, vol. 55, no. 6, pp. 579–599, Oct. 2002.

[7]P. Hubert and A. Poursartip, "A Review of Flow and Compaction Modelling Relevant to Thermoset Matrix Laminate Processing," *J. Reinf. Plast. Compos.*, vol. 17, no. 4, pp. 286–318, Mar. 1998.

[8]V. Rohatgi, L. J. Lee, and A. Melton, "Overview of fibre preforming," in *Resin Transfer Moulding for Aerospace Structures*, T. M. Kruckenberg and R. Paton, Eds. Springer Netherlands, 1998, pp. 148–176.

[9]V. Rohatgi and L. J. Lee, "Moldability of Tackified Fiber Preforms in Liquid Composite Molding," *J. Compos. Mater.*, vol. 31, no. 7, pp. 720–744, Apr. 1997.

[10] C.-H. Shih and L. J. Lee, "Tackification of Textile Fiber Preforms in Resin Transfer Molding," *J. Compos. Mater.*, vol. 35, no. 21, pp. 1954–1981, Nov. 2001.

[11] G. Estrada, C. Vieux-Pernon, and S. G. Advani, "Experimental Characterization of the Influence of Tackifier Material on Preform Permeability," *J. Compos. Mater.*, vol. 36, no. 19, pp. 2297–2310, Oct. 2002.

[12] J. Chen, D. Backes, and K. Jayaraman, "Dynamics of binder displacement in liquid molding," *Polym. Compos.*, vol. 17, no. 1, pp. 23–33, Feb. 1996.

[13] L. Aktas, D. P. Bauman, S. T. Bowen, M. C. Saha, and M. C. Altan, "Effect of Distribution Media Length and Multiwalled Carbon Nanotubes on the Formation of Voids in VARTM Composites," *J. Eng. Mater. Technol.*, vol. 133, no. 4, pp. 041006–041006, Oct. 2011.

[14] F. F. Luz, S. C. Amico, J. Á. Souza, E. S. Barbosa, and A. G. B. de Lima, "Resin Transfer Molding Process: Fundamentals, Numerical Computation and Experiments," in *Numerical Analysis of Heat and Mass Transfer in Porous Media*, J. M. P. Q. Delgado, A. G. B. de Lima, and M. V. da Silva, Eds. Springer Berlin Heidelberg, 2012, pp. 121–151.

[15] K. Han, S. Jiang, C. Zhang, and B. Wang, "Flow modeling and simulation of SCRIMP for composites manufacturing," *Compos. Part Appl. Sci. Manuf.*, vol. 31, no. 1, pp. 79–86, Jan. 2000.

[16] P. Ermanni, C. Di Fratta, F. Trochu, and L. Nicolais, "Molding: Liquid Composite Molding (LCM)," in *Wiley Encyclopedia of Composites*, John Wiley & Sons, Inc., 2011.

[17] S. G. Advani and E. M. Sozer, *Process Modeling in Composites Manufacturing, Second Edition*. CRC Press, 2012.

[18] G. Morren, M. Bottiglieri, S. Bossuyt, H. Sol, D. Lecompte, B. Verleye, and S. V. Lomov, "A reference specimen for permeability measurements of fibrous reinforcements for RTM," *Compos. Part Appl. Sci. Manuf.*, vol. 40, no. 3, pp. 244–250, Mar. 2009.

[19] C. Lai and W. Young, "The effects of preforming induced variable permeabilities on the rtm molding flow," *Polym. Compos.*, vol. 20, no. 2, pp. 225–239, 1999.

[20] V. Michaud and L. Nicolais, "Fibrous Preforms and Preforming," in *Wiley Encyclopedia of Composites*, John Wiley & Sons, Inc., 2011.

[21] J. C. Brody and J. W. Gillespie, "Reactive and non-reactive binders in glass/vinyl ester composites," *Polym. Compos.*, vol. 26, no. 3, pp. 377–387, Jun. 2005.

[22] S. Aranda, F. Klunker, and G. Ziegmann, "Influence of the Binding System on the Compaction Behaviour of NCF Carbon Fibre Reinforcements," *18th Int. Conf. Compos. Mater.*, Aug. 2011.

[23] M. Tanoglu, S. Robert, D. Heider, S. H. McKnight, V. Brachos, and J. W. Gillespie Jr., "Effects of thermoplastic preforming binder on the properties of S2-glass fabric reinforced epoxy composites," *Int. J. Adhes. Adhes.*, vol. 21, no. 3, pp. 187–195, 2001.

[24] M. Tanoğlu and A. Tuğrul Seyhan, "Investigating the effects of a polyester preforming binder on the mechanical and ballistic performance of E-glass fiber reinforced polyester composites," *Int. J. Adhes. Adhes.*, vol. 23, no. 1, pp. 1–8, 2003.

[25] J. Li, C. Zhang, R. Liang, and B. Wang, "Statistical characterization and robust design of RTM processes," *Compos. Part Appl. Sci. Manuf.*, vol. 36, no. 5, pp. 564–580, May 2005.

[26] S. J. Sommerlot, T. J. Luchini, and A. C. Loos, "Modeling Advancing Flow Fronts in Composite Manufacturing," in *Proceedings of the American Society for Composites 29th Technical Conference*, San Diego, CA, September 8-10.

[27] C. H. Park and L. Woo, “Modeling void formation and unsaturated flow in liquid composite molding processes: a survey and review,” *J. Reinf. Plast. Compos.*, vol. 30, no. 11, pp. 957–977, Jun. 2011.

[28] K.-T. Hsiao, R. Little, O. Restrepo, and B. Minaie, “A study of direct cure kinetics characterization during liquid composite molding,” *Compos. Part Appl. Sci. Manuf.*, vol. 37, no. 6, pp. 925–933, Jun. 2006.

[29] A. Shojaei, S. R. Ghaffarian, and S. M. H. Karimian, “Modeling and simulation approaches in the resin transfer molding process: A review,” *Polym. Compos.*, vol. 24, no. 4, pp. 525–544, 2003.

[30] H. Abdellaoui and J. Echaabi, “Rheological models for modeling the viscoelastic behavior in liquid composite molding processes (LCM) review,” *J. Reinf. Plast. Compos.*, vol. 33, no. 8, pp. 714–732, Apr. 2014.

[31] B. Chen, A. H.-D. Cheng, and T.-W. Chou, “A nonlinear compaction model for fibrous preforms,” *Compos. Part Appl. Sci. Manuf.*, vol. 32, no. 5, pp. 701–707, May 2001.

[32] M. Matsudaira and H. Qin, “Features and Mechanical Parameters of a Fabric’s Compressional Property,” *J. Text. Inst.*, vol. 86, no. 3, pp. 476–486, Jan. 1995.

[33] B. Chen, E. J. Lang, and T.-W. Chou, “Experimental and theoretical studies of fabric compaction behavior in resin transfer molding,” *Mater. Sci. Eng. A*, vol. 317, no. 1–2, pp. 188–196, Oct. 2001.

[34] V. Michaud and A. Mortensen, “Infiltration processing of fibre reinforced composites: governing phenomena,” *Compos. Part Appl. Sci. Manuf.*, vol. 32, no. 8, pp. 981–996, Aug. 2001.

[35] M. Li, Y. Gu, Z. Zhang, and Z. Sun, “A simple method for the measurement of compaction and corresponding transverse permeability of composite prepregs,” *Polym. Compos.*, vol. 28, no. 1, pp. 61–70, Feb. 2007.

[36] B. W. Grimsley, “Characterization of the Vacuum Assisted Resin Transfer Molding Process for Fabrication of Aerospace Composites,” Virginia Polytechnic Institute and State University, Blacksburg, VA, 2005.

[37] B. W. Grimsley, R. J. Cano, P. Hubert, A. C. Loos, C. B. Kellen, and B. J. Jensen, “Preform Characterization in VARTM Process Model Development,” presented at the 36th International SAMPE Technical Conference, San Diego, CA, 2004.

[38] A. A. Somashekar, S. Bickerton, and D. Bhattacharyya, “An experimental investigation of non-elastic deformation of fibrous reinforcements in composites manufacturing,” *Compos. Part Appl. Sci. Manuf.*, vol. 37, no. 6, pp. 858–867, Jun. 2006.

[39] Y. R. Kim, S. P. McCarthy, and J. P. Fanucci, “Compressibility and relaxation of fiber reinforcements during composite processing,” *Polym. Compos.*, vol. 12, no. 1, pp. 13–19, 1991.

[40] C. M. van Wyk, “20—Note on the Compressibility of Wool,” *J. Text. Inst. Trans.*, vol. 37, no. 12, pp. T285–T292, Dec. 1946.

[41] G. L. Batch, S. Cumiskey, and C. W. Macosko, “Compaction of fiber reinforcements,” *Polym. Compos.*, vol. 23, no. 3, pp. 307–318, 2002.

[42] A. C. Loos and J. D. MacRae, “A process simulation model for the manufacture of a blade-stiffened panel by the resin film infusion process,” *Compos. Sci. Technol.*, vol. 56, no. 3, pp. 273–289, 1996.

[43] V. H. Hammond, A. C. Loos, H. B. Dexter, and G. Hasko, “Verification of a two-dimensional infiltration model for the resin transfer molding process,” Virginia Polytechnic Institute and State University, Blacksburg, VA, CCMS‐93‐15, VPI‐E‐93‐09, Aug. 1993.

[44] G. Tuncol, “Modeling the Vacuum Assisted Resin Transfer Molding (VARTM) Process for Fabrication of Fiber/Metal Hybrid Laminates,” Michigan State University, East Lansing, MI, 2010.

[45] J. C. Fingerson, A. C. Loos, and H. B. Dexter, “Verification of a Three-Dimensional Resin Transfer Molding Process Simulation Model,” Virginia Polytechnic Institute and State University, Blacksburg, VA, CCMS-95-10, VPI-E-95-04, Sep. 1995.

[46] F. Robitaille and R. Gauvin, “Compaction of textile reinforcements for composites manufacturing. I: Review of experimental results,” *Polym. Compos.*, vol. 19, no. 2, pp. 198–216, 1998.

[47] V. J. Michaud, A. Mortensen, and J. L. Sommer, “Infiltration of fibrous preforms by a pure metal: Part V. Influence of preform compressibility,” *Metall. Mater. Trans. A*, vol. 30, no. 2, pp. 471–482, Feb. 1999.

[48] P. Boisse, *Composite Reinforcements for Optimum Performance*. Elsevier, 2011.

[49] S. Bickerton, S. Comas-Cardona, I. Razali, M. Deléglise, W. A. Walbran, C. Binétruy, and P. Krawczak, “Spatial Compaction and Saturated Permeability Variations of Fibre Reinforcements,” presented at the 9th International Conference on Flow Processes in Composite Materials, Montréal, Canada, 2008.

[50] Z. Cai and T. Gutowski, “The 3-D Deformation Behavior of a Lubricated Fiber Bundle,” *J. Compos. Mater.*, vol. 26, no. 8, pp. 1207–1237, Aug. 1992.

[51] S. Toll, “Packing mechanics of fiber reinforcements,” *Polym. Eng. Sci.*, vol. 38, no. 8, pp. 1337–1350, 1998.

[52] S. Toll and J.-A. E. Manson, “Elastic Compression of a Fiber Network,” *J. Appl. Mech.*, vol. 62, no. 1, pp. 223–226, Mar. 1995.

[53] B. Chen and T.-W. Chou, “Compaction of woven-fabric preforms in liquid composite molding processes: single-layer deformation,” *Compos. Sci. Technol.*, vol. 59, no. 10, pp. 1519–1526, Aug. 1999.

[54] B. Chen and T.-W. Chou, “Compaction of woven-fabric preforms: nesting and multi-layer deformation,” *Compos. Sci. Technol.*, vol. 60, no. 12–13, pp. 2223–2231, Sep. 2000.

[55] I. Verpoest and S. V. Lomov, “Virtual textile composites software WiseTex: Integration with micro-mechanical, permeability and structural analysis,” *Compos. Sci. Technol.*, vol. 65, no. 15–16, pp. 2563–2574, Dec. 2005.

[56] H. Lin, M. Sherburn, J. Crookston, A. C. Long, M. J. Clifford, and I. A. Jones, “Finite element modelling of fabric compression,” *Model. Simul. Mater. Sci. Eng.*, vol. 16, no. 3, p. 035010, Apr. 2008.

[57] Q. T. Nguyen, E. Vidal-Sallé, P. Boisse, C. H. Park, A. Saouab, J. Bréard, and G. Hivet, “Mesoscopic scale analyses of textile composite reinforcement compaction,” *Compos. Part B Eng.*, vol. 44, no. 1, pp. 231–241, Jan. 2013.

[58] G. Hivet and P. Boisse, “Consistent 3D geometrical model of fabric elementary cell. Application to a meshing preprocessor for 3D finite element analysis,” *Finite Elem. Anal. Des.*, vol. 42, no. 1, pp. 25–49, 2005.

[59] H. Darcy, *Les fontaines publiques de la ville de Dijon: exposition et application ...* Victor Dalmont, 1856.

[60] N. K. Naik, M. Sirisha, and A. Inani, “Permeability characterization of polymer matrix composites by RTM/VARTM,” *Prog. Aerosp. Sci.*, vol. 65, pp. 22–40, Feb. 2014.

[61] J. R. Weitzenböck, R. A. Shenoi, and P. A. Wilson, “Measurement of principal permeability with the channel flow experiment,” *Polym. Compos.*, vol. 20, no. 2, pp. 321–335, Apr. 1999.

[62] R. S. Parnas, A. J. Salem, T. A. K. Sadiq, H.-P. Wang, and S. G. Advani, “The interaction between micro- and macro-scopic flow in RTM preforms,” *Compos. Struct.*, vol. 27, no. 1–2, pp. 93–107, 1994.

[63] R. Gauvin, A. Kerachni, and B. Fisa, “Variation of Mat Surface Density and Its Effect on Permeability Evaluation for RTM Modelling,” *J. Reinf. Plast. Compos.*, vol. 13, no. 4, pp. 371–383, Apr. 1994.

[64] S. Drapier, A. Pagot, A. Vautrin, and P. Henrat, “Influence of the stitching density on the transverse permeability of non-crimped new concept (NC2) multiaxial reinforcements: measurements and predictions,” *Compos. Sci. Technol.*, vol. 62, no. 15, pp. 1979–1991, Nov. 2002.

[65] A. Shojaei, F. Trochu, S. R. Ghaffarian, S. M. H. Karimian, and L. Lessard, "An Experimental Study of Saturated and Unsaturated Permeabilities in Resin Transfer Molding Based on Unidirectional Flow Measurements," *J. Reinf. Plast. Compos.*, vol. 23, no. 14, pp. 1515–1536, Sep. 2004.

[66] R. Arbter, J. M. Beraud, C. Binetruy, L. Bizet, J. Bréard, S. Comas-Cardona, C. Demaria, A. Endruweit, P. Ermanni, F. Gommer, S. Hasanovic, P. Henrat, F. Klunker, B. Laine, S. Lavanchy, S. V. Lomov, A. Long, V. Michaud, G. Morren, E. Ruiz, H. Sol, F. Trochu, B. Verleye, M. Wietgrefe, W. Wu, and G. Ziegmann, "Experimental determination of the permeability of textiles: A benchmark exercise," *Compos. Part Appl. Sci. Manuf.*, vol. 42, no. 9, pp. 1157–1168, Sep. 2011.

[67] T. S. Lundström, R. Stenberg, R. Bergström, H. Partanen, and P. A. Birkeland, "In-plane permeability measurements: a nordic round-robin study," *Compos. Part Appl. Sci. Manuf.*, vol. 31, no. 1, pp. 29–43, Jan. 2000.

[68] J. B. Alms, N. Correia, S. G. Advani, and E. Ruiz, "Experimental Procedures to Run Longitudinal Injections to Measure Unsaturated Permeability of LCM Reinforcements," 2010.

[69] N. Vernet, E. Ruiz, S. Advani, J. B. Alms, M. Aubert, M. Barburski, B. Barari, J. M. Beraud, D. C. Berg, N. Correia, M. Danzi, T. Delavière, M. Dickert, C. Di Fratta, A. Endruweit, P. Ermanni, G. Francucci, J. A. Garcia, A. George, C. Hahn, F. Klunker, S. V. Lomov, A. Long, B. Louis, J. Maldonado, R. Meier, V. Michaud, H. Perrin, K. Pillai, E. Rodriguez, F. Trochu, S. Verheyden, M. Wietgrefe, W. Xiong, S. Zaremba, and G. Ziegmann, "Experimental determination of the permeability of engineering textiles: Benchmark II," *Compos. Part Appl. Sci. Manuf.*, vol. 61, pp. 172–184, Jun. 2014.

[70] R. S. Parnas, K. M. Flynn, and M. E. Dal-Favero, "A permeability database for composites manufacturing," *Polym. Compos.*, vol. 18, no. 5, pp. 623–633, Oct. 1997.

[71] R. S. Parnas, J. G. Howard, T. L. Luce, and S. G. Advani, "Permeability characterization. Part 1: A proposed standard reference fabric for permeability," *Polym. Compos.*, vol. 16, no. 6, pp. 429–445, 1995.

[72] K. Okonkwo, P. Simacek, S. G. Advani, and R. S. Parnas, "Characterization of 3D fiber preform permeability tensor in radial flow using an inverse algorithm based on sensors and simulation," *Compos. Part Appl. Sci. Manuf.*, vol. 42, no. 10, pp. 1283–1292, Oct. 2011.

[73] D. L. Woerdeman, F. R. Phelan, and R. S. Parnas, "Interpretation of 3-D permeability measurements for RTM modeling," *Polym. Compos.*, vol. 16, no. 6, pp. 470–480, 1995.

[74] J. R. Weitzenböck, R. A. Shenoi, and P. A. Wilson, "Measurement of three-dimensional permeability," *Compos. Part Appl. Sci. Manuf.*, vol. 29, no. 1–2, pp. 159–169, 1998.

[75] S. H. Ahn, W. I. Lee, and G. S. Springer, "Measurement of the Three-Dimensional Permeability of Fiber Preforms Using Embedded Fiber Optic Sensors," *J. Compos. Mater.*, vol. 29, no. 6, pp. 714–733, Apr. 1995.

[76] P. B. Nedanov and S. G. Advani, “A Method to Determine 3D Permeability of Fibrous Reinforcements,” *J. Compos. Mater.*, vol. 36, no. 2, pp. 241–254, Jan. 2002.

[77] F. LeBel, “Experimental Characterization by Fluorescence of Capillary Flows in the Fiber Tows of Engineering Fabrics,” *Open J. Inorg. Non-Met. Mater.*, vol. 02, no. 03, pp. 25–45, 2012.

[78] G. L. Batch, Y.-T. Chen, and C. W. Macoskot, “Capillary Impregnation of Aligned Fibrous Beds: Experiments and Model,” *J. Reinf. Plast. Compos.*, vol. 15, no. 10, pp. 1027–1051, Oct. 1996.

[79] S. C. Amico and C. Lekakou, “Axial impregnation of a fiber bundle. Part 1: Capillary experiments,” *Polym. Compos.*, vol. 23, no. 2, pp. 249–263, 2002.

[80] K. Hoes, D. Dinescu, H. Sol, M. Vanheule, R. S. Parnas, Y. Luo, and I. Verpoest, “New set-up for measurement of permeability properties of fibrous reinforcements for RTM,” *Compos. Part Appl. Sci. Manuf.*, vol. 33, no. 7, pp. 959–969, Jul. 2002.

[81] J. R. Weitzenböck, R. A. Shenoi, and P. A. Wilson, “Radial flow permeability measurement. Part B: Application,” *Compos. Part Appl. Sci. Manuf.*, vol. 30, no. 6, pp. 797–813, Jun. 1999.

[82] Y. R. Kim, S. P. McCarthy, J. P. Fanucci, S. C. Nolet, and C. KOPPERNAES, “Resin flow through fiber reinforcements during composite processing,” *SAMPE Q.*, vol. 22, no. 3, pp. 16–22, 1991.

[83] G. Lebrun, C. D. Rudd, and R. Gauvin, “Laminate Temperature Distributions and Filling Tine Prediction during Non-Isothermal Impregnation of Fibre Preforms,” *J. Reinf. Plast. Compos.*, vol. 14, no. 10, pp. 1069–1080, Oct. 1995.

[84] T. J. Luchini, S. J. Sommerlot, and A. C. Loos, “Unit Cell Modeling to Predict Permeability for Composite Manufacturing,” in *Proceedings of the American Society for Composites 29th Technical Conference*, San Diego, CA, September 8-10.

[85] T. G. Gutowski, Z. Cai, S. Bauer, D. Boucher, J. Kingery, and S. Wineman, “Consolidation Experiments for Laminate Composites,” *J. Compos. Mater.*, vol. 21, no. 7, pp. 650–669, Jul. 1987.

[86] B. R. Gebart, “Permeability of Unidirectional Reinforcements for RTM,” *J. Compos. Mater.*, vol. 26, no. 8, pp. 1100–1133, Aug. 1992.

[87] X. Zeng, A. C. Long, and A. Endruweit, “Numerical prediction of permeability of textiles for the international benchmark exercise,” in *Proceedings of the 11th International Conference on Flow Processing in Composite Materials*, Auckland, New Zealand, 2012.

[88] Z.-R. Chen, L. Ye, and M. Lu, “Permeability Predictions for Woven Fabric Preforms,” *J. Compos. Mater.*, Dec. 2009.

[89] H. Tan, E. M. Languri, and K. M. Pillai, “Prediction of Permeability in a dual-scale fiber mat using two different unit cells,” presented at the The 9th International Conference on Flow Processes in Composite Materials, Montréal, Canada, 2008.

[90] J. Westhuizen and J. P. D. Plessis, “Quantification of Unidirectional Fiber Bed Permeability,” *J. Compos. Mater.*, vol. 28, no. 7, pp. 619–637, May 1994.

[91] J. Van der Westhuizen and J. Prieur Du Plessis, “An attempt to quantify fibre bed permeability utilizing the phase average Navier-Stokes equation,” *Compos. Part Appl. Sci. Manuf.*, vol. 27, no. 4, pp. 263–269, 1996.

[92] Z. Cai and A. L. Berdichevsky, “An improved self-consistent method for estimating the permeability of a fiber assembly,” *Polym. Compos.*, vol. 14, no. 4, pp. 314–323, 1993.

[93] M. V. Bruschke and S. G. Advani, “Flow of generalized Newtonian fluids across a periodic array of cylinders,” *J. Rheol. 1978-Present*, vol. 37, no. 3, pp. 479–498, May 1993.

[94] L. Skartsis, B. Khomami, and J. L. Kardos, “A semi-analytical one-dimensional model for viscoelastic impregnation of fibrous media,” *J. Adv. Mater.*, vol. 25, no. 3, pp. 38–44, 1994.

[95] M. Nordlund and T. S. Lundstrom, “Numerical Study of the Local Permeability of Noncrimp Fabrics,” *J. Compos. Mater.*, vol. 39, no. 10, pp. 929–947, May 2005.

[96] C. C. Wong, A. C. Long, M. Sherburn, F. Robitaille, P. Harrison, and C. D. Rudd, “Comparisons of novel and efficient approaches for permeability prediction based on the fabric architecture,” *Compos. Part Appl. Sci. Manuf.*, vol. 37, no. 6, pp. 847–857, Jun. 2006.

[97] J. M. P. Q. Delgado, A. G. B. de Lima, and M. V. da Silva, *Numerical Analysis of Heat and Mass Transfer in Porous Media*, vol. 27. Springer, 2012.

[98] G. Francucci, E. S. Rodríguez, and A. Vázquez, “Study of saturated and unsaturated permeability in natural fiber fabrics,” *Compos. Part Appl. Sci. Manuf.*, vol. 41, no. 1, pp. 16–21, Jan. 2010.

[99] K. M. Pillai, “Governing equations for unsaturated flow through woven fiber mats. Part 1. Isothermal flows,” *Compos. Part Appl. Sci. Manuf.*, vol. 33, no. 7, pp. 1007–1019, Jul. 2002.

[100] A. Endruweit and A. C. Long, “A model for the in-plane permeability of triaxially braided reinforcements,” *Compos. Part Appl. Sci. Manuf.*, vol. 42, no. 2, pp. 165–172, Feb. 2011.

[101] G. H. Hasko, H. B. Dexter, and M. H. Weideman, “Resin transfer molding of textile preforms for aircraft structural applications,” in *Ninth DOD/NASA/FAA Conference on Fibrous Composites in Structural Design*, 1992, pp. 1303–1315.

[102] T. A. K. Sadiq, S. G. Advani, and R. S. Parnas, “Experimental investigation of transverse flow through aligned cylinders,” *Int. J. Multiph. Flow*, vol. 21, no. 5, pp. 755–774, 1995.

[103] P. Ferland, D. Guittard, and F. Trochu, “Concurrent methods for permeability measurement in resin transfer molding,” *Polym. Compos.*, vol. 17, no. 1, pp. 149–158, 1996.

[104] M. Devillard, K.-T. Hsiao, A. Gokce, and S. G. Advani, “On-line characterization of bulk permeability and race-tracking during the filling stage in resin transfer molding process,” *J. Compos. Mater.*, vol. 37, no. 17, pp. 1525–1541, 2003.

[105] D. Bender, J. Schuster, and D. Heider, “Flow rate control during vacuum-assisted resin transfer molding (VARTM) processing,” *Compos. Sci. Technol.*, vol. 66, no. 13, pp. 2265–2271, 2006.

[106] S. Bickerton, E. M. Sozer, P. \vSimácek, and S. G. Advani, “Fabric structure and mold curvature effects on preform permeability and mold filling in the RTM process. Part II. Predictions and comparisons with experiments,” *Compos. Part Appl. Sci. Manuf.*, vol. 31, no. 5, pp. 439–458, 2000.

[107] S. Bickerton, E. M. Sozer, P. J. Graham, and S. G. Advani, “Fabric structure and mold curvature effects on preform permeability and mold filling in the RTM process. Part I. Experiments,” *Compos. Part Appl. Sci. Manuf.*, vol. 31, no. 5, pp. 423–438, 2000.

[108] C.-L. Lai and W.-B. Young, “Model resin permeation of fiber reinforcements after shear deformation,” *Polym. Compos.*, vol. 18, no. 5, pp. 642–648, 1997.

[109] W.-B. Young and S. F. Wu, “Permeability measurement of bidirectional woven glass fibers,” *J. Reinf. Plast. Compos.*, vol. 14, no. 10, pp. 1108–1120, 1995.

[110] N. Patel, V. Rohatgi, and L. J. Lee, “Micro scale flow behavior and void formation mechanism during impregnation through a unidirectional stitched fiberglass mat,” *Polym. Eng. Sci.*, vol. 35, no. 10, pp. 837–851, 1995.

[111] Y.-H. Lai, B. Khomami, and J. L. Kardos, “Accurate permeability characterization of preforms used in polymer matrix composite fabrication processes,” *Polym. Compos.*, vol. 18, no. 3, pp. 368–377, 1997.

[112] M. V. Bruschke and S. G. Advani, “RTM: filling simulation of complex three dimensional shell-like structures,” *Sampe Q.*, vol. 23, no. 1, pp. 2–11, 1991.

[113] L. Ding, C. Shih, Z. Liang, C. Zhang, and B. Wang, “In situ measurement and monitoring of whole-field permeability profile of fiber preform for liquid composite molding processes,” *Compos. Part Appl. Sci. Manuf.*, vol. 34, no. 8, pp. 779–789, Aug. 2003.

[114] S. Scholz, J. W. Gillespie Jr., and D. Heider, “Measurement of transverse permeability using gaseous and liquid flow,” *Compos. Part Appl. Sci. Manuf.*, vol. 38, no. 9, pp. 2034–2040, Sep. 2007.

[115] V. H. Hammond and A. C. Loos, “The Effects of Fluid Type and Viscosity on the Steady-State and Advancing Front Permeability Behavior of Textile Preforms,” *J. Reinf. Plast. Compos.*, vol. 16, no. 1, pp. 50–72, Jan. 1997.

[116] Y. Luo, I. Verpoest, K. Hoes, M. Vanheule, H. Sol, and A. Cardon, “Permeability measurement of textile reinforcements with several test fluids,” *Compos. Part Appl. Sci. Manuf.*, vol. 32, no. 10, pp. 1497–1504, Oct. 2001.

[117] D. A. Steenkamer, S. H. McKnight, D. J. Wilkins, and V. M. Karbhari, “Experimental characterization of permeability and fibre wetting for liquid moulding,” *J. Mater. Sci.*, vol. 30, no. 12, pp. 3207–3215, Jun. 1995.

[118] T. Bahners, “The Do’s and Don’ts of Wettability Characterization in Textiles,” *J. Adhes. Sci. Technol.*, vol. 25, no. 16, pp. 2005–2021, Jan. 2011.

[119] C. Rulison, “Two-component surface energy characterization as a predictor of wettability and dispersability,” KRUSS Application Note AN213, 2000.

[120] K. L. Mittal, *Contact Angle, Wettability and Adhesion*. CRC Press, 2006.

[121] C. D. Volpe, L. Fambri, S. Siboni, and M. Brugnara, “Wettability of Porous Materials III: Is the Wilhelmy Method Useful for Fabrics Analysis?,” *J. Adhes. Sci. Technol.*, vol. 24, no. 1, pp. 149–169, Jan. 2010.

[122] J. R. Sayre, “Vacuum-Assisted Resin Transfer Molding (VARTM) Model Development, Verification, and Process Analysis,” Virginia Polytechnic Institute and State University, Blacksburg, VA, 2000.

[123] K. J. Ahn, J. C. Seferis, and J. C. Berg, “Simultaneous measurements of permeability and capillary pressure of thermosetting matrices in woven fabric reinforcements,” *Polym. Compos.*, vol. 12, no. 3, pp. 146–152, 1991.

[124] S. Amico and C. Lekakou, “An experimental study of the permeability and capillary pressure in resin-transfer moulding,” *Compos. Sci. Technol.*, vol. 61, no. 13, pp. 1945–1959, Oct. 2001.

[125] Y. D. Parseval, K. M. Pillai, and S. G. Advani, “A Simple Model for the Variation of Permeability due to Partial Saturation in Dual Scale Porous Media,” *Transp. Porous Media*, vol. 27, no. 3, pp. 243–264, Jun. 1997.

[126] K. M. Pillai and S. G. Advani, “A Model for Unsaturated Flow in Woven Fiber Preforms during Mold Filling in Resin Transfer Molding,” *J. Compos. Mater.*, vol. 32, no. 19, pp. 1753–1783, Oct. 1998.

[127] Y. Wang, M. Moatamedi, and S. M. Grove, “Continuum Dual-scale Modeling of Liquid Composite Molding Processes,” *J. Reinf. Plast. Compos.*, vol. 28, no. 12, pp. 1469–1484, Jun. 2009.

[128] H. Tan and K. M. Pillai, “Fast liquid composite molding simulation of unsaturated flow in dual-scale fiber mats using the imbibition characteristics of a fabric-based unit cell,” *Polym. Compos.*, vol. 31, no. 10, pp. 1790–1807, Oct. 2010.

[129] H. Tan and K. M. Pillai, “Multiscale modeling of unsaturated flow in dual-scale fiber preforms of liquid composite molding I: Isothermal flows,” *Compos. Part Appl. Sci. Manuf.*, vol. 43, no. 1, pp. 1–13, Jan. 2012.

[130] B. Z. Babu and K. M. Pillai, “Experimental Investigation of the Effect of Fiber-mat Architecture on the Unsaturated Flow in Liquid Composite Molding,” *J. Compos. Mater.*, vol. 38, no. 1, pp. 57–79, Jan. 2004.

[131] J. G. Williams, C. E. M. Morris, and B. C. Ennis, “Liquid flow through aligned fiber beds,” *Polym. Eng. Sci.*, vol. 14, no. 6, pp. 413–419, 1974.

[132] B. R. Gebart and P. Lidström, “Measurement of in-plane permeability of anisotropic fiber reinforcements,” *Polym. Compos.*, vol. 17, no. 1, pp. 43–51, 1996.

[133] V. H. Hammond and A. C. Loos, “The Effects of Fluid Type and Viscosity on the Steady-State and Advancing Front Permeability Behavior of Textile Preforms,” *J. Reinf. Plast. Compos.*, vol. 16, no. 1, pp. 50–72, Jan. 1997.

[134] J. Bréard, Y. Henzel, F. Trochu, and R. Gauvin, “Analysis of dynamic flows through porous media. Part I: Comparison between saturated and unsaturated flows in fibrous reinforcements,” *Polym. Compos.*, vol. 24, no. 3, pp. 391–408, 2003.

[135] S. K. Kim and I. M. Daniel, “Observation of Permeability Dependence on Flow Rate and Implications for Liquid Composite Molding,” *J. Compos. Mater.*, vol. 41, no. 7, pp. 837–849, Apr. 2007.

[136] C. Lekakou, M. A. K. Johari, D. Norman, and M. G. Bader, “Measurement techniques and effects on in-plane permeability of woven cloths in resin transfer moulding,” *Compos. Part Appl. Sci. Manuf.*, vol. 27, no. 5, pp. 401–408, 1996.

[137] K. M. Pillai, “Modeling the Unsaturated Flow in Liquid Composite Molding Processes: A Review and Some Thoughts,” *J. Compos. Mater.*, vol. 38, no. 23, pp. 2097–2118, Dec. 2004.

[138] J. Bréard, A. Saouab, and G. Bouquet, “Numerical simulation of void formation in LCM,” *Compos. Part Appl. Sci. Manuf.*, vol. 34, no. 6, pp. 517–523, Jun. 2003.

[139] C.-H. Shih and L. J. Lee, “Effect of fiber architecture on permeability in liquid composite molding,” *Polym. Compos.*, vol. 19, no. 5, pp. 626–639, Oct. 1998.

[140] J. P. Chick, C. D. Rudd, P. A. Van Leeuwen, and T. I. Frenay, “Material characterization for flow modeling in structural reaction injection molding,” *Polym. Compos.*, vol. 17, no. 1, pp. 124–135, 1996.

[141] A. W. Chan, D. E. Larive, and R. J. Morgan, “Anisotropic Permeability of Fiber Preforms: Constant Flow Rate Measurement,” *J. Compos. Mater.*, vol. 27, no. 10, pp. 996–1008, Oct. 1993.

[142] W. B. Young, K. Rupel, K. Han, L. J. Lee, and M. J. Liou, “Analysis of resin injection molding in molds with preplaced fiber mats. II: Numerical simulation and experiments of mold filling,” *Polym. Compos.*, vol. 12, no. 1, pp. 30–38, 1991.

[143] L. Trevino, K. Rupel, W. B. Young, M. J. Liou, and L. J. Lee, “Analysis of resin injection molding in molds with preplaced fiber mats. I: Permeability and compressibility measurements,” *Polym. Compos.*, vol. 12, no. 1, pp. 20–29, 1991.

[144] B. Y. Kim, G. J. Nam, and J. W. Lee, “Optimization of filling process in RTM using a genetic algorithm and experimental design method,” *Polym. Compos.*, vol. 23, no. 1, pp. 72–86, 2002.

[145] P. Forchheimer, *Hydraulik*. B.G. Teubner, 1914.

[146] E. Heardman, C. Lekakou, and M. G. Bader, “In-plane permeability of sheared fabrics,” *Compos. Part Appl. Sci. Manuf.*, vol. 32, no. 7, pp. 933–940, Jul. 2001.

[147] P. Smith, C. D. Rudd, and A. C. Long, “The effect of shear deformation on the processing and mechanical properties of aligned reinforcements,” *Compos. Sci. Technol.*, vol. 57, no. 3, pp. 327–344, 1997.

[148] C.-L. Lai and W.-B. Young, “Model resin permeation of fiber reinforcements after shear deformation,” *Polym. Compos.*, vol. 18, no. 5, pp. 642–648, 1997.

[149] A. Hammami, F. Trochu, R. Gauvin, and S. Wirth, “Directional Permeability Measurement of Deformed Reinforcement,” *J. Reinf. Plast. Compos.*, vol. 15, no. 6, pp. 552–562, Jun. 1996.

[150] F. D. Dungan, M. T. Senoguz, A. M. Sastry, and D. A. Faillaci, “On the Use of Darcy Permeability in Sheared Fabrics,” *J. Reinf. Plast. Compos.*, vol. 18, no. 5, pp. 472–484, Mar. 1999.

[151] A. Endruweit, X. Zeng, and A. C. Long, “Effect of specimen history on structure and in-plane permeability of woven fabrics,” *J. Compos. Mater.*, May 2014.

[152] J. Wang, J. R. Page, and R. Paton, “Experimental investigation of the draping properties of reinforcement fabrics,” *Compos. Sci. Technol.*, vol. 58, no. 2, pp. 229–237, 1998.

[153] C. Demaría, E. Ruiz, and F. Trochu, “In-plane anisotropic permeability characterization of deformed woven fabrics by unidirectional injection. Part II: Prediction model and numerical simulations,” *Polym. Compos.*, vol. 28, no. 6, pp. 812–827, Dec. 2007.

[154] P. Simacek and S. G. Advani, “Permeability model for a woven fabric,” *Polym. Compos.*, vol. 17, no. 6, pp. 887–899, Dec. 1996.

[155] T. M. McBride and J. Chen, “Unit-cell geometry in plain-weave fabrics during shear deformations,” *Compos. Sci. Technol.*, vol. 57, no. 3, pp. 345–351, 1997.

[156] A. Endruweit and P. Ermanni, “The in-plane permeability of sheared textiles. Experimental observations and a predictive conversion model,” *Compos. Part Appl. Sci. Manuf.*, vol. 35, no. 4, pp. 439–451, Apr. 2004.

[157] M. Louis and U. Huber, “Investigation of shearing effects on the permeability of woven fabrics and implementation into LCM simulation,” *Compos. Sci. Technol.*, vol. 63, no. 14, pp. 2081–2088, Nov. 2003.

[158] F. Loix, P. Badel, L. Orgéas, C. Geindreau, and P. Boisse, “Woven fabric permeability: From textile deformation to fluid flow mesoscale simulations,” *Compos. Sci. Technol.*, vol. 68, no. 7–8, pp. 1624–1630, Jun. 2008.

[159] A. Endruweit, P. McGregor, A. C. Long, and M. S. Johnson, “Influence of the fabric architecture on the variations in experimentally determined in-plane permeability values,” *Compos. Sci. Technol.*, vol. 66, no. 11–12, pp. 1778–1792, Sep. 2006.

[160] F. D. Dungan, M. T. Senoguz, A. M. Sastry, and D. A. Faillaci, “Simulations and Experiments on Low-Pressure Permeation of Fabrics: Part I—3D Modeling of Unbalanced Fabric,” *J. Compos. Mater.*, vol. 35, no. 14, pp. 1250–1284, Jul. 2001.

[161] K. Hoes, D. Dinescu, H. Sol, R. S. Parnas, and S. Lomov, “Study of nesting induced scatter of permeability values in layered reinforcement fabrics,” *Compos. Part Appl. Sci. Manuf.*, vol. 35, no. 12, pp. 1407–1418, Dec. 2004.

[162] V. Achim and E. Ruiz, “Guiding selection for reduced process development time in RTM,” *Int. J. Mater. Form.*, vol. 3, no. 2, pp. 1277–1286, Aug. 2009.

[163] O. Restrepo, K.-T. Hsiao, A. Rodriguez, and B. Minaie, “Development of adaptive injection flow rate and pressure control algorithms for resin transfer molding,” *Compos. Part Appl. Sci. Manuf.*, vol. 38, no. 6, pp. 1547–1568, Jun. 2007.

[164] M. O. W. Richardson and Z. Y. Zhang, “Experimental investigation and flow visualisation of the resin transfer mould filling process for non-woven hemp reinforced phenolic composites,” *Compos. Part Appl. Sci. Manuf.*, vol. 31, no. 12, pp. 1303–1310, Dec. 2000.

[165] J. Ni, Y. Zhao, L. James Lee, and S. Nakamura, “Analysis of two-regional flow in liquid composite molding,” *Polym. Compos.*, vol. 18, no. 2, pp. 254–269, 1997.

[166] R. Gauvin and F. Trochu, “Key issues in numerical simulation for liquid composite molding processes,” *Polym. Compos.*, vol. 19, no. 3, pp. 233–240, 1998.

[167] J. M. Lawrence, J. Barr, R. Karmakar, and S. G. Advani, “Characterization of preform permeability in the presence of race tracking,” *Compos. Part Appl. Sci. Manuf.*, vol. 35, no. 12, pp. 1393–1405, Dec. 2004.

[168] S. Bickerton and S. G. Advani, “Characterization and modeling of race-tracking in liquidcomposite molding processes,” *Compos. Sci. Technol.*, vol. 59, no. 15, pp. 2215–2229, Nov. 1999.

[169] W.-B. Young and C.-L. Lai, “Analysis of the edge effect in resin transfer molding,” *Compos. Part Appl. Sci. Manuf.*, vol. 28, no. 9–10, pp. 817–822, 1997.

[170] A. George, “Optimization of Resin Infusion Processing for Composite Materials: Simulation and Characterization Strategies,” University of Stuttgart, Stuttgart, Germany, 2011.

[171] M. C. McCrary-Dennis and O. I. Okoli, “A review of multiscale composite manufacturing and challenges,” *J. Reinf. Plast. Compos.*, vol. 31, no. 24, pp. 1687–1711, Dec. 2012.

[172] T. Mahrholz, J. Stängle, and M. Sinapius, “Quantitation of the reinforcement effect of silica nanoparticles in epoxy resins used in liquid composite moulding processes,” *Compos. Part Appl. Sci. Manuf.*, vol. 40, no. 3, pp. 235–243, Mar. 2009.

[173] R. Umer, E. M. Waggy, and A. C. Loos, “Processing characteristics and mechanical properties of glass fabric reinforcements coated with graphite nanoparticles,” presented at the 26th Annual Technical Conference of the American Society for Composites 2011 and the 2nd Joint US-Canada Conference on Composites, 2011, vol. 1, pp. 775–787.

[174] D. Chen, “Dynamic Contact Angle Analyzer Tutorial.” Thermo Cahn Instruments, Jan-2003.

[175] E. Drown, “Surface Tension Measurement Training,” 16-Feb-2015.

[176] “SC-15: Toughened Epoxy Resin System.” Applied Poleramic Inc.

[177] M. J. Schick, *Surface Characteristics of Fibers and Textiles*, Part II. New York, New York: CRC Press, 1977.

[178] G. E. Hammer and L. T. Drzal, “Graphite fiber surface analysis by X-ray photoelectron spectroscopy and polar/dispersive free energy analysis,” *Appl. Surf. Sci.*, vol. 4, no. 3–4, pp. 340–355, Apr. 1980.

[179] F. M. White, *Fluid Mechanics*. McGraw Hill, 2011.

[180] R. L. Bendure, “Dynamic adhesion tension measurement,” *J. Colloid Interface Sci.*, vol. 42, no. 1, pp. 137–144, Jan. 1973.

[181] J. Verrey, V. Michaud, and J.-A. E. Månson, “Dynamic capillary effects in liquid composite moulding with non-crimp fabrics,” *Compos. Part Appl. Sci. Manuf.*, vol. 37, no. 1, pp. 92–102, Jan. 2006.

[182] A. Mortensen and T. Wong, “Infiltration of fibrous preforms by a pure metal: Part III. capillary phenomena,” *Metall. Trans. A*, vol. 21, no. 8, pp. 2257–2263, Aug. 1990.

[183] J. T. Gostick, M. W. Fowler, M. D. Pritzker, M. A. Ioannidis, and L. M. Behra, “In-plane and through-plane gas permeability of carbon fiber electrode backing layers,” *J. Power Sources*, vol. 162, no. 1, pp. 228–238, Nov. 2006.

[184] D. Cornell and D. L. Katz, “Flow of Gases through Consolidated Porous Media,” *Ind. Eng. Chem.*, vol. 45, no. 10, pp. 2145–2152, Oct. 1953.

[185] “Fluent 6.3 User’s Guide.” Fluent Inc., Sep-2006.

[186] T. H. Chilton and A. P. Colburn, “Pressure Drop in Packed Tubes,” *Ind. Eng. Chem.*, vol. 23, no. 8, pp. 913–919, Aug. 1931.

[187] L. Green and P. Duwez, “Fluid flow through porous metals,” *J. Appl. Mech.*, vol. 18, pp. 39–45, 1951.

[188] S. Ergun, “Fluid flow through packed columns,” *Chem. Eng. Prog.*, vol. 48, pp. 89–94.

[189] H. Ma and D. W. Ruth, “The microscopic analysis of high forchheimer number flow in porous media,” *Transp. Porous Media*, vol. 13, no. 2, pp. 139–160, Nov. 1993.

[190] F. Thauvin and K. K. Mohanty, “Network Modeling of Non-Darcy Flow Through Porous Media,” *Transp. Porous Media*, vol. 31, no. 1, pp. 19–37, Apr. 1998.

[191] Z. Zeng and R. Grigg, “A Criterion for Non-Darcy Flow in Porous Media,” *Transp. Porous Media*, vol. 63, no. 1, pp. 57–69, Apr. 2006.

[192] S. J. Sommerlot, T. J. Luchini, and A. C. Loos, “Permeability Measurement and Flow Front Modeling for Composite Manufacturing,” in *Proceedings of the Composites and Advanced Materials Expo*, Orlando, FL, October 13-16.

[193] J. R. Weitzenböck, R. A. Shenoi, and P. A. Wilson, “Radial flow permeability measurement. Part A: Theory,” *Compos. Part Appl. Sci. Manuf.*, vol. 30, no. 6, pp. 781–796, Jun. 1999.